# Design framework for bamboo culms

A study of bamboo reciprocal structures

by

**Martha Cecilia Godina Rodríguez**

A thesis submitted for the degree of

Doctor of Philosophy

of the

University College London

Department of Civil, Environmental and Geomatic Engineering

August 2019

I, Martha Cecilia Godina Rodríguez confirm that the work presented in this thesis is my own. Where information has been derived from other sources, I confirm that this has been indicated in the thesis.

**Abstract**

Bamboo is a fast-growing plant and renewable material that has the potential to contribute to the development of a more sustainable construction industry. However, the poor understanding of the use of round bamboo (culm) as a building material, including appropriate methods for determining its material properties, jointing techniques and structural systems, prevents its wider use in construction. The cause of many of the issues of bamboo in construction is associated with its inherent variable and irregular properties.

This thesis presents a design framework set out to address these issues by incorporating the non-uniform properties of bamboo as part of the design process. It consists of various methods, mostly based on digital technologies, for determining, analysing and managing the data gathered of geometric, physical and mechanical properties to develop a discretised digital model of bamboo culms with non-uniform embedded properties. The geometry of bamboo culms is determined using 3D scanning. The mechanical properties are also measured by a combination of mechanical testing on small samples, image processing of the microstructure and numerical models. Methods that minimise the time to measure physical properties were tested, including the adaptation of the data obtained from a moisture meter designed for wood. In this research, the framework was demonstrated by using reciprocal systems as a potentially sound structural system for the construction of wide span bamboo structures. Reciprocal systems have the advantage of joining only two elements at a time, thus simplifying the design of connections.

This research provides insight into the viability of transferring these digital technologies to the bamboo industry with the aim of providing a platform for the design and construction of safe bamboo structures thereby encouraging the usage of bamboo for sustainable construction. The advantages and challenges of the proposed methods are discussed, and possible directions for future research are outlined.

## Impact Statement

The potential impact of this research is in the environmental and technological areas. The developed framework provides a platform for the potential of technology integration to the bamboo industry as a means to address some of the most common issues associated with bamboo culms in construction, namely the non-uniform properties.

The time frame of this research is incrementally and at international level, particularly in developing countries where the majority of the urbanisation will be concentrated in the next decades (UN, 2018a). The proposed framework was developed to be used project based. In this thesis the framework was tested and validated by using one-to-one scale prototypes of small size with two different bamboo species. The framework needs to be further validated in a project based before transferring the methods and technologies directly in industry. It is expected that its fully implementation benefits the bamboo industry enabling the safe and efficient use of bamboo culms to locations where bamboo grows, and also contributes to the current construction demands with sustainable and affordable materials.

This research opens new opportunities for collaboration with industry in bamboo plantations and design consultancies working with natural materials for construction, and inside academia for the further developments of methods and implementation of the whole framework. This research will be disseminated through publishing in journal papers and its implementation must be accompanied by training courses for the transfer of technology.

**Acknowledgements**

I would like to thank all the people that supported, encouraged or inspired me throughout this research. First of all, I would like to thank my supervisors for their support at different steps of this journey. I want to thank Dr. Rodolfo Lorenzo for giving me the opportunity to start this project. My sincere gratitude to Prof. Gert van der Heijden for his guidance, support and constructive feedback in every aspect of my research, I am very grateful for that. I also want to thank my examiners, Dr Wen-Shao Chang and Dr. Pedro Ferreira, for their engagement and their feedback which helped me to improve this work.

My research involved plenty of laboratory work, which allowed me to collaborate and work alongside many people. I first want to thank the technicians from the Civil, Environmental and Geomatic Engineering Department at UCL, especially to Leslie Irwin for all his support with my experimental work. I also want to thank Chuhee and Leonel who joined the bamboo research team at UCL, walking part of this journey with company was much better. Thank you also to Dr-Ing. Oliva and Marcos Ontiveros for their warm welcome during the two research stays at UNAM in 2016 and 2017. I also want to thank Pedro Ortega, who helped me with the fabrication of timber connections during my research stay at UNAM. I am thankful to The Institute of Making at UCL, for their support and for providing the space and tools necessary to explore several aspects of my research. I also want to thank David Trujillo and Suneina Jangra from Coventry University and Magdalena Trujillo from UNAM for the bamboo material and the test results shared. This material and data made possible the validation of an important part of this thesis.

I am thankful for the financial support provided by the Engineering and Physical Sciences Research Council (EPSRC).

I am grateful to have shared this journey with all my friends and colleagues from UCL. I am very lucky to have them in my life, thank you for all the memories.

Finally, my deepest gratitude is for my family in Mexico and UK. Thank you to my parents and my brother, for being always present in my life during all my PhD even at thousand miles away. Thank you dad, for answering always all my questions. And thank you Mau, for being always by my side, your love and patience were invaluable all this time.

To my parents, Monchis and Mau.
I love you all.

# Contents

# List of Figures

# List of Tables

# Nomenclature

**Chapter 3**

| | |
|---|---|
| $\rho$ | Density |
| $\rho_0$ | Oven-dry density |
| $A$ | Area of bamboo cross-section |
| $D$ | Diameter of bamboo |
| $E_c$ | Compressive elastic modulus |
| $E_{eq,b}$ | Equivalent elastic modulus from bimodulus model |
| $E_{eq,c}$ | Equivalent elastic modulus from composite model |
| $E_{l,i}$ | Elastic modulus of each lamina |
| $f_c$ | Compressive strength |
| $f_v$ | Shear strength |
| $I$ | Second moment of area of bamboo cross-section |
| $t$ | Thickness of bamboo |
| $t_i$ | Thickness of each lamina |
| $vf$ | Radial distribution of volume fraction |
| $w$ | Moisture content |
| VF | Volume fraction |

**Chapter 4**

| | |
|---|---|
| $\beta$ | Angle of rollers and supports |
| $\gamma$ | Ovalisation of bamboo cross-section |
| $\lambda$ | Out-of-straightness |

$\Phi$ Shape factor

$a$ Lead or linear motion

$c$ Circumference of bamboo

$D$ Diameter of bamboo

$D_b$ Diameter at the bottom of the culm

$D_R$ Diameter taper ratio

$D_t$ Diameter at the top of the culm

$d_{max}$ Maximum orthogonal distance between bamboo coordinates and new bamboo longitudinal axis.

$l_D$ Length between two diameter measurements

$l_t$ Length between two thickness measurements

$r$ Radius of bamboo at the middle of the culm wall

$r_{max}$ Maximum radius of bamboo

$r_{min}$ Minimum radius of bamboo

$t$ Thickness of bamboo

$t_b$ Thickness at the bottom of the culm

$t_R$ Thickness taper ratio

$t_t$ Thickness at the top of the culm

**Chapter 5**

$\rho$ Density of bamboo

$\rho_0$ Oven-dry density

$\rho_w$ Air-dried density at moisture content $w$

$\rho_y$ Wet density of bamboo sample

$a_f$ Area of the fibres

$a_m$ Area of the matrix

$dA$ Area of for a long element in the width direction of the sample

$E_c$ Compressive elastic modulus

$E_{l,i}$ Elastic modulus for each lamina

$F$ Final dimension

$I$ Initial dimension

$K_s$ Correction factor to consider the influence of moisture content on the volumetric shrinkage

$l_1$ Thickness of the outer lamina

$l_2$ Thickness of the middle lamina

$l_3$ Thickness of the inner lamina

$m_0$ Oven-dried mass of bamboo sample

$m_0$ Oven-dry mass of bamboo sample

$m_1$ Green mass of bamboo sample

$m_w$ Mass of the bamboo sample at moisture content $w$

$s$ Shrinkage in percentage

$t_1$ Thickness of the outer lamina

$t_2$ Thickness of the outer and middle lamina

$t_3$ Thickness of of the whole lamina

$V$ Volume

$V_0$ Volume of the oven-dried bamboo sample

$V_1$ Green volume

$V_w$ Volume of the bamboo sample at moisture content $w$

$V_{max}$ Volume of the bamboo sample with saturated water

$vf$ Volume fraction in the radial direction

$vf_i$ Volume fraction for each lamina

$vf_{avg}$ Average volume fraction for thw whole lamina

$vf_{guadua}$ Model describing the variation of volume fraction in the radial direction for guadua species

$vf_{oldhamii}$ Model describing the variation of volume fraction in the radial direction for oldhamii species

$w$ Moisture content

$w_b$ Width of bamboo sample

$x_1$ Radial position in the culm wall thickness indicating the inner side of the outer lamina

$x_2$ Radial position in the culm wall thickness indicating the inner side of the middle lamina

$x_3$ Radial position in the culm wall thickness indicating the inner side of the inner lamina

RS Reference scale measurement from hand-held moisture meter

VF Volume fraction

$\text{VF}_{vb}$ Volume fraction of vascular bundles

**Chapter 6**

$[C]$ Stiffness matrix for a transversely isotropic material

$[L]$ Submatrix $[L]$ for a transversely isotropic material

$[M]$ Submatrix $[M]$ for a transversely isotropic material

$[Q]$ Stiffness matrix for a single lamina

$[S]$ Compliance matrix for a transversely isotropic material

$\alpha$ Angle from the vertical axis of the cross-section to a portion in the tensile zone

$\alpha_{ij}$, $\beta_{ij}$, $\delta_{ij}$ Elements of the compliance matrices of the laminate

$\alpha_{ij}^{\varrho}$, $\beta_{ij}^{\varrho}$, $\delta_{ij}^{\varrho}$ Elements of the compliance matrices of the laminate at the neutral plane

$\beta$ Angle from the vertical axis of the cross-section to a portion in the compressive zone

$\beta_{11}^{MP}, \hat{\delta}_{11}^{MP}$ Elements of compliance matrix at midplane

$\chi_{xz}$ Angle of rotation from the normals at the reference plane

$\delta$ Deflection in the bamboo beam under transverse loads

$\Delta_L$ Length of small element

$\epsilon_c$ Strains in the compressive zone

$\epsilon_t$ Strains in the tensile zone

$\epsilon_x$ Normal strain in the $x$ direction

$\epsilon_x^\circ$ Normal strain in the $x$ direction at the reference plane

$\epsilon_y$ Normal strain in the $y$ direction

$\epsilon_y^\circ$ Normal strain in the $y$ direction at the reference plane

$\epsilon_z$ Normal strain in the $z$ direction

$\epsilon_\alpha$ Strains in a portion of the compressive zone of the cross-section

$\epsilon_\beta$ Strains in a portion of the tensile zone of the cross-section

$\gamma$ Angle from 0 to $\pi$ from the vertical axis at the tensile zone

$\gamma_{xy}$ Shear strain in the $x-y$ plane

$\gamma_{xy}^\circ$ Shear strain in the $x-y$ plane at the reference plane

$\gamma_{xz}$ Shear strain in the $x-z$ plane

$\gamma_{yz}$ Shear strain in the $y-z$ plane

$\hat{\alpha}$ Angular deformation from the $x$ axis

$\hat{\beta}$ Angular deformation from the $y$ axis

$\hat{\beta}_{11}^{MP}, \hat{\delta}_{11}^{MP}$ Elements of compliance matrix for close sections at midplane

$\hat{\varrho}$ Distance between the reference plane and neutral plane for closed section orthotropic symmetrical layout

$\hat{EI}_{yy}, \hat{EI}_{zz}$ Bending stiffness of the beam in the $yy$ and $zz$ directions

$\hat{R}$ Radius at the midplane of the cross-section thickness

$\nu_{13}$ Longitudinal Poisson's ratio in the $1-3$ plane

$\nu_{21}$ Longitudinal Poisson's ratio in the $2-1$ plane

$\nu_{23}$ Poisson's ratio in the $2-3$ plane

$\nu_{ij}$ Poisson's ratio

$\sigma_c$ Compressive strength of bamboo

$\sigma_f$ Fibre tensile strength

$\sigma_m$ Matrix tensile strength

$\sigma_t$ Tensile strength of bamboo

| | |
|---|---|
| $\sigma_u$ | Bending strength |
| $\sigma_z$ | Normal stress out-of-plane |
| $\sigma_z$ | Out-of-plane normal stress |
| $\tau$ | Transverse shear stress |
| $\tau_u$ | Shear stress measured from bending test |
| $\tau_{xy}$ | Shear stress in the $x-y$ plane |
| $\tau_{xz}$ | Out-of-plane shear stress in the $x-z$ plane |
| $\tau_{xz}$ | Shear stress in the $x-z$ plane |
| $\tau_{xz}$ | Shear stress out-of-plane in the $x-z$ plane |
| $\tau_{yz}$ | Out-of-plane shear stress in the $y-z$ plane |
| $\tau_{yz}$ | Shear stress in the $y-z$ plane |
| $\tau_{yz}$ | Shear stress out-of-plane in the $y-z$ plane |
| $\theta$ | Angle from the vertical axis of the cross-section to the neutral axis |
| $\tilde{\varrho}$ | Distance between the reference plane and neutral plane for open section orthotropic symmetrical layout |
| $\zeta$ | Angle between the shear plane and tilted plane in small sample to test the shear strength of bamboo |
| $A$ | Area of bamboo cross-section |
| $A_c$ | Area of the cross-section in the compressive zone |
| $A_t$ | Area of the cross-section in the tensile zone |
| $D$ | Diameter of bamboo |
| $D_{avg}$ | Average diameter |
| $E$ | Elastic modulus |
| $E_1$ | Modulus of elasticity in the longitudinal direction |
| $E_2$ | Modulus of elasticity in the transverse direction |
| $E_3$ | Modulus of elasticity in the transverse direction (out-of-plane) |
| $E_b$ | Elastic modulus from bending test |
| $E_c$ | Compressive elastic modulus from small coupons |

$E_f$ Elastic modulus of the fibre

$E_m$ Elastic modulus of the matrix

$E_t$ Tensile elastic modulus

$E_{avg}$ Average elastic modulus

$E_{c,f}$ Compressive elastic modulus from full culm specimens

$E_{c,g}, E_{c,o}$ Lineal models for the relationship between $E_c$ and VF for guadua and olhdamii species

$E_{eq,b}$ Equivalent bending elastic modulus from bimodulus model

$E_{eq_c}$ Equivalent bending elastic modulus from composite material model

$E_{eq}$ Equivalent bending elastic modulus

$E_{l1}, E_{l2}, E_{l3}$ Elastic modulus for the outer, middle and inner laminas

$F$ Applied maximum load

$f_c$ Compressive strength from small coupons

$F_c$ Compressive forces acting in the cross-section

$F_t$ Tensile forces acting in the cross-section

$f_t$ Tensile strength estimated

$F_t, F_{tA}, F_{tB}$ Horizontal forces

$f_v$ Shear strength from small coupons

$f_x$ Force acting on a small element in the $x$ direction

$f_y$ Force acting on a small element in the $y$ direction

$f_z$ Force acting on a small element in the $z$ direction

$f_{c,f}$ Compressive strength from full culm specimens

$f_{c,m}$ Maximum compressive stresses in the cross-section calculated from bimodulus model

$f_{t,m}$ Maximum tensile stresses in the cross-section calculated from bimodulus model

$f_{v,f}$ Shear strength from full culm specimens

$f_{v,m}$ Maximum shear stresses in the cross-section calculated from bimodulus model

$G_{12}$ Longitudinal shear modulus

$G_{13}$ Longitudinal shear modulus in the $1-3$ plane

$G_{23}$ Longitudinal shear modulus in the $2-3$ plane

$h_b$ Distance from the reference plane to the inner layer of the laminate

$h_t$ Distance from the reference plane to the outer layer of the laminate

$I$ Second moment of are of bamboo cross-section

$I_B$ Second moment of area of bamboo

$I_c$ Second moment of area of a portion in the compressive zone of the cross-section

$I_t$ Second moment of area of a portion in the tensile zone of the cross-section

$K$ Variable $= \left[\frac{1}{R\left[(vf-n)[R\theta+2(x-R)\sin\theta+\frac{1}{2}R\sin 2\theta]+n\pi R\right]}\right]$

$K_{E_c,w}, K_{f_c,w}, K_{f_v,w}$ Correction factors to adjust the results of $E_c$, $f_c$ and $f_v$ to 12% moisture content

$L$ Clear span

$l_1, l_2, l_3$ Thickness of the outer, middle and inner laminas

$M$ Bending moment in the bamboo cross-section

$M_\alpha$ Bending moment in tensile zone of the bamboo cross-section

$M_\beta$ Bending moment in the compressive zone of the bamboo cross-section

$M_A, M_B$ Moments caused in a small element due to horizontal forces $\Delta F_t$ acting over a length $\Delta_L$

$N$ Total number of bamboo culms

$n$ Ratio $E_c$ to $E_t$

$Q$ Moment of the segment about the neutral axis of the section

$q$ Shear flow

$R$ Radius of bamboo from the neutral plane

$t$ Thickness of bamboo

$u$ Displacement in the $x$ direction of the laminate

$V$ Internal shear forces

$v$ Displacement in the $y$ direction of the laminate

$w$ Deformation of the cross-section in the vertical direction

$x$ Distance from the neutral plane to the bottom edge of the beam cross-section

$x_1, x_2, x_3$ Position of the inner side of each lamina (outer, middle and inner)

$y_\alpha$ Distance from the centroid of the cross-section to a portion $d_\alpha$ in the tensile zone

$y_\beta$ Distance from the centroid of the cross-section to a portion $d_\beta$ in the compressive zone

$z_0$ Distance from the reference plane to the inner side of inner layer of laminate

$z_K$ Distance from the reference plane to the outer side of outer layer of laminate

$z_k$ Distance from the reference plane to the inner side of middle layer of laminate

$z_{K-1}$ Distance from the reference plane to the inner side of outer layer of laminate

$[A]$, $[B]$, $[D]$ Laminate stiffness matrices

VF Volume fraction

**Chapter 7**

$[\boldsymbol{Ce_i}]$ Matrices for the elements at each iteration for the first step

$[\boldsymbol{E}]$ Matrix indicating the elements for each iteration for the second step

$[\boldsymbol{T}]$ Translation matrix

$[\boldsymbol{Ve}]$ Matrix indicating the vertices for each iteration for the first step

$[\boldsymbol{V}]$ Matrix indicating the direction of the bamboos in the elements

$[\boldsymbol{x_1}]$ Vector with angles $\alpha$ from the design variable for geometric transformations

$[\boldsymbol{x_2}]$ Vector with distances $d$ from the design variable for geometric transformations

$[\boldsymbol{X_c}]$ Design variable matrix, indicating the culms that can be used for each element in the structure

$[\boldsymbol{X}]$ Design variable for geometric transformations

$\alpha$ Angle from the design variable for the geometric transformation

$\eta$ Normalised value

$\Gamma$ Tolerances for the translations in the design variable

$\hat{\alpha}$ Dihedral angle

$\lambda$ Rotational angle

$\mu$ Space between outer edge surface of two bamboo culms in one connection

$\rho$ Radius of curvature

$A, B, C, D$ Possible allowed distances for constraint criteria in longitudinal direction for timber connections

$b$ Bamboo culms

$c$ Connections

$d$ Diameters at internodes

$d$ Distances from the design variable for the geometric transformation

$e, e_i, e_o$ Elements, and inner and outer elements

$EI$ Bending stiffness

$F$ Coordinates of feasible regions

$f$ Faces of mesh

$l$ Length between connections

$LB_1, UB_1$ Lower and upper bound for $\alpha$ in the design variable

$LB_2, UB_2$ Lower and upper bound for $d$ in the design variable

$M$ Bending moment

$n$ Vector normal to face

$p$ Rotational vector

$P_0, P_1$ Endpoints of connectors

$r_1, r_2$ Radius of the two bamboo culms jointed at each connection

$s$ Bamboo node coordinates

$t, t_u, t_l$ Coordinates of the feasible regions

$u$ Eccentricities

$u_c$ Target eccentricities

$v$ Vertex

$w$ Tolerances for the eccentricities in the inequality constraints

$x_c$ Coordinate of the design variable to minimise

$xs$ Distance between node and intranode coordinates

$xt$ Coordinates of intranode limits for each node in the culms

**Chapter 8**

$\nu$ Poisson's ratio

$\rho$ Density

$A_x$ Magnitude of axial stresses

$B_y$ Magnitude of bending stresses in the $y$ direction

$B_z$ Magnitude of bending stresses in the $z$ direction

$D$ Diameter for internode

$E$ Elastic modulus

$F_x$ Magnitude of axial forces

$F_y$ Magnitude of shear forces in $y$ direction

$F_z$ Magnitude of shear forces in $z$ direction

$F_{yz}$ Resultant shear force

$G$ Shear modulus

$K_{xy}$ Stiffness of spring support

$M_{xx}$ Magnitude of torsional moments

$M_{yy}$ Magnitude of bending moments in the $y$ direction

$M_{yz}$ Resultant bending moment

$M_{zz}$ Magnitude of bending moments in the $z$ direction

$R_{xyz}$ Rotations at the nodes in radians

$R_{xy}$ Horizontal reaction forces

$S_y$ Magnitude of shear stresses in the $y$ direction

$S_z$ Magnitude of shear stresses in the $z$ direction

$t$ Thickness for internode

$U_z$ Vertical displacements

$U_{xy}$ Horizontal displacements

**Chapter 9**

| | |
|---|---|
| $\alpha$ | Hoop stress deformation factor |
| $\beta$ | Angle between two bamboo culms |
| $\mu$ | Coefficient of friction |
| $\sigma_A$ | Maximum stress at Point A |
| $\sigma_B$ | Maximum stress at Point B |
| $\sigma_\theta$ | Circumferential normal stress |
| $\theta$ | Angle to define the depth of the groove in timber block |
| $A$ | Area of the ring in the longitudinal direction |
| $a$ | Depth of the chord of groove in timber block |
| $c$ | Distance from groove to centre of steel threaded rod |
| $D$ | Diameter of bamboo |
| $e$ | Distance between the centroid and the neutral axis |
| $F$ | Frictional force |
| $f$ | Width dimension of timber blocks at both sides of chord |
| $h, g$ | Thickness for middle, and bottom and top timber blocks |
| $I$ | Second moment of area of a longitudinal section of the ring |
| $K_2$ | Factor $1 - \alpha$ |
| $L$ | Length of the ring |
| $LT_M$ | Load term given for the type of load |
| $M$ | Moment |
| $M_A$ | Moment at Point A |
| $M_{yy}, M_{zz}$ | Bending moments in the $y$ and $z$ direction |
| $N$ | Force normal to the frictional force |
| $R$ | Radius of the ring |
| $r$ | Radius of bamboo |
| $r_n$ | Distance from the centre to the neutral axis |

| | |
|---|---|
| $t$ | Thickness of bamboo |
| $W$ | Applied load |
| $w, w_2$ | Width of timber blocks in both directions |
| $z_1$ | Chord of groove in timber block |
| ø | Diameter of steel threaded rod |

# Part I

# Introduction

# Chapter 1

# Introduction

## 1.1 Context and motivation

Bamboo is a fast-growing, renewable material that has the potential to contribute to the development of a more sustainable construction industry. Sustainability is central to the current concerns of climate change. According to the United Nations, 95% of the urbanisation in the next decades will be concentrated in developing countries (UN, 2018a). Promoting the use of local materials for the construction of sustainable and resilient buildings in the least developed countries is one of the goals of the global agenda on sustainable development set by the United Nations for the 2030 (UN-Habitat, 2016). Figure 1.1 shows the worldwide distribution of some bamboo species used for construction according to Rao et al. (1998) and the location of developing and least developed countries as listed by the United Nations (UN, 2018b). The convenient location of bamboos is an opportunity to exploit its advantages as a construction material while addressing the current needs identified by the United Nations without the extra cost and environmental effects associated with manufactured materials.

The use of bamboo in construction dates back thousands of years. It has been used extensively in regions where structural bamboo species are endemic as it is a lightweight material with extraordinary mechanical properties (e.g. its stiffness to weight ratio is comparable to that of steel, and its strength to weight ratio is higher than that of steel). Its potential as a construction material is illustrated with multiple examples around the globe such as shelters, huts, houses, sheds, bridges and scaffoldings among others. Figure 1.2 shows some early examples. Most of these constructions have been built based on empirical knowledge passed through generations. Although this experience constitutes a very valuable body of knowledge from which many lessons can be learned, traditional bamboo uses are gradually disappearing (Lobovikov et al., 2007). Furthermore, some traditional structures (e.g. trusses) underused the material or are not very efficient structurally (Janssen, 1995).

Despite the structural and environmental advantages, bamboo is not yet widely adopted as a building material. The lack of appropriate codes and standards for its safe use

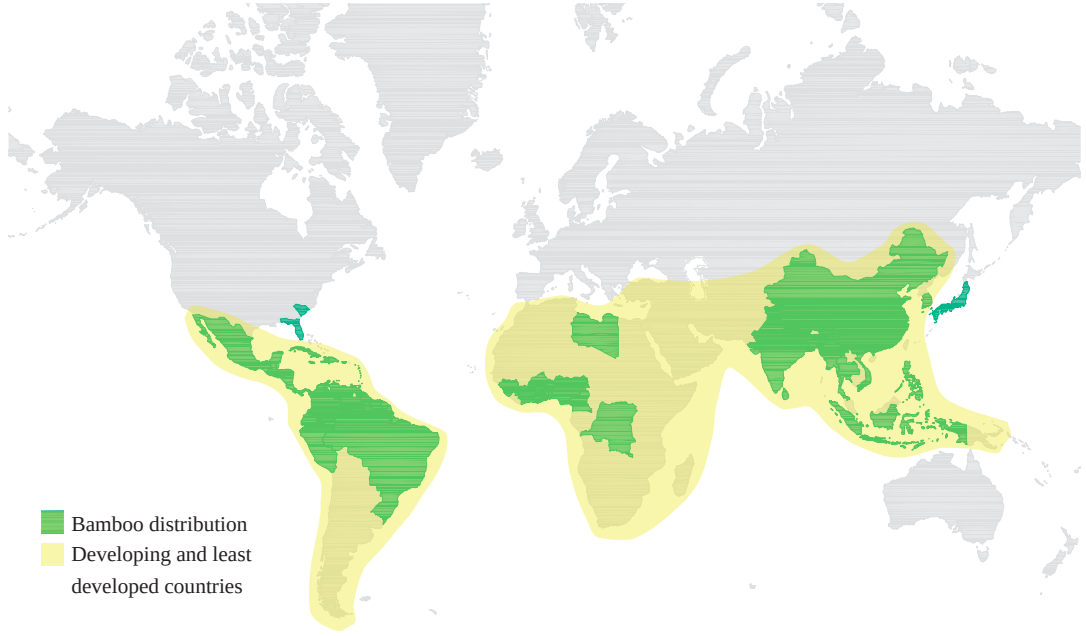


**Figure 1.1:** Worldwide distribution of priority species of bamboo used as building material according to Rao et al. (1998). The location of developing and least developed countries are indicated in yellow. These were taken as in UN (2018b).

prevents its full exploitation as a construction material. Scientific research on the material properties of bamboo culms is relatively new. The first standard for round bamboo was published by the Bureau of Indian Standards in New Delhi, India in 1973 (BIS-IS-6874, 1973). Furthermore, while considerable research on the mechanical properties of bamboo culms has been carried out over the past decades (Janssen, 1981; Arce-Villalobos, 1993; Amada et al., 1997; Harries et al., 2012), the research directions are very diverse, and the testing protocols used differ among authors.

There is currently an increasing interest on utilising bamboo as a building material either in its natural form (Harries et al., 2012) or as raw material for the development

**(a)** **(b)**

**Figure 1.2:** (a) A cottage built from bamboo in Colombia (Empson, 1836). (b) Emergency shelter bamboo rafter roof (Dunkelberg, 1985).

of laminated bamboo (Sharma et al., 2015). This can be due to the current need to use more sustainable materials in construction together with the latest showcase of multiple bamboo pavilions built worldwide which exhibit the structural potential of bamboo with innovative designs (see Figure 1.3).

Some examples of pavilions built in China, Germany and Latin America are shown in Figure 1.3. To compensate for the lack of appropriate codes and standards, experimental tests on connections, material and structures are required to guarantee that the structures are safe. Figure 1.4a shows the experimental tests on a full-scale prototype built for the ZERI pavilion in Manizales, Colombia before its construction for the EXPO 2000 in Hanover, Germany (Minke, 2012). In addition to these, further tests on bamboo culms and the connection designs were carried out in Germany to fulfil the requirements and obtain a building permit (Minke, 2012). Similarly, loading test on a full-scale prototype of a section for the nomadic museum in Mexico was carried out using sandbags to simulate the actual loading (Minke, 2012). Likewise, for the German-Chinese house at the EXPO 2010, a series of tests were performed for a connection system (see Figure 1.5) made with concrete and steel (Heinsdorff, 2013). While these structures show the potential of bamboo culms as structural material, it is not economic to consider these type of tests for each bamboo structure.


**Figure 1.3:** (a) ZERI pavilion, EXPO 2000 in Hanover Germany (Minke, 2012). (b-c) Nomadic museum in Mexico City (Vélez, 2015) and the (f) interior view of nomadic museum (Frey, 2011). (d-e) Bamboo pavilions for the exhibition 'Germany and China - Moving ahead together' by Markus Heinsdorff since 2007 installed successively in five Chinese megacities (Heinsdorff, 2013). (g-h) The german-chinese house at the EXPO 2010 in Shanghai (Heinsdorff, 2013).

**(a)** **(b)**

**Figure 1.4:** Experimental tests. (a) Full scale ZERI pavilion in Colombia, and (b) full scale section prototype of the nomadic museum pavilion (Minke, 2012).

**Figure 1.5:** Connections design, preparation, fabrication and testing for the german-chinese house at the EXPO 2010 (Heinsdorff, 2013).

The challenges of building with bamboo culms comprise many areas. Besides the lack of scientific data, there are practical and cultural issues that need to be overcome. It is a natural material susceptible to decay and the attack of living organisms (Liese and Köhl, 2015). It is also a hygroscopic material that reacts to environmental changes such as moisture content and relative humidity. It is prone to longitudinal splitting, and many jointing techniques, in particular, those utilising fasteners such as nails, screws dowels or pins have been associated with the splitting of bamboo culms (see Figure 1.6) due to the concentration of stresses developed between the bamboo and the fasteners used (Janssen, 1995; Minke, 2012). Furthermore, the variable and irregular properties hinder the design of connection systems as well as the appropriate fitting of components.

The concerns of the lack of knowledge in material properties (Hidalgo, 1978), together with the need to deliver more practical solutions (Janssen, 1981), appropriate design of connections (Follet and Jayanetti, 2008), particularly those avoiding perforations of the culm (Janssen, 1995), and sound structural systems (Lessard and Chouinard, 1980) have been previously highlighted. Nevertheless, thirty years later the need to develop standardised test methods that consider, among other aspects, the culm geometry and the different

**(a)** **(b)**

**Figure 1.6:** (a) Splitting of bamboo culm in connection (Dunkelberg, 1985). (b) Cracked culm in location of dowel rod.

species still exists (Harries et al., 2012), as well as the development of novel jointing techniques and structural systems. The first international standards for bamboo culms were published in 2004 (ISO, 2004a,b,c). These comprise the structural design and determination of physical and mechanical properties, but there is no reference about how to deal with non-uniform properties. Some researchers have attempted to measure the geometric irregularities (Arce-Villalobos, 1993; Ordóñez Candelaria and Salomón Quintana, 2009; Richard, 2013; Harries et al., 2017). However, until now no systematic method for the determination of these properties has been implemented or tested. Similarly, despite the susceptibility to splitting, the majority of the jointing techniques requires penetrating the culm cross-section.

The core of many of the issues lies in the fact that bamboo is not a uniform material. Furthermore, the variability of bamboo it is not only within the culm (e.g. longitudinal and transverse) and among culms, but also among species. Therefore, it is challenging to develop standardised methods to determine its properties. Similarly, there are no guidelines on how to deal with practical issues in construction practices. Although these issues are common knowledge, there are no strategies to overcome or address them. The current interest in developing engineered bamboo composites with standardised shape and dimensions can potentially overcome some of these issues. However, this comes with environmental costs and the potential to fully exploit bamboo culms for construction in its natural form remains unexplored.

## 1.2 Rationale

Although the advantages of bamboo as construction material are evident, there are still many fundamental aspects that need to be addressed such as determination of material properties and jointing techniques. The development of traditional structural materials (e.g. concrete, steel and timber) in the second half of the twentieth century have been huge. Yet, the advances of bamboo as a construction material is very slow.

To address the main challenges outlined for bamboo in construction, we need to consider all the aspects together rather than in isolation. As many of the issues are caused by the inherent variable and irregular properties, a reasonable question is:

**How can we develop a new design approach for bamboo construction that can incorporate the non-uniform properties ?**

Standardisation of material properties is key for the development of traditional construction materials, but treating bamboo culms as standard elements is not appropriate. Measuring these non-uniform properties (i.e. the variations and irregularities of the geometric, physical and mechanical properties) is very laborious. Nevertheless, the last decades have seen unprecedented innovation in digital technology. These have found multiple applications in distinct fields from healthcare to the arts, and architecture, engineering and construction are not an exemption. New digital technologies including fabrication, virtual reality, 3D laser scanning and photogrammetry among others, together with the computational advances in structural analysis and 3D modelling software are responsible for many of the innovations in these fields.

In this thesis, the potential of digital technologies is explored to address the low level of technological development of bamboo construction. The focus is placed on developing a new approach to measure the non-uniform material properties, with the aim of using them for the structural analysis and design for safe and efficient structural use.

## 1.3 Research objectives

The main goal of this research is to develop a design framework for bamboo culms to incorporate the non-uniform properties into the design process in view of eventually transferring it to the bamboo industry.

The framework consists of two main stages. In the first stage a methodology is developed for determining the non-uniform properties (geometric, physical and mechanical) of bamboo culms. The second stage comprises the methods to incorporate the non-uniform properties of bamboo into the different steps of the design process.

In order to place this new framework in context, the type of structural systems and jointing techniques is also considered. For this, reciprocal structures were adopted and used as case study. Reciprocal structures are self-supported structures that can be used to span large spaces without intermediate columns. In these structures, only two elements are connected at a time, therefore can potentially simplify the design of connection systems, which is one of the main challenges when building with bamboo. In this thesis, we will focus on reciprocal structures with mechanical connectors. The primary goals and specific objectives of the thesis are listed below.

**g.1 To develop a methodology for determining the non-uniform bamboo prop-**

**erties.**

1) To develop a method for determining the non-uniform geometric properties of bamboo culms, by using digital technologies that can be further transferable to the construction industry.
2) To review the available methods for determining the physical properties of bamboo culms, and devise methods for the rapid determination of these properties.
3) To develop a methodology for determining the mechanical properties of bamboo culms using a combination of numerical and experimental methods.
4) To create a discretised database of material properties for structural modelling.

**g.2 To develop the methods for the incorporation of the non-uniform bamboo properties into the design process of reciprocal structures.**

1) To develop methods for the definition of the geometry of reciprocal structures by taking into account the change in bamboo diameters.
2) To develop a method for the optimal selection and position of bamboo culms for each element in a structure.
3) To develop a method for linking the digital models and the physical structures in construction.

**g.3 To investigate the structural behaviour of bamboo reciprocal structures.**

1) To investigate possible connection systems for bamboo culms in reciprocal structures and assess their structural performance.
2) To develop an understanding of the global elastic structural behaviour of bamboo reciprocal structures and evaluate the effect of using SBD against considering bamboo culms as uniform elements.

## 1.4 Outline of thesis

This thesis is divided into four parts. Part I presents the introduction and the main goals of the research. Chapter 2 introduces bamboo culms and presents a critical review of the methods available for the determination of its geometrical, physical and mechanical properties. Chapter 3 presents the overview of the design framework for bamboo culms. It outlines the two main research areas for this framework: (i) the development of the methodology for the structural bamboo database (SBD), and (ii) the incorporation of this SBD into the design process.

Part II introduces the methodology to establish the structural bamboo database (SBD) of geometrical, physical and mechanical properties. Chapter 4 presents a novel method for determining the geometrical properties of bamboo using 3D scanning technologies. Chapter 5 presents the methods for determining the physical properties of bamboo.

Chapter 6 introduces the methodology for determining the mechanical properties for their use in structural analysis. Preliminary experiments are carried out to gain insight into the appropriate methods to adopt for this methodology.

Part III introduces the methods for the incorporation of the SBD into the design process. Chapter 7 presents the method for the generation of reciprocal structures and the methods to incorporate the non-uniform geometric properties of bamboo into the structural skeleton. Chapter 8 presents the proposal of two possible connection systems for bamboo culms and preliminary tests and analysis to evaluate their structural performance. Chapter 9 investigates the global structural behaviour of bamboo reciprocal systems using numerical analysis.

Finally, Part IV presents the conclusions. Chapter 10 summarises the main contributions of this research and outlines possible directions for future research.

# Chapter 2

# Literature review

## 2.1 Bamboo structure

Bamboo is a giant grass belonging to the Bambusoideae subfamily of the Poeceae (or Graminae) family (Liese and Köhl, 2015). It is the fastest growing plant (Liese and Köhl, 2015) and can typically reach its total height, which can be up to 30 m, during the first year (Liese and Weiner, 1996), and can be harvested from 3 to 6 years (Limaye, 1952; Liese and Weiner, 1996). There are 1642 bamboo species (Vorontsova et al., 2016a), endemic to all the continents except Europe and Antartica as it grows mainly in the tropical and subtropical regions (Grosser and Liese, 1971; Liese and Köhl, 2015). These correspond to about 75 genera, which are classified into the Arundinarieae (temperate woody bamboos), Bambuseae (tropical woody bamboos), and Olyreae (herbaceous bamboos) tribes (Liese, 1998; Liese and Köhl, 2015). Among all the species, some have been identified as building material (Rao et al., 1998), the rest are used for all sorts of applications, from food to crafts, furniture, accessories, clothes and more. Knowledge on the structure of bamboo culms is fundamental for the understanding of physical and mechanical properties as these properties are determined by the culm structure and the properties of the material from which the culm is made (Grosser and Liese, 1971; Liese, 1998; Gibson et al., 2010).

Throughout this thesis three different bamboo species were used for experimental work; Moso (*Phyllostachys pubescens*); Oldhamii (*Bambusa oldhamii*); and Guadua (*Guadua angustifolia Kunth*). Moso is the most important commercial bamboo species in China (Liese and Köhl, 2015); it is commonly used as building material, for scaffoldings (Chung and Yu, 2002) as well as for domestic and agricultural items (Rao et al., 1998). Guadua bamboo is one of the species with the most commercial interest in South America (Trujillo and Jangra, 2016). It has been broadly used as structural material among other things (Hidalgo, 1978; Liese and Köhl, 2015; Correal and Arbeláez, 2010). Oldhamii bamboo is native to China and has been naturalised to several regions including Mexico, Central America, Caribbean and Western South America, Eastern Asia and New Zealand (Vorontsova et al., 2016a). It has been used as building material and for furniture fabrication (Rao et al., 1998).

### 2.1.1 Bamboo morphology

The morphology of bamboos resembles that of all the grasses consisting of a tapered hollow cylinder. The culms are characterised by two main parts, nodes and internodes (Liese, 1998), as shown in Figure 2.1. The internodes are the sections between the nodes, which are usually straight to the naked eye. The nodes provide a transverse connection within the culm wall through the diaphragm formed in the hollow part of the culm (Grosser and Liese, 1971). In the outer surface, the nodes can be identified by the intranode consisting of the nodal ridge and the sheath scar (Grosser and Liese, 1971). The culm wall thickness is surrounded by an inner and outer layer called pith ring and cortex respectively (Liese, 1998) (see Figure 2.1). The pith ring is the layer located at the central cavity, and it consists of parenchyma cells that surround the lacuna, which sometimes become thick and lignified and for some species is coated with a membrane which is either attached or slightly loose (Liese, 1998). The cortex or epidermis consists of a wax coating layer, and its main function is to prevent the water penetration through the inside of the culm wall (Liese and Weiner, 1996).

The structure of bamboo is non-uniform, it changes gradually in size across and along the culm (Grosser and Liese, 1971), causing a decrease in diameter and thickness from bottom to top, and a change of internode length (Liese, 1998; Amada et al., 1997). The longitudinal variations are not proportional to the length of the culm, as the rate of change in thickness at the bottom part of the culm has been reported to be higher (Grosser and Liese, 1971). This feature can be observed in Figure 2.2, where the variation of thickness at the bottom is higher than that at the top. These variations in structure are reflected

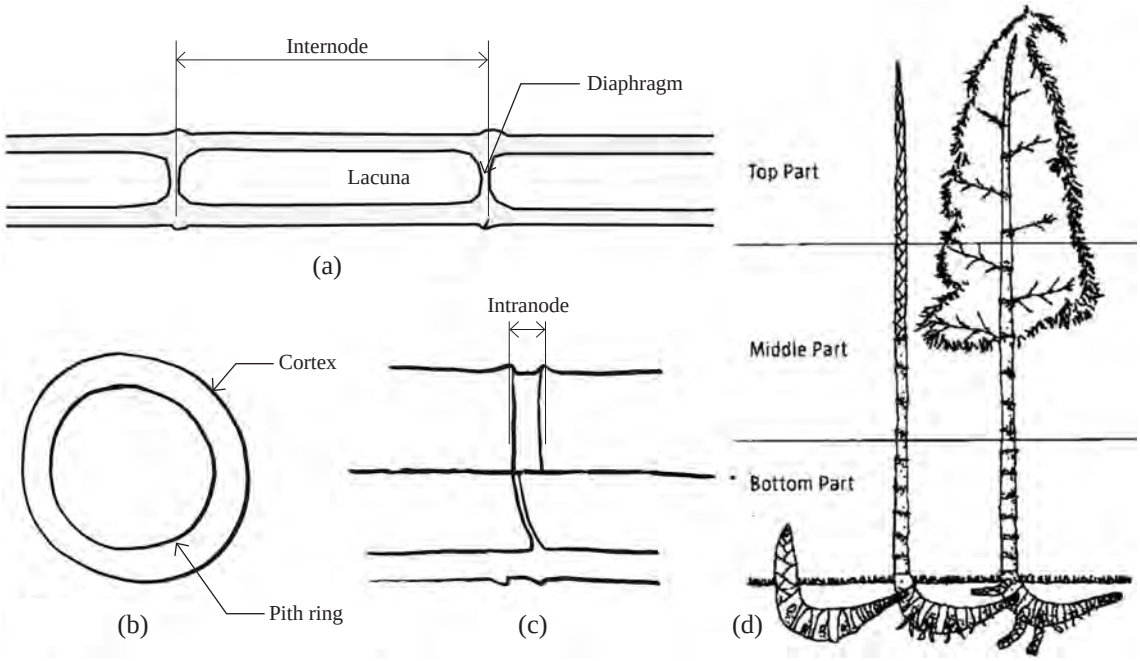


**Figure 2.1:** Culm Structure. (a) Internode in longitudinal section. (b) Cross-section. (c) Intranode in node. (d) Bamboo plant (Minke, 2012).

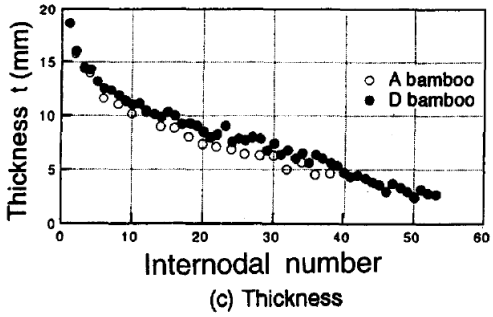


**Figure 2.2:** Variation of thickness along the length of the culm from bottom to top (Amada et al., 1997).

in physical and mechanical properties.

In addition, there are differences among species and between each culm. Table 2.1 provides average values for bamboo species identified as building material (Rao et al., 1998). It should be noted that the list of priority species has not been updated since 1998 (Liese and Köhl, 2015). In 2005, (IS-6874, 2008b) reported that sixteen species from 100 different species tested were suitable for construction. All these species were native to India, and eight of them appear in Table 2.1. Recently, a list of all the known species of

**Table 2.1:** Dimensions of some priority bamboo species (Rao et al., 1998).

| Bamboo species | Range or Average Dimensions | | | |
|---|---|---|---|---|
| | Diameter (mm) | Thickness (mm) | Internode Length (mm) | Height (m) |
| Bambusa balcoa | 80 - 150 | 20 - 25 | 300 - 450 | 20 - 24 |
| Bambusa bambos | 150 - 180 | 10 - 15 | 200 - 400 | 15 - 30 |
| Bambusa polymorpha | 150 | 10 - 20 | | 25 |
| Bambusa textilis | 30 - 50 | | 350 - 600 | 15 |
| Bambusa tulda | 50 - 100 | 4 - 7 | 400 - 700 | 30 |
| Bambusa vulgaris | 50 - 100 | 07 - 15 | 250 - 350 | 8 - 20 |
| Cephalostachyum pergracile | | | | 7 - 30 |
| Dendrocalamus asper | 80 - 200 | 11 - 20 | 200 - 450 | 20 - 30 |
| Dendrocalamus giganteus | 100 - 200 | 25 | 400 - 500 | 24 - 60 |
| Dendrocalamus latiflorus | 80 - 200 | 5 - 30 | 200 - 700 | 14 - 25 |
| Dendrocalamus strictus | 80 - 200 | 25 - 80 | | 30 - 45 |
| Gigantochloa apus | 80 - 300 | 40 - 130 | 15 | 36 - 45 |
| Gigantochloa levis | 50 - 160 | 10 - 12 | 450 | 30 |
| Gigantochloa pseudoarundinacea | 50 - 130 | 20 | 350 - 450 | 7 - 30 |
| Guadua angustifolia | 200 | | | 30 |
| Melocanna baccifera | 50 - 70 | 5 - 12 | 200 - 500 | 10 - 20 |
| Ochlandra spp | 20 - 50 | | | 5 - 10 |
| Phyllostachys pubescens | 180 | | | 10 - 20 |
| Thyrostachys siamensis | | | 150 - 300 | 8 - 16 |

bamboo has been published (Vorontsova et al., 2016a,b). An update of the classification based on their utilisation would be very valuable.

### 2.1.2 Bamboo anatomy

The anatomy of bamboo refers to the microscopical characteristics of the internal structure (e.g. fibres and matrix). The culm wall of bamboo is characterised by vascular bundles embedded in parenchyma cells (Grosser and Liese, 1971), as shown in Figure 2.3 with the fibres embedded in the matrix. The vascular bundles consist of sclerenchyma cells (constituted by fibres), vessels, and sieve tubes with companion cells (Grosser and Liese, 1971). The fibres are usually contained within the vascular bundles, or as isolated fibre bundles and are oriented in the longitudinal direction (Liese, 1998). On average the culm wall thickness consists of 52% matrix, 40% fibres and 8% conducting tissue (Liese, 1998).

Although there are variations among each bamboo culm, the variations across and along the culm are more significant (Liese, 1987). In the transverse direction, the vascular bundles change in shape and size, and are gradually distributed increasing in number from the inner to the outer part (from approximately 15 to 60 %) as shown in Figure 2.3, where about half of the fibres are concentrated in the outer third section (Liese, 1998). Table 2.2 presents the average in percentage for the fibre, parenchyma and conducting tissue of bamboo for the inner, middle and outer sections.

The longitudinal variations are characterised by a decrease in the quantity of vascular bundles with the culm height (Grosser and Liese, 1971). Both volume fraction (Amada et al., 1997) and density (Gnanaharan et al., 1994) have been reported to increase towards the top. Volume fraction in this case is the percentage of fibres in the culm wall with respect the percentage of all the materials (i.e. fibres and matrix) of the culm wall.

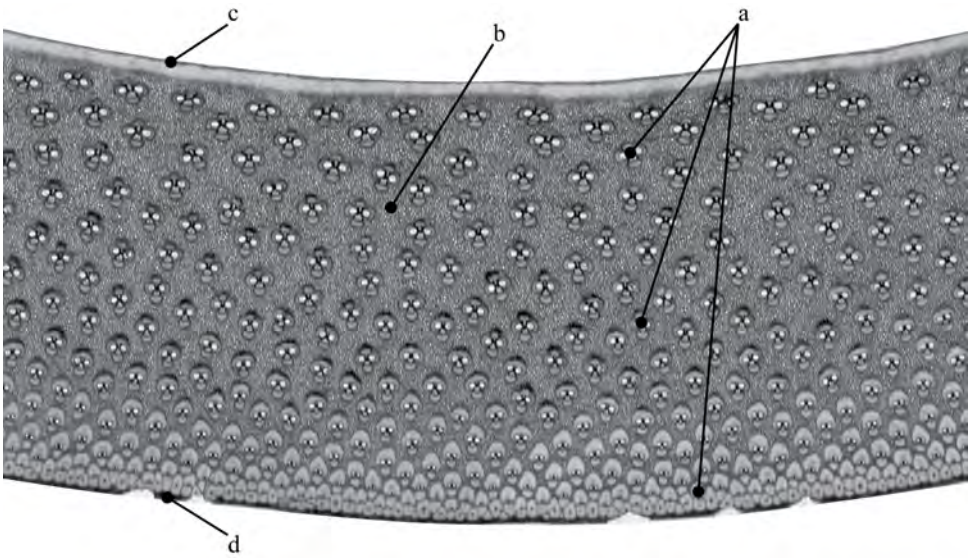


**Figure 2.3:** Culm wall cross-section: a) vascular bundles, b) parenchyma cells, c) pith ring, and d) cortex.

**Table 2.2:** Distribution of fibre, parenchyma and conducting tissue in the inner, middle and outer section of the culm wall thickness (Grosser and Liese, 1974).

| constituent | outer | middle | inner |
|---|---|---|---|
| | % | % | % |
| fibre | 48.8 | 32.8 | 18.4 |
| parenchyma | 24.0 | 33.1 | 42.9 |
| conducting tissue | 20.8 | 37.2 | 42.0 |

In the nodes, the bundles are bent towards the lacuna to create the diaphragm forming irregular bundles in distribution and orientation (Grosser and Liese, 1971).

## 2.2 Physical and mechanical properties of bamboo culms

This section presents key relationships between the physical and mechanical properties found in the literature with the aim to inform the development of the methods to determine material properties in the design framework. Five different aspects were reviewed, these are (a) the effect of physical properties (moisture content and volume fraction) on mechanical properties; (b) the stress-strain relationship to understand the behaviour of the material in the different directions; (c) the transverse and longitudinal variations of physical and mechanical properties; (d) and the longitudinal and (e) transverse mechanical properties of bamboo culms.

### 2.2.1 Effect of physical properties on mechanical properties

Bamboo is a hygroscopic material, and as such it responds to the environmental conditions by adjusting the content of water to the relative humidity and temperature that is subjected. Moisture content in bamboo culms is influenced by several factors such as species, season, environmental conditions, and for some species the position along the culm (Liese, 1987; Chung and Yu, 2002). In the timber industry, moisture content is one of the most important factors because it directly affects other physical and mechanical properties. It is estimated that about 80% of the problems that occurred in-service are related to moisture content (TRADA, 2016).

The dimensional changes of bamboo culms due to variations in moisture content occurs mainly in the transverse direction. The longitudinal direction remains almost constant (Hamdan et al., 2007). The dimensional change occurred in bamboo culms from the green condition up to 20% of moisture content was reported linear and between 4% and 14% for the transverse direction. According to Liese and Tang (2015), the shrinkage in bamboo from green condition stops below 70 to 40 % and starts again at values below the fibre saturation point. They also reported that the shrinkage for the fibres was similar to timber, whereas the shrinkage in the parenchyma cells was less.

The influence of moisture content on mechanical properties is proportional for culms

with a moisture content below the fibre saturation point (FSP), a phenomenon that is also observed in wood (Glass and Zelinka, 2010; Jiang et al., 2012). The fibre saturation point is where the cell walls are completely saturated, but there is no free water in the cell cavities (Dinwoodie, 2000). Below the FSP, the mechanical properties of bamboo are a function of the moisture content. However, above the FSP, moisture content has no influence. The FSP in bamboo is about 20% to 30% depending on the species (Jiang et al., 2012). The culm is said to be in equilibrium moisture content(EMC) when it is no longer gaining or losing of water.

The swelling or shrinkage caused by the change in moisture content modifies the culm structure, which in turns affect the mechanical properties of bamboo. This means that the structure and physical properties (e.g. moisture content, density and volume fraction) play an important role in the mechanical behaviour of bamboo culms. See for example Figure 2.4 and the relationship between compressive strength and volume fraction. Similar behaviour was observed for the compressive strength and density (Dixon and Gibson, 2014), as well as for the tensile (Amada et al., 1997; Zhou et al., 2012) and flexural properties (Dixon and Gibson, 2014; P.G.Dixon et al., 2015). Nevertheless, the type of sample was also found to be important. For example, Gnanaharan et al. (1994) reported that the bending properties in split specimens are highly correlated to density, but that the correlation observed for the full culm specimens was low.

It is important to mention that the majority of the literature reporting on volume fraction refers to the volume fraction of vascular bundles. (Dixon and Gibson, 2014) measured the volume fraction and solid fraction of vascular bundles, using higher magnification for the latter. The difference lies in that for the solid fraction the area of the vessels is subtracted from the total area of the vascular bundles. They concluded that the volume fraction of fibres and volume fraction of vascular bundles are very similar for moso species, as the percentage of solids in vascular bundles is very high.

Moisture content is considered to be the physical property with the higher influence on mechanical properties (Chung and Yu, 2002). The compressive strength and stiffness (Janssen, 1981; Chung and Yu, 2002) and the bending strength (Limaye, 1952; Chung

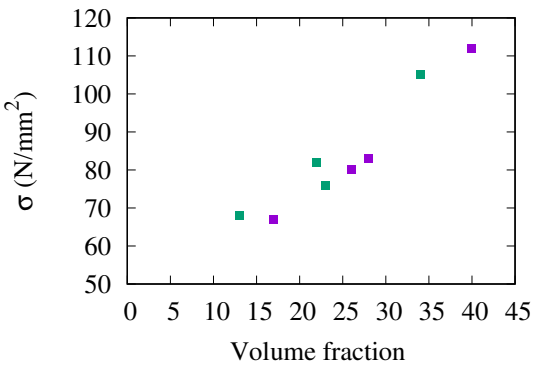


**Figure 2.4:** Relationship between compressive strength and volume fraction of vascular bundle plotted from data tabulated by Ota (1950).

and Yu, 2002) tends to increase with a decrease of moisture content. Furthermore, the bending strength can increase up to 40 to 50 % on dry mature (older than 2.5 years old) bamboos, and for young bamboos the increase is even higher due to the high moisture content (Limaye, 1952). Nevertheless, different patterns have been found between species and therefore trends cannot be generalised to other species. For instance, Chung and Yu (2002) reported a reduction of bending strength by half under wet conditions for bamboo culms of the species Kao Jue, and a constant bending strength for the Mao Jue bamboo species regardless the moisture content.

### 2.2.2 Stress-strain relationships

Several authors have studied the mechanical properties of bamboo for different purposes, and as such the methods used are different. Figures 2.5, 2.6 and 2.7 show the stress-strain (or load-deflection) relationship for the tensile compressive and bending behaviour.

The tensile behaviour is characterised by a linear relationship and a brittle failure. On the contrary, the load-deflection relationship for the compressive and bending loads show a ductile behaviour characterised by a linear relationship followed by the yield of the material before failure.

The tensile behaviour is mainly governed by the tensile strength and stiffness of the fibres (Janssen, 1981; Zhou et al., 2012). However, while the amount of fibres influences the compressive behaviour of bamboo (Janssen, 1981), the compressive strength of fibre reinforced materials are governed by microbuckling of the fibres (Daniel and Ishai, 2006). The buckling strength of fibres alone is very low (Janssen, 1981), but in the composite, the matrix helps to transfer the stresses within the fibres (Daniel and Ishai, 2006). Obataya et al. (2007) investigated the compressive behaviour and the role of the parenchyma cells under longitudinal compressive load. They suggested that although parenchyma cells do not contribute to the stiffness of the bamboo, the transverse expansion help to prevent the buckling of the fibres by keeping them aligned while undergoing compressive loads. By

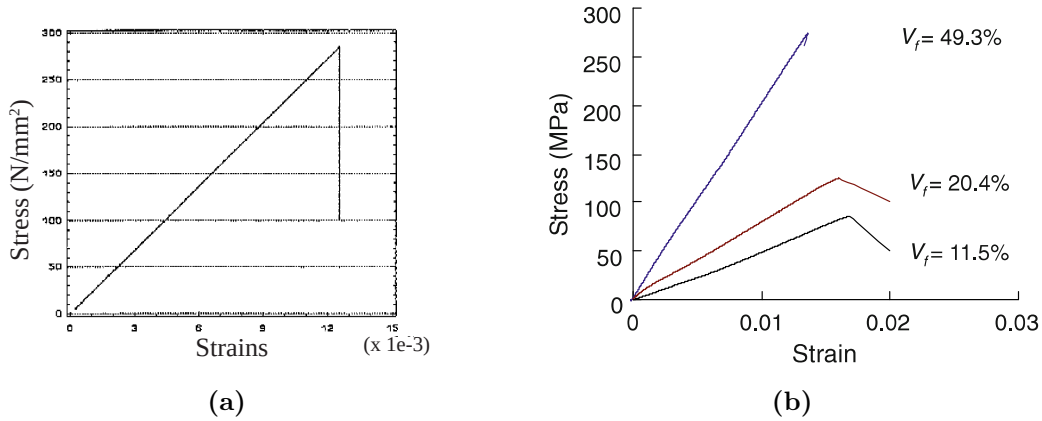


**Figure 2.5:** Stress-strain curves for tensile tests on different bamboo samples. (a) Bamboo strip (Arce-Villalobos, 1993). (b) Bamboo blocks taken from the cross-section with different volume fraction (Shao et al., 2010).

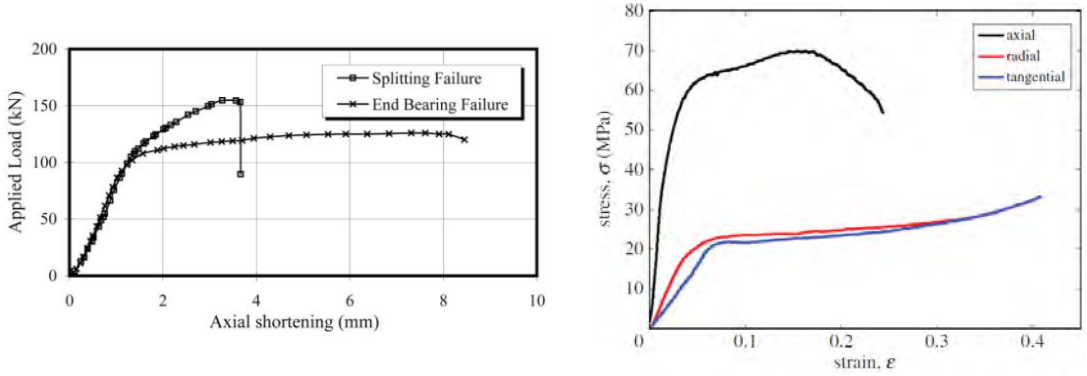


**(a)** **(b)**

**Figure 2.6:** Load deflection curve of bamboos specimens under compressive load. (a) Full culm (Chung and Yu, 2002). (b) Small samples (Dixon and Gibson, 2014).

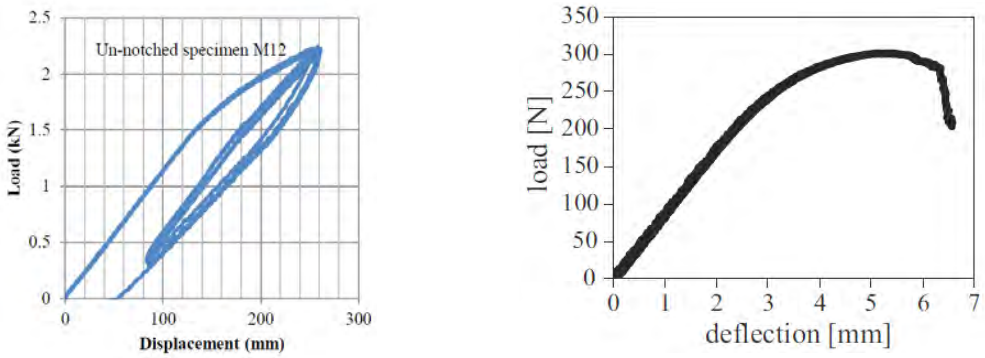


**(a)** **(b)**

**Figure 2.7:** Load-displacement curves of bamboo in bending. (a) Full culm sample (Richard, 2013). (b) Small samples (P.G.Dixon et al., 2015).

microscopic investigation, they observed the microbuckling of the parenchyma cells, which allows the densification of the material, avoiding in this manner the large-scale buckling of the fibres.

### 2.2.3 Variations of mechanical properties owing to its graded structure

Bamboo has been categorised as a functionally graded material (Amada et al., 1997; Nogata and Takahashi, 1995; Richard and Harries, 2015). The concept of functionally graded materials is used to describe the varying composition and properties throughout the volume of the material (Mahamood and Akinlabi, 2017). There is a direct influence between the graded distribution of constituents in the material to the mechanical performance of a structure created from that material. Wegst and Ashby (2004) highlight that it is the structure and arrangement of the constituents of the material which defines the mechanical efficiency of it and not so much the properties of individual constituents.

Figures 2.8 and 2.9 show the pattern of variation through-thickness for the longitudinal mechanical properties (i.e. tensile, compressive and flexural). These tend to increase from

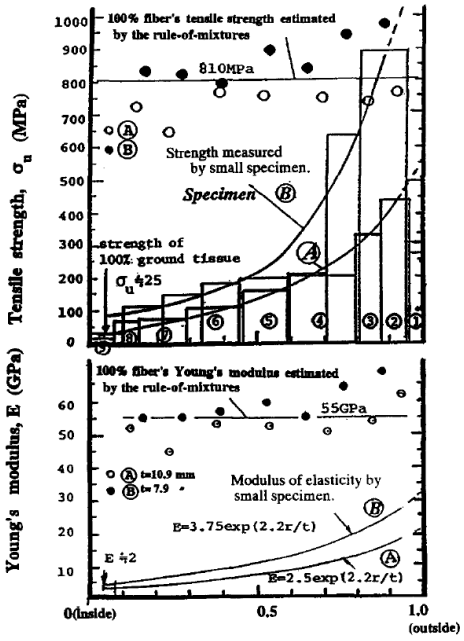


(a)

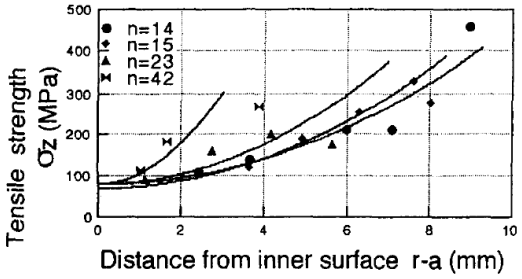


(b)

**Figure 2.8:** Variation of tensile properties across the culm wall thickness. a) Variation of Young's modulus and tensile strength (Nogata and Takahashi, 1995). b) Variation of tensile strength (Amada et al., 1997), r-a refers to the thickness in mm, and n refers to the internode number.

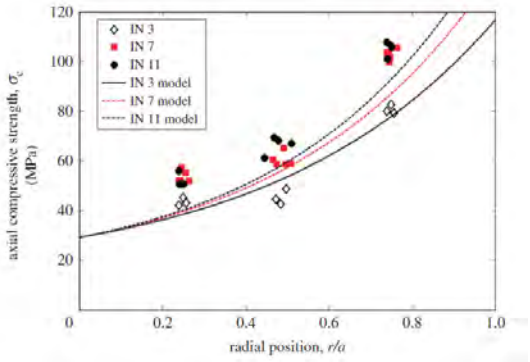


(a)

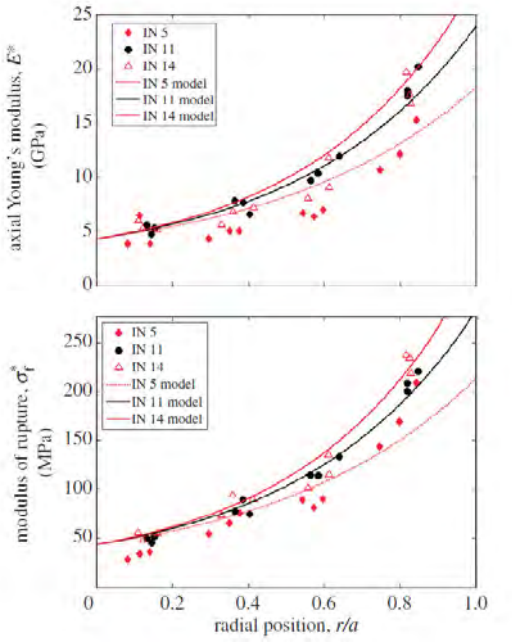


(b)

**Figure 2.9:** Variation of (a) compressive and (b) flexural properties of bamboo culms across the culm wall section (Dixon and Gibson, 2014), r/a refers to the radial position normalised to the thickness, and IN refers to the internode number.

the inner to the outer part of the culm wall (Nogata and Takahashi, 1995; Amada et al., 1997; Dixon and Gibson, 2014), similar to the variation of fibres described in the previous Section 2.1.

Likewise, variations of longitudinal mechanical properties have been reported. An increase of the tensile strength and stiffness from the bottom to the top part of the culm, which also coincides with the increase of volume fraction along the culm, was reported by several authors (Nogata and Takahashi, 1995; Amada et al., 1997, 1996; Zhou et al., 2012). Similarly, an increase of compressive strength from bottom to top was also observed (Janssen, 1981). However, differences of the compressive behaviour between species with respect the longitudinal direction have also been observed. Chung and Yu (2002) found an increase of compressive strength and stiffness from bottom to top for the bamboo species Mao Jue, and constant values for compressive properties for the bamboo species Kao Jue.

The variations in the transverse and longitudinal directions are different. Yu et al. (2008) investigated the density, shrinkage and tensile properties of bamboo across the culm wall and also at different heights. Figure 2.10 shows the radial and longitudinal variations for density. While there are longitudinal variations from bottom to top, these are not as significant as in the radial direction. Similar variations were also reported for the tensile strength and stiffness. The modulus of elasticity increases from 9.6 to 26.9 kN/mm$^2$ in the radial and from 15.4 to 17.4 kN/mm$^2$ in the longitudinal direction, and the tensile strength from 113.4 to 295.6 N/mm$^2$ in the radial and from 175.6 to 177.8 N/mm$^2$ in the longitudinal direction (Yu et al., 2008).

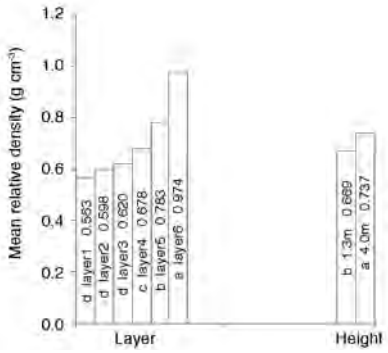


**Figure 2.10:** Variations of density in the radial and longitudinal directions (Yu et al., 2008).

### 2.2.4 Longitudinal mechanical properties

#### 2.2.4.1 Tensile properties

Table 2.3 provides a review of the tensile values for the strength and stiffness of bamboo and its constituents (i.e. the fibres and matrix).

There is a linear relationship between the tensile strength and stiffness with the volume fraction of fibres (Amada et al., 1997; Zhou et al., 2012). Some authors (Janssen, 1981;

**Table 2.3:** Tensile Properties of Bamboos, Fibres and Matrix

| Bamboo species | Tensile Strength | | | Tensile Stiffness | | |
|---|---|---|---|---|---|---|
| | Bamboo ($N/mm^2$) | Fibre ($N/mm^2$) | Matrix ($N/mm^2$) | Bamboo ($kN/mm^2$) | Fibre ($kN/mm^2$) | Matrix ($kN/mm^2$) |
| - (Janssen, 1981) | 160.00 | | | | | |
| Bambsusa Tulda (Janssen, 1981) | | | | 15.75 | | |
| Dendrocalamus strictus (Janssen, 1981) | | | | 15.00 | | |
| Moso (Chuma et al., 1990) | | 498 | 73 | | 48 | 0.26 |
| Moso (Nogata and Takahashi, 1995) | | 810 | | | 55 | |
| Moso (Amada et al., 1997) | | 610 | 50 | | 46 | 2 |
| Moso (Yu et al., 2008) | 115 - 309 | | | 9 - 27 | | |
| Moso blocks (Shao et al., 2010) | | 581.70 | 19 | | 40.4 | 0.22 |
| Moso fibres (Shao et al., 2010) | | 482.2 | | | 33.9 | |
| - Zhou et al. (2012) | | 450 | 11 | | 30 | 0.12 |

Arce-Villalobos, 1993) have developed a rule of thumbs for the estimation of tensile properties based on the percentage of fibres and density. This is an important relationship as there are many issues associated with the methods for determining the tensile properties of bamboo (Arce-Villalobos, 1993; Richard and Harries, 2015) such as gripping of the samples and end restraints. Nevertheless, is important to note that the majority of these relationships have been studied in the radial direction, and further investigation is required to assess its wider applicability, like along the culm and among culms.

The tensile strength of nodes have also been investigated and, unlike the internodes, these were reported to behave as an isotropic material (Amada et al., 1997). The tensile strength and stiffness of the node is approximately between 30 to 40% of that of the internode (Arce-Villalobos, 1993).

#### 2.2.4.2 Compressive properties

Table 2.4 provides a review of the compressive properties reported in the literature. Many factors have been reported to influence the compressive strength including volume fraction, density, moisture content and position along the culm (Janssen, 1981; Chung and Yu, 2002; Correal and Arbeláez, 2010). These have also been reported to influence the tensile strength. As shown in Figure 2.4, the compressive strength tends to increase with an increase of volume fraction, and a similar relationship was reported for the compressive strength against density (Dixon and Gibson, 2014). The influence of nodes in the compressive strength of bamboo is not significant (Atrops, 1969; Janssen, 1981).

**Table 2.4:** Compressive Properties of Bamboos

| Type of sample and bamboo species | Compressive Strength ($N/mm^2$) | Compressive Stiffness ($kN/mm^2$) |
|---|---|---|
| [a]Bambusa Blumeana (Janssen, 1981) | 70 | |
| [b]Bambusa Blumeana (Janssen, 1981) | 64 | |
| [b]Guadua s.p. (Arce-Villalobos, 1993) | 51 | 19 |
| [b]Kao Jue (Chung and Yu, 2002) | 44 - 99 | 2.5 - 16.1 |
| [b]Mao Jue (Chung and Yu, 2002) | 48 - 114 | 3.6 - 11.0 |
| [c]Mao Zhu and Kao Zhu (Lo et al., 2008) | 45 - 65 | |
| [c]Guadua angustifolia Kunth (Correal and Arbeláez, 2010) | 36.7 | 16.3 - 17.9 |
| [a]Moso (Dixon and Gibson, 2014) | 69 | |

Type of samples:
(a) small sample taken from bamboo cross-section.
(b) sample corresponding to a full cross-section.
(c) sample corresponding to a full cross-section. Test according to ISO (2004b).

Several failure mechanisms have been identified in full culm specimens under compressive load. Janssen (1981) reported that splitting and crushing for culm specimens and found no relationship between failure type and moisture content. On the other hand, Chung and Yu (2002) reported a relationship between splitting failure and low moisture content and bearing type failure with high moisture content. Furthermore, Arce-Villalobos (1993) identified four failure types such as splitting, contact stresses, failure due to the variable thickness and lateral buckling. However, these failure types were associated with the test methods.

#### 2.2.4.3 Flexural properties

Table 2.5 provides an overview of the average bending strength and stiffness of bamboo. The species and tests methods used vary among authors (e.g. shape and size of the specimen, 3 or 4 point bending tests, set-up, etc.), and as such it is expected to result in different values. The IS-6874 (2008b) code provided the bending properties for sixteen bamboo species native to India for green and dry conditions. The bending properties of a structural element depend on the properties of the material as well as the structural shape of the cross-section. In the case of bamboo culms, the hollow shape of the cross-section together with the mechanical properties and the gradient distribution of the constituents (i.e. fibre and matrix) through-thickness, define the mechanical efficiency of the culm in bending (Wegst, 2011). For example, Vaessen and Janssen (1997) reported an increase of 10% of bending stiffness due to the distribution of fibre through the culm wall.

The type of stresses causing failure in a bamboo culm subjected to bending are not always normal stresses. In many cases, the bending behaviour is governed by a combination of shear, crushing and tension perpendicular to the fibre (Gnanaharan et al., 1994). This has been associated with the length of the tested specimen (Vaessen and Janssen, 1997). The most frequent failure modes identified by Trujillo et al. (2017) were a failure under support and shear caused at the shear span, followed by compression at the top and tension perpendicular to the grain. Wegst and Ashby (2007) and Gibson et al. (2010), identified

**Table 2.5:** Flexural Properties of Bamboos

| Bamboo species | Flexural Strength ($N/mm^2$) | Flexural Stiffness ($kN/mm^2$) |
|---|---|---|
| Bambusa blumeana (Janssen, 1981) | 84 | 20.5 |
| Guadua angustifolia (Gnanaharan et al., 1994) | 72.6 | 17.61 |
| Bambusa pervariabilis (Kao Jue) (Chung and Yu, 2002) | 48 - 118 | 11.0 - 39.30 |
| Phyllostachys pubescens (Mao Jue) (Chung and Yu, 2002) | 50 - 132 | 7.1 - 18.2 |
| Phyllostachys pubescens (Moso) (Obataya et al., 2007) | | 15.0 - 16.0 |
| Phyllostachys pubescens (Moso) (Dixon and Gibson, 2014) | 130 | 10.6 |
| Moso and Tre Gai (P.G.Dixon et al., 2015) | 50 - 250 | 5.0 - 20.0 |
| Guadua angustifolia Kunth (P.G.Dixon et al., 2015) | 50 - 250 | 10.0 - 35.0 |
| Guadua angustifolia Kunth (Correal and Arbeláez, 2010) | 89 - 104 | 17.2 |

and described three different failure mechanisms for orthotropic circular tubes as bamboos. The first is related to the loss of stiffness of the culm caused by the ovalisation during the gradual increase of transverse forces. The second is related to the normal stresses developed in the longitudinal axis, and the third refers to the longitudinal shear failure and was associated to the circumferential stresses also caused by the ovalisation.

Under green conditions, Limaye (1952) reported an increase in the bending modulus of elasticity from bottom to top and a decrease in the modulus of rupture for Dendrocalamus strictus. However, Correal and Arbeláez (2010) reported a constant bending modulus of elasticity in the longitudinal direction and an increase of modulus of rupture towards the top of the culm for Guadua a.k. species.

#### 2.2.4.4 Shear properties

The shear properties parallel to the fibres is a critical aspect for bamboo culms. Many failures in bamboo joints have been linked either with the splitting of the culm or shear failure (Janssen, 1981). In addition, longitudinal shear has been identified as one of the main causes of failure during bending.

The pure longitudinal shear behaviour of bamboo culms can be relatively simple to analyse. However, it is the interaction among shear and other parameters such as bending, splitting and transverse tensile properties that results in a more complicated mechanisms that is not yet well understood (Limaye, 1952; Janssen, 1981; Arce-Villalobos, 1993; Gnanaharan et al., 1994; Mitch et al., 2010). For instance, when loaded transverse to the fibre, the culm is subjected to normal tensile and compressive stresses due to bending, but it is also subjected to shear stresses. Therefore, high shear stresses generated at the neutral axis during bending can cause failure of the culm. The shear strength reported by Janssen (1981) using different test methods was between 5.90 to 10.26 $N/mm^2$, where the highest strength was reported for those of full culm samples with four shear planes, as the test method specified by the ISO (2004b) standard.Correal and Arbeláez (2010) found a rather constant shear strength along the culm from 7.1 to 7.8 $N/mm^2$ for Guadua species following the test method described by the ISO (2004b) standard.

### 2.2.5 Transverse mechanical properties

Since bamboo is an orthotropic material, its properties are different in its two main orthogonal directions. Nevertheless, despite the fact that the transverse direction is the weakest, very little is known about the transverse properties of bamboo.

Arce-Villalobos (1993) reported that the transverse modulus of elasticity is about one eight of that in the longitudinal direction. He suggested that the transverse tangential strain is likely to have a constant value, as he observed that the values for the three different species were very similar, and described the transverse behaviour as elastic and characterised by a brittle failure.

Mitch et al. (2010) developed a split pin test to investigate the transverse tensile properties of bamboo with the aim of gaining insight into the splitting behaviour of bamboo culms. They reported average failure stress of 1.0 $N/mm^2$ and a stress intensity factor of 0.17 $N/mm^2(m^{1/2})$. García et al. (2012) proposed a test method to analyse the elastic properties of bamboo culm in the transverse direction. They reported a transverse elastic modulus of 398 $N/mm^2$, and a transverse-longitudinal shear modulus of 581 $N/mm^2$.

In addition, Sharma et al. (2013) developed a test method to investigate the transverse compressive behaviour of bamboo culms. Table 2.6 provides the data for the transverse elastic modulus and the stresses at two orthogonal directions (where EW is the transverse direction). Additionally, they reported that the neutral axis in the transverse direction is shifted from the middle of the culm wall thickness to the outer side of the culm to about 0.66 and 0.80 of the culm wall thickness. Harries et al. (2012) provided a review of the methods available to characterise the splitting behaviour in view of the standardisation of the test methods and particularly with the aim to provide practical solutions that can be applied in the field.

**Table 2.6:** Transverse compressive properties of bamboos (Sharma et al., 2013).

| Bamboo species | Transverse E ($N/mm^2$) | MOR NS ($N/mm^2$) | MOR EW ($N/mm^2$) |
|---|---|---|---|
| Phyllostachys Aurea (Thin-walled specimens) | 526 | 11.5 | 6.5 |
| Bambusa stenostachya (Thick-walled specimens) | 492 | 5.8 | 3.3 |
| Bambusa stenostachya (Thick-walled specimens) | 2113 | | |

## 2.3 Methods for determining bamboo culm properties

This section provides an overview of the current methods available for determining the properties of bamboo culms in research as well as in codes and standards.

### 2.3.1 Geometric properties

Currently, no codes or standards provide methods for geometric measurements that enable capturing the variable and irregular properties of bamboo culms. The ISO (2004b) stand-

ard specifies the measurement of diameter and thickness as the average values taken from two orthogonal positions in the cross-section, which for the thickness can only be taken at both ends. Nevertheless, according to the data reported by Banik (2015), the changes in diameter and thickness along the culm are not linear since the dimensions at the middle of the culm does not correspond to the average from the bottom and top. On average, from the data reported of ten bamboo species, the diameter can be underestimated by 12%, whereas the thickness can be overestimated by 17%. Therefore, simple calculations of the second moment of area from the bottom and top of the culm resulted in a percentage difference of 40% lower than that measured from the average values from the bottom, middle and top. It is a significant difference that can lead to underuse the material. In addition, it was found that the ratio thickness to diameter is lower for the middle section, thus having a thinner cross-section.

Some standards provide a set of tolerances for tapering and out-of-straightness. The ISO (2004a) standard specifies that the culms shall have a maximum of 1 to 170 of taper for buckling analysis, which for the same purposes the second moment of area is reduced to 90 % in order to consider the taper of the culm. The Indian code IS-6874 (2008a) specifies that the taper (defined as the ratio of the difference of diameters to length) must be less than 5.8 mm and the out-of-straightness no more than 75 mm in 6 metres, which is equal to 12.5 mm per metre. Nevertheless, none of these documents provides description of how to measure and calculate these properties.

Some authors have developed their own methods in an effort to capture the non-uniform geometric properties of bamboo. For example, Arce-Villalobos (1993) reported an error of up to 16% when calculating the area by considering the shape of the cross-section as a circle instead of an ellipse. Ordóñez Candelaria and Salomón Quintana (2009) reported an error of 10% when considering the second moment of area of a regular and irregular shape. Their method consists of digitalised images taken from the cross-section. These were imported to AutoCAD where the inner and outer circumferences are drawn and from those, the second moment of area is directly determined by the software tools.

In addition, the out-of-straightness reported for four batches of the species *Dendrocalamus giganteus* (Dendrocalamus), *Phyllostachys pubescens* (Moso) and *Bambusa stenostachya* (Tre Gai) were reported as: (1) from 7 to 15 mm over a span of 2896 mm (moso), (2) from 5 to 11 mm over a span of 2286 mm (tre gai), (3) from 13 to 38 mm over a span of 3000 mm (Dendrocalamus) and, (4) from 2 to 24 mm over a span of 2760 mm (moso) (Richard, 2013). The average out-of-straightness per metre for these four batches are 3.8, 3.5, 8.5 and 4.7 mm/m respectively. For this, a special jig was devised to measure the out-of-straightness of the culm in the longitudinal axis. This jig consisted of two parallel strings from where the out-of-straightness at the centre of each internode is measured.

The influence of the tapering and ovalisation on the mechanical behaviour of bamboo culms has also been investigated. Bahtiar et al. (2013) studied the impact of the ovalisation of the culms cross-section subjected to bending loads. They conclude that the modulus of rupture can be overestimated (up to 6.5%) or underestimated (up to 8.7%) depending

on the orientation of the culms and the direction of the applied loads. Nugroho and Bahtiar (2013, 2012) investigated the influence of the taper of the culm on the flexural behaviour. Ignoring the taper along the culm in a four-point bending test can overestimate the bending strength due to the shift of maximum stresses from the centre. They provided a ratio to correct for this effect (Nugroho and Bahtiar, 2013).

Additionally, Harries et al. (2017) investigated the effect of geometry and material properties along the length of the culm on the buckling behaviour of bamboo. They concluded that the middle height properties can give an appropriate estimate for the buckling behaviour in comparison with that of a tapered geometry analysis, but that the midrange (from bottom and top) can result in a non-conservative approximation.

Although none of these studies provides a systematic method that can be implemented for measuring these properties, these studies pointed out the relevance of determining the non-uniform properties of bamboo.

Finally, some authors have proposed a classification system based on geometric properties of bamboo. Harries et al. (2017) suggested a ratio of $D/t > 8$ and $D/t < 8$ (where $D$ and $t$ are the diamter and thickness respectively) for thin-walled and thick-walled species respectively in order to distinguish between the two, and as a possible classification system for the different behavioural types. In addition, the IS-6874 (2008b) classified the bamboo into three groups based on mechanical properties, and for each classification, they further categorised them into different grades based on the mean outer diameter of the culms.

### 2.3.2 Physical and mechanical properties

A review of the current building codes and standards on bamboo is provided by Gatóo et al. (2014). As mentioned, the first standard on round bamboo was BIS-IS-6874 (1973) and it was followed by IS-8242 (1976). The superseded standard IS-6874 (2008a) includes tests methods for the determination of moisture content, density, shrinkage, static bending strength, compressive strength parallel to the fibre, tensile strength parallel to the fibre and shear strength parallel to the fibre. In addition, the National Building Code of India (IS-6874, 2008b), provides values for physical and mechanical properties for round Indian bamboos in green and air-dry condition, as well as safe working stresses for structural design.

The first international standard for bamboo culms published in 2004 by the International Organization for Standardization (ISO) issued three documents; Bamboo - Structural design ISO (2004a); Bamboo - Determination of physical and mechanical properties Part 1: Requirements ISO (2004b) and; Bamboo - Determination of physical and mechanical properties Part 2: Laboratory manual ISO (2004c). The ISO (2004a) standard provides guidance for structural design based on limit state and allowable stresses procedures. The ISO (2004b), was designed for the determination of physical and mechanical properties of round bamboo culms. It comprises the methods for evaluation of moisture content, mass per volume, shrinkage, compression, bending, shear and tension. As these

were the first international standards, they do not invalidate the previous national codes or current construction practices that are based on experience from previous generations. These standards have been revised and supported since the beginning by the International Network for Bamboo and Rattan (INBAR). The ISO (2004b) standard have been recently superseded by the ISO (2019) standard.

Some countries including Colombia, Ecuador, Peru, Jamaica, Ethiopia and India (Harries and Sharma, 2016) have adopted or adapted the test methods provided by ISO (2004b).

In 2007 the Ministry of construction of the People's Republic of China published a standard for determining the physical and mechanical properties of bamboo from small samples (JG/T-199, 2007). It is the first comprehensive standard based on small samples.

More recently, a series of technical series published by The Institute of Structural Engineers (Kaminski et al., 2016, 2017), proposed a methodology for the derivation of design values for bamboo structures. Their methodology is based on testing methods according to ISO (2004b) for full culm specimens. Furthermore, Trujillo and Jangra (2016) proposed potential grading methodologies for the determination of flexural properties of bamboo, flexural strength and stiffness. In addition, Harries and Glucksman (2016a,b) presented a test-kit-in-a-backpack with the aim of performing rapid field tests in areas where technical equipment is not available. It consists of an apparatus that basically replaces a testing machine, which can be operated by non-technical personnel.

#### 2.3.2.1 Test methods for tensile properties

Test methods to determine the tensile properties, in particular, tensile strength, are difficult to perform due to problems in the grips, caused by the low shear and transverse capacity of bamboos (Janssen, 1981). The standard test method for determining tensile strength and stiffness is provided by ISO (2004b). Failures have been reported in the grips rather than in the gauge area, or due to the high shear stresses produced in the transition zone between the gauge length and the grip points (Janssen, 1981; Arce-Villalobos, 1993). Furthermore, Richard and Harries (2015) highlighted that due to the gradient radial distribution of fibre, the test set-up (i.e. fixed or free end restraints, and orientation of samples) influence the results as these are affected by non-uniform bending stresses that are not taken into account in current test methods (ISO, 2004b).

#### 2.3.2.2 Test methods for compressive properties

The test methods for the determination of compressive behaviour have been investigated previously in order to define the best shape and size of the specimen. Janssen (1981) and Arce-Villalobos (1993) give a comprehensive review of the test specimens investigated previously for small samples, full culms, and full culms of long length. Janssen (1981), devised a testing plan in small and full culm specimens and conclude that the small samples can be used in order to determine the compressive strength of bamboo culms. Arce-Villalobos (1993) highlighted the problems that arose in compression tests by the

friction developed between the radial surface of the culm ends and the steel plates of the testing machines. This issue was previously identified by Meyer and Ekelund (1922), and a test set up for preventing the friction was proposed. The current ISO (2004b) standard takes into consideration this phenomenon, and specifies in the test method a device with steel wedges, wax and teflon to prevent this. An explanation of this phenomenon is explained by Janssen (2005).

#### 2.3.2.3 Test methods for flexural properties

Gnanaharan et al. (1994) investigated the effect of the specimen geometry for determining the flexural properties. The tests were carried out with three different types of specimens, long full culm, short full culm according to BIS-IS-6874 (1973), and split bamboos, from which the bending strength and stiffness were calculated. They conclude that short specimens do not truly represent the bending behaviour of bamboo culms and that the specimens usually fail by crushing or shear under relatively low loads. Also, they reported that split specimens shows a different behaviour than that from the full culm.

Vaessen and Janssen (1997) investigated the critical length for a culm under transverse loads to ensure failure by bending stresses rather than shear stresses. They provided a diameter to length ratio which informed the current ISO (2004b) standard.

#### 2.3.2.4 Test methods for transverse properties

Although the transverse properties have been highlighted as crucial for the understanding of bamboo Arce-Villalobos (1993), current codes and standards do not cover test methods for determining these properties. The JG/T-199 (2007) provides a test method for determining the compressive strength in the perpendicular direction. However, these are based on small samples, and no direct relationship can be done for a hollow shape of the cross-section of bamboo. As mentioned in Subsection 2.2.5, some authors have developed test methods to investigate the transverse properties of bamboo. Some tests are more related to the splitting capacity of bamboo (Mitch et al., 2010), while others to the transverse compressive capacity of the culm (Sharma et al., 2013). Harries et al. (2012) provide a review of these methods.

#### 2.3.2.5 Test methods for physical properties

The moisture content and density, have been measured using oven-dry methods. Although the test methods are relatively simple to carry out, the main drawback is that they take a considerable amount of time.

Currently, no standard specifies a method for determining the volume fraction of bamboo. There are several methods available for the determination of volume fraction in engineered composite materials such as the matrix digestion method, optical methods and one based on the density of the composite and densities of the constituents (i.e.fibre and matrix) (Daniel and Ishai, 2006; Herakovich, 1998). Although no systematic method has

been transferred or developed for bamboo, some researchers (Amada et al., 1997; Nogata and Takahashi, 1995; Zhou et al., 2012; Dixon and Gibson, 2014) have measured the volume fraction of bamboo using photographs or microscopic images.

## 2.4 Summary

This chapter provides an overview of the geometrical, physical and mechanical properties of bamboo culms, including the currently available methods to determine these. The relevant conclusions are summarised below.

- Despite the high dependence of the mechanical properties of bamboo culms on its micro and macro structure and the considerable longitudinal variations, the current codes and standards do not take into consideration how to deal with these aspects.
- The importance of measuring the non-uniform geometric properties of bamboo culms has been highlighted by several authors with the efforts to quantify these properties. However, no practical or systematic methods have been proposed nor any design guidelines that advises on how to deal with these properties for the design or construction of bamboo structures.
- The variations of mechanical properties in the longitudinal direction have been associated with the change in geometry, density and structure of the cross-section such as volume fraction (Nogata and Takahashi, 1995; Amada et al., 1997; Janssen, 1981; Zhou et al., 2012). However, for some species, the strength and stiffness in the longitudinal direction do not change significantly (Chung and Yu, 2002; Correal and Arbeláez, 2010).
- The geometric properties do not change linearly along the culm, and therefore the arithmetic means calculated from bottom to top do not truly represent the average properties of bamboo culms.
- From the data reported by Banik (2015), the thinnest sections are located at the mid-height of the culm.
- The radial variations across the culm wall are higher than the longitudinal variations along the culm.
- The measurement of physical properties is crucial for the evaluation of the mechanical properties of bamboo culms. The current methods rely on oven-based procedures that although well established, take a significant amount of time.
- The direction of the studies of the mechanical properties of bamboo culms is very diverse. Some studies focused on the inherent relationships between the micro structure and the mechanical properties with the aim of gaining an understanding for the development of new concepts or for developing new materials (e.g. structural

bamboo products) (Nogata and Takahashi, 1995; Dixon and Gibson, 2014). Other studies investigated the influence of certain parameters inherent to the material (Amada et al., 1997, 1996). And some others studies, focused on the development and standardisation of test methods (Harries et al., 2012; Sharma et al., 2013). It is evident that well-established methods are required for bamboo culms. Furthermore, robust design guidelines that consider all the aspects from the acquisition of the raw material to the construction practices are needed.

- Although full culm tests are very valuable for gaining insight into the mechanical behaviour of bamboo culms, there are many issues associated with the test methods provided in ISO (2004b) that need to be addressed (Janssen, 1981; Arce-Villalobos, 1993; Richard, 2013; Richard and Harries, 2015). Also, while full culm specimens have the potential to include geometric irregularities and radial variation (Harries et al., 2012), these test methods are susceptible to sample orientation (Bahtiar et al., 2013). In addition, since each culm is different, the inherent geometric variations of one culm influence its mechanical response and therefore hinders its comparison to the mechanical behaviour of other culms.

- The methods to test tensile properties of bamboo are complicated because the gripping methods can trigger failure in the grips rather than in the middle part of the specimen. In addition, as the bamboo has a gradient surface, the gripping method can be arranged radially or tangentially. Although, the test set-up can influence the results, there are no guidelines for the appropriate set-up regarding the direction of the grips, and this affect the results (Richard and Harries, 2015). Therefore, it can be difficult to achieve reliability and repeatability.

- Poor correlation was found between the bending behaviour of small split samples and full culm specimens.

# Chapter 3

# Overview of the design framework

This chapter provides an overview of the proposed design framework for bamboo culms in construction. The development of this framework, which is the main aim of this thesis, was a progressive process. It started from the gaps and main challenges identified from the literature, which are introduced here, and it was gradually developed throughout this thesis. Here, the scope and the links between the different stages and methods of this framework are outlined to give a general overview.

Figure 3.1 depicts the flowchart of the fundamental properties and processes for each of the stages of the design framework respectively. The goal of the first stage is outlined in **g.1** and consists of establishing a database of structural bamboo. This database is project based. This means that the data is to be determined for all the culms available to use for a particular project. Throughout this thesis, the acronym SBD is used to refer to the *Structural Bamboo Database* developed in this stage. The second stage refers to all the methods to incorporate the SBD into the design process. These are particularly designed for reciprocal systems and are outlined in **g.2**. The last goal is concerned with the study of

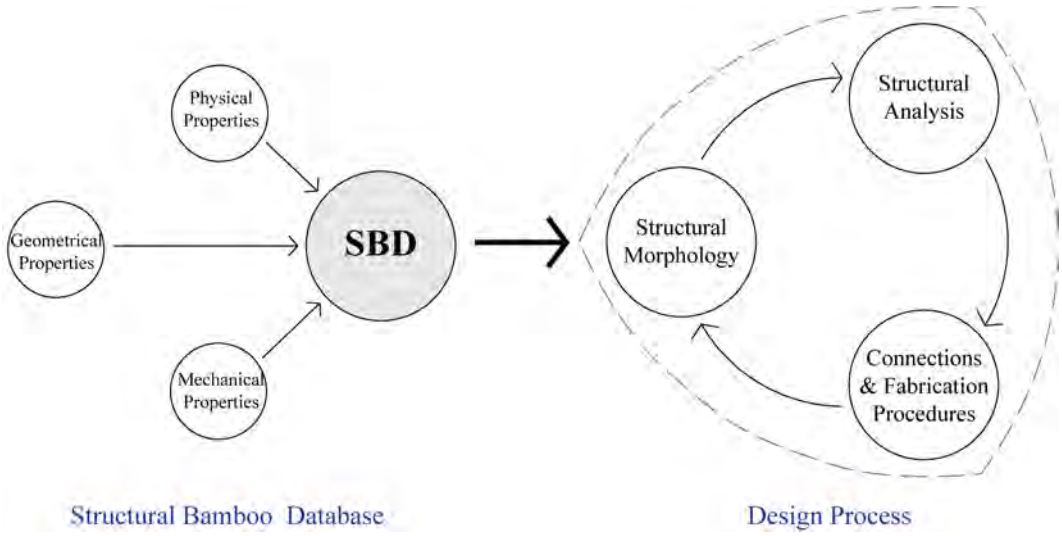


**Figure 3.1:** Design framework for bamboo culms.

possible connection systems and the structural behaviour of bamboo reciprocal systems.

## 3.1 Structural bamboo database (SBD)

Figure 3.2 outlines the methodology for establishing the SBD, from the preparation of the raw material to the final determination of the material properties.

The preparation of the culms refers to a systematic approach to managing the raw material and keeping track of individual bamboo culms. It is done prior to starting the steps for determining the material properties. The description of the preparation methods together with the challenges found while handling the bamboo culms is in Appendix A. Following the preparation of the culms, the samples for determining the geometric, physical and mechanical properties are prepared.

As previously discussed (see Section 1.3), one of the main drivers for the development of this framework is to provide methods with the potential to be implemented in bamboo construction. Therefore, the feasibility of these methods to be developed into transferable technology to the bamboo industry is key. The parameters considered for a method to be transferable are the repeatability, time, cost, skill labour and practicalities so that the amount of work is minimised and the majority of the steps can be automated to allow a systematic reproduction of the steps with reliable results.

The geometrical properties are measured from the full culm identified as prepared culms in Figure 3.2, which is to be used as a structural element. There are two different types of mechanical testing samples specified in the current standards. The ISO (2004b) standard specifies the use of samples consisting of the whole cross-section of bamboo, referred to here as *full culm specimens*. On the other hand, the JG/T-199 (2007) code specifies the use of a small piece of bamboo, which is cut out from the cross-section,

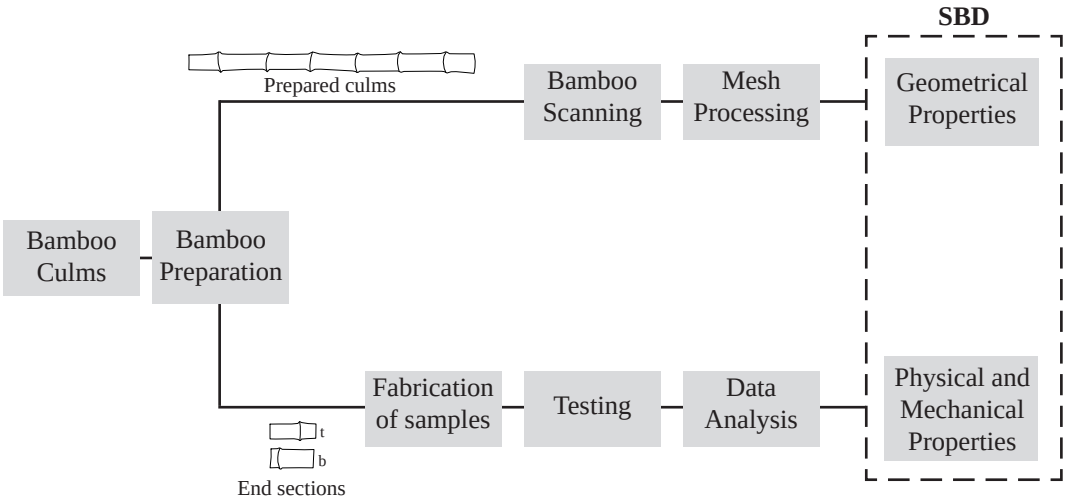


**Figure 3.2:** Flowchart of the methodology to determine the SBD.

referred to here as *small coupons*.

The shape and size of the samples to test the mechanical properties is a crucial aspect for this framework. Based on the issues associated with full culm specimens (refer to the literature review in Section 2.4), in addition to the costs of the amount of material and the capacity of testing machines required to test full culms, small coupons are adopted as a means to determine the physical and mechanical properties of bamboo culms in a systematic approach.

From the literature we know that bending tests in split specimens do not represent the behaviour of full culms and that the current tensile test have many issues associated with the test set-up (see Section 2.3). Therefore, axial compressive tests are used as a surrogate for estimating the bending elastic modulus. Also, due to the nature of the methodology that requires to test each culm, the compression test set-up can significantly reduce the preparation time in comparison with tensile tests.

The portions from which the samples for physical and mechanical properties are obtained are depicted in Figure 3.2. These correspond to the end sections from bottom and top of the culm. We know from the literature that the longitudinal variations in strength and stiffness are associated with the variations in the structure and the change of geometric dimensions of bamboo. As the physical and geometric properties are also part of the SBD, these can be taken into consideration for the estimation of the mechanical properties of each structural element (i.e. each bamboo culm) by interpolation.

The test methods available in current standards (ISO, 2004b,c; JG/T-199, 2007) for determining the physical properties are based on the traditional oven-dry methods. Although this is an effective way to calculate properties such as density and moisture content, these methods are appropriate for research but not for the industry where the time constraints are a key factor. The time required for the JG/T-199 (2007) code to determine these properties is at least one day, while for the ISO (2004b) a minimum of two days is required, considering the time the samples need to be in the oven and the successive measurements until the samples are dried. Herein, methods that can potentially eliminate the oven-dry method for the estimation of moisture content and density are explored.

Determination of volume fraction is not considered in any of the codes or standards currently available for bamboo. However, it will be considered as part of the proposed methodology to estimate the mechanical properties.

## 3.2 Incorporation of SBD into the design process

Figure 3.3 presents the design workflow for incorporating the non-uniform properties of bamboo culms using the SBD into the iterative design process. There are three aspects to consider, the SBD, the structural geometry of the reciprocal system and the type of connection system.

Based on these three inputs, a procedure is introduced so that for each element in the reciprocal system, the bamboo culm that better fits some pre-defined constraints is

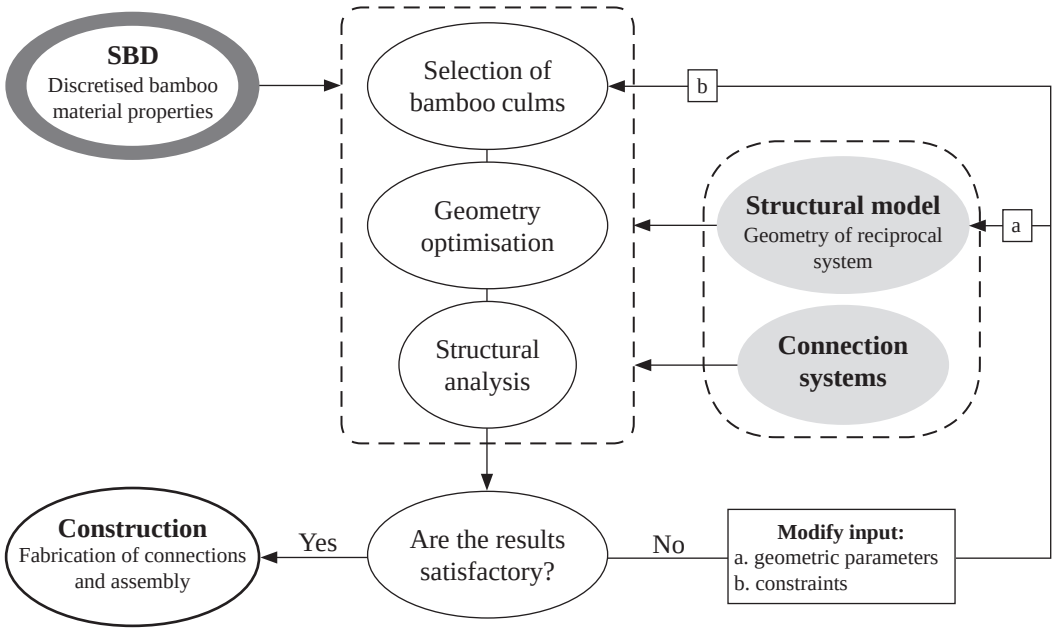


**Figure 3.3:** Flowchart of transfer of data between SBD, structural model and design process.

selected and linked to the given element. These constraints can be based on the geometric or mechanical criterion. As seen in Chapter 1, many authors have recommended to joint bamboo culms as close as possible to the nodes. This is one of the key aspects that will be taken into consideration for the selection of bamboo culms. The criterion for the methods to select the bamboo culms for each element in the structure is based mainly on geometric constraints so that all the elements can fit together preventing clashing between physical connections and nodes in bamboo.

Once the culms are selected for each element, the overall geometry is optimised so that the distance between the elements in each connection is enough to accommodate the diameters of both bamboo culms meeting at that point. Next, the elastic structural behaviour is evaluated and the iterative process started by modifying the constraints and geometric parameters as necessary until a satisfactory solution is found. Subsequently, the details for the fabrication of the connections and assembly of the reciprocal system is made based on the defined solution.

As mentioned in Chapter 1 one of the main challenges are the jointing techniques for bamboo culms. While several type of connections have been proposed and utilised in building structures, either for temporary or permanent structures, there is very little scientific knowledge regarding jointing techniques for bamboo culms. Furthermore, despite the issues identified with the splitting of the culms in connections with mechanical fasteners that perforates the bamboo culm wall, many of the proposed connections rely on fastening systems. In this thesis the development of possible connection systems for bamboo based on clamping systems is investigated. The criteria consist of preventing penetration of the bamboo culm cross-section, workability and prefabrication, stiffness as well as harnessing

as much as possible the capacity of the culms.

## 3.3 Summary

This chapter briefly outlined the main idea of the design framework. The development of each of the stages is provided in the chapters of Part II and III respectively.

The design framework outlined here attempts to address the issues associated with the conceptual, structural and construction practices with bamboo. The focus of the subsequent chapters is gathering enough data to evaluate the potential of the methods and of the design framework as a whole to be further transfer to industry.

# Part II

# Structural bamboo database (SBD)

# Chapter 4

# Geometrical properties of structural bamboo

This chapter presents the initial explorations and development of the method for determining the discretised geometric properties of the SBD using 3D scanning technologies. The specific objectives of this chapter are outlined below.

- To devise a procedure for the 3D shape acquisition (i.e. 3D mesh) of the surface of bamboo culms, around the circumference and along the culm.
- To establish the methodology to determine the geometric properties from the 3D mesh.
- To study the variable and irregular properties of the scanned bamboos to develop an understanding of the non-uniform geometry of bamboo culms and identify the critical properties to include in the design framework.

In this chapter two different bamboo species were used: moso (*Phyllostachys pubescens*) and oldhamii (*Bambusa oldhamii*) bamboos.

Moso bamboo was mostly used in the majority of the experimental work at UCL. It was obtained from UK bamboo supplies limited (UK-Bamboo, 2014), and was harvested from plantations located in the Anji county in Zhejiang province, China. The culms were about 4 to 6 six years old, and approximately 75 mm in average diameter and 4 m long. Some of them were treated with sodium carbonate, anti-mould and anti-insects water solutions, while others were only kiln and air-dried. They were usually kept in an open warehouse in China, and in a dry enclosed warehouse in the UK. There was no data (e.g. treatment, age, etc.) available for all the batches of culms ordered, which is a common issue when obtaining bamboo from suppliers. However, no significant difference were found among the different batched of bamboo culm tested.

Oldhamii bamboo was used for the determination of a complete set of SBD, including the geometrical properties presented in this chapter. It consists of 100 oldhamii bamboo culms, of 5 m in length, and an average diameter of 70 mm approximately. These were

obtained from Bambuver (Bambuver, 2016) located in Huatusco, Veracruz, Mexico. The culms were treated by leaching at high temperature and were around 3 to 5 years old. This batch of culms was used during two research stays in 2016 and 2017 at National Autonomous University of Mexico UNAM, in the Structures Laboratory of the Faculty of Architecture, where the culms were scanned.

Figure 4.1 shows the key features to scan from each bamboo culm, namely the outer surface of bamboo culms, including the sheath scar and nodal ridge, with enough detail to identify the nodes, and the culm ends. The geometric properties to determine are classified in two groups and are listed in Table 4.1. The first group consists of the geometry for the structural modelling, namely the structural node coordinates ($x$, $y$ and $z$ coordinates at the nodes and internodes of bamboo culms), and the diameter and thickness of the cross-section. The second group refers to the auxiliary data used in the design process. These are: the node width, to define the position of the bamboo culms and prevent clashing between bamboo nodes and connections; a reference point, consisting of an indentation used as a guide for linking the digital model with the physical culm; the brep geometry, consisting of a boundary representation of the shape of bamboo using connected surfaces; and the index, which is a binary data indicating whether the data corresponds to a node or internode.

Since we learned from the literature that besides the asymmetrical properties, the longitudinal variations are not linear and the changes are different among species, certain geometric variations and irregularities are analysed. This analysis will help to understand the significance of these properties to decide on whether to include them or not as part of the design process. For example, it will help us to define if the out-of-straightness within

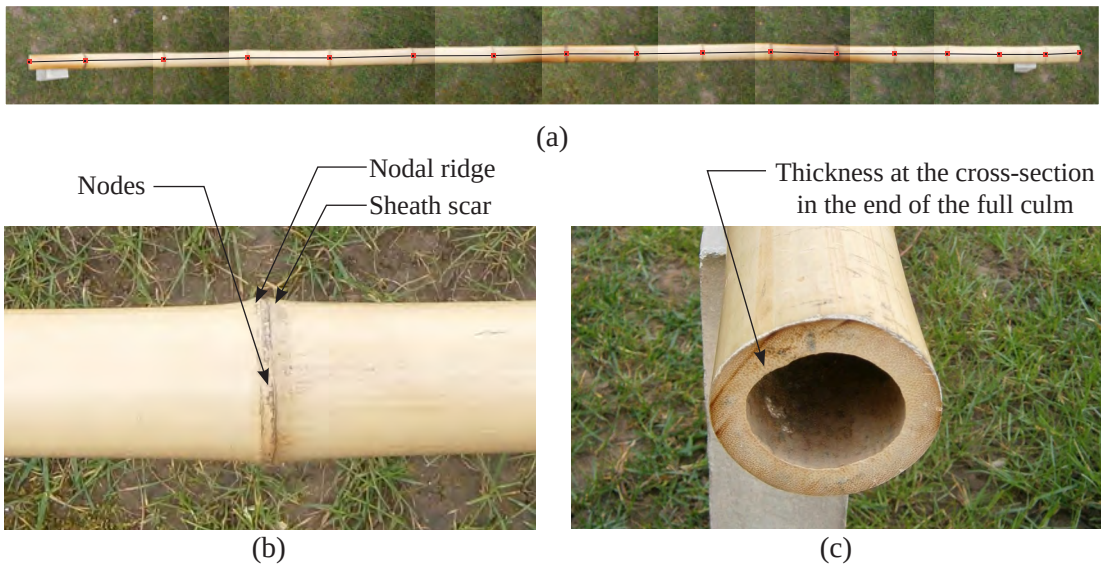


**Figure 4.1:** Key aspects of the geometry to scan: (a) outer surface of the culm in the longitudinal direction; (b) nodal ridge and shear scar geometry to identify the position of the nodes; and (c) the cross-section thickness at both ends of the full culm.

a single internode is insignificant or not. Table 4.2 provides the list of the variable and irregular parameters evaluated. Note that the variable properties are those associated with the gradient nature of bamboo along and across the culm, whereas the irregular properties are related to the inherent unsymmetrical properties of natural materials.

**Table 4.1:** Geometric properties for the SBD.

| Discretisation properties for structural modelling | Auxiliary data for design process |
|---|---|
| Nodes coordinates | Node width coordinates |
| Internode coordinates | Reference point |
| Diameter | Brep geometry |
| Thickness | Index |

**Table 4.2:** Non-uniform geometric properties evaluated

| Variations | Irregularities |
|---|---|
| Thickness variation due to taper | Out-of-straightness |
| Diameter variation due to taper | Ovalisation |
| Shape factor variation due to taper | |
| Internode length | |

## 4.1 Measurement of geometric properties using 3D scan

The development of 3D scanning technologies is relatively new, it dates back to the second half of the twentieth century (Breuckmann, 2014). This technology has been gradually developed, and nowadays, high definition 3D scanning enables the accurate measurement of surfaces. It has been widely used in areas such as reverse engineering (Wang, 2011), arts, archaeology and cultural heritage, for example. Here, we use a 3D scanning techniques (Artec-3D, 2015) to develop a practical method for the systematic measurement of the geometrical properties of bamboo culms.

The overall procedure is divided into two stages. The first is the actual scanning of bamboo culms, including the set-up and the process to scan them. The second is concerned with the processing of the acquired 3D data to determine the required geometrical properties. Below, preliminary investigations and the proposed methods are presented for both stages, followed by the evaluation of the non-uniform properties from the scanned data and the validation of this method.

### 4.1.1 Preliminary scanning

Preliminary explorations on the scanning of the outer surface of the culm were carried out with the aim of determining the feasibility to adopt 3D scanning technologies. The material used was a bamboo culm of the moso species with an average diameter of 70 mm.

Figure 4.2 shows the set-up used. It consists of a robotic arm, Kuka KR10 R1100 six-axis (Kuka, 2015), with an Artec Space Spider 3D scanner (Artec-3D, 2015) attached to it. The process requires fully fixing the culm on one end and scanning the culm lengthwise. This manoeuvre is repeated five times, each time rotating the culm approximately 72° to cover the whole surface. Since the length of the culm was limited to the reach of the robot arm, a short piece of bamboo of approximately 1.0 m was used. Before the scanning, several targets were attached around the culm in order to compare the auto and manual alignment processes.

The hand-held 3D scan has a resolution of up to 0.1 mm and a point accuracy of 0.05 mm. The 3D scanner works with blueLED light which makes it safe to use. It is capable of scanning objects without targets on the surface. During the scanning process a sequence of frames (i.e. 3D surfaces) are captured. These frames are then stick together to create the full scanned surface. The area scanned per frame depends on the field of view of the scanner. For the Artec Spider the field of view ranges between 90 x 70 mm to 180-140 mm for the closest and furthest range (Artec-3D, 2015). Therefore, it was possible to capture the whole diameter in each frame. The approximate distance between the scanned object and the 3D scanner is of 220 mm. The 3D data processing Artec software for editing allows exporting the results as a 3D mesh to further import to CAD software.

Once the culm was fully scanned, the next step was to post-process the data in the Artec software to generate the 3D mesh. In general, the steps to generate the 3D model consists of editing individual scans, alignment of scans (if applicable), global data registration, the fusion of all scans into a single 3D model, removal of outliers, and final editing of the 3D model. The first of these steps refers to making a visual inspection of the scanning models to define whether it needs to be edited for possible errors such as misalignment of frames, the capture of unwanted objects, gaps in the surface and noise. The second step for alignment of the scans is only required when several scans of the same culm have been


**Figure 4.2:** Artec scanner mounted on a kuka robot for preliminary investigations on the scanning of bamboo culms.

done. The software allows for automatic or manual alignment. The global registration converts all the scans into the same coordinate system. Following this, the outliers, which are pieces of data detached from the main surface can be removed. Then, the fusion process merges all the frames to create a single 3D polygonal model. Finally, the model can be edited to remove unwanted data, misaligned frames, to fill gaps, remove noise or to perform mesh simplification to reduce the number of polygons and optimise the size of the model and of the file.

Figure 4.3 depicts the output of 3D mesh data. Although several targets were used around the surface of the culm, the auto-alignment of the five scans was not optimal. Therefore, the scans were manually aligned using the targets as guides in the Artec software. After the alignment, the data was exported as a 3D mesh in a .stl file.

In order to determine the specific geometric properties of bamboo, a simple algorithm was devised to evaluate the 3D mesh (see Figure 4.4). The aim was to determine the longitudinal axis of the culm through a series of 3D coordinates. It was implemented in the CAD modelling software Rhinoceros (McNeel, 2017) and the plug-in Grasshopper.

The method consists of a series of planes to intersect the 3D mesh, obtain circumferential curves, and then calculate the centroid of each curve. Figure 4.4 depicts the process. First, two endpoints are manually selected, one at each end of the culm, from which $yz$ planes are created. It is important to mention that the resulting 3D mesh from the scanning is in all cases oriented roughly in the $x$ direction of the 3D coordinate system. The two planes mentioned above, are used to intersect the culm mesh. For this, it is assumed that the culm mesh is a cylinder. Therefore, the centroid of the circumferential curves resulting from the intersection between the cylinder and the planes is the same regardless of the orientation of each plane, as long as it intersects the entire cross-section of the cylinder. Once the centroids at the ends are obtained, a line passing through these two points is created, and this is considered as the longitudinal reference axis, from which a series of plane sections are generated and oriented normal to this line. Similarly, these planes are intersected with the 3D mesh to generate the respective circumferential curves

**Figure 4.3:** Output of the mesh of the outside geometry of the culm.

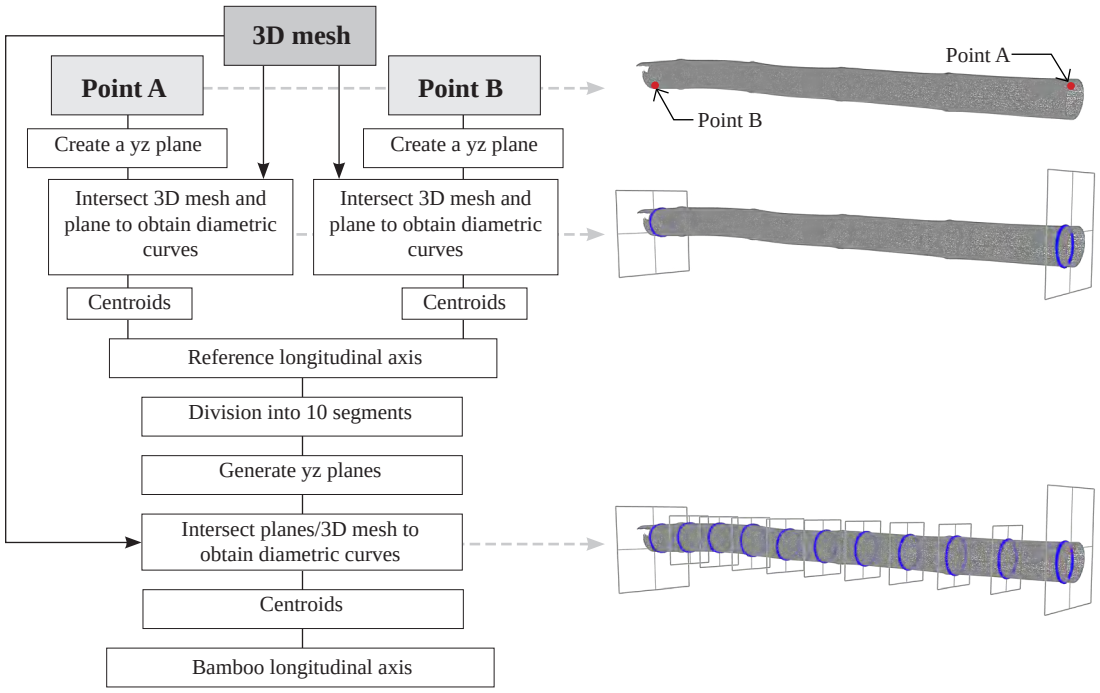


**Figure 4.4:** Flowchart to determine geometric properties from raw scan data.

and centroids. Finally, the bamboo longitudinal axis is created by joining all the centroids together with a polyline as shown in Figure 4.5.

The method successfully generated the required data. However, some limitations needs to be addressed. In this case, the size of the robot is a limitation for scanning long culms. Also, this method requires five different scans to complete a single culm, in which one of the ends is not possible to scan, and the thickness is not captured. Finally, the need to manually align the scan output takes a considerable amount of time. The method presented below take these initial findings to develop a more robust method.

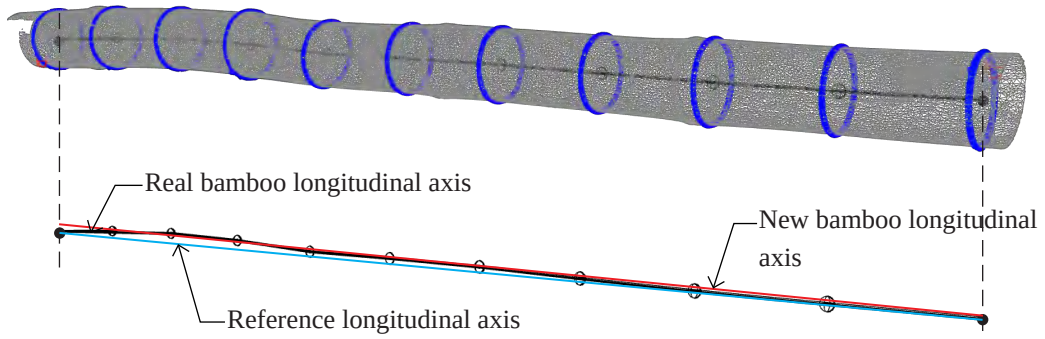


**Figure 4.5:** Preliminary process to determine the culm axis.

### 4.1.2 Scanning method

The frame and specific process to scan each culm was developed by the members of the bamboo research group at UCL and is briefly outlined here. The author contribution to this method is in the post-processing of the 3D mesh to determine the geometric properties and presented in Section 4.2.

Figure 4.6 shows the set-up for the proposed scanning method. It consists of a more robust and systematic process to scan the outer surface of bamboo culms, including the thickness at the ends of the culm.

The method was designed with the aim of scanning the whole culm in a single pass. Unlike the previous method, this method consists of a fixed 3D scan and a moving bamboo culm. Although it requires a manual process for the movement of the culm, the main advantage of this method is that it captures the whole surface in a single scan (i.e. single pass), without the need of extra alignment or use of targets. For this process, a skeletal frame was designed and built (see Figure 4.6). It consists of an aluminium frame provided with roller supports that allowed the horizontal movement by rotary motion. The procedure requires to rotate the culm from each end manually.

In order to allow linear movement by rotating the culm, the pair of rollers is oriented at an angle $\beta$, as shown in Figure 4.7. This angle defines the linear movement per each cycle (i.e. rotation of the culm in the longitudinal axis of $2\pi$). The angle $\beta$ was set up so that the linear movement was visible within the field of view of the Artec spider to guarantee to capture the whole surface and prevent a helix ribbon as output. Figure 4.8 shows a diagram with the relationship between the angle $\beta$, the circumference of the culm diameter $c$, and the linear movement $a$ refer to as lead. The lead $a$ per cycle is set lower than the field of view of the scanner, and the $\beta$ for a given $a$ and circumference of bamboo

**Figure 4.6:** Skeletal frame for the scanning process.

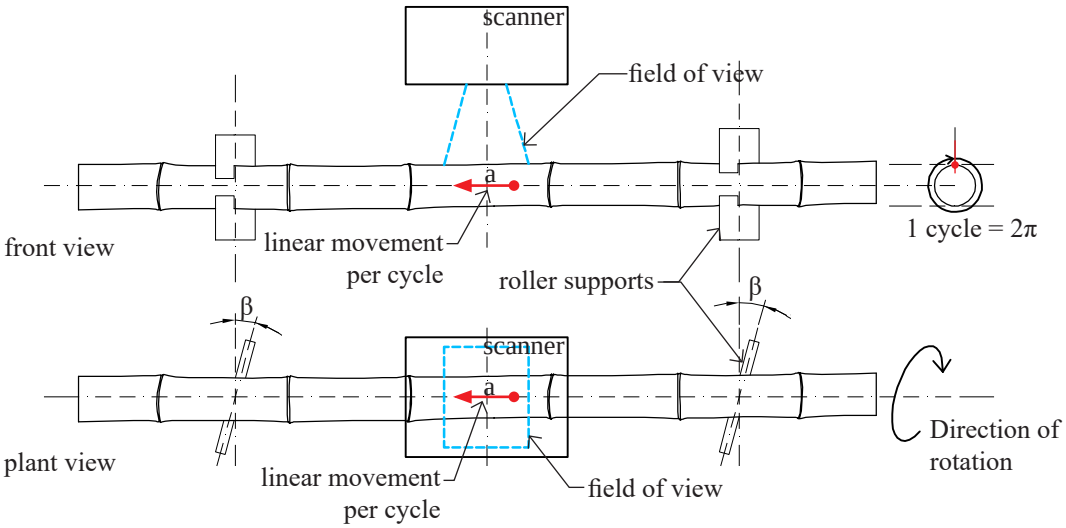


**Figure 4.7:** Movement of culm during scanning process.

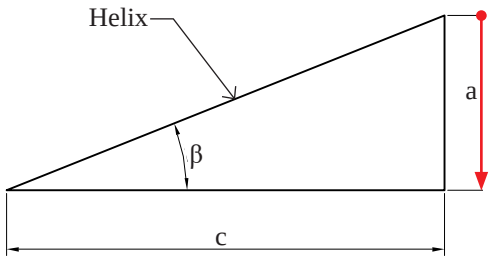


**Figure 4.8:** Relationship between angle $\beta$, circumference $c$ and linear movement.

can then be calculated using the following relation

$$\beta = \arctan \frac{a}{\pi D} \tag{4.1}$$

where $D$ is the diameter of bamboo.

Using this method, the scanning frames are self-aligned. Therefore, no extra manual alignment is required, and no extra features or targets are necessary, reducing in this way the preparation process. In average, a culm of 4 m long was scanned in approximately 5 minutes using this method.

In order to capture the thickness at the ends of the culm during the scanning process, a surface that represents the inner surface of the culm was created using a rolled paper. Figure 4.6 show a rolled paper stuck to a plastic paper and inserted inside the internode of the culm. This allows capturing the surface of the paper that is tangent to the inner side of the culm to allow for measurements of the thickness.

## 4.2 Procedure to evaluate the 3D mesh for determining the geometrical properties

Figure 4.9 presents the flowchart of the general overview of the processes to determine the geometric properties from the output 3D mesh (in .stl file). This was implemented in the modelling software Rhinoceros 3D (McNeel, 2017) and the plugins Grasshopper and GhPython. The detailed description of how the geometric properties of the SBD were determined is provided below.

The first step is to identify the nodes, ends and reference point by evaluating the 3D mesh and selecting the 3D points corresponding to the respective geometries. The identification of the nodes and reference point is made by evaluating the angles between the vectors normal to every two adjacent faces in the mesh. Figure 4.10 shows the vectors for each of the faces in a node and internode area. Note that for the faces that are in the internode area, the angle between vectors is relatively large, or almost parallel, in comparison to the angle between vectors corresponding to the node area. Figure 4.11a shows the threshold of angles from which the nodes are identified. For all the angles between 30° and 45°, the endpoints of the edges shared by both faces, from which the angle is measured, are selected.

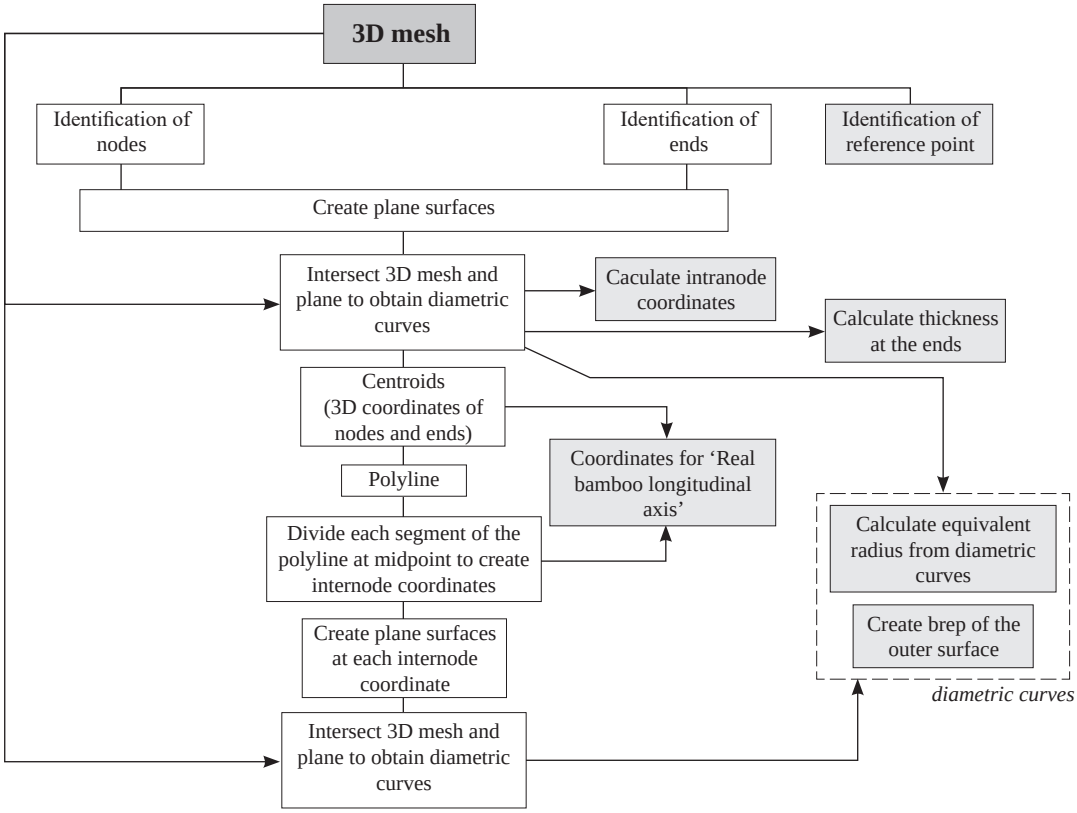


**Figure 4.9:** Overview of the general processes for determining the geometric properties from the 3D scanning data.

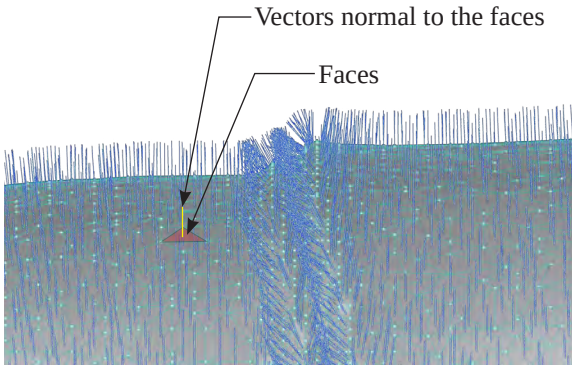


**Figure 4.10:** Vectors normal to the faces of the mesh.

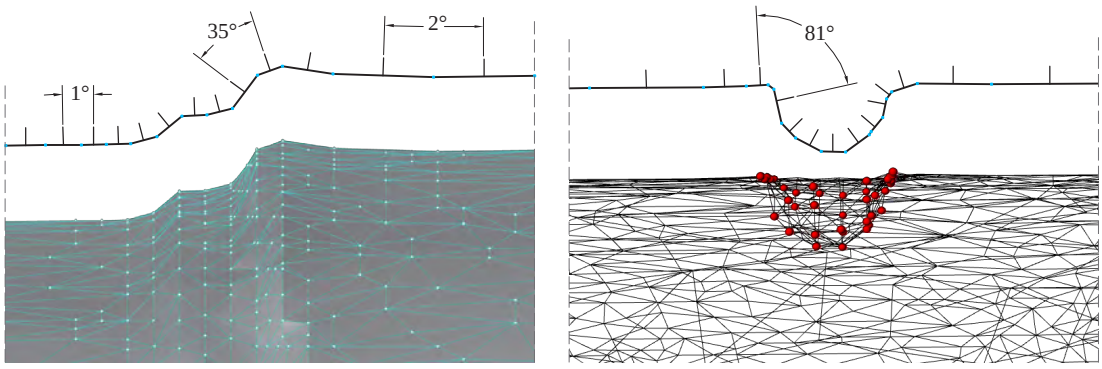


**Figure 4.11:** (a) Identification of nodes and (b) reference point in 3D mesh.

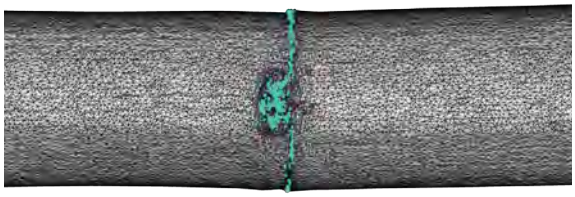

**Figure 4.12:** Selection of 3D coordinates at nodes including those at the emerging branch.

Similarly, to determine the location of the reference point, a threshold was defined as shown in Figure 4.11b. The details for creating the indentation in the culm as a reference point are provided in Appendix A. The endpoints are defined when the angle is $> 80°$, and the reference point is computed as the mean of all the 3D coordinates.

Once these points were selected, the circumferential curves at the nodes and ends were created. It is important to highlight that for some culms the defects (e.g. emerging branches or cracks) were more pronounced. The point coordinates of such features were also recorded as shown in Figure 4.12. These were manually removed in order to prevent tilted circumferential curves. The points were grouped into several batches in order to distinguish the nodes from the ends.

The circumferential curves were defined by creating the best fitting plane for each group of points (e.g. nodes and ends), see Figure 4.13. The intersection between the 3D culm mesh and the plane meshes is computed using the best fitting planes in order to obtain the circumferential curves and the respective centroids of each curve as shown in Figure 4.13. For the nodes, these curves and centroids represent the position and direction of the nodes. Note that for the curves at the ends the plane can be tilted due to the angle of the cut during the preparation of the culms (see Figure 4.14). This tilted plane is prevented by taking the plane normal to the vector defined by the centroid of the end curve and the closest node centroid.

Figure 4.15 depicts the circumferential curves at the ends, nodes and internodes, the brep geometry and the longitudinal axis. The circumferential curves at the internodes were determined by using a plane normal to a vector passing through each two adjacent node coordinates. Similarly, the intersection between these planes and the 3D mesh of bamboo is computed to determine the circumferential curves and the centroids, which represent the internode coordinates. The brep was defined using the circumferential curves obtained from the intersection between the mesh and the planes along the culm.

To create the lofted surface we used the mesh planes of the ends, nodes and internodes. These planes are offset so that the geometric detail around them can be captured. The

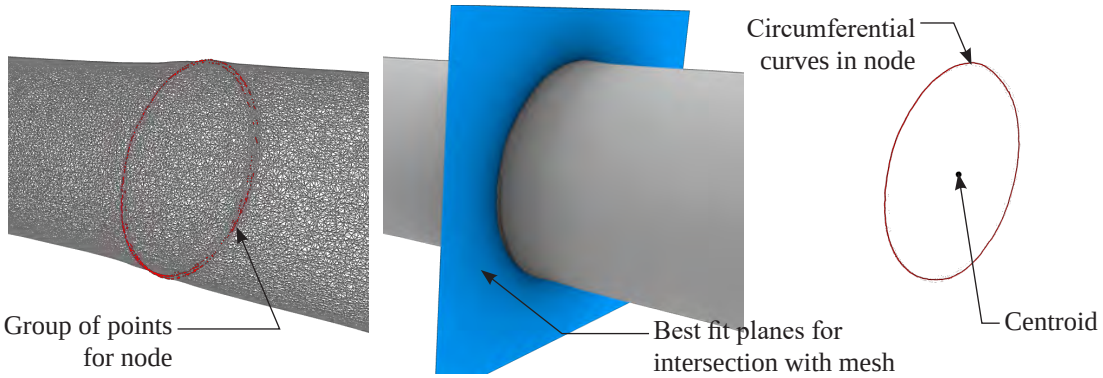


**Figure 4.13:** Evaluation of 3D mesh to select points at nodes, create fit planes and compute circumferential curves and centroids.

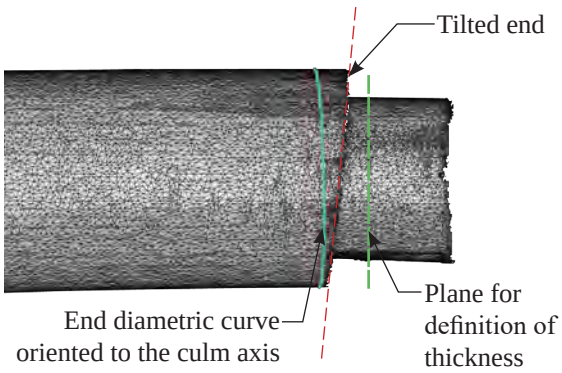


**Figure 4.14:** Adjustment of the circumferential curve at the end of the culm.

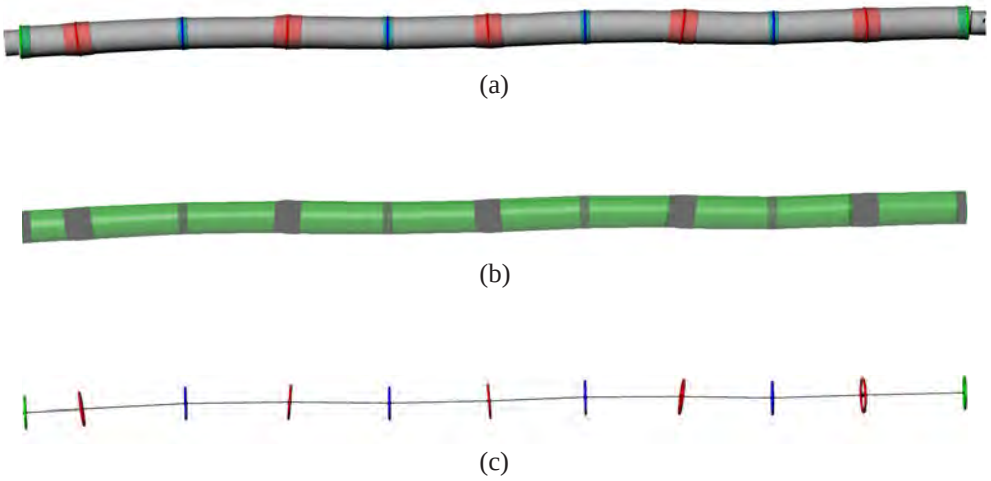


**Figure 4.15:** Geometry along the culm. (a) Circumferential curves obtained from the 3D mesh. (b) Brep created using the circumferential curves. (c) Longitudinal axis and circumferential curves at the ends, nodes and internodes.

planes for the nodes and internodes are offset to both sides, and the planes at the ends are offset towards the inner side of the culm. All these planes are used to intersect the mesh and create circumferential curves that are used to create the lofted surface. The longitudinal axis of the culm is created by a polyline using the centroid of the nodes, internodes and ends.

The diameters are obtained at each point along the culm, by evaluating the mean equivalent radius of each circumferential curve and their respective centroids. The thickness is defined at both ends. The end planes are offset towards the mesh created using the surface of the paper inside the internode (see Figure 4.14). Similarly, the circumferential curves resulting from the intersection of these planes and the mesh are computed, and these are projected back to the end planes. The difference between the radius of the inner and outer curves is defined as the thickness. Care shall be taken when installing the paper inside the internode, as from some scans the paper was clearly not tangent to the inner part of the internode.

The node width coordinates are obtained by evaluating the radius around each node as in Figure 4.16. The node planes are offset to both sides, and the radius are evaluated at each point. The intranode coordinate is defined when the difference between the radius from adjacent curves is

$$(r_i - r_{i+1}) \approx 0.0\text{mm} \tag{4.2}$$

where $r$ is the radius, and $i$ indicates the index of the curve evaluated.

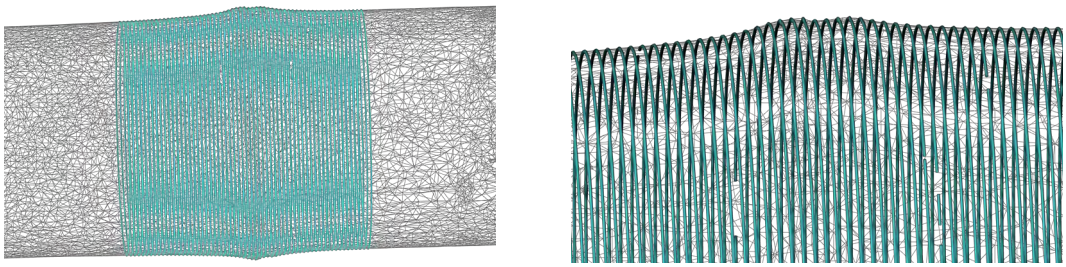

**Figure 4.16:** Definition of intranode coordinates.

### 4.2.1 Validation of digital and physical bamboo geometrical properties

The digital and physical dimensions of three moso bamboo culms and forty oldhamii bamboo culms were compared for validation. The culms were scanned following the previously outlined process.

The diameters of the moso bamboo were measured at three different points along the length (see Figure 4.17). These were measured with a vernier of 0.01 mm of resolution. The differences between the diameters measured from the physical culm and the digital model are provided in Table 4.3. The average difference is of 0.20 mm and the maximum recorded of 0.45 mm. The average culm diameter was of 40 mm. Therefore, the maximum error measured is $< 1.2\%$.

For the oldhamii culms, the thickness and diameters were measured. The thickness was measured at four orthogonal sides in the top and bottom part of the culm. The diameter was measured at two opposite orthogonal sides where one of the sides correspond to the position of the reference point. However, these measurements were taken approximately two months after the culms were scanned, thus differences between the digital and physical dimensions are not entirely caused by scanning error measurements, but might be caused due to changes of the dimensions due to the hygrothermal properties of bamboo. These

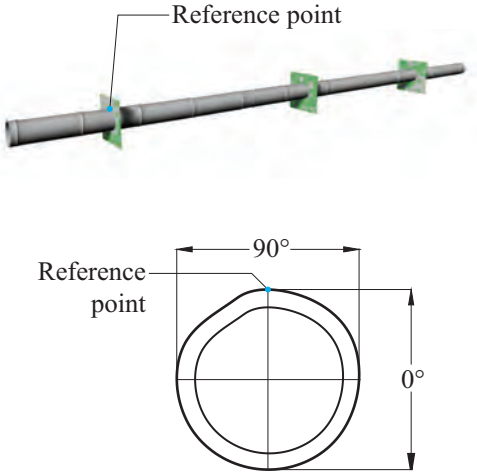


**Figure 4.17:** Position of measurements of diamters in bamboo culm.

**Table 4.3:** Differences in mm between digital data and physical measurements on moso bamboo culms.

| Culm | Position 1 | | Position 2 | | Position 3 | |
|---|---|---|---|---|---|---|
| | 0° | 90° | 0° | 90° | 0° | 90° |
| C1b | 0.03 | 0.24 | 0.06 | 0.32 | 0.06 | 0.36 |
| C1t | 0.16 | 0.04 | 0.16 | 0.30 | 0.39 | 0.45 |
| C3b | 0.21 | 0.00 | 0.31 | 0.15 | 0.21 | 0.16 |

**Table 4.4:** Difference in mm and percentage difference between digital data and physical measurements for 3 moso and 40 oldhamii bamboos.

| | Moso | Oldhamii | | |
|---|---|---|---|---|
| | Diameter | Thickness | | Diameter |
| | | top | bottom | |
| Difference (mm) | 0.45 | 0.57 | 0.48 | 0.67 |
| Percentage error (%) | 1.2 | 9.9 | 6.7 | 1.1 |

changes as well as the environmental properties (temperature and relative humidity of the storage) were not quantified. Table 4.4 provides the average difference for the thickness at the top and bottom and the diameter from the digital and physical dimensions.

It is important to note that the resolution for the fusion method used (i.e. fast fusion) is 0.50 mm, and for large objects (> 100 cm) the maximum acceptable error of the scan is considered as 0.40 mm (Artec-3D, 2017). Overall, the percentage error measured for both batches (moso and oldhamii) is similar. However, the percentage error of the thickness is more significant (up to 10%, refer to Table 4.4), as they both have roughly the same error in millimetres, see for example difference in mm and percentage error in Table 4.4.

We can estimate the possible dimensional change in millimetres occurred whilst in storage for two months. This can be done by using the dimensional change in percentage ($\Delta D$ %) as estimated in the next Chapter 5 and provided in Table 5.2. The average moisture content measured at UNAM laboratory where the culms were scanned was 10% and the moisture content for the majority of the culms at UCL where the culms were used for mechanical testing were 8.2%. Considering that the culms lost 2% of moisture content, the shrinkage in diameter and thickness was 0.37 and 0.28 mm respectively on average. This is only an approximation, but it means that at least the error in mm for the diameter and thickness is 0.30 and 0.25 mm if we take into consideration possible variations due to change in moisture content.

## 4.3 Analysis of variations and irregularities in bamboo culms geometry

This section presents the variations in thickness, diameter, shape factor and internode length, and the irregularities including the out-of-straightness and ovalisation.

The material used for this analysis consists of moso (*Phyllostachys pubescens*) and oldhamii (*Bambusa oldhamii*) bamboos. The data obtained from 139 scans completed as part of the batch of oldhamii culms is presented to illustrate these parameters. Forty-two culms were scanned complete (i.e. about 4500 mm in length) and 52 of them were scanned at halves, as these culms were cut at the middle with the aim to obtain data from the thickness at the mid-height.

### 4.3.1 Thickness variation

The thickness taper ratio can be defined as the change in culm wall thickness per linear metre as follows

$$t_R = \frac{t_b - t_t}{l_t} \tag{4.3}$$

where $t_R$ is the thickness taper ratio in mm/m, $t_b$ and $t_t$ are the thickness at the bottom and top respectively, and $l_t$ is the total length between the two measurements.

Figure 4.18a shows the variation of thickness along the length for a moso bamboo culm. The thickness decreases from 9.0 mm at the bottom to 4.2 mm at the top, over a length of 3460 mm. The thickness taper ratio calculated as in Equation (4.3) is 1.4 mm/m, assumes that is a linear relationship between the thickness of the culm over the length. However, if we estimate the thickness of each internode based on this linear relationship, the value obtained will overestimate the thickness. A better model for this relationship is a quadratic polynomial, which results in a coefficient of determination $R^2$ of 0.99 in comparison with 0.90 from that of a linear model.

The average thickness taper ratio for the batch of 139 oldhamii culms in length between

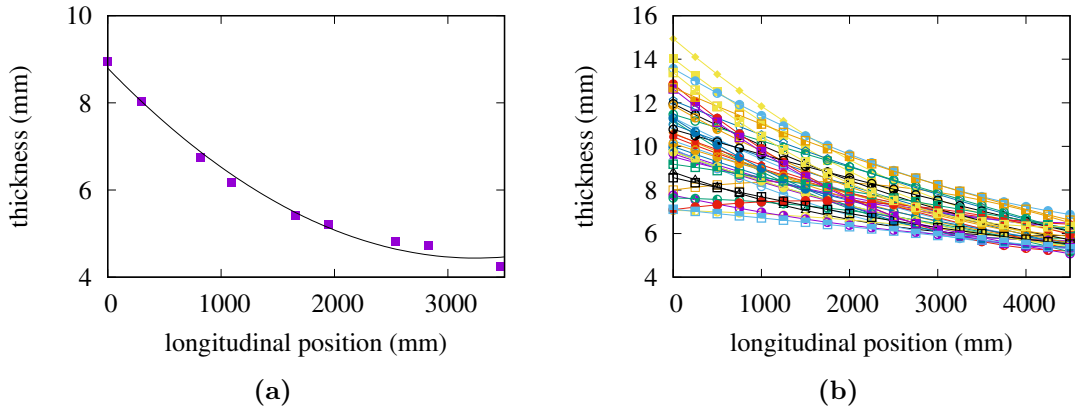


**Figure 4.18:** (a) Variation of thickness in the longitudinal direction from bottom to top for a moso bamboo culm. The curve represent a quadratic polynomial function with a $R^2$ of 0.99. The thickness at different positions in the longitudinal direction for this culm are obtained using: $t(x) = 4.133 \times 10^{-7}x^2 - 0.002684x + 8.796$. (b) Variation of thickness in the longitudinal direction for the oldhamii culms scanned at halves. The data was measured at three points (bottom, middle and top) and presented from bottom to top. The best fit curve for this data is a quadratic function. The average was of $R^2$ of 0.984.

the ranges of 1800 to 4500 mm was found to be 0.9 mm/m with a standard deviation of 0.48. Figure 4.18b shows the thickness variation along the length for the oldhamii bamboo corresponding to the culms scanned at halves and measured at three points (bottom, middle and top). The thickness of these culms was obtained at three different parts, bottom, middle and top. Similar to the moso bamboo, the function that better describes this set of data was a quadratic polynomial. On average, the coefficient of determination $R^2$ for the quadratic and linear model of all these culms is of 0.984 and 0.904 respectively. Interestingly, although a quadratic function best describes the variation of the thickness, the rate of change, or thickness taper ratio differs for each culm. This could be due to the position of the culm sample in the bamboo plant (i.e. bottom, middle or top).

Furthermore, the thickness at the bottom part of the culm varies significantly in comparison with the thickness towards the top (see Figure 4.18b ). This agrees with the fact that the thickness at the bottom of the culm changes at a higher rate, as seen in the literature review in Section 2.1. The values measured for the bottom range between 7 to 15 mm, while those for the top are between 5 to 6.9 mm.

For geometric discretisation, the thickness is estimated at each internode using the quadratic equation given by

$$t_1 = a(x_1 - x_0)^2 + t_0 \tag{4.4}$$

where $x$ and $t$ refer to the longitudinal position in the culm wall and the thickness respectively, and the subscripts 0 and 1 refer to the positions at the bottom and top of the culm respectively. The points at any $x$ position are estimated by solving for $a$. From the culms depicted in Figure 4.18b, if the thickness at the midpoint of the culm is calculated based on a linear model, the thickness is overestimated on average by 9%, and a maximum of 24%, which impacts the calculation of the section properties directly. In the discretisation of the geometric properties of bamboo, the estimation of thickness for each internode is done using Equation 4.4.

### 4.3.2 Diameter variation

The diameter taper ratio can be approximated linear as follows

$$D_R = \frac{D_b - D_t}{l_D} \tag{4.5}$$

where $D_R$ is the diameter taper ratio in mm/m, $D_b$ and $D_t$ are the diameters at the bottom and top respectively, and $l_D$ is the total length between the two measurements. Equation 4.5 is usually defined as the taper of the culm (Nugroho and Bahtiar, 2013).

The $D_R$ for the moso bamboo was found to be of 2.5 mm/m (see Figure 4.19). As mention in the previous Section 4.2, this methodology allows the measurement of the diameter at each internode, and thus prevent the need to estimate an average diameter for the entire culm. Figure 4.19a depicts the change in diameter from bottom to top for a moso bamboo culm, the same culm used for Figure 4.18a. The model that better describes the

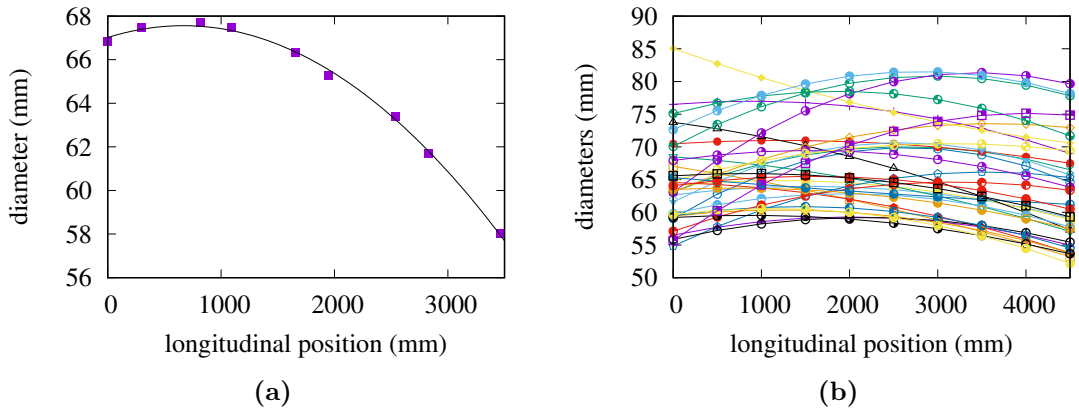


**Figure 4.19:** (a) Variation of diameter in the longitudinal direction from bottom to top for a moso bamboo culm. The curve represent a quadratic polynomial function with a $R^2$ of 0.998. The diameter at different positions in the longitudinal direction for this culm are obtained using: $D(x) = -1.229 \times 10^{-6}x^2 + 0.001635x + 67.02$. (b) Variation of diameter in the longitudinal direction from bottom to top for the oldhamii full culms scanned. The curves represent the quadratic functions that best describes the set of data for each culm, with a $R^2$ of 0.95.

diameter data is also a quadratic polynomial with a coefficient of determination of 0.998 in comparison with 0.81 for that of a linear model.

The average $D_R$ for the batch of 134 oldhamii culms in length of ranges from 1800 to 4500 mm was found to be 1.6 mm/m with a standard deviation of 1.7. From these culms, 22 of them have a higher diameter at the top. This is not consistent with the common pattern reported for bamboo that it decreases towards the top. However, recall from the literature (Banik, 2015) that thinnest sections are located at the middle of the culm. This highlight the importance and the need for a method to determine geometric properties of bamboo, as the variations are different for each individual culm.

Figure 4.19b shows the diameter variation for the oldhamii bamboo culms scanned from the first batch. These correspond to the culms that were not cut by half and were scanned complete, with an approximate length of 4500 mm. On average the coefficient of determination for the quadratic and linear model for these culms is of 0.95 and 0.66 respectively.

### 4.3.3 Shape factor

The shape factor $\Phi$ is a dimensionless value that indicates the ratio of the radius to the thickness for a cross-section. This ratio is an indication of how thin or thick is the cross-section. For a hollow circular tube (Wegst and Ashby, 2007; Ashby, 2011; Wegst, 2011) it is defined as

$$\Phi = \frac{r}{t} \tag{4.6}$$

where $r$ is the radius and $t$ is the thickness of the culm. Figure 4.20 illustrates the variation of $\Phi$ from bottom to top. These correspond to 42 oldhamii bamboo culms of approximately 4500 mm long (the same as shown in Figure 4.19b). It can be seen that for all these cases

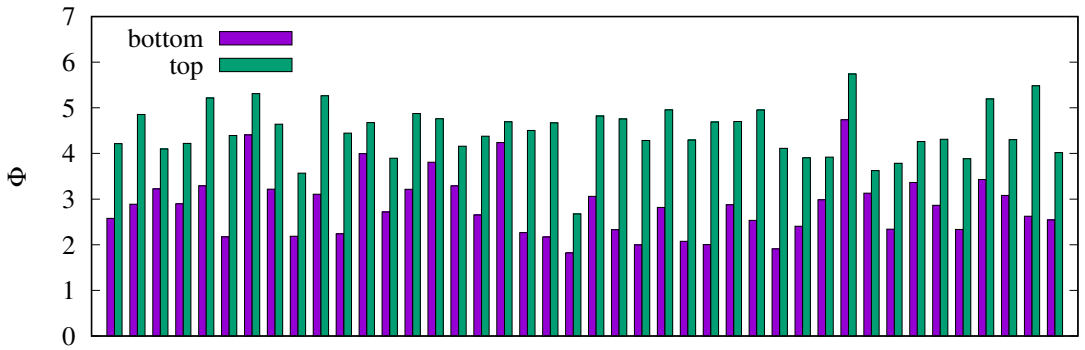


**Figure 4.20:** Shape factor Φ of the series of oldhamii culms of 4500 mm in length.

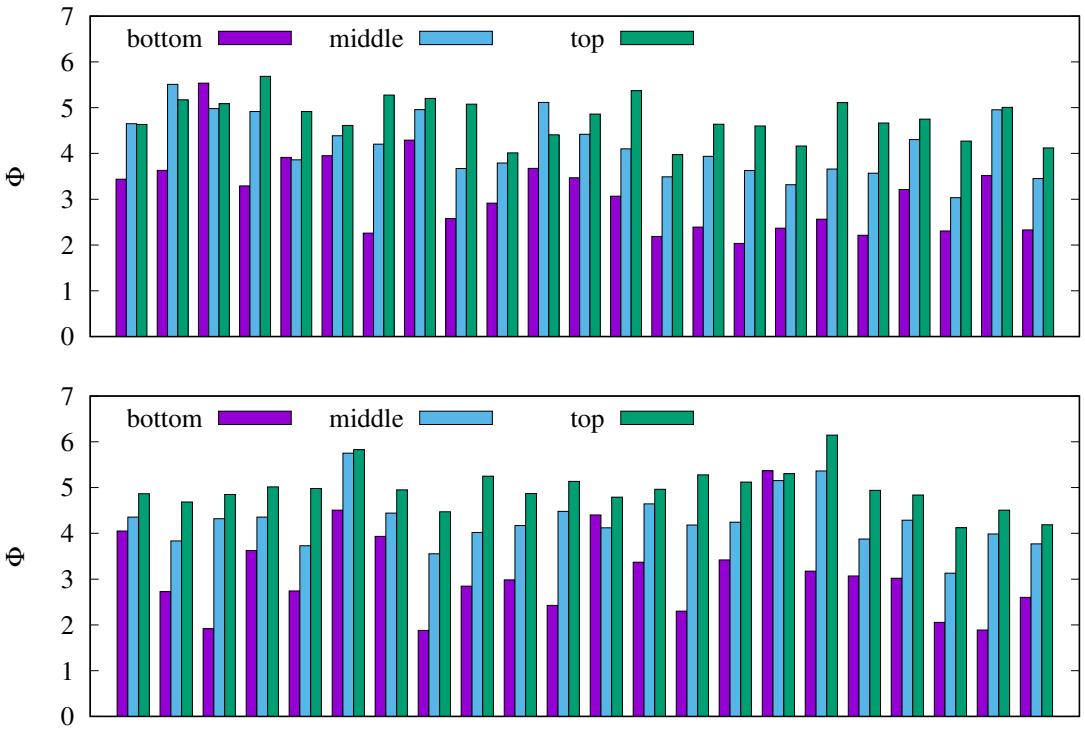


**Figure 4.21:** Shape factor Φ of the series of oldhamii culms at bottom, middle and top.

the top part becomes thinner, regardless that for some the diameter increases.

Figure 4.21 shows the variation of Φ calculated from the culms cut at the half and thus capturing the variation at three different points. The average length is of 2250 mm. In general, although for some culms the diameter is higher at the top, the shape factor consistently increases towards the top. Nevertheless, taking into account the variations of the middle part of the culm, we observed that for some culms the Φ at the middle is similar to that of the top, and two of them even higher than the top.

### 4.3.4 Internode length

Figure 4.22 shows the variation of internode length from bottom to top for all the oldhamii culms scanned in its full length. As usual, the highest internode length is located at the midpoint of the culm from which it starts decreasing. The length of the internodes for these culms range from 279 to 612 mm. This parameter is important for the selection of culms to use for each element in the structure if clashing between nodes and connections is to be prevented.

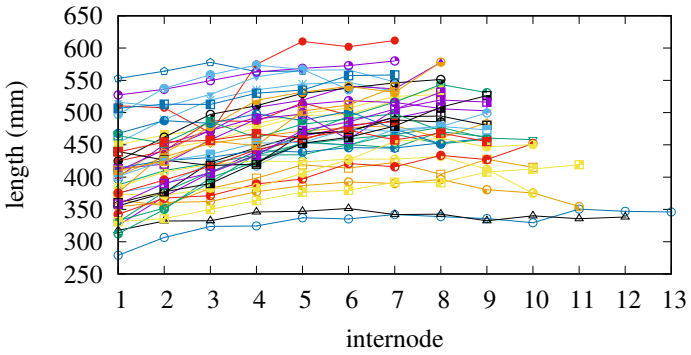


**Figure 4.22:** Internode length.

### 4.3.5 Out-of-straightness

The out-of-straightness $\lambda$ of bamboo measures the skew and deviation of the centroidal axis if the culm, equivalent to the geometric imperfection in structural elements (see Figure 4.23). Herein, it is defined as the maximum distance $d_{max}$ from all the 3D point coordinates to the longitudinal axis. The longitudinal axis, in this case, is a straight line that corresponds to the best fit line that minimises the sum of square distances measured perpendicular to the line. In addition to the out-of-straightness of the culm, the out-of-straightness within each internode is also evaluated.

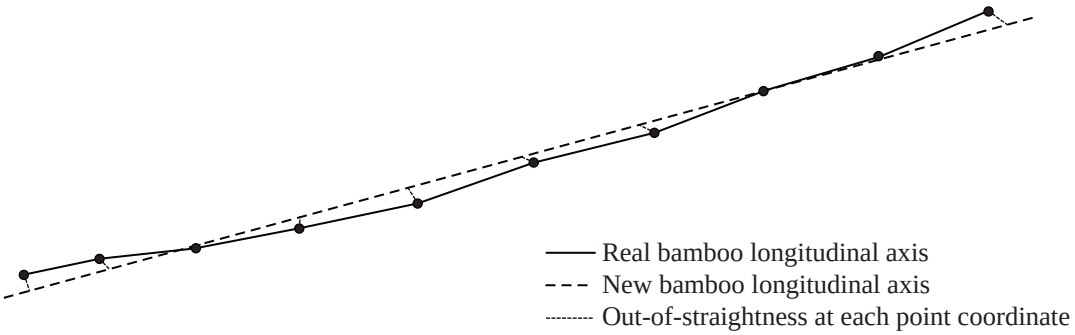


**Figure 4.23:** Representation of the out-of-straightness of the real axis of bamboo culms at each point coordinate.

Figure 4.24 shows the $\lambda$ for the batch of oldhamii bamboo culms scanned, separated into

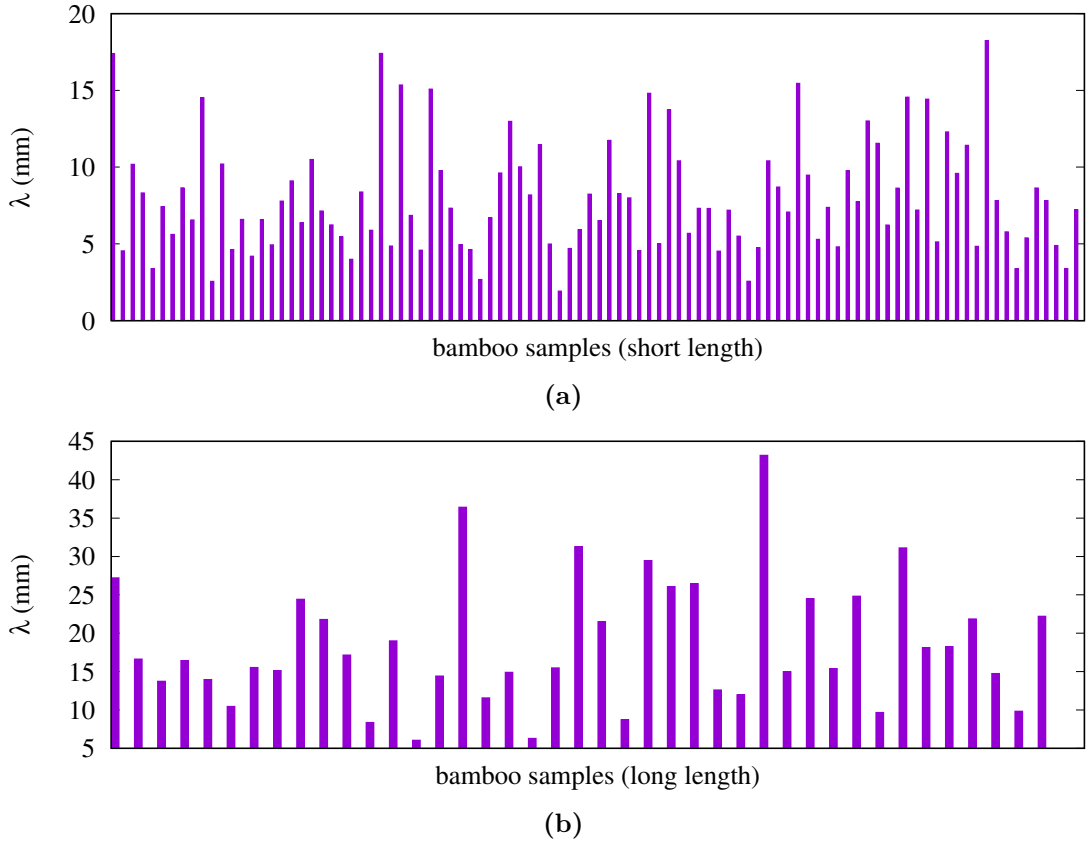


**Figure 4.24:** Ouf-of-straightness $\lambda$ of oldhamii bamboo culms for (a) short and (b) long lengths.

short and long lengths of approximately 2200 and 4500 mm respectively. The maximum $\lambda$ for the short and long culms is 18.25 and 43.18 mm respectively.

The normalised out-of-straightness $\lambda_n$ for all the short and long culms was calculated as

$$\lambda_n = \frac{d_{max}}{l} \tag{4.7}$$

where $l$ refer to the length of the culm. Table 4.5 provides the average and standard deviation values for $\lambda_n$ for short and long culms. It is interesting to note, that the average $\lambda_n$ estimated from the data available in the literature (Richard, 2013) for four different species lies within the same values (3.8, 3.5, 8.5 and 4.7 mm/m).

As mentioned, the straight line used for the evaluation of $\lambda$ of bamboo is the least square fitting curve. This can be used as a measure to compare and assess the out-of-straightness of all the culms in one batch and as a guide for the selection of the culms.

**Table 4.5:** Out-of-straightness

| | Short culms | Long culms |
|---|---|---|
| | (mm/m) | (mm/m) |
| mean $\lambda_n$ | 3.55 | 4.23 |
| std $\lambda_n$ | 1.63 | 1.87 |

However, this axis is only a reference as it does not exists physically. These culms are going to be cut to a certain length to become an element of a structure. The out-of-straightness of this new element is unknown until the new element length and position along the bamboo are defined. In order to evaluate how off does $\lambda$ is from the maximum out-of-straightness of the culm from two points along its length, additional analysis is carried out.

The out-of-straightness of the new bamboo element $\lambda_b$ was evaluated by segmenting the culms. As in general the $\lambda_b$ decrease with length, the length of the element used for this evaluation is of 2000 and 4000 mm for the short and long culms. For each culm, the element was evaluated at discretised positions from bottom to top. Figure 4.25 shows the first two and last evaluated positions with intervals of 10 mm. The small interval distance was selected to calculate the maximum $\lambda_b$ for each culm. In this figure, $a$ refers to the new bamboo element of length $l$ ($l_1, l_2$, etc.), and the indices $i$ and $n$ refer to the intervals and the total number of intervals in each culm in order to evaluate the full length. The maximum distance $d_{max}$ calculated for all the intervals is taken as the $\lambda_b$ for that culm at that specific element length $l$.

As expected, $\lambda_b > \lambda$ (see Figure 4.26). The average ratio $\lambda_b$ to $\lambda$ is of 1.45, estimated from short and long culms. Therefore, we can estimate that the maximum out-of-straightness of the culm is $1.45\lambda$, which occurs when the element length is similar to that of the length of the culm. The ratio calculated for short and long culms for elements of

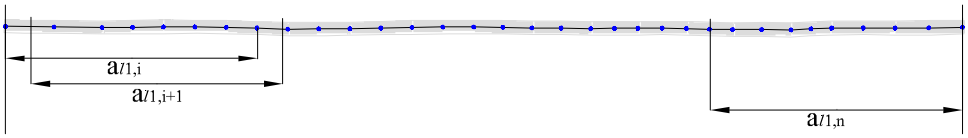


**Figure 4.25:** Evaluation of the out-of-straightness at different intervals along the length of the culm.

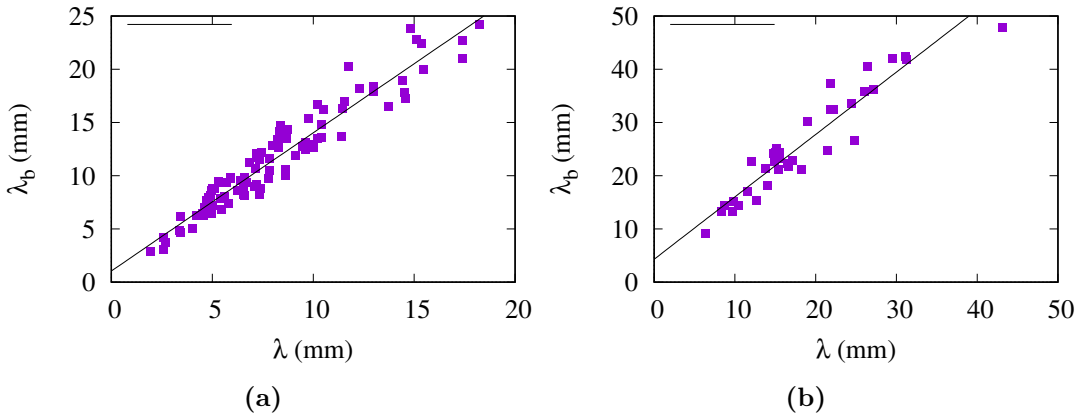


**Figure 4.26:** Relationship between $\lambda$ and $\lambda_b$ for (a) short and (b) long elements.

1000 mm is of $1.03\lambda$ and $0.54\lambda$ respectively.

The deviation of the internode $h$ with respect to its two adjacent nodes is investigated as shown in Figure 4.27. This deviation is considered as the out-of-straightness of each internode. Table 4.6 provides the minimum, maximum and average values for the deviation of the internode normalised by the length of the internode $h_n$.

The maximum values are significant, as the deviation represent 2.2 % of the length of the internode.

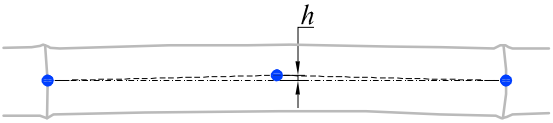


**Figure 4.27:** Deviation of the internodes respect the line passing through its two nodes.

**Table 4.6:** Deviation of the internodes

| | minimum | average | maximum |
|---|---|---|---|
| $h_n$ (mm/m) | 0.11 | 5.32 | 21.76 |

### 4.3.6 Ovalisation of the cross-section

Figure 4.28 illustrates two different shapes that the cross-section of bamboo can take. The ovalisation $\gamma$ can be defined as the ratio between the smallest and largest dimension in the cross-section as

$$\gamma = \frac{r_{min}}{r_{max}} \tag{4.8}$$

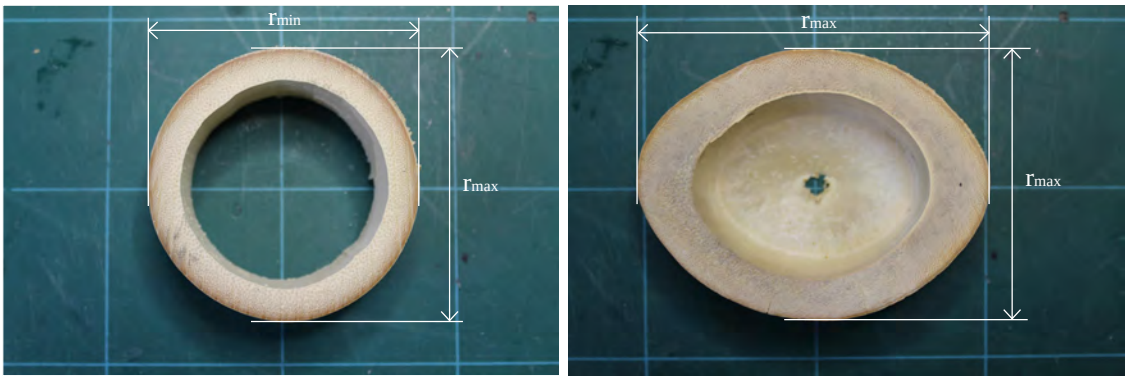


**(a)** **(b)**

**Figure 4.28:** The cross-sectional shape of bamboo can be (a) circular or (b) have a high degree of ovalisation.

where $r_{min}$ and $r_{max}$ are the minimum and maximum radius measured in the cross-section. It is important to note that the radius measured in this methodology corresponds to the equivalent radius of the cross-section, as the cross-section is not regular and thus opposite radius taken from the centroid can be different. For the two samples in Figure 4.28 the $\gamma$ is of 1.0 and 0.77 for the more regular and elongated shapes. The impact of the ovalisation of the cross-section for modelling of bamboo culm in structural analysis lies the fact that the cross-section is not symmetrical. Therefore, the second moment of area is different in the two orthogonal axes of the cross-section. The impact of this feature for structural analysis relies on the direction of the culm with respect to the applied loads.

For example, consider two cross-sections with circular and ellipse shapes respectively, and assuming that both have the same area and an ovalisation of 0.77. The second moment of area for the ellipse shape decreases 23.2 % in the minor direction and increases 18.8 % in the major direction. The ratios of the second moment of inertia for the minor and major directions with respect to the circular shape are of 0.79 and 1.20 respectively.

The $\gamma$ for all the oldhamii culms at each coordinate point was calculated. The minimum and maximum equivalent radius measured from each of the circumferential curves were used. Figure 4.29 shows the maximum, minimum and average $\gamma$ values obtained from each culm. The average $\gamma$ for all the culms is 0.95. Similarly, by considering a circular and ellipse shapes the ratios for the minor and major directions with respect to the circular shape are of 0.95 and 1.05 respectively. Note that the values for the minimum and maximum radius are not taken orthogonally to each other, and does not represent the radius oriented at the principal directions.

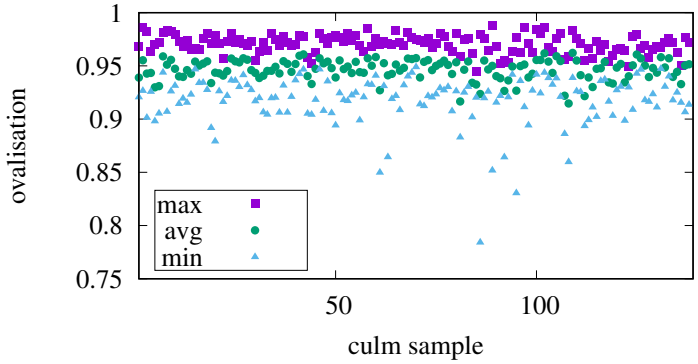


**Figure 4.29:** Ovalisation of all the oldhamii bamboo.

## 4.4 Discretisation of geometric properties for SBD

The geometric properties for the SBD determined by using the method presented in this chapter are provided in Table 4.7. The properties in grey colour corresponds to the data used for discretisation of structural modelling. The rest of the properties correspond to the auxiliary data used throughout the design process. Recall that each of the coordinates correspond to nodes and internodes. Each two coordinates will define a segment (i.e.

**Table 4.7:** Geometric properties for the SBD.

| index | Coordinates | | | Diameter | Thickness | xt coord | | | Ref point | | | Brep |
|---|---|---|---|---|---|---|---|---|---|---|---|---|
| 0 | x | y | z | D | t | x | y | z | x | y | z | brep |
| 1 | x | y | z | D | t | x | y | z | | | | |

structural element) of bamboo, and the diameter and thickness from that segment is taken as the one measured at the internode (e.g. index 0). Finally, for each culm, only one reference point and brep are obtained, and the total xt coordinates (corresponding to the width of the node) are twice the number of node coordinates (see Figure 4.30).

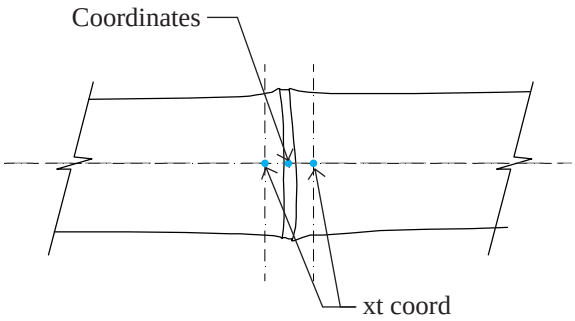


**Figure 4.30:** Type of coordinates for the discretised geometric properties.

## 4.5 Summary

This chapter presented a novel method for the systematic measurement of geometric properties of bamboo culms. Table 4.7 presents the discretised geometric properties determined for the SBD using this method. This constitutes the first attempt to systematically determine the geometric properties of bamboo culms for construction. The acquisition of geometric properties using 3D scanning opens a new possibility for the construction of bamboo structures with the potential to exploit its inherent variable properties in the conceptual and structural design, as well as in the practical aspects in construction. The proposed method, although not fully validated or sufficiently robust, successfully enables the acquisition of the relevant geometric properties to input into the design process.

Initial investigations to devise an appropriate method for scanning bamboo culms were presented together with the outline of the proposed method. The maximum error resulting from the difference between the measurement of the diameters from the 3D mesh and the direct measuring using a digital caliper was 1.2 % for the diameter of moso bamboos. A similar percentage was found for the oldhamii culms in the diameter (i.e. 1.1 %). As expected, since the error in millimetres is similar for the diameter and thickness (between 0.45 to 0.67 mm, see Tables 4.3 and 4.4), the percentage error calculated for the thickness is higher, about 8% on average. Some aspects were identified that require further attention. For example, it is labour intensive as it requires manual input to rotate the culm while

scanning. In addition, the method does not consider defects on the bamboo surface such as cracks or emerging branches at the nodes. Some of these features introduce noise, and thus manual input is required to eliminate undesired 3D coordinates corresponding to these features. In addition, a more robust and accurate method to capture the thickness at the ends is recommended.

The issues associated with the changes in dimensions (i.e. swelling or shrinkage) during storage were highlighted. Measuring the geometric properties is challenging, as these are subjected to changes influenced by the environmental conditions before and during assembly, and after construction, while in service. Ideally, the moisture content at the time of scanning and the percentage of shrinkage per moisture content (i.e. dimensional change for each species) must be known so that dimensional changes caused by changes in the environment can be estimated.

The thickness continuously decreases towards the top of the culm over a length of 4500 mm in average and was best described by a quadratic function with concave upwards shape. A similar trend was found for the moso bamboo, of approximately 3500 mm in length, used in the preliminary experiments measured at nine different positions along the culm. The description of the gradual change of thickness is important, as usually the thickness at the bottom and top of the culm are measured. Nevertheless, the arithmetic mean from bottom and top, overestimates the thickness for moso and oldhamii bamboo species. Overall, the thickness and diameter taper ratio was higher for the moso species.

Likewise, the general trend of the diameter of bamboo is to gradually decrease towards the top of the culm for bamboos of about 4500 mm in length. The diameter for oldhamii bamboo was described by a quadratic function with concave downwards shape. The diameters measured from the moso bamboo used in preliminary experiments were also described by a quadratic model. Unlike the consistency observed in the decrease of thickness, the diameters for some oldhamii bamboo (16% of the total scanned culms) were found to increase towards the top part of the culm. This pattern is opposite to the general trend that the geometric dimensions decrease towards the top. However, the same was found for a pair of guadua bamboo reported in the Section 6.3 for the determination of mechanical properties. This pattern is not fully understood but reinforces the need to measure and consider these variations in design. However, it is interesting to note that although the diameter increases for some culms, the shape factor for bottom and top tends to increase towards the top for all the culms of 4500 mm in length, hence implying that regardless of the small increase of diameter, the cross-section of the culms become thinner towards the top of the culm.

The out-of-straightness $\lambda$ of the culm was measured using the least squares fittings. The average out-of-straightness $\lambda_n$ normalised to the length was found to be 3.6 and 4.2 mm/m for the short and long culms respectively. A constant was derived to estimate the maximum out-of-straightness of the culm when cut and used as element in a structure. The geometric discretisation will take into account these imperfections. However, the evaluation of the out-of-straightness of bamboo is important for a future categorisation of

culms based in their axial compressive capacity.

In addition to the out-of-straightness, the deviation of the internodes with respect to its two adjacent nodes was measured to assess the straightness of the internodes. The minimum, average and maximum values measured are 0.11, 5.32 and 21.76 mm/m respectively. This parameter is important as for very straight culms were the deviation of the internodes is negligible, the discretisation of structural modelling of bamboo culms can be simplified to one coordinate per node only. For this batch of culms, the deviation can be up to 2.2% of the length of the internode (i.e. approximately 10 mm over an internode length of approximately 450 mm). Therefore, for these culms, a node coordinate in the middle of the internode is considered to take into account this deviation, and prevent issues with the assembly of elements and adequate fitting of components. This shall be evaluated for each species.

The average ovalisation for all the oldhamii batch was found to be 0.95. The impact that the ovalisation has in the second moment of area was found to be significant. For a section with 0.77 ovalisation, it was found that the ratio of the second moment of area of the circular to ovalised shape is 0.79 for the minor direction and 1.20 for the major direction.

# Chapter 5

# Physical properties of structural bamboo

This chapter is concerned with the methods for determining the physical properties for the SBD. The specific objectives of this chapter are listed below.

- To calibrate a wood moisture meter to three different bamboo species for the rapid determination of the moisture content.
- To estimate the oven-dry density based on simple measurements of volume and weighting and moisture content.
- To develop a method to quantify the volume fraction.
- To investigate the transverse and longitudinal shrinkage.

## 5.1 Moisture content

Moisture content is the percentage of water contained in the material. As a hygroscopic material, bamboo is susceptible to changes in the temperature and relative humidity of the environment. Moisture content $w$ according to ISO (2004b) and JG/T-199 (2007) is defined as

$$w = \frac{m_1 - m_0}{m_0} \times 100 \tag{5.1}$$

where $m_1$ is the weight of the tested sample, and $m_0$ is the weight of the oven-dry sample, according to the notation in JG/T-199 (2007).

### 5.1.1 Calibration of a hand-held moisture meter to three bamboo species

Handheld moisture meters are widely used in the timber industry and provide a rapid means to check the moisture content of timber elements. These meters are calibrated for wood products, with some having a correction factor for different types of species with

different specific gravities. However, there are currently no moisture meters available in the market that are calibrated for any bamboo species.

There are several types of hand-held moisture meters, which can be classified in conductance and capacitive-admittance meters (ASTM-D4444-13, 2013; TRADA, 2016). Capacitance-admittance meters are time-saving and portable devices that enable the measurement of moisture content by using radio frequency signals. These are mostly used on flat surfaces, by placing the device directly on the surface of the material. However, due to the curved surface of bamboo culms, complete surface contact is not possible. Conductance meters are pin-type meters that measure moisture content by the electrical resistance between two points. The fundamental principle is that at higher moisture contents the electrical resistance decreases (ASTM-D4444-13, 2013).

Herein, a conductance type hand-held moisture meter is adopted as a means to determine the moisture content of bamboo culms quickly. A hand-held wood moisture meter was calibrated for three different bamboo species (guadua, oldhamii and moso). The device is a BD-2100 pin-type moisture meter from Delmhorst (Delmhorst, 2011). It has insulated pins and a slide hammer electrode to allow the easy penetration in the culm wall surface. These insulated pins allow the readings of moisture content only at the tip of the needle, preventing the results from being influenced by wet conditions of the penetrated surface. The moisture meter provides moisture readings for wood between 6 and 40 %. In addition, it allows for measuring the percentage of water on a relative basis for non-wood materials, named in this device as reference scale $RS$. The $RS$ readings are recorded in the range from 0 to 100, which gives a relative indication of how much water there is in the material.

The procedure to calibrate the moisture meter is outlined below. The objective is to find the relationship between the $RS$ readings and the moisture content $w$ in percentage measured by the oven-dry method. It consists of a sequence of measurements with both methods, over a period of time for different moisture content. Drying bamboo at high temperatures (between 60 to 120°) has been found to have a significant impact in the hygroscopic properties of bamboo (Wu, 1992). Therefore, with the aim of preventing disturbing these properties, a method to take sample weights consecutively from wet to dry conditions was devised.

The method consists of preparing the samples by water immersion and gradually oven-drying them while taking the measurements at some defined time schedules until they are fully dried. It was assumed that the readings from the needles of the moisture meter are done at the same depth in all the samples. The needles are inserted in the culm just as much as the tip of the needle is inserted in the sample. The material and equipment required are: i) bamboo samples cut in half-rings, ii) tissues, iii) oven, iv) desiccator, and v) weighing scale (precision of 0.001 g according to JG/T-199 (2007)). The steps are described below.

**w.1** Preparation of the samples. The samples are cut in half-ring shape of 25 mm in length (see Figure 5.1). Usually, half-ring is enough for four readings in one sample

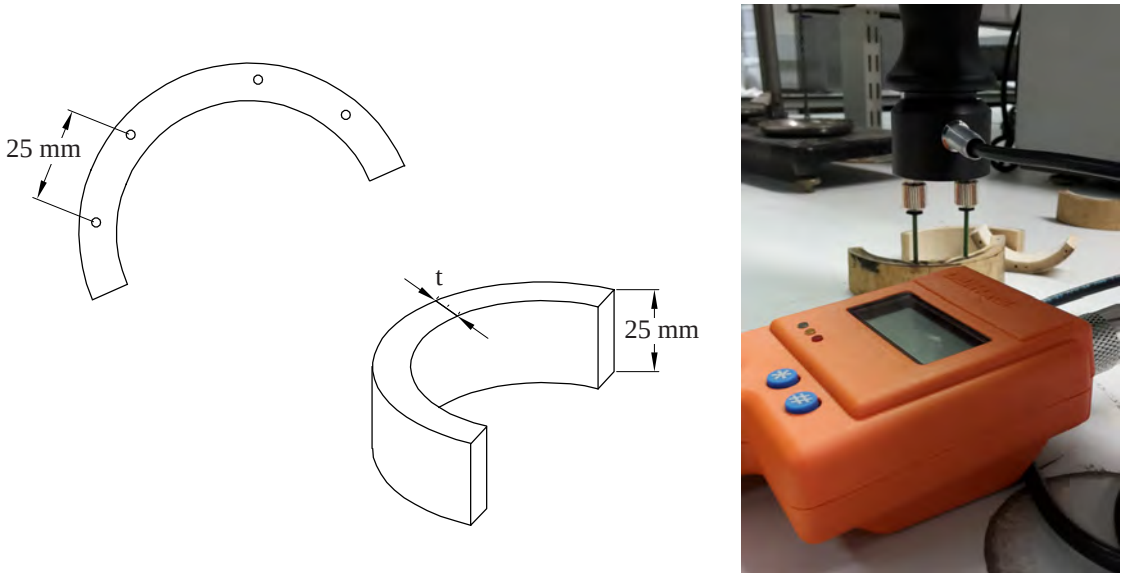


**Figure 5.1:** Bamboo sample dimensions for calibration of moisture meter, and recording of $RS$.

as the needles are separated by 25 mm, but this will depend on the culm diameter. Divide all the samples into different batches with a maximum of 8 samples per batch. This will reduce the time the samples are out from the oven while taking the measurements, and reduce the possibility of been affected by environmental conditions.

**w.2** Water absorption. The samples from one batch are placed in a water container for 1 hour. A plastic lid is placed on the top of the samples inside the container in order to fully submerged them in water.

**w.3** The samples are taken out from the water container and dried with a tissue to eliminate the excess of water.

**w.4** Readings of $RS$ and weights.

- Weighing of the samples in the balance
- Measure $RS$ with the moisture meter. Insert the pins into the sample, with the pins aligned parallel to the fibre. Record the $RS$ while the pins are inserted. Do not tilt the pins before or after insertion.

**w.5** Recording the data during oven-dry process. The samples are placed in the oven at 103° ± 2°. The next three readings are made at the following time lapses: i) 20 min, ii) 10 min, and iii) 10 min. The time lapses refer only to the time that the samples were kept in the oven. After each time lapse, the samples are taken out from the oven and placed in a dessicator for approximately 10 min or until the samples are cold down before weighing. After dessicator record the readings of $RS$ and weights as in step **w.4**.

**w.6** Fully dry process. After all the readings are recorded, the samples are placed in the oven until fully dry.

The samples were obtained from different sources. Material specification for moso and oldhamii bamboos is provided in Chapter 4 and for guadua in Section 6.3. Figures 5.2a, 5.2b and 5.2c show the moisture content $w$ plotted against the $RS$ values for the guadua, oldhamii and moso bamboo species. For all the species, the curve that best fit the data is a quadratic curve. In order to minimise the effect of outliers, the robust regression method bisquare weights was used and implemented in Matlab (MathWorks, 2016) program. This method minimises the weighted sum of squares. The weights are distributed so that the closer the data sample is to the fit line the greater the weight, and vice-versa. Table 5.1 provides the coefficient of determination for these curves and the model coefficients for a quadratic equation in the form

$$w = a_0 RS^2 + a_1 RS + a_2 \tag{5.2}$$

where $RS$ is the variable. It is interesting to note that the coefficients of the quadratic equation for the three curves are very similar. Figure 5.2d shows the combination of the three species together, and the coefficients are also presented in Table 5.1. For the same

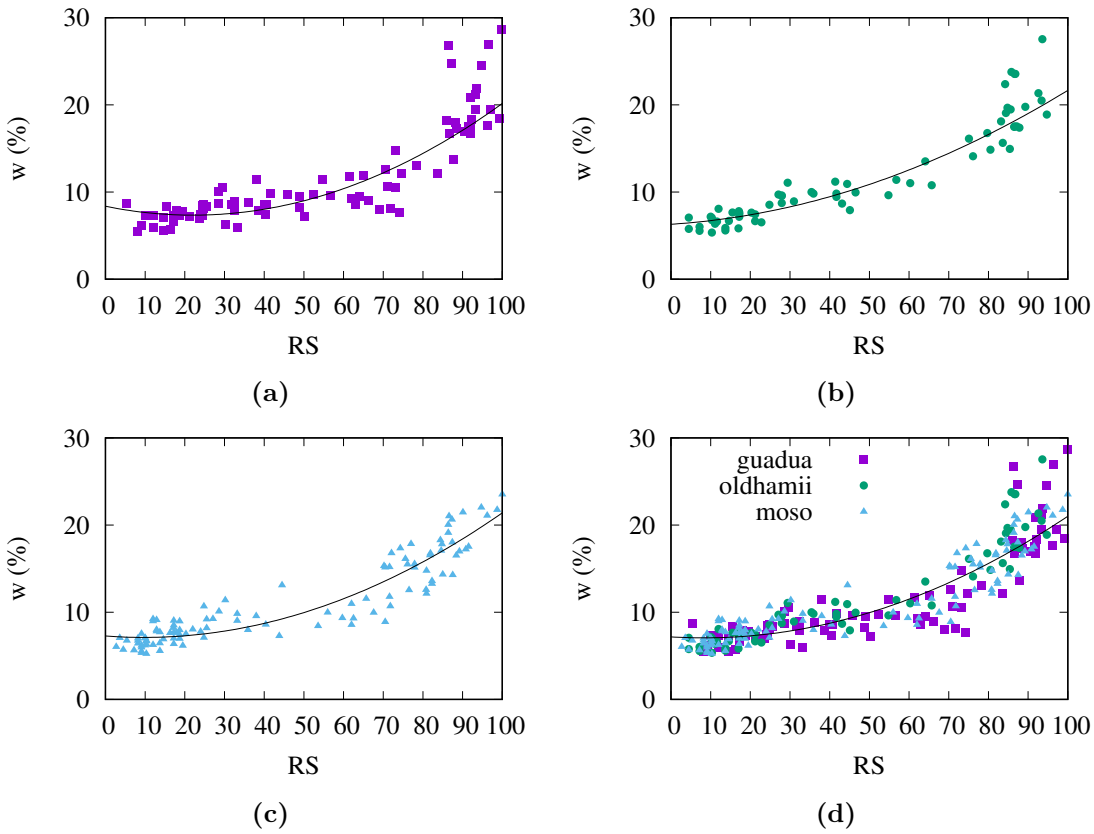


**Figure 5.2:** Relationship between oven-dried moisture content ($w$) and reference scale (RS) from moisture meter for (a) guadua, (b) oldhamii, (c) moso, and (d) all three species.

**Table 5.1:** Model coefficients of moisture meter calibration curves.

| Species | $a_0$ | $a_1$ | $a_2$ | $R^2$ |
|---|---|---|---|---|
| Guadua | 0.002107 | -0.09281 | 8.37 | 0.89 |
| Oldhami | 0.00124 | 0.02924 | 6.305 | 0.93 |
| Moso | 0.00179 | -0.0392 | 7.375 | 0.86 |
| Three species | 0.00166 | -0.0273 | 7.175 | 0.88 |

*RS* the percentage difference between the moisture content determined from the curve of the three species against each of the curves for the individual species is <0.1%. Therefore, the model obtained from the data of the three species is adopted for the estimation of moisture content for any of these three species.

## 5.2 Density

Density is defined as the mass per unit volume. Usually, the density calculated from the ovendry mass and volume is used for design specifications in wood construction, while the ovendry mass and green volume is considered as the basic specific gravity (Glass and Zelinka, 2010). The JG/T-199 (2007) specifies three different types of densities, including the ovendry density $\rho_0$. Here, $\rho_0$ is indirectly estimated based on the density at moisture content $w$ and direct measurements of the volume of the sample.

The JG/T-199 (2007) specifies the calculation of three different densities

$$\rho_0 = \frac{m_0}{V_0} \times 10^6 \tag{5.3}$$

$$\rho_w = \rho_0[1 + 0.01(1 - K_s)w] \tag{5.4}$$

$$\rho_y = \frac{m_0}{V_{max}} \times 10^6 \tag{5.5}$$

where $\rho_0$ is the oven-dry density, $\rho_w$ is the air-dried density at moisture content $w$, and $\rho_y$ is the wet density. The $V_0$ and $V_{max}$ refers to the volume of the oven-dry sample and the sample with saturated water, and $K_s$ is the correction factor to consider the influence of moisture content on the volumetric shrinkage and is defined as

$$K_s = \frac{V_w - V_0}{V_0 w} \times 100\% \tag{5.6}$$

where $V_w$ refers to the volume of the sample at moisture content $w$.

Herein, the oven-dry density $\rho_0$ is indirectly estimated from the density of the sample at moisture content $w$. From Equation (5.4) we know that $\rho_w$ is a function of $\rho_0$, $K_s$ and $w$. However, we still require to oven-dry the samples for measuring the dry volume in Equation (5.6).

The density of a sample for given moisture content is usually calculated using the weight and volume at the same moisture content (Dinwoodie, 2000; Glass and Zelinka,

2010); thus this can be expressed as

$$\rho = \frac{m}{V} \tag{5.7}$$

where $m$ and $V$ refer to the weight and volume measured at the same moisture content, which is usually zero if the ovendry density is required. Now, assuming that the air-dried density of Equation (5.4) is the same as the density at a given moisture content from Equation (5.7), the Equation (5.4) can be rewritten as

$$\rho_w = \frac{m_1}{V_w} \tag{5.8}$$

Additionally, having measured the moisture content as described in the previous Section 5.1, the oven-dry weight $m_0$ and the weight of the tested sample $m_1$, can be calculated by rearranging Equation (5.1) as

$$m_0 = \frac{m_1}{1 + w/100} \tag{5.9}$$

and,

$$m_1 = m_0\Big(1 + \frac{w}{100}\Big) \tag{5.10}$$

Therefore, by replacing the left-hand side of Equation (5.4) with the right-hand side of Equation (5.8), and solving for $V_0$, we can estimate the oven-dry density $\rho_0$.

Based on this, the derivation to find an expression to approximate $\rho_0$ is considered. The mathematical derivation presented below is been made by Dr. Rodolfo Lorenzo.

Substituting Equation (5.6) into Equation (5.4) we have

$$\rho_w = \rho_0\Big[1 + \frac{w}{100}\Big(1 - \frac{100V_w - 100V_0}{V_0 w}\Big)\Big] \tag{5.11}$$

now, by simplifying and substituting Equations (5.8) and (5.3) into Equation (5.11) it gives

$$\frac{m_1}{V_w} = \frac{m_0}{V_0}\left[2 + \frac{w}{100} - \frac{V_w}{V_0}\right] \tag{5.12}$$

and by multiplying both sides of the equation by $V_0^2$, we have

$$\frac{m_1 V_0^2}{m_0 V_w} = \Big(2 + \frac{w}{100}\Big)V_0 - V_w \tag{5.13}$$

Next, by setting the equation to zero, we obtain the quadratic equation with $V_0$ as a variable

$$\frac{m_1}{m_0 V_w}V_0^2 - \Big(2 + \frac{w}{100}\Big)V_0 + V_w = 0 \tag{5.14}$$

and substituting Equation (5.10) into Equation (5.14) we have

$$\frac{(1 + w/100)}{V_w}V_0^2 - \Big(2 + \frac{w}{100}\Big)V_0 + V_w = 0 \tag{5.15}$$

now, by solving for $V_0$ then gives

$$V_0 = \frac{-[-(2 + w/100)] \pm \sqrt{[-(2 + w/100)]^2 - 4\frac{(1+w/100)}{V_w}V_w}}{\frac{2(1+w/100)}{V_w}} \tag{5.16}$$

and simplifying

$$V_0 = \frac{2 + w/100 \pm \sqrt{(4 + 4w/100 + w^2/10000 - 4 - 4w/100}}{\frac{2+2w/100}{V_w}} \tag{5.17}$$

and further

$$V_0 = \frac{(2 + w/100 \pm w/100)V_w}{2 + 2w/100} \tag{5.18}$$

From Equation (5.18) we have two different solutions for $V_0$, given by

$$V_0 = V_w \tag{5.19}$$

and,

$$V_0 = \frac{V_w}{1 + w/100} \tag{5.20}$$

Now, substituting Equations (5.9) and (5.20) into Equation (5.3) we have that

$$\rho_0 = \rho_w \tag{5.21}$$

and, substituting Equations (5.9) and (5.19) into Equation (5.3) we have that

$$\rho_0 = \frac{\rho_w}{1 + w/100} \tag{5.22}$$

To determine $\rho_0$, Equation (5.21) is considered as the trivial solution, and thus Equation (5.22) is adopted as an approximation of $\rho_0$. This can be estimated from the moisture content $w$ measured from the tested samples as in the previous Section 5.1 and the simply weighing and measuring of the volume of the samples at the moisture content of the tested samples. Note that Equation (5.22) is equivalent to the ratio dry weight to wet volume as specified by the ISO (2004b) standard as

$$\rho_0 = \frac{m_0}{V_w} \tag{5.23}$$

The percentage difference between determining the density by using the moisture content or directly the dry mass as in Equations (5.22) or (5.23) is 1.6 %, for the guadua and oldhamii samples corresponding to the batches described in Section 6.3. Comparisons between Equations (5.22) and (5.3) were not carried out for this thesis. In this methodology Equation 5.22 is adopted as surrogate for the indirect estimation of dry density.

## 5.3 Volume fraction

This section presents the method devised to quantify the volume fraction of bamboo and its radial distribution for the estimation of input parameters for the bimodulus and composite models in Chapter 6. One of the main requirements for this method is to prevent the need to use sophisticated equipment such as scanning electron microscope (SEM). The method consists of image analysis of photographs of the cross-section of bamboo obtained using a digital camera.

### 5.3.1 Image analysis for volume fraction calculation

The method was developed in Matlab (MathWorks, 2014) program, and consists of converting RGB images into binary images in order to distinguish between fibres and matrix and counting the total number of pixels corresponding to each. The method is divided into four steps: (i) image capture, (ii) definition of area of interest on screen, (iii) binarisation of the image, and (iv) calculation of volume fraction.

#### 5.3.1.1 Equipment and set-up

The set-up and selection of equipment was done by members of the bamboo research group at UCL.

The size of the sample in the cross-section plane is of 15 mm width x thickness. Before the mechanical test, the samples were prepared by gradually grinding the cross-section surface with a silicon carbide sanding paper of 1200 grit and 600 grit to provide a clean and smooth finish surface.

The images were taken with a digital camera Nikon D7200, and Nikon Nikkor Lenses AF-S DX Micro NIKKOR 85 mm f/3.5G ED VR. An electronic flash Metz mecablitz 15 MS-1 was used to guarantee the precise level of light in the macro shots. The images were taken at a distance of 130 mm from the camera lenses and were saved as JPEG images with dimensions of 2992 x 2000 and file size between 1500 to 2500 kB.

#### 5.3.1.2 Area of interest

Once the images are captured, the first step is to define the area of interest from which the volume fraction is going to be analysed. For this step, it is assumed that the cross-section of bamboo is a hollow circle. The definition of the area of interest is the only step that requires manual input. For each image, four points are selected directly on the screen, as indicated in Figure 5.3. Points A, B and C lie on the arc that defines the outer diameter of the culm. Points A and C correspond to the corners of the sample in the outer surface and points B and E are selected approximately in the middle of the section at the outer and inner side of the culm wall respectively. These last two points define the thickness of the sample. By repeating these steps each time, the COV in percentage from each manual selection is of 0.36 %. This difference was considered negligible.

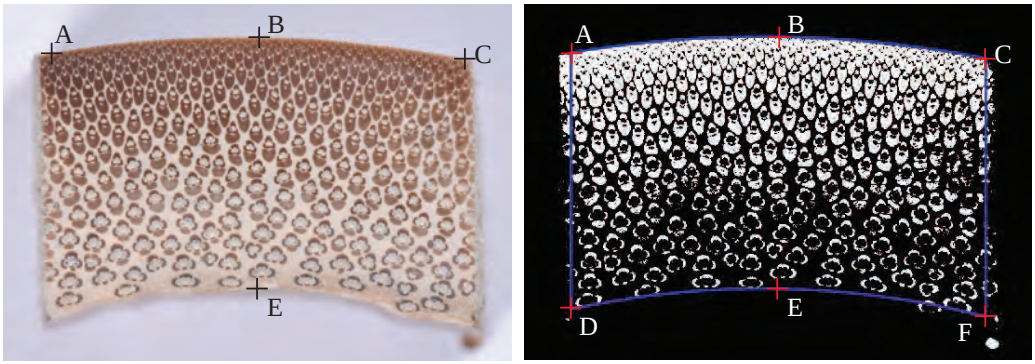


**(a)** **(b)**

**Figure 5.3:** (a) Points A, B, C and E to select directly from image in order to identify the area of interest. (b) Binary image of the sample cross-section and area of interest for an oldhamii sample.

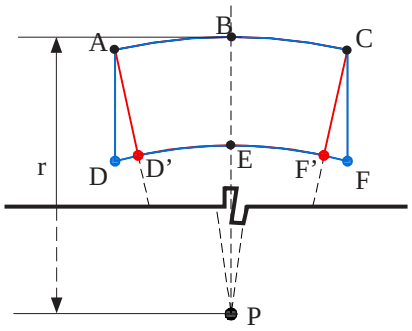


**Figure 5.4:** Diagram of the geometry of the area of interest to crop image for volume fraction analysis.

The area of interest is defined by closed polygons as depicted in Figure 5.4. From the selected points, the equivalent centre P and the radius r of the culm cross-section are defined. Using the equation of the circle the position of the points D, D', F and F' are calculated to define the area of interest. Note that there are two different polygons in Figure 5.4. The first one is defined by points A, C, D and F, and has sides parallel to each other. The other one is defined by the points A, C, D' and F', and has sides oriented in the radial direction.

Because of the extra area at the inner corners of the rectangular crop, this results in a slightly lower $v_f$. On average, the difference between both polygons is approximately 1% of $v_f$, within a range from 0.10 to 2.4 %. However, it was observed that those samples with a higher difference were of a very irregular shape.

For this method, the rectangular crop (i.e. with sides parallel to each other) was selected, as it has the same shape of the samples used to determine the mechanical properties that are going to be compared against $v_f$. For cases where the $v_f$ of the whole section is required (i.e. $2\pi$), the radial crop is a better approximation.

#### 5.3.1.3 Binarisation process

This step consists of converting the image into a binary image before counting the number of pixels corresponding to the vascular bundles and matrix respectively.

First, the RGB image is converted to a greyscale intensity image as in Figure 5.5a using the *rgb2gray* function. Before converting the greyscale image into a binary image, a filter and thresholding were applied for an optimal segmentation. Segmentation refers to the separation between white and black pixels. Using the function *imgaussfilt* a 2-D Gaussian filter is applied to the image with 0.10 standard deviation. This filter eliminates noise (e.g. isolated pixels) and small details from the image.

Subsequently, a threshold based on the brightness values of the image pixels is defined, which is later used for the selection of black and white pixels in the binarisation process. Thresholding is a technique used to divide an image into different regions based on the intensity value of pixels of the image (Gonzalez and Woods, 2008). This was accomplished using the Otsu's method with the *graythresh* function. The Otsu's method (Otsu, 1979) is a global method that automatically defines the thresholding for the image based on the histogram of the images (Gonzalez and Woods, 2008). It is particularly useful for bimodal images where there is high contrast between the background and the object of interest, which for this case is the matrix and the vascular bundles.

Figure 5.6 shows the histogram of one of the images for the analysis of the volume fraction of vascular bundles. In this plot, the x axis represents the intensity value of the pixels from 0 to 256 of the greyscale image, and the y axis the number of pixels corresponding to each intensity value (Gonzalez and Woods, 2008). From this figure, we can distinguish two different classes of pixels, one representing the vascular bundles and the other the matrix. Once the threshold is defined, the greyscale image is converted to a binary image using the threshold value obtained by Otsu's method.

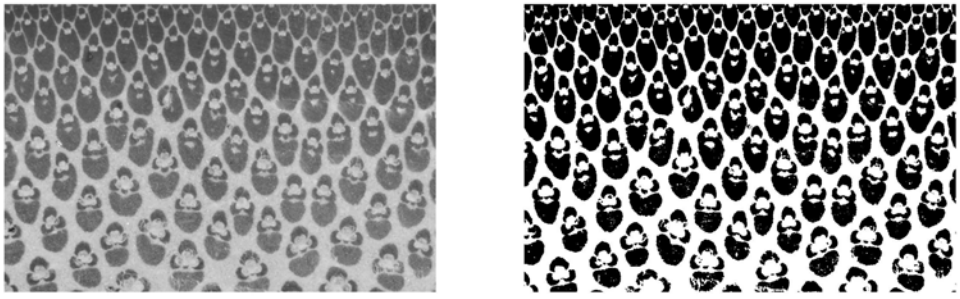

**(a)** **(b)**

**Figure 5.5:** (a) Greyscale image. (b) Binary image.

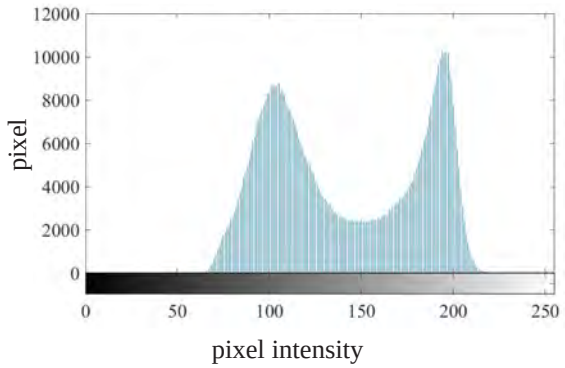


**Figure 5.6:** Histogram of the intensity greyscale image for binarisation process.

#### 5.3.1.4 Quantification of volume fraction

Using the binary image (see for example Figure 5.5b) the area of the fibres and matrix is calculated by adding up the number of pixels corresponding to each constituent. The volume fraction of the vascular bundles $\mathrm{v}_b$ is defined by

$$\mathrm{v}_b = \frac{a_f}{a_f + a_m} \tag{5.24}$$

where $a_f$ and $a_m$ are the area of the fibres and matrix respectively.

### 5.3.2 Estimation of volume fraction for bimodulus model

From Equation (5.24) we have the volume fraction of vascular bundles including the conducting tissue. As seen from the literature, the vascular bundles consists of conducting tissue and fibres, and the average conducting tissue in the culm is 8% (Liese, 1998). Here, it is considered that the volume fraction $\mathrm{v}_f$ corresponds to the $\mathrm{v}_b$ minus the subtraction of the percentage of conducting tissue in the culm, as

$$\mathrm{v}_f = \frac{a_f}{a_f + a_m} - 0.08 \tag{5.25}$$

where 0.08 is the percentage of conducting tissue in decimal. The volume fraction $\mathrm{v}_f$ calculated as in Equation 5.25 is used as input for the bimodulus model presented in Subsection 6.2.2.

### 5.3.3 Estimation of parameters for composite model

The composite model presented in Subsection 6.2, considers a laminate of three layers. This subsection analyses the fibre distribution in the radial direction and proposes a subdivision of the culm wall thickness into three layers to estimate the parameters for modelling bamboo as a composite material. The relevant parameters to estimate are the thickness and the elastic modulus of each lamina. First, the through-thickness fibre distribution is

analysed for two species (guadua and oldhamii) to define a model to use for the estimation of the parameters. Then a method to subdivide the thickness into three sections is proposed, and using this subdivision the thickness $t$ and the elastic modulus $E_l$ of each lamina are determined.

#### 5.3.3.1 Fibre distribution through-thickness

Figure 5.7a depicts the fibre distribution for a typical sample of oldhamii species, corresponding to the one presented in Figure 5.3. To determine each of the plotted points, the thickness (i.e. BE in Figure 5.3) was divided into ten sections and the volume fraction was calculated for each segment using Equation (5.24). Note that in this step, the correction for the conducting tissue is not considered. This is because the distribution of conducting tissue in the radial direction does not follow the same trend as the vascular bundles (Liese, 1998). Nevertheless, this step is not concerned with the quantitative value of volume fraction, but with the pattern of distribution throughout the thickness. We can observe that the volume fraction distribution quantified using the image analysis presented in Subsection 5.3.1 agrees with the average distribution from the literature (Grosser and Liese, 1974) (see Figure 5.7).

Figure 5.8 shows the range of volume fraction distribution across the thickness for 142 guadua and 126 oldhamii samples presented in Section 6.3. In general, the oldhamii species present higher values of volume fraction, but both present similar distributions.

It was observed that for some samples, the first and last plotted points of $v_b$ in the radial direction dropped notably from their adjacent points. This aspect was further investigated by analysing the original image, and it was concluded that the inner and outer layers (i.e.

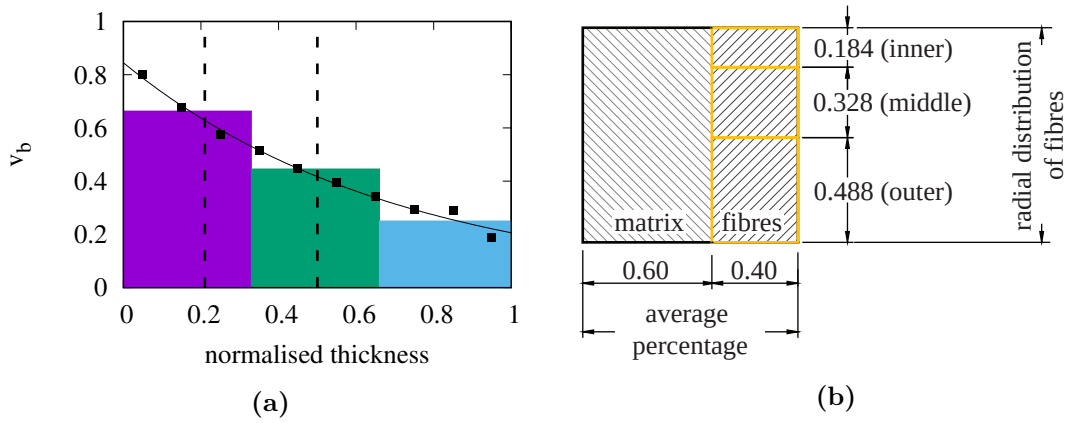


**Figure 5.7:** (a) Distribution of $v_b$ throughout the thickness. The points are plotted in the normalised radial position $x/t$, where $x$ is the radial position and $t$=1 is the thickness of the sample. The exponential curve is $v_b(x) = 0.845\exp(-1.41x)$. The vertical lines in black depicts the division between the three layers. The colored bars depicts the volume fraction of fibres for the outer, middle and inner sections according to Grosser and Liese (1974). (b) The horizontal axis represents the percentage of fibres and matrix (including conducting tissue) according to Liese (1998). The vertical axis represents the distribution of fibres in percentage for the outer, middle and inner sections in the radial direction according to Grosser and Liese (1974).

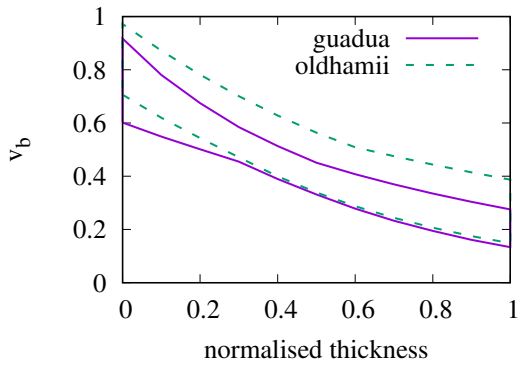


**Figure 5.8:** Range of fibre distribution for guadua and oldhamii samples.

pith ring and cortex respectively) were causing this feature. Figure 5.9 shows the image of two different species. For the moso species, these layers are absent, while for the guadua bamboo the inner and outer layers are evident. In this investigation the calculation of the $v_b$ was done considering the whole area of the wall thickness, therefore taking into account the effect of these layers. Recall from the literature that the wall thickness is surrounded by an inner and outer layer called pith ring and cortex respectively, which can be different for each species. The effect of these in the area of the culm is not quantified.

To determine the model that better represents the radial distribution of $v_b$, the linear, quadratic and exponential models were evaluated. The coefficients of determination for these models are 0.964, 0.989 and 0.991 respectively. Overall, the coefficient was higher for the exponential and quadratic models, which use the nonlinear squares method and the linear least squares method respectively. The latest is more susceptible to outliers. As a result, the samples showing a drop of the plotted points (from the inner and outer layers) are impacted and can lead to flipping the curve shape from upwards to downwards, which is not consistent with the distribution observed in the samples. Therefore, the exponential model of the form

$$v_b(x) = a \exp(bx) \tag{5.26}$$

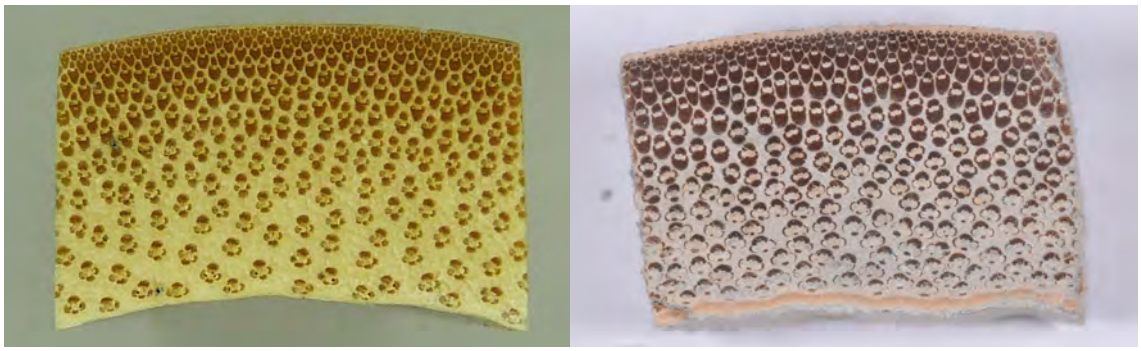

**(a)** **(b)**

**Figure 5.9:** Images for volume fraction specimens at cross-section. (a) Moso species. (b) Guadua species.

was used to describe the radial distribution of $\mathrm{v}_b$.

The exponential models and the coefficients $a$ and $b$ for the average values of the guadua and oldhamii species are

$$\mathrm{v}_{b,guadua} = 0.767\exp(-1.36x) \tag{5.27}$$

$$\mathrm{v}_{b,oldhamii} = 0.834\exp(-1.26x) \tag{5.28}$$

#### 5.3.3.2 Estimation of thickness and elastic modulus for the composite laminate of three layers

To determine the parameters of each of the laminas, it is assumed that each lamina contains the same volume fraction with respect the overall volume fraction of the whole section. The $\mathrm{v}_b$ at different positions in the radial direction, from the outer to the inner edge, is calculated using Equation (5.26).

The volume fraction of each of the laminas $\Delta\mathrm{v}_b$ with respect to the overall volume fraction of the sample is

$$\Delta\mathrm{v}_b = \frac{\mathrm{v}_{b,0} - \mathrm{v}_{b,1}}{3} = \frac{a - a\exp(bx)}{3} = \frac{a}{3}(1 - \exp(bx)) \qquad \text{for} \quad x = 1 \tag{5.29}$$

where the coefficients $a$ and $b$ are obtained from Equations (5.27) and (5.28) as appropriate.

The radial position of each of the laminas (see Figure 5.10) at the inner side of the sample is estimated as

$$\mathrm{x}_i = \frac{\ln\frac{(a - i\Delta\mathrm{v}_b)}{a}}{b} \tag{5.30}$$

where $i$ is the number of laminas (i.e. 1 for the outer, 2 for the middle or 3 for the inner), and where $x_3 = \mathrm{t} = 1$. Therefore, the thickness of each of the laminas is estimated as

$$t_i = x_i - x_{i-1} \tag{5.31}$$

Next, to estimate the elastic modulus of each lamina $E_{l,i}$ we assume that the elastic

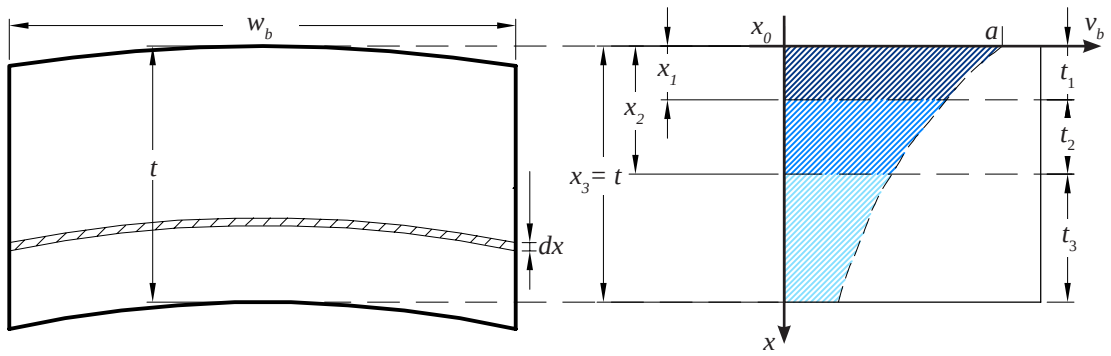


**Figure 5.10:** Sample cross-section and volume fraction distribution through-thickness.

modulus is proportional to the volume fraction. First, we need to quantify the volume fraction of each lamina and the average volume fraction of the whole section. For a culm wall section with straight sides as shown in Figure 5.10, the area of a long element with thickness $dx$ can be approximated as a rectangular section, therefore

$$dA = w_b d\mathrm{x} \tag{5.32}$$

Similarly, the volume fraction of a small differential element in the radial direction can be estimated by integrating Equations 5.26 and 5.32 as

$$\int \mathrm{v}_b dA_i \quad = \quad \int a \exp(bx) w_b dx \quad = \quad \frac{w_b a}{b} \exp(bx) \Big|_{x_{i-1}}^{x_i} \tag{5.33}$$

The $\mathrm{v}_b$ for each lamina is obtained by dividing Equation (5.33) by the area of each lamina, as

$$\mathrm{v}_{b,i} = \frac{\int_{x_{i-1}}^{x_i} \mathrm{v}_b dA}{\int_{x_{i-1}}^{x_i} dA} \tag{5.34}$$

The average $\mathrm{v}_b$ for the whole sample is given by

$$\mathrm{v}_{b,avg} = \frac{\int_{x_0}^{x_3} \mathrm{v}_b dA}{\int_{x_0}^{x_3} dA} \tag{5.35}$$

Finally, $E_{l,i}$ is estimated as a function of the volume fraction of each lamina as

$$E_{l,i} = \frac{\mathrm{v}_b}{\mathrm{v}_{b,avg}} E_c \tag{5.36}$$

where the $E_c$ corresponds to the elastic modulus measured as described in Section 6.2 for the corresponding sample.

Using equations 5.31 and 5.36 the thickness and elastic modulus of each lamina for the composite model are estimated.

## 5.4 Shrinkage

One of the effects of the hygroscopic properties of bamboo is the dimensional changes caused by changes in the moisture content of the culm. These changes are either shrinkage or swelling in the length, diameter and thickness directions. Due to the anisotropic properties, composite nature and cross-section shape of bamboo these changes are different in each direction.

A series of tests on moso bamboo were carried out to investigate the shrinkage for the thickness, diameter and length. The specimens were taken from the same culm used for the study of the mechanical properties (see Figure 6.7). The shrinkage was calculated according to ISO (2004b) as

$$s = \frac{I - F}{I} \times 100 \tag{5.37}$$

**Table 5.2:** Shrinkage of wall thickness, diameter and length along the length of the culm.

| Direction | Shrinkage (%) | $\Delta D$ % |
|---|---|---|
| Thickness | 1.20 | 0.138 |
| Diameter | 1.61 | 0.185 |
| Length | 0.081 | 0.009 |

where $s$ refers to the shrinkage in percentage, and $I$ and $F$ denote the initial and final dimensions in mm for the diameter, thickness and length respectively. Table 5.2 presents the percentage of shrinkage for samples with an average moisture content of 8.7 %. The shrinkage in the longitudinal direction was not significant. It was observed that the reduction in diameter size occurred from the outside to the inside. The outer culm surface experience changes whereas the inner culm surface remain almost the same.

The third column of Table 5.2 indicates the percentage of shrinkage per cent of moisture content, which is the dimensional change $\Delta D$ in timber (Glass and Zelinka, 2010). Based on the shrinkage and moisture content values provided for six different species (Liese and Tang, 2015), the average $\Delta D$ for the radial direction can be calculated as $\frac{0.131\%}{w}$. This is very similar to the $\Delta D$ for the thickness found in this study. There are no details in the study provided by (Liese and Tang, 2015) that indicates whether the radial direction was measured using the thickness or diameter. Nevertheless, the close values of shrinkage between thickness and diameter in this research, and those presented for the radial and tangential directions according to Liese and Tang (2015) suggests that shrinkage per cent of moisture content is linear. In wood, the relation between shrinkage and moisture content at low ranges, between 6 to 14 %, is considered to be linear (Glass and Zelinka, 2010).

## 5.5 Discretisation of physical properties for SBD

Table 5.3 presents the data for a typical example of the physical properties for the SBD. The properties coloured in grey refer to those for the discretisation of the structural modelling, and those in white to the auxiliary data for the methodology as specified in the principles of the design framework as shown in Figure 6.32. The density for each of the elements in the structural model is considered as a linear interpolation between the bottom and top densities estimated for each culm and the total length of the culm.

**Table 5.3:** Physical properties for the SBD.

| Moisture content | | | Volume fraction | | | Density |
|---|---|---|---|---|---|---|
| $w_{E_c}$ | $w_{f_c}$ | $w_{f_v}$ | $v_f$ | $t_1$<br>$t_2$<br>$t_3$ | $E_{l_1}$<br>$E_{l_2}$<br>$E_{l_3}$ | $\rho$ |

## 5.6 Summary

This chapter investigates the potential for adopting alternative methods for determining the physical properties of bamboo culms with the aim of minimising time. Table 5.3 presents the discretised physical properties for the SBD.

The hand-held moisture meter BD-2100 from Delmhorst designed for wood, was calibrated to three different bamboo species (guadua, oldhamii and moso). A quadratic model described the relationship between oven-dry moisture content and the RS readings from the moisture meter for the three species. Since the three species were found to have very similar relationships, a general model for the three species was proposed ($w$(RS)= 0.00166 $RS^2$ - 0.0273 RS + 7.175), with a coefficient of determination of 0.88. This calibration enables the rapid measurements of moisture content using this hand-held device.

The oven-dry density $\rho_0$ was indirectly estimated from the density of the sample at moisture content $w$. The derivation of the equation for the estimation of $\rho_0$ was outlined. This was equivalent to the oven-dry mass divided by the volume of the sample at moisture content $w$. The percentage difference between the density $\rho_0$ estimated using the moisture content as a reference and the oven-dry mass is 1.6 %.

Furthermore, a method for the analysis of the volume fraction of vascular bundles and its distribution across the thickness was developed. The proposed method uses a digital camera and simple image analysis using Matlab. A correction for the volume fraction of fibres to take into account the area of the conducting tissue within the vascular bundles was provided, as it was assumed that the area corresponding to the pixels of the fibres included the conducting tissue. The radial distribution of $v_b$ across the thickness was also investigated. Exponential models were proposed to describe the variation through thickness for the guadua and oldhamii species. The radial distribution was found to be consistent with that reported in the literature. A particular feature was observed for the guadua samples that was absent in the moso and oldhamii species. Inner and outer layers characterised the sample cross-section for the guadua species. This could be the cause of the lower values of $v_b$ for the guadua species in comparison to those of the oldhamii species. However, this needs to be further investigated. The thickness and the elastic modulus for each lamina were calculated for the input parameters in the composite material model by using the exponential models for the distribution of $v_b$.

In addition, the dimensional change due to a decrease in moisture content was investigated to understand the behaviour and take into consideration possible implications. The shrinkage in the diameter, thickness and length was determined for a batch of moso bamboo. The shrinkage in the longitudinal direction is negligible. The shrinkage was higher for the diameter in the outer part of the culm wall thickness. The dimensional change for the diameter and thickness was of 0.19 and 0.14 % respectively. From the literature (see Section 2.1), we know that the shrinkage of the fibre is similar to that of timber, but the shrinkage of parenchyma is smaller (Liese and Tang, 2015). This can explain the higher shrinkage observed towards the outer part of the culm wall thickness in contrast to the

inner part, caused by the higher percentage of fibres in the outer wall.

# Chapter 6

# Mechanical properties of structural bamboo

This chapter develops a methodology for determining the mechanical properties for structural analysis and design of bamboo structures. The chapter is divided into three main sections, and the specific objectives for each are described below.

- To gain insight into the mechanical behaviour of bamboo culms, through a series of pilot tests to inform the development of this methodology.
- To describe the proposed methodology, including material models and test methods.
- To carry out an experimental programme for the validation of the methodology.

## 6.1 Mechanics of bamboo culms

This section presents a series of experimental programmes to investigate: (i) the influence of radial fibre distribution on compressive behaviour, (ii) the differences in mechanical behaviour between using full culm specimens and small coupons for the compressive strength and stiffness, and the shear strength, as well as the longitudinal variation of some physical and mechanical properties, and finally (iii) possible structural mechanisms for the prediction of bending elastic modulus of full culms from the compressive elastic modulus on small coupons. In addition, the failure behaviour of the full culms is discussed.

### 6.1.1 Influence of radial fibre distribution on compressive behaviour

The mechanical properties reported for bamboo lie within a very wide range (see Tables 2.3, 2.4 and 2.5). Unlike homogeneous and isotropic materials, bamboo has a gradient structure that impacts its mechanical response under load. For example, Richard and Harries (2015) found that the radial distribution of fibres and the end restraint condition (i.e. free or fixed) influence the bamboo tensile test. They reported a non-uniform strain distribution in samples taken with the width in the radial direction. This was attributed

to the fibre gradation in the radial direction and whether the sample was fixed or free to rotate. On the other hand, they found a roughly uniform strain distribution across the width of samples taken in the tangential direction at three different positions of the culm wall (i.e. inner, middle and outer). Also, Obataya et al. (2007) investigate the difference in flexural behaviour of strips of bamboo subjected to transverse loads applied with different set-up (i.e. outer surface oriented in tension zone and outer surface oriented in compression zone). They conclude that the specimens loaded with the outer surface in the tensile zone present a higher radius of curvature, thus having more flexural ductility than those specimens with the inner surface in the tensile zone. This behaviour was associated with the composite nature of bamboo, where the outer surface is strained, and the inner surface is compressed, especially for the samples including the whole thickness as opposed to those from local areas in the radial direction (e.g. outer or middle). It is reasonable to think that similar behaviour occurs when bamboos are subjected to compressive loads.

Since the framework described in Chapter 3 is concerned with small samples subjected to compressive forces, in this subsection we investigate the influence of fibre gradation in compression tests.

#### 6.1.1.1 Materials and methods

Bamboo specimens of the moso (*Phyllostachys pubescens*) species were used. The experimental programme consisted of two series of tests (a pilot test and a set of 16 samples) on small coupons subjected to compressive loads to measure the strains on the inner and outer surface. The tests were carried out according to JG/T-199 (2007). All the samples were small coupons of $15 \times t \times 60$ mm in the tangential, radial and longitudinal directions respectively. The tests were carried out in a testing machine Instron 3345 (Instron, 2002, 2004) with a load cell of 5 kN capacity. The compressive elastic modulus was determined in the range of 5 to 20 N/mm$^2$, in the linear elastic regime.

The standard JG/T-199 (2007) specifies the use of a testing machine equipped with spherical seated platens. However, the test set-up was prepared using fixed loading plates to have uniform strain across the whole sample. The fabrication and quality control section of the JG/T-199 (2007) specifies the tolerances for the length of the specimens as 1.0 mm, and that the longitudinal and transverse planes shall be orthogonal. However, the standard does not define tolerance values for these orthogonal sides. In order to prevent any strain concentrations caused by the tolerances in these orthogonal planes, the length of the samples was measured at both sides with a digital caliper of 0.01 mm resolution. The average differences from both sides for all samples was of 0.03 mm. As this tolerance was more than one order of magnitude to that specified by the JG/T-199 (2007) the deviations measured were considered negligible.

The first pilot test was prepared with strain gauges of a linear pattern (VISHAY, 2017) CEA-XX-125UN-120 oriented in the direction of the fibre in the inner and outer sides of the culm wall. The second series of tests consisted of 16 samples prepared with

spray paint on one radial side to capture strain distributions through the culm wall (see Figure 6.1a). The strains were measured using digital image correlation (DIC) method to observe the whole strain field. It was found that spray painting bamboo with white, grey and black colours was more sensitive to the deformation of the material than using a conventional self-adhesive sticker. The results using this technique presented less noise than those prepared with a self-adhesive sticker. The test set-up was as in Figure 6.1b. Two Kodak Megaplus ES 1.0 cameras with Fujinon-TV high-quality lenses were placed in front of the testing machine. The samples were shot for the entire duration of the tests at a rate of two images per second. The images were processed with the software VIC-3D from Correlated Solutions, from which the displacements were obtained. The strains at the centre and top of the specimens were further evaluated in Matlab.

**(a)** **(b)**

**Figure 6.1:** (a) Small coupon prepared with spray paint for DIC analysis. (b) Set-up of the cameras for the DIC measurements.

#### 6.1.1.2 Results

The stress-strain curves for the inner and outer part of the sample prepared with strain gauges are in Figure 6.2a. The results show higher strains in the outer part of the culm wall and therefore lower stiffness, which is opposite to what was expected. Since the volume fraction is higher for the outer part of the culm (see Figure 6.2b) and the stiffness of bamboo has been reported to be proportional to the volume fraction (Amada et al., 1996), we expected the outer part to be stiffer than the inside. The cause of this behaviour is further investigated with the results using DIC.

From the samples prepared with spray paint, some showed higher vertical displacements concentrated in the top inner part of the sample. Figure 6.3 shows one of the samples where this behaviour was observed. This suggests that the strains change from point to point, due to the heterogeneity and gradient structure of the material. However, we know that theoretically, according to the compatibility of deformations, the strains are assumed to be uniform throughout the sample. Some representative strain distributions across the culm wall are depicted in Figure 6.4a. These were calculated at the middle of the sample as indicated in Figure 6.4b with a typical sample and strain field. As seen

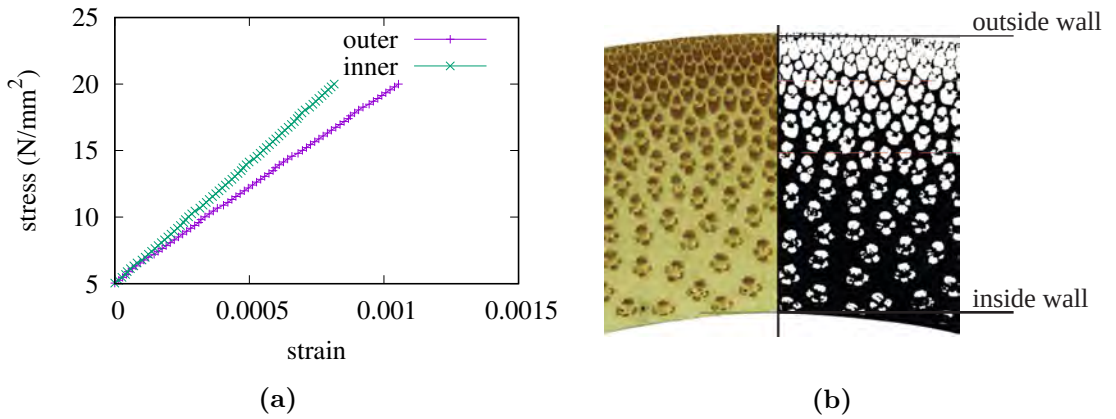


**Figure 6.2:** (a) Stress-strain curves calculated from the inner and outer side of the coupon. (b) Fibre distribution across the culm wall thickness and binary image for image analysis of volume fraction of vascular bundle sheaths.

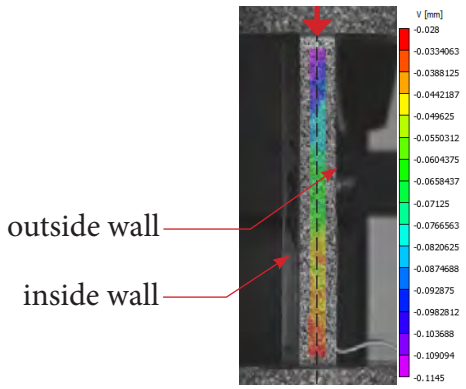


**Figure 6.3:** Small coupon under axial compressive load showing the vertical displacements in the area of interest of the culm wall, adapted from Godina and Lorenzo (2015).

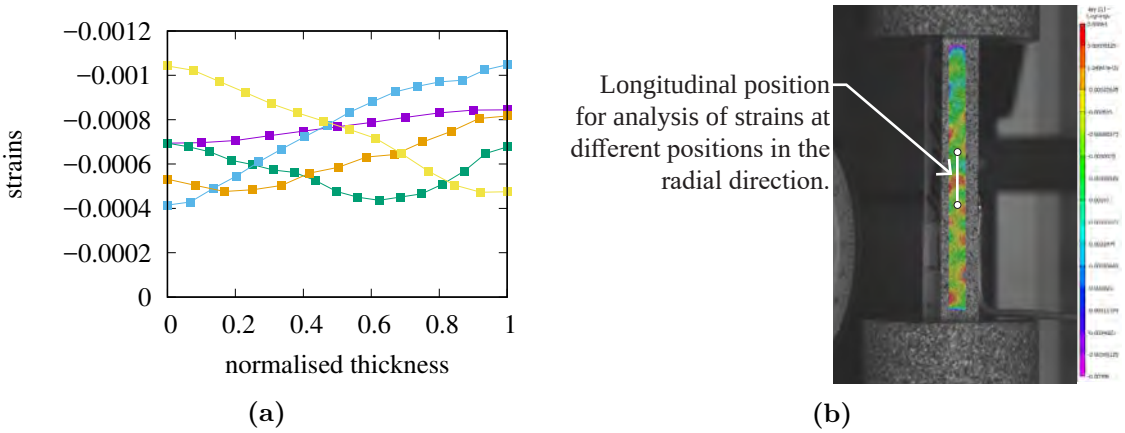


**Figure 6.4:** (a) Representative strain distributions in the radial direction from the inner to the outer part of the normalised thickness (note that the thickness corresponds to the thickness of the area of interest). Negative strain sign indicates compression. (b) Strain field indicating the vertical position where strains where analysed.

from Figure 6.4a, the strains are non-uniform across the thickness. While some of the samples presented roughly a uniform distribution, the mechanism that causes the strain

variation in the radial direction for some of the samples is not clear. The assumption of the uniform deformation of the overall sample throughout the cross-section is due to the fixed loading plate. Nevertheless, the clearances of the pin, which is attaching the loading cylinder to the load cell, allowed very small movement. This movement was sufficient to enable small rotations of the loading cylinder and prevent uniform vertical displacements. These rotations are relevant because we are dealing with very small deformations in this tests (approximately $< 0.1$ mm). Figure 6.5 shows the vertical displacements of the top coordinates of the area of interest of a representative sample to show this behaviour. This is significant because if the loading plate is compressing more the inner part of the sample it might be causing densification of the matrix. The maximum compressive stress applied in this tests was 20 N/mm$^2$. However, the compressive strength of the inner part of the culm for moso bamboo is approximately 30 N/mm$^2$ (Dixon and Gibson, 2014), while that of the parenchyma cells is 0.3 N/mm$^2$ (Gibson, 2012). In some cases, this might explain the strain results from the inner to the outer part of the surface that leads to discrepancy. The densification at the top inner part of the specimen that is in direct contact with the steel plates is not quantified at the mid-length of the specimen. Therefore, the measurements at the middle part in the inner side of the culm wall do not capture the strains occurring in the whole length of the specimen, and thus leading to an apparent higher stiffness towards the inner side of the culm wall, which is not true.

Since the distribution of strains changes among samples (as seen from Figure 6.4a), it is also possible that the test is very sensible to the tolerances of the sample and the roughness of the top and bottom surface in contact with the loading plates. Furthermore, the lateral expansion of the sample might be affecting the results. If we assume that the Poisson's ratio changes in the radial direction due to the gradient density, the horizontal displacements will change and thus affecting the deformed shape of the sample.

It is important to note that non-uniform strain distributions in the radial direction were also observed in tensile tests (Richard and Harries, 2015). Figure 6.6 shows the distribution of strains in the radial direction for samples subjected to tensile forces with

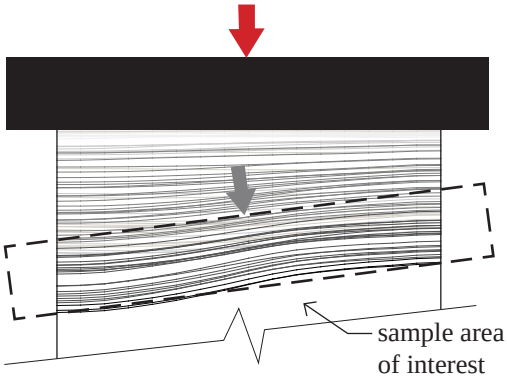


**Figure 6.5:** Vertical displacement of the top part of the area of interest of one representative sample. The displacements are show as the load is progressively applied and the difference in vertical displacement from the inner to the outer part for this example is 0.02 mm.

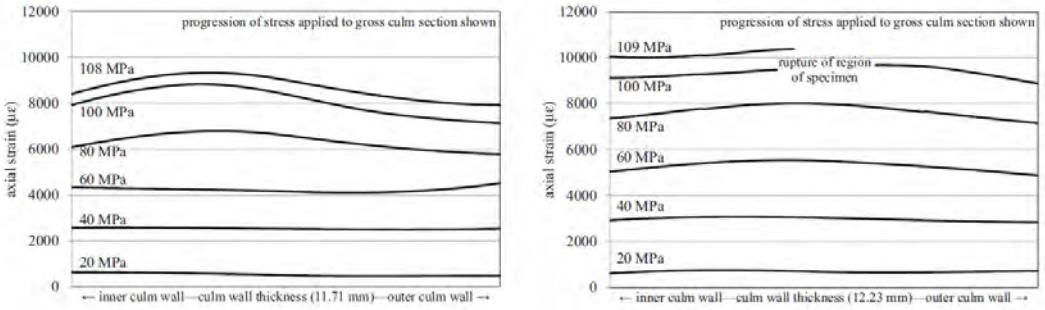


(a) (b)

**Figure 6.6:** Strain distributions through thickness from tensile tests for (a) free and (b) fixed samples by Richard and Harries (2015).

free and fixed end conditions. Although non-uniform strains were more significant in samples with free ends, non-uniform strains were also reported for samples with fixed ends. The authors suggested that the samples with free ends were subjected to bending. In our case, bending stresses were not considered since the loading cylinder allowed only a small amount of rotation due to the clearances and the load was applied in the linear elastic regime. Further compression tests to observe the strain distributions using self-aligning spherical seatings will give insight into the appearance of possible bending stresses caused by the fibre gradation.

These results highlight the sensitivity of the material to the test set-up, tolerances (including bamboo roughness surface at the top and bottom planes in contact with loading plates) and strain measurements. Like for the flexural and tensile behaviours (Obataya et al., 2007; Richard and Harries, 2015), the compressive behaviour is also affected by the radial distribution of fibres and possibly the specific function of the matrix and fibre under compressive loads. In this study, DIC allowed to gain insight into the influence of the test set-up in the strain distributions, which help the understanding of results like those measured using strain gauges at the inner and outer part.

### 6.1.2 Comparison of mechanical behaviour between full culm and small coupons testing

Since the methodology is concerned with small coupon testing, this subsection investigates the differences in mechanical response owing to the size and shape of the samples. A series of tests to determine the compressive strength, compressive stiffness and shear strength using small coupons and full culm specimens were carried out. In addition, the set of samples for the compression tests were taken at different positions along the length to quantify the longitudinal variations in compressive strength and stiffness as well as some physical properties.

#### 6.1.2.1 Materials and methods

Two bamboo culms of the moso (*Phyllostachys pubescens*) species were used. One was used for the tests under compressive loads and physical properties and the other for the shear tests.

The specimens for the compressive tests and physical properties are depicted in Figure 6.7. The culm length was 4.0 m and was divided into four portions (bottom, middle bottom, middle top and top), for each portion two segments were taken (each corresponding to an internode), from where the set of samples were fabricated. The dimensions for diameter and thickness for each of the locations are provided in Table 6.1. The material properties determined from each segment were the compressive elastic modulus in full culm $E_{cf}$ and small coupon $E_c$, the compressive strength for full culms $\sigma_{ult}$ and small coupons $f_c$, the volume fraction $v_b$, density $\rho$ and moisture content $w$.

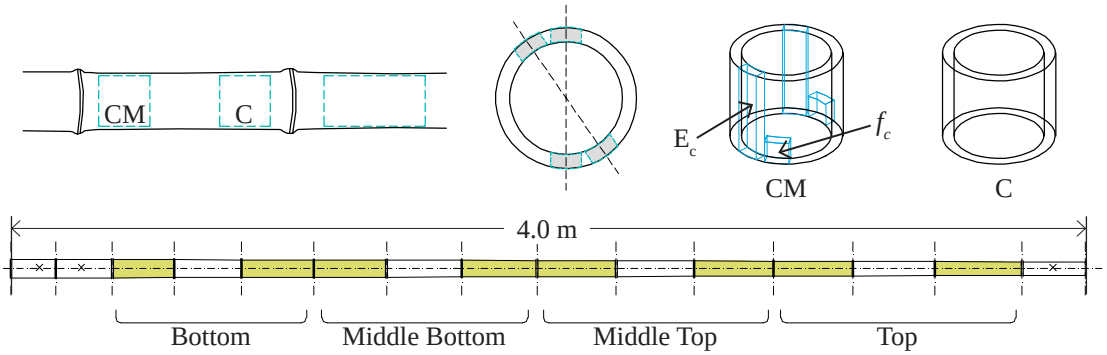


**Figure 6.7:** Diagram of full culm showing the four portions from which 8 sections were taken for fabrication of samples. For each section, two cylinders were cut CM and C. The small coupons are fabricated from CM and the C cylinder is used for full culm specimens.

**Table 6.1:** Cross-section dimensions for each of the sample locations for compressive tests and physical properties.

| | Diameter | Thickness |
|---|---|---|
| | (mm) | (mm) |
| PRE-T | 66.8 | 8.9 |
| B01 | 67.5 | 8.0 |
| B03 | 67.7 | 6.7 |
| MB01 | 67.5 | 6.2 |
| MB03 | 66.3 | 5.4 |
| MT01 | 65.3 | 5.2 |
| MT03 | 63.4 | 4.8 |
| T01 | 61.7 | 4.7 |
| T03 | 58 | 4.2 |

Full culm tests were performed according to ISO (2004b,c). The specimens used for determination of compressive strength and stiffness were cut at length equal to the diameter and were prepared with two strain gauges at orthogonal and opposite sides. The test set-up consisted of steel wedges, teflon and wax at both ends of the specimen between the

steel platens. The test methods were carried out in a testing machine Controls Advantest 9 (ControlsGroup, 2012) of 300 kN capacity equipped with spherical seated platens. The elastic modulus was calculated as a linear relationship between 20 and 80% of the maximum load at failure (ISO, 2004b).

The small coupon tests were carried out according to JG/T-199 (2007). The coupon for the elastic modulus consisted of bamboo pieces of 15 $\times$ $t$ $\times$ 60 mm for the tangential, radial and longitudinal directions respectively. The testing machine used was Instron (Instron, 2002, 2004) 3345 with a load cell of 5 kN capacity. The strains were measured with strain gauges attached to the outer surface of the culm. The load was applied at a constant rate of 13 N/mm$^2$ per minute, for six times within the range of 5 to 20 N/mm$^2$. The average readings of stress and strain values from the last three loadings were used for the analysis of the $E_c$, and it was calculated as

$$E_c = 20\Delta P / A\Delta l \tag{6.1}$$

where $\Delta P$ is the total applied load between the range of 5 and 20 N/mm$^2$, $\Delta l$ is the deformation measured between the same range of stresses, $A$ is the area calculated as 15 $\times$ $t$ and 20 is the initial length in mm where the strains are measured.

The specimens for compressive strength consisted of small cubes of 15 $\times$ $t$ $\times$ 15 mm, in the tangential radial and longitudinal directions respectively. The test methods were carried out in the same testing machine Controls Advantest 9 (ControlsGroup, 2012) described above. The displacements were measured with an axial displacement transducer mounted to the testing machine to measure the movement of the crosshead. The load was applied to a constant rate of 80 N/mm$^2$ per minute, until failure. The calculation of the compressive strength was as

$$f_c = \frac{P_{max}}{A} \tag{6.2}$$

where $P_{max}$ is the maximum load at failure.

Density and moisture content were calculated according to ISO (2004b). The volume fraction was calculated by image analysis, from photographs taken from the samples used for elastic modulus (refer to Section 5.3).

A total of 2 samples to test the shear strength using full culms were fabricated according to ISO (2004b,c), and 8 samples for small coupons according to JG/T-199 (2007). The average dimensions of the culms for all these samples were 78 and 9 mm for the diameter and thickness respectively. The full culm specimens for shear strength $\tau$ were tested on the same Controls (ControlsGroup, 2012) testing machine with a loading rate of 0.01 mm/s. The sample for the shear strength $f_v$ in small coupons is depicted in Figure 6.8. It consists of a rectangular prism containing the curvature of the bamboo and a notch cut from where the load is applied. The shear plane corresponds to the plane created by the notch parallel to the fibre. A shear fixture was designed and fabricated based on simple drawings provided in the standard JG/T-199 (2007). The tests were carried out in the testing machine Instron (Instron, 2002, 2004) 3345 of 5 kN load cell capacity, equipped with

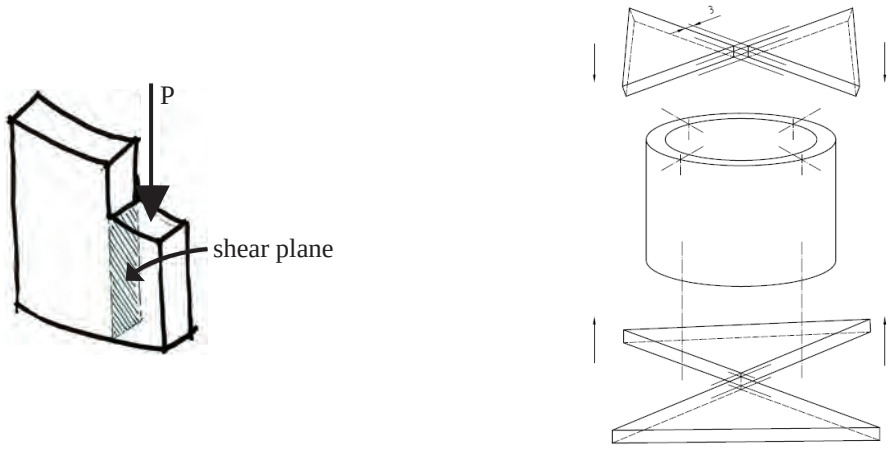


**Figure 6.8:** Samples for shear strength testing. (a) Diagram of the small sample showing the shear plane as described by the JG/T-199 (2007) standard. (b) Full culm cross-section sample with four shear planes (ISO, 2004b).

spherical seated platens. The displacements were recorded from the crosshead readings. The load was applied at a constant rate of 10 N/mm$^2$ per minute, until failure. The shear strength of both test methods was calculated as

$$f_v = \frac{P_{max}}{A_s} \tag{6.3}$$

where $A_s$ is the total area of the shear plane.

#### 6.1.2.2 Results

Figure 6.9 shows the stress-strain curve corresponding to the sample PRE-T from Table 6.1. It shows the linear portions from which the compressive elastic modulus for the small coupons $E_c$, and full culm specimens $E_{cf}$ is to be calculated according to JG/T-199 (2007) and ISO (2004b) respectively. It is clear that the calculation of $E_{cf}$ captures the nonlinear

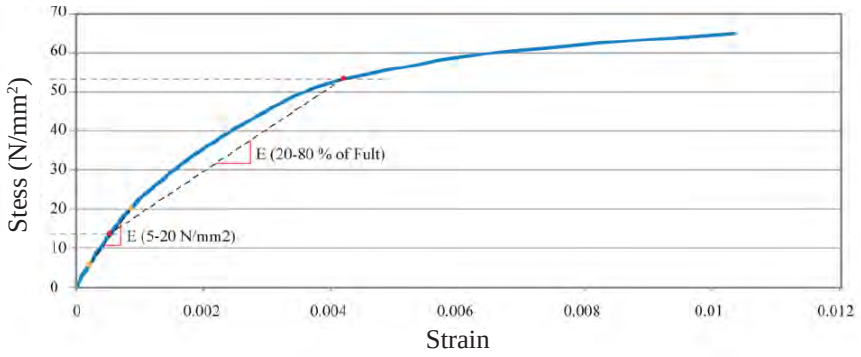


**Figure 6.9:** Stress-strain of bamboo culm specimens under compressive load for full culm and small coupons (Godina and Lorenzo, 2015).

behaviour of bamboo. For this study, the elastic modulus for full culm and small coupons were calculated under the same range of stresses, between 5 to 20 N/mm$^2$ according to JG/T-199 (2007), with the aim of comparing these two results.

The stress-strain curves of all the samples are provided in Figure 6.10. The individual comparison for the full culm and small coupon at each location is in the Appendix B. In general, the behaviour is similar to that found in the literature (refer to Chapter 2). However, there are two curves with a slightly different shape (see samples B03 and MT03 in Figure 6.10). This could have been influenced by bedding errors associated with the contact between the bamboo sample and the top and bottom end plates, similar to those occurring when testing soil stiffness (Heymann, 2015).

These errors might have been influenced by the test set-up. A typical set-up for the full culm tests is depicted in Figure 6.11. It was observed that the steel wedges damaged some of the specimens by generating a cut through the thickness. In some cases, these cuts lead to longitudinal splitting, which can influence the readings (see Figure 6.12). Overall,

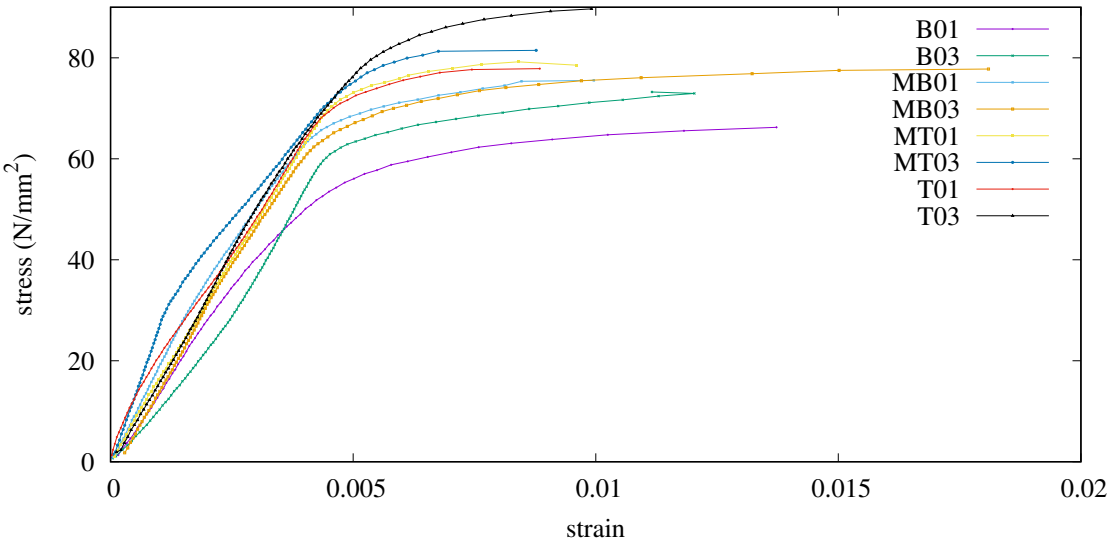


**Figure 6.10:** Stress-strain curve of all full culm specimens.

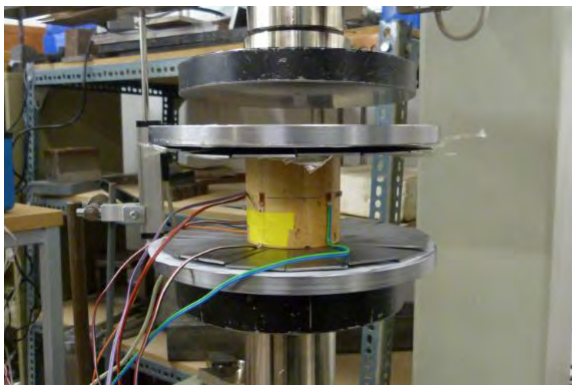

**Figure 6.11:** Full culm specimens test set-up.

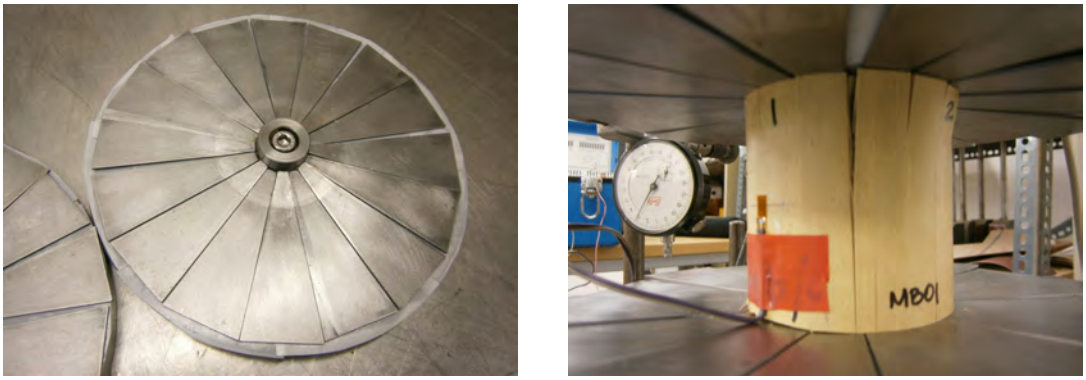


**(a)** **(b)**

**Figure 6.12:** (a) Steel wedges. (b) Failure at steel wedges location.

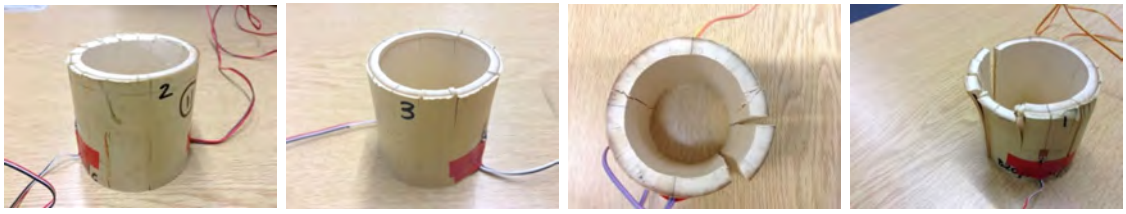

**(a)** **(b)** **(c)** **(d)**

**Figure 6.13:** Failure of the full culm specimens under compression. (a) Penetration of the steel wedges in the culm wall thickness. (b) Densification of the inner side of the culm wall thickness. (c) Longitudinal splitting. (d) Combination of failure mechanisms, including bending and barrel shape, delamination, densification and local buckling.

the tests were time-consuming and tedious due to the preparations of the set-up. Also,

Figure 6.13 shows some of the failed samples. In general the outer part presented local buckling, whereas the inner part shows densification. The failure mode in small coupons was characterised by i) crushing at the bottom part in particular in the inner side, together with local buckling of some fibres in this same area, and ii) buckling at the top outer surface. Only one of the coupons showed a small area which started to delaminate. However, it coincided with the area of failure.

Table 6.2 provides the results for each of the samples. It is interesting to note that the samples with higher percentage error are those two samples with a different stress-strain curve suggesting that the behaviour, and hence the results, were affected by the test set-up. The percentage difference between elastic modulus tested from full culm and small coupons range between 13 and 39%, and if we ignore the two samples with different stress-strain curves, the range lies between 13 and 21%. Note that these values are common in

**Table 6.2:** Elastic modulus from full culm and small coupons.

| | B01 | B03 | MB01 | MB03 | MT01 | MT03 | T01 | T03 |
|---|---|---|---|---|---|---|---|---|
| Full culm (kN/mm$^2$) | 15.1 | 11.6 | 19.2 | 16.7 | 16 | 26.9 | 18.5 | 16.1 |
| Small coupon (kN/mm$^2$) | 13.2 | 16.6 | 16.4 | 14.5 | 19.8 | 18.1 | 21.3 | 18.4 |
| Percentage difference (%) | 13.4 | 35.5 | 15.7 | 14.1 | 21.2 | 39.11 | 14.1 | 13.3 |

natural materials. For example, the coefficient of variations in wood for the modulus of elasticity and rupture ranges between 10 and 30% (Dinwoodie, 2000), and for the tensile strength of bamboo was reported between 16 and 41% (Richard and Harries, 2015) for different end restraints.

Figures 6.14a and 6.14b show an increase of compressive elastic modulus and compressive strength towards the top of the culm respectively. Although the compressive strength in both types of samples was found to increase with height, the results from small coupons were found to be lower by approximately 9.6 %. The lower compressive strength in small coupons could be a result of eccentric moments that causes the shift of the resultant force from the centroid when the loading plates are free to rotate. However, this effect and the test method provided by JG/T-199 (2007) is no further analysed in this study.

The lengthwise variation of volume fraction $v_b$, and density $\rho$ is depicted in Figure 6.15. Both increase towards the top of the culm. The relationship between $v_b$, and $\rho$ is shown in Figure 6.16a. Unlike the strong relationship between density and volume fraction in cellular solids materials such as wood (Gibson, 2005), the coefficient of determination found here was 0.53. The relationship between compressive elastic modulus $E_c$ and $v_b$ is plotted in Figure 6.16b, it has a coefficient of determination of 0.62. If we assume a linear relationship between these properties, the elastic modulus of the fibre and matrix can be estimated by applying the rule of mixtures as

$$E = E_f v_b + E_m(1 - v_b) \tag{6.4}$$

$$E_f = 35530 \quad \mathrm{N/mm^2} \tag{6.5}$$

$$E_m = 2496 \quad \mathrm{N/mm^2} \tag{6.6}$$

where $E_f$ and $E_m$ are the elastic modulus for the fibre and matrix respectively. No strong correlations were found for $E_c$ and $\rho$, $f_c$ and $v_b$, and $f_c$ and $\rho$.

The typical failure during a shear test in full culms is depicted in Figure 6.17a. The

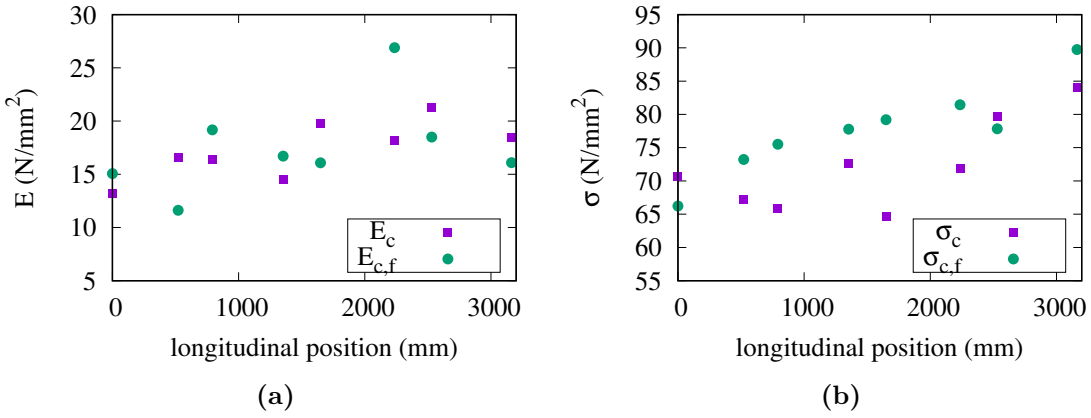


**Figure 6.14:** Comparison of results between full culm specimens and small coupons for (a) compressive elastic modulus and (b) compressive strength.

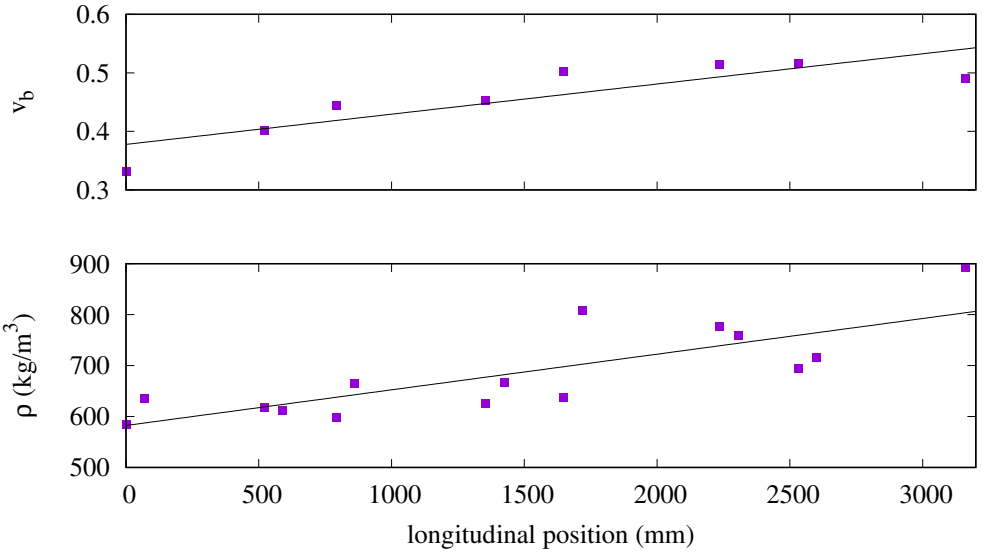


**Figure 6.15:** Variation of physical properties along the culm

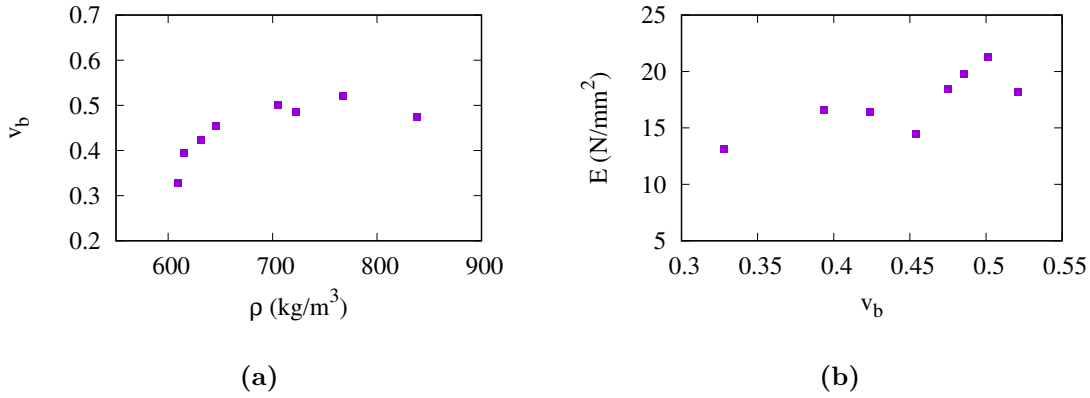


**Figure 6.16:** (a) Relationship between $v_b$ and $\rho$. (b) Relationship between $E_c$ and $v_b$.

failure occurred in two of the four shear planes of the specimen. Similar behaviour, where failure occured in only two planes, was previously observed by Richard (2013). This could be associated with the irregularity of the material. The four shear planes are not equal, as the material is non-symmetrical and non-uniform, thus the shear strength of the four shear planes differs. In this case, the failure will occur in the weakest shear planes and the rest the rest of the shear planes will not break. On the other hand, the shear failure on small coupons was characterised by a clean cut located at the shear plane. Figures 6.17b and 6.17c show the test set up and the typical failure in small coupons. While both shear tests presents some challenges due to the complexities of the test set-up and bespoke fabrication of fixtures, the full-culm test could be more representative for the entire cross-section of the material as the value represent the lower shear strength of the four shear planes. However, some other issues have been highlighted by Richard (2013) with the full-culm samples. He observed failure in between shear planes possibly caused by flexure due to the sample initial conditions. This again shows the importance and difficulties of

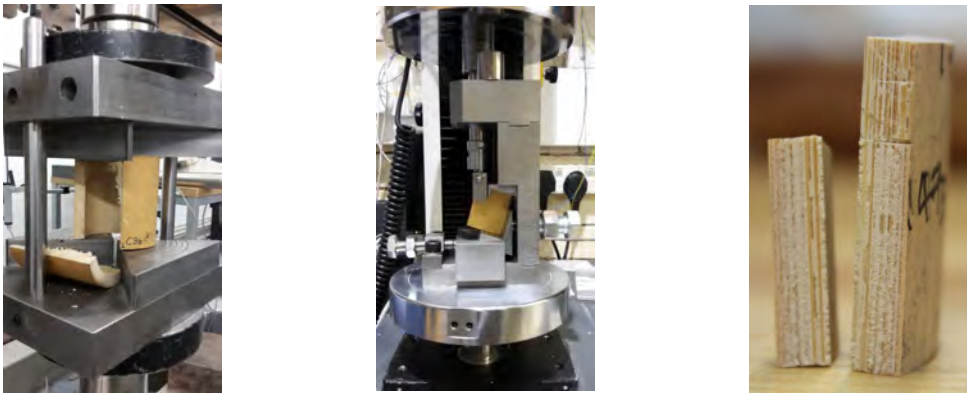

**(a)** **(b)** **(c)**

**Figure 6.17:** (a) Full culm shear test. (b) Small coupon shear test. (c) Typical failure in small coupons.

the application of load and the contact surface between the sample and the loading plates in the test set-up using full-culm samples.

### 6.1.3 Flexural elastic modulus of bamboo culms

This study presents a series of tests to identify possible mechanisms to predict the behaviour of full culm bamboos under transverse loads from the behaviour of small coupons subjected to axial compressive loads. In this study the bending elastic modulus $E_b$ from full culms and the compressive elastic modulus $E_c$ from small coupons is determined to investigate any possible relationships. In addition, the failure mode of bamboo culms under transverse loads is discussed, and the maximum normal $\sigma_u$, and shear stresses $\tau_u$ are calculated.

#### 6.1.3.1 Materials and methods

All the full culm specimens and small coupons were obtained from a moso (*Phyllostachys pubescens*) bamboo culm. The culm was of 4 m long with an average diameter and thickness of 38 and 4.4 mm respectively. Figure 6.18 depicts the locations from which both types of samples (full culm and small coupons) were taken. A total of two full culm specimens were cut, corresponding to the bottom and top part of the culm respectively. The small coupons were obtained from three different locations (bottom, middle and top) along the culm. A total of twelve small coupons were obtained (4 for each section).

The tests for $E_c$ were carried out according to JG/T-199 (2007), as described in Subsection 6.1.1. The full culm tests were carried out according to ISO (2004b,c). The test method consists of a four-point bending test. One exception to this test method was the loading blocks. The ISO (2004b,c) specifies the use of loading and supports blocks with the length equal to the size of the internodes at the loading and support points. However, this assumes that for each full culm specimen, there will be an internode centred at these points. In addition, since the internodes in these culms were very long, it was not

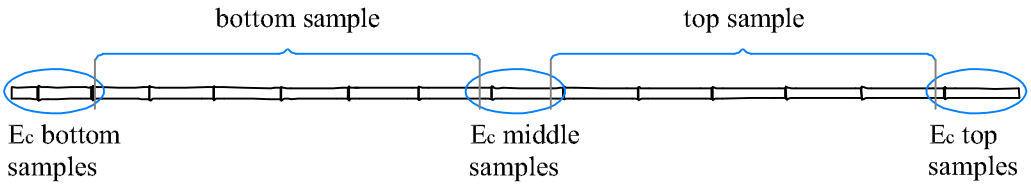


**Figure 6.18:** Diagram for location of samples for bending tests and $E_c$ specimens.

possible to apply the load using loading blocks with the length of the internodes. There is no guidance in the ISO (2004b,c) for these two crucial aspects of the set-up. However, with the aim of generating a constant bending moment in the middle of the specimen, it was decided to use small aluminium loading blocks located at the internodes and place at thirds of the clear span. These tests were carried out in a testing machine Instron 3345 (refer to the description in Subsection 6.1.2). The load was applied to a constant rate of 0.5 mm/s. The ultimate normal stress $\sigma_{ult}$ and flexural elastic modulus $E$ were calculated according to ISO (2004b). The ultimate normal stress is given by

$$\sigma_{ult} = F \times L \times \frac{D/2}{6} / I_B \tag{6.7}$$

where $F$ is the maximum load, $L$ refers to the clear span, $D$ is the outer average diameter measured at two opposite sides, and $I_B$ is the second moment of area calculated as

$$I_B = \pi/64\Big[D^4 - (D-2t)^4\Big] \tag{6.8}$$

where $t$ is the average thickness measured at four points in two orthogonal directions. The bending elastic modulus is calculated as

$$E_b = 23 \times F \times L^3/1296 \times \delta \times I_B \tag{6.9}$$

where $\delta$ is the deflection, and $F$ is the load in the linear regime.

Considering the simple supported beam with two point loads, the shear stresses $\tau_{ult}$ were calculated as

$$\tau_u = \frac{F/2}{A} \tag{6.10}$$

where $A$ is the area of the cross-section calculated from the averaged diameter and thickness measured. Table 6.3 shows the dimensions for the bottom and top full culm specimens.

**Table 6.3:** Dimensions of full culm tests under transverse loads.

| | bottom | top |
|---|---|---|
| Diameter (mm) | 39 | 34 |
| Thickness (mm) | 4.5 | 4.6 |

#### 6.1.3.2 Results

The results for the average values of $E_c$ from the small coupons are presented in Table 6.4. The $E_c$ tends to increase towards the top of the culm, in accordance with the findings from the previous Subsection 6.1.2.

**Table 6.4:** $E_c$ values along the culm.

| $E_c$ | | |
|---|---|---|
| Bottom ($kN/mm^2$) | Middle ($kN/mm^2$) | Top ($kN/mm^2$) |
| 13.18 | 14.32 | 16.79 |

Figure 6.19 shows the load-deflection curves for both full culm tests, and Table 6.5 presents the results. As expected due to the smaller cross-section, $E_b$ decreases towards the top of the culm. In contrast, $\sigma_u$ is higher at the top, whereas $\tau_u$ was constant.

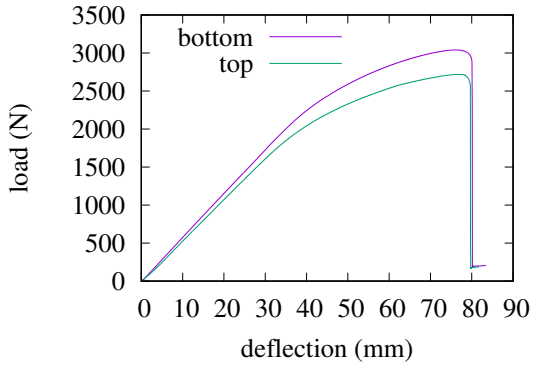


**Figure 6.19:** Load-deflection curve of bending tests.

**Table 6.5:** $E_b$ and $\sigma_u$ from full culm bending tests.

| $E_b$ | | $\sigma_u$ | | $\tau_u$ | |
|---|---|---|---|---|---|
| Bottom ($kN/mm^2$) | Top ($N/mm^2$) | Bottom ($kN/mm^2$) | Top ($N/mm^2$) | Bottom ($N/mm^2$) | Top ($N/mm^2$) |
| 22.2 | 21.8 | 157 | 167 | 3.1 | 3.2 |

The load-deflection curves in Figure 6.19 show the similar ductile behaviour observed in bamboo under compressive loads. Both curves present a linear portion followed by the yield of the material and the subsequent failure.

The failed specimens are shown in Figure 6.20. In both cases, the failure occurred under the loading block towards the top part of the culm. As soon as the culms failed, a crack propagated to both sides. The splitting in the bottom culm specimen was extended towards the top end, eventually causing the complete collapse of the culm. The crack at the top culm specimen extended only throughout two internodes, and the culm recovered most of its initial shape after the load was removed. As soon as the specimen failed,

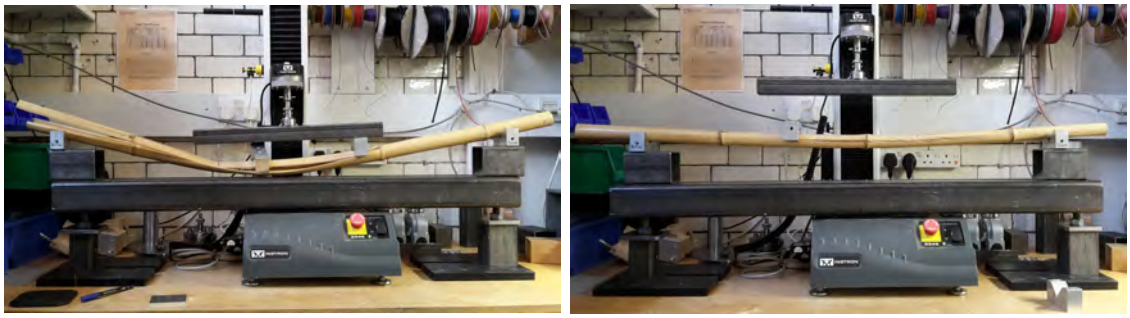

**(a)** **(b)**

**Figure 6.20:** Failure of bamboo culms under 4-point bending loads(a) Bottom culm (b) Top part.

the culm undergoes a brittle fracture due to the occurrence of splitting. However, this happened after large deformations occurred beyond the elastic regime.

The normal stresses at which the culm failed (see Table 6.5), are significantly higher than the compressive strength found the literature (refer to Table 2.4) and those calculated in the previous Subsection 6.1.2. Thus suggesting that tensile stresses developed in the cross-section play an important role. Elements subjected to bending moments developed normal and shear stresses. It has been previously highlighted the susceptibility of bamboo to splitting and the failure of the culm due to longitudinal shear when subjected to bending moments (Vaessen and Janssen, 1997; Harries et al., 2012; Trujillo and Jangra, 2016; Trujillo et al., 2017). The splitting behaviour is caused either by failure mode I or II (Bodig and Jayne, 1982), which are transverse tension or longitudinal shear. However, the splitting behaviour of bamboo occurring during bending is not well understood.

There are many types of stresses (axial tension and compression, longitudinal shear and transverse tension) developed in the cross-section that can trigger failure. In timber, two different normal stress distributions are identified that are related to the type of timber (Bodig and Jayne, 1982). One for those types of timbers with ultimate stress in tension greater than in compression, and another with the ultimate tensile stress smaller than the ultimate compressive stress. For bamboo, the tensile strength is significantly greater than the compressive strength (see Tables 2.3 and 2.4). For those timbers that are capable of sustaining greater tensile stresses, the normal stress distribution under bending changes progressively as the load is increased (Bodig and Jayne, 1982; Bechtel and Norris, 1959). For small bending moments, the stress distribution can be described as linear. However, as the load is further increased there is a point at which the compressive strength is exceeded, and thus the neutral plane is shifted towards the tensile zone causing tension failure (see Figure 6.21).

Although these studies in timber consider a rectangular cross-section, a similar behaviour might be occurring in the cross-section of bamboo culms. This suggests that the interaction between tension and compression in the culm cross-section when subjected to transverse loads is key for the estimation of bending properties of bamboo from axial behaviour.

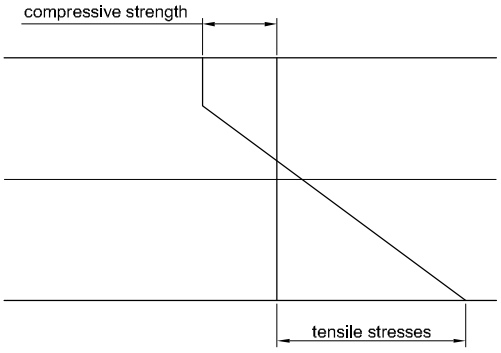


**Figure 6.21:** Normal stress distribution in for a timber cross-section with tensile strength higher than compressive strength.

### 6.1.4 Summary

This section presented a series of experimental investigations to gain insight into different aspects related to the mechanical behaviour of bamboo culms to inform the development of the methodology in next Section 6.2. The key findings are summarised below.

- The non-uniform strain distribution throughout the thickness shows the effect of the radial fibre distribution and the particular function of the matrix and fibres under axial compressive loads. This shows the high sensitivity of the material on the test set-up and strain measurements was found to be of great importance.
- The compressive elastic modulus of full culms and small coupons was found to be equivalent when measured under the same range of stresses (between 5 to 20 $N/mm^2$). On average, the percentage difference between both values was 21%, which is common in bamboo and other natural materials.
- The average compressive strength of small coupons was 9.6% lower than that measured in full culms. It was suggested that this might be caused by the test method and the inherent radial fibre distribution of bamboo. However, this aspect needs to be further addressed.
- The steel wedges used for the set-up of the compressive tests in full culms can cause cuts throughout the thickness and possibly bedding errors due to the contact between the steel wedges and the top and bottom parts of the bamboo sample.
- The test method for shear strength in full culm specimens tends to fail only in two of the four shear planes. It was assumed that full-culm tests are representative of the lowest shear strength of the four shear planes. On the other hand, the shear failure for all the small coupons was characterised by a clean cut passing through the shear plane.
- The compressive strength $f_c$, compressive stiffness $E_c$, bending strength $\sigma_u$, volume fraction $v_b$ and density $\rho$ were found to increase towards the top. On the other hand,

the bending stiffness $E_b$ decreases with the decrease in the size of the culm cross-section. This shows the dependence of the mechanical behaviour on the physical properties of the material, and confirms the need to take into consideration the variations along the culm when analysing the structural behaviour of bamboo culms.

- The elastic modulus of the fibre and matrix estimated from the compressive tests using the rule of mixtures for moso species was $E_f = 35{,}530$ N/mm$^2$ and $E_m = 2496$ N/mm$^2$.
- The flexural behaviour of bamboo shows a ductile behaviour, similar to the one observed under axial compressive loads. The interaction between the tensile and compressive mechanisms of bamboo culms when subjected to transverse loads was suggested to be an important parameter for the estimation of the flexural behaviour of bamboo.

## 6.2 Methodology for determination of mechanical properties for SBD

The methodology presented here is the core of this chapter as it describes the proposed material models and test methods for determining the mechanical properties of bamboo culms.

### 6.2.1 Composite material model for bamboo

In the previous section, we have seen that the compressive behaviour of bamboo is also influenced by the radial distribution of volume fraction and the particular role of the fibre and matrix. Here, composite material theory is used to model the radial variations and estimate the equivalent bending stiffness of bamboo by extrapolation from the compressive elastic modulus tested on small coupons.

Composite materials are fibre reinforced materials created by two or more constituents such as fibres and matrix, bonded together to produce a superior material than each of its constituents by separate. The study of composite materials at the micromechanical scale consists of the analysis of each of the constituents, and at the macromechanical scale, the properties are averaged, and thus the material is assumed to be homogeneous (Daniel and Ishai, 2006). Using macromechanical analysis of composites, the equivalent modulus of elasticity in bending $E_{eq,c}$ is estimated.

To model the radial fibre distribution, the cross-section of bamboo is modelled as a laminate with several layers across the culm wall. Usually, the study of the variations in the culm wall thickness of bamboo is divided into three parts (i.e. inner, middle and outer). Also, when segmented into six layers, the tensile elastic modulus from the two inner layers and the two middle layers were not different (Yu et al., 2008). In this methodology, a laminate of three layers is proposed.

#### 6.2.1.1 Material model symmetry and assumptions

The material model and the nomenclature are adopted from Kollar and Springer (2003).

The behaviour of composite materials depends on the arrangement and directions of the fibres. As seen from the literature, in Section 2.1 the fibres are oriented in the longitudinal direction of the culm. The proposed model is characterised by a transversely isotropic laminate as the one shown in Figure 6.22. Transversely isotropic materials are orthotropic materials with three planes of symmetry, and in which one of the planes behaves as an isotropic material (Kollar and Springer, 2003).

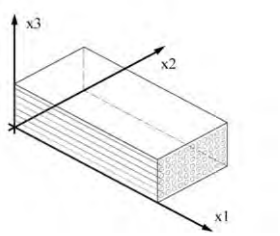


**Figure 6.22:** Transversely isotropic material

Laminated composites are materials made of several layers stacked together. The fibres are aligned in the $x_1$ direction, and the $x_2 - x_3$ plane represents the isotropic plane, which is perpendicular to the direction of the fibres (see Figure 6.22). The division of the culm thickness into three layers was made by considering the same percentage of fibres in each layer as described in Subsection 5.3.3.1. The main assumptions of the model are described below.

**a.1** The material model is linear elastic.

**a.2** It is considered as a transversely isotropic material.

**a.3** Plane-stress condition is assumed.

**a.4** It is a laminate made up of three layers to model the radial gradient distribution of fibres.

**a.5** It is considered as a thin laminate so that the thickness of the laminate is small in comparison with the dimensions in the other two planes of symmetry.

**a.6** The thin laminate undergo only small deformations.

**a.7** The strains vary linearly through the thickness of the laminate.

**a.8** The cross-section of a beam made of this material is idealised as a hollow circle.

#### 6.2.1.2 Strain-displacement relations

From Figure 6.23a we have the deformations in the longitudinal direction of a long element. By definition, the strain is equal to the deformation divided by the initial length, as

$$\epsilon_x = \frac{\Delta'_x - \Delta_x}{\Delta_x} = \frac{\partial u}{\partial x} \tag{6.11}$$

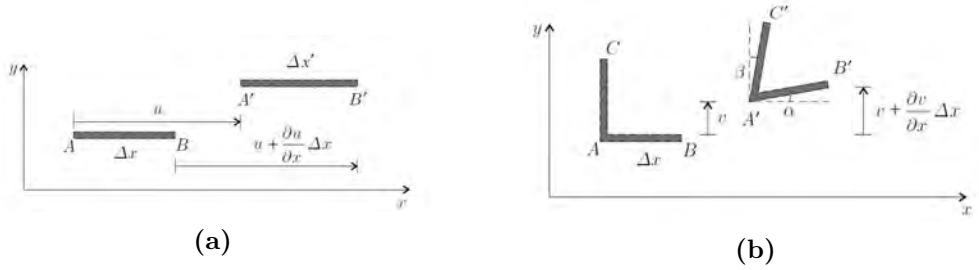


**Figure 6.23:** (a)Normal strain, and shear strain (Kollar and Springer, 2003).

where $\epsilon_x$ is the normal strain in the x direction, $\Delta_x$ and $\Delta'_x$ are the initial and deformed lengths of the long element, and $u$ is the displacement of point A in Figure 6.23a. Similarly, the normal strains $\epsilon_y$ and $\epsilon_z$ in the y and z directions are

$$\epsilon_y = \frac{\partial v}{\partial y} \tag{6.12}$$

$$\epsilon_z = \frac{\partial w}{\partial z} \tag{6.13}$$

where $u$ and $w$ are the displacements in the $y$ and $z$ directions.

The shear deformations are depicted for an element A,B and C in Figure 6.23b. The shear strain $\gamma_{xy}$ is defined by the sum of the angles $\hat{\alpha}$ and $\hat{\beta}$ (the hat is added to $\alpha$ and $\beta$ in order to prevent conflict of nomenclature with the bimodulus model), where

$$\hat{\alpha} \approx \tan\hat{\alpha} = \frac{(v + \frac{\partial v}{\partial x}\Delta_x) - v}{\Delta_x} = \frac{\partial v}{\partial x} \tag{6.14}$$

and,

$$\hat{\beta} = \frac{\partial u}{\partial y} \tag{6.15}$$

Therefore the shear strains are

$$\gamma_{xy} = \frac{\partial u}{\partial y} + \frac{\partial v}{\partial x} \tag{6.16}$$

$$\gamma_{yz} = \frac{\partial v}{\partial z} + \frac{\partial w}{\partial y} \tag{6.17}$$

$$\gamma_{xz} = \frac{\partial u}{\partial z} + \frac{\partial w}{\partial x} \tag{6.18}$$

#### 6.2.1.3 Equilibrium conditions

The equilibrium equations of a small element $\Delta x \Delta y \Delta z$ as in Figure 6.24, consists of three equations by considering the force moment balance as

$$\frac{\partial \sigma_x}{\partial x} + \frac{\partial \tau_{yx}}{\partial y} + \frac{\partial \tau_{zx}}{\partial z} + f_x = 0 \tag{6.19}$$

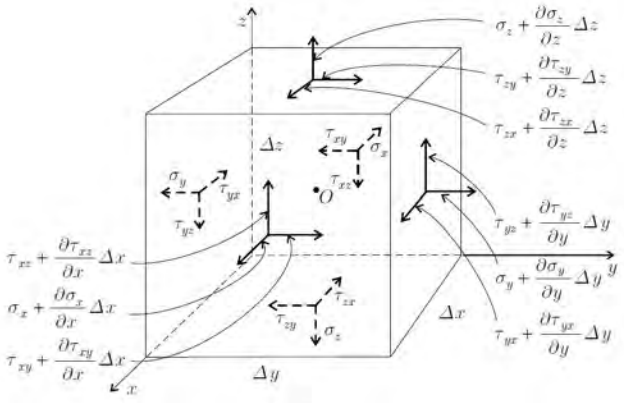

**Figure 6.24:** Force and moment balance on a small element $\Delta x \Delta y \Delta z$ (Kollar and Springer, 2003).

$$\frac{\partial \tau_{xy}}{\partial x} + \frac{\partial \sigma_y}{\partial y} + \frac{\partial \tau_{zy}}{\partial z} + f_y = 0 \tag{6.20}$$

$$\frac{\partial \tau_{xz}}{\partial x} + \frac{\partial \tau_{yz}}{\partial y} + \frac{\partial \sigma_z}{\partial z} + f_z = 0 \tag{6.21}$$

where $f_x$, $f_y$ and $f_z$ are the forces in the x, y and z directions respectively (see Figure 6.25), and where the following equations apply

$$\tau_{yz} = \tau_{zy} \tag{6.22}$$

$$\tau_{xz} = \tau_{zx} \tag{6.23}$$

$$\tau_{xy} = \tau_{yx} \tag{6.24}$$

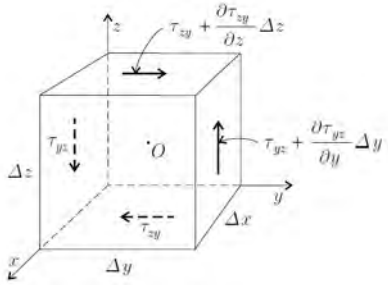

**Figure 6.25:** Moment balance about an axis in the $x$ direction (Kollar and Springer, 2003).

#### 6.2.1.4 Stress-strain relationships

The stress-strain relationships depend on the arrangement of the fibres. The compliance matrix for a transversely isotropic material is

$$[S] = \begin{bmatrix} S_{11} & S_{12} & S_{12} & 0 & 0 & 0 \\ S_{12} & S_{22} & S_{23} & 0 & 0 & 0 \\ S_{12} & S_{23} & S_{22} & 0 & 0 & 0 \\ 0 & 0 & 0 & 2(S_{22} - S_{23})0 & 0 & \\ 0 & 0 & 0 & 0 & S_{66} & 0 \\ 0 & 0 & 0 & 0 & 0 & S_{66} \end{bmatrix} \tag{6.25}$$

from which the stress-strain relationships are

$$\begin{Bmatrix} \epsilon_1 \\ \epsilon_2 \\ \epsilon_3 \\ \gamma_{23} \\ \gamma_{13} \\ \gamma_{12} \end{Bmatrix} = \begin{bmatrix} S_{11} & S_{12} & S_{12} & 0 & 0 & 0 \\ S_{12} & S_{22} & S_{23} & 0 & 0 & 0 \\ S_{12} & S_{23} & S_{22} & 0 & 0 & 0 \\ 0 & 0 & 0 & 2(S_{22} - S_{23}) & 0 & 0 \\ 0 & 0 & 0 & 0 & S_{66} & 0 \\ 0 & 0 & 0 & 0 & 0 & S_{66} \end{bmatrix} \begin{Bmatrix} \sigma_1 \\ \sigma_2 \\ \sigma_3 \\ \tau_{23} \\ \tau_{13} \\ \tau_{12} \end{Bmatrix} \tag{6.26}$$

Furthermore, as the stiffness matrix is the inverse of the compliance matrix, we have

$$[C] = \begin{bmatrix} C_{11} & C_{12} & C_{12} & 0 & 0 & 0 \\ C_{12} & C_{22} & C_{23} & 0 & 0 & 0 \\ C_{12} & C_{23} & C_{22} & 0 & 0 & 0 \\ 0 & 0 & 0 & \frac{C_{22}-C_{23}}{2} & 0 & 0 \\ 0 & 0 & 0 & 0 & C_{66} & 0 \\ 0 & 0 & 0 & 0 & 0 & C_{66} \end{bmatrix} \tag{6.27}$$

The stiffness matrix in engineering form is

$$[C] = \begin{bmatrix} & & & \begin{bmatrix} 0 & 0 & 0 \\ 0 & 0 & 0 \\ 0 & 0 & 0 \end{bmatrix} \\ & [L] & & \\ & & & \\ \begin{bmatrix} 0 & 0 & 0 \\ 0 & 0 & 0 \\ 0 & 0 & 0 \end{bmatrix} & & [M] & \end{bmatrix} \tag{6.28}$$

where the submatrices $[L]$ and $[M]$ for a transversely isotropic material are

$$[L] = \frac{1}{D} \begin{bmatrix} E_1(1-\nu_{23}^2) & E_2\nu_{12}(1+\nu_{23}) & E_2\nu_{12}(1+\nu_{23}) \\ E_2\nu_{12}(1+\nu_{23}) & E_2(1-\frac{E_2}{E_1}\nu_{12}^2) & E_2(\nu_{23}+\frac{E_2}{E_1}\nu_{12}^2) \\ E_2\nu_{12}(1+\nu_{23}) & E_2(\nu_{23}+\frac{E_2}{E_1}\nu_{12}^2) & E_2(1-\frac{E_2}{E_1}\nu_{12}^2) \end{bmatrix} \tag{6.29}$$

where

$$D = 1 - \nu_{23}^2 - 2(1 + \nu_{23})\frac{E_2}{E_1}\nu_{12}^2 \tag{6.30}$$

and

$$[M] = \begin{bmatrix} \frac{E_2}{2(1+\nu_{23})} & 0 & 0 \\ 0 & G_{12} & 0 \\ 0 & 0 & G_{12} \end{bmatrix} \tag{6.31}$$

The total number of elements of the stiffness and compliance matrix is 12. However, as the matrix is symmetric, the elements are reduced to 9. Furthermore, due to the isotropic property of the plane $x_2$ - $x_3$, the following constants are related

$$E_3 = E_2, \quad G_{13} = G_{12}, \quad \nu_{13} = \nu_{12} \tag{6.32}$$

$$G_{23} = \frac{E_2}{2(1 + \nu_{23})} \tag{6.33}$$

Therefore, for a transversely isotropic material, there are five independent constants

$$E_1, \quad E_2, \quad G_{12}, \quad \nu_{12}, \quad \nu_{23} \tag{6.34}$$

#### 6.2.1.5 Plane-stress condition of lamina

From assumption **a.4** we know that we require a laminate of three different layers. In the next Subsection 6.2.1.6 we will see how to consider three layers of laminas together to create a thin laminate. These are analysed based on plate theory, in which plane stress conditions are usually applied because the out-of-plane normal and both out-of-plane shear stresses are very small in comparison with the in-plane normal and shear stresses, and thus are negligible.

For a lamina under plane-stress condition, the further simplifications apply

$$\sigma_z = 0 \tag{6.35}$$

$$\tau_{yz} = 0 \tag{6.36}$$

$$\tau_{xz} = 0 \tag{6.37}$$

Therefore, the equilibrium equations from Equations (6.19) to (6.21) are reduced to Equations (6.19) and (6.20). As a result, the compliance matrix from Equation (6.26) is reduced to

$$\begin{Bmatrix} \epsilon_1 \\ \epsilon_2 \\ \gamma_{12} \end{Bmatrix} = \begin{bmatrix} S_{11} & S_{12} & S_{16} \\ S_{12} & S_{22} & S_{26} \\ S_{16} & S_{26} & S_{66} \end{bmatrix} \begin{Bmatrix} \sigma_1 \\ \sigma_2 \\ \tau_{12} \end{Bmatrix} \tag{6.38}$$

and similarly, the stress-strain relationships are obtained by inverting Equation (6.38), as

$$\begin{Bmatrix} \sigma_1 \\ \sigma_2 \\ \tau_{12} \end{Bmatrix} = \begin{bmatrix} Q_{11} & Q_{12} & Q_{16} \\ Q_{12} & Q_{22} & Q_{26} \\ Q_{16} & Q_{26} & Q_{66} \end{bmatrix} \begin{Bmatrix} \epsilon_1 \\ \epsilon_2 \\ \gamma_{12} \end{Bmatrix} \tag{6.39}$$

where $Q_{ij}$ denote the in-plane elements of the stiffness matrix. This relationship can be simplified by the following notation

$$\begin{Bmatrix} \sigma_1 \\ \sigma_2 \\ \tau_{xy} \end{Bmatrix} = [Q] \begin{Bmatrix} \epsilon_1 \\ \epsilon_2 \\ \gamma_{12} \end{Bmatrix} \tag{6.40}$$

After all these simplifications and by taking into account the condition of

$$\frac{\nu_{ij}}{E_i} = \frac{\nu_{ji}}{E_j} \tag{6.41}$$

the independent constants for the laminate are reduced to four

$$E_1, \quad E_2, \quad G_{12}, \quad \nu_{12} \tag{6.42}$$

For a transversely isotropic material, the elements of the stiffness matrix in engineering form are

$$[Q] = \begin{bmatrix} \frac{E_1}{D} & \frac{\nu_{12}E_2}{D} & 0 \\ \frac{\nu_{12}E_2}{D} & \frac{E_2}{D} & 0 \\ 0 & 0 & G_{12} \end{bmatrix} \tag{6.43}$$

where

$$D = 1 - \frac{E_2}{E_1}\nu_{12}^2 = 1 - \nu_{12}\nu_{21} \tag{6.44}$$

#### 6.2.1.6 Laminate

Figure 6.26 shows the laminate made up of 3 laminas. Each of these laminas has different properties. The laminate is unsymmetrical from the reference plane, which is the same as the midplane. Therefore, the neutral plane do not coincide with the reference plane. Due

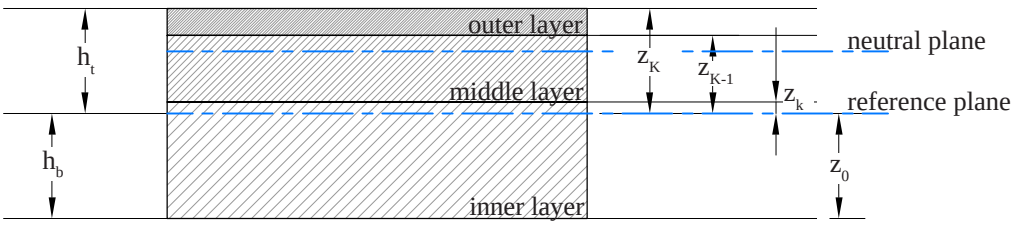


**Figure 6.26:** Reference and neutral plane of the laminate.

to this unsymmetrical layup, the strains at the reference plane are not zero. As a result, the normal and shear strains are

$$\epsilon_x^\circ = \frac{\partial u^\circ}{\partial x}, \quad \epsilon_y^\circ = \frac{\partial v^\circ}{\partial y}, \quad \gamma_{xy}^\circ = \frac{\partial u^\circ}{\partial y} + \frac{\partial v^\circ}{\partial x} \tag{6.45}$$

where $u$ and $v$ refer to the displacements in the $x$ and $y$ directions and the superscript $\circ$ denotes the reference plane. Similarly, assuming small deflections and that normals to the reference surface remains normal and also straight, the angle of rotations taken from the normals at the reference plane as shown in Figure 6.27 is

$$\chi_{xz} = \frac{\partial w^\circ}{\partial x} \tag{6.46}$$

where $w^\circ$ refers to the displacement out of the plane as depicted in Figure 6.27. Thus, the total displacement is

$$u = u^\circ - z\chi_{xz} = u^\circ - z\frac{\partial w^\circ}{\partial x} \tag{6.47}$$

Similarly, for the $y$ direction, we have

$$v = v^\circ - z\frac{\partial w^\circ}{\partial y} \tag{6.48}$$

Furthermore, by substituting Equations (6.47) and (6.48) into Equations (6.11), (6.12) and (6.16) we obtain

$$\epsilon_x = \frac{\partial u^\circ}{\partial x} - z\frac{\partial^2 w^\circ}{\partial x^2} \tag{6.49}$$

$$\epsilon_y = \frac{\partial v^\circ}{\partial y} - z\frac{\partial^2 w^\circ}{\partial y^2} \tag{6.50}$$

$$\gamma_{xy} = \frac{\partial u^\circ}{\partial y} + \frac{\partial v^\circ}{\partial x} - z\frac{2\partial^2 w^\circ}{\partial x \partial y} \tag{6.51}$$

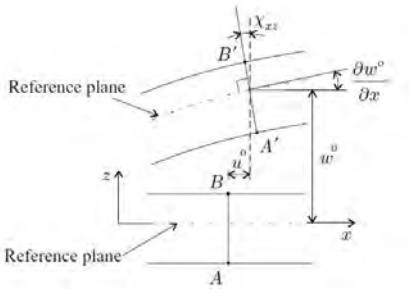


**Figure 6.27:** Deformations of the laminate at the reference plane (Kollar and Springer, 2003).

where the ratio in the last term of the right hand side of these equations correspond to the curvatures $\kappa_x$, $\kappa_y$ and $\kappa_{xy}$ for the reference plane. In matrix form, we have

$$\begin{Bmatrix} \epsilon_x \\ \epsilon_y \\ \gamma_{xy} \end{Bmatrix} = \begin{Bmatrix} \epsilon_x^\circ \\ \epsilon_y^\circ \\ \gamma_{xy}^\circ \end{Bmatrix} + z \begin{Bmatrix} \kappa_x \\ \kappa_y \\ \kappa_{xy} \end{Bmatrix} \tag{6.52}$$

The laminate stiffness matrices are characterised by the matrices $[A]$, $[B]$ and $[D]$, as

$$\begin{bmatrix} A_{11} & A_{12} & 0 \\ A_{12} & A_{22} & 0 \\ 0 & 0 & A_{66} \end{bmatrix}, \quad \begin{bmatrix} B_{11} & B_{12} & 0 \\ B_{12} & B_{22} & 0 \\ 0 & 0 & B_{66} \end{bmatrix}, \quad \begin{bmatrix} D_{11} & D_{12} & 0 \\ D_{12} & D_{22} & 0 \\ 0 & 0 & D_{66} \end{bmatrix} \tag{6.53}$$

where

$$[A] = \int_{-h_b}^{h_t} [Q] dz, \quad [B] = \int_{-h_b}^{h_t} z[Q] dz, \quad [D] = \int_{-h_b}^{h_t} z^2[Q] dz \tag{6.54}$$

where the $-h_b$ and $h_t$ refers to the distance from the reference plane to the laminate surface (see Figure 6.26), $[Q]$ denotes the matrix of a single lamina, and $dz$ refer to the distances from the reference plane to the laminas surface. Therefore, the elements of each of these matrices are

$$A_{ij} = \int_{-h_b}^{h_t} Q_{ij} dz, \quad B_{ij} = \int_{-h_b}^{h_t} z Q_{ij} dz, \quad D_{ij} = \int_{-h_b}^{h_t} z^2 Q_{ij} dz \tag{6.55}$$

In addition, as $[Q]$ is constant through each lamina, Equation (6.55) can be replaced by summations as

$$A_{ij} = \sum_{k=1}^{K} (Q_{ij})_k (z_k - z_{k-1}) \tag{6.56}$$

$$B_{ij} = \frac{1}{2} \sum_{k=1}^{K} (Q_{ij})_k (z_k^2 - z_{k-1}^2) \tag{6.57}$$

$$D_{ij} = \frac{1}{3} \sum_{k=1}^{K} (Q_{ij})_k (z_k^3 - z_{k-1}^3) \tag{6.58}$$

where $K = 3$ and is the total number of layers in the laminate, $(Q_{ij})_k$ is the stiffness matrix of each lamina, and $z_k$ and $z_{k-1}$ are the distances from the reference plane to the furthest and closest surface of each layer respectively (see Figure 6.26).

Furthermore, the compliance and stiffness matrices are related as

$$\begin{bmatrix} \alpha_{11} & \alpha_{12} & 0 & \beta_{11} & \beta_{12} & 0 \\ \alpha_{12} & \alpha_{22} & 0 & \beta_{21} & \beta_{22} & 0 \\ 0 & 0 & \alpha_{66} & 0 & 0 & \beta_{66} \\ \beta_{11} & \beta_{21} & 0 & \delta_{11} & \delta_{12} & 0 \\ \beta_{12} & \beta_{22} & 0 & \delta_{12} & \delta_{22} & 0 \\ 0 & 0 & \beta_{66} & 0 & 0 & \delta_{66} \end{bmatrix} = \begin{bmatrix} A_{11} & A_{12} & 0 & B_{11} & B_{12} & 0 \\ A_{12} & A_{22} & 0 & B_{21} & B_{22} & 0 \\ 0 & 0 & A_{66} & 0 & 0 & B_{66} \\ B_{11} & B_{21} & 0 & D_{11} & D_{12} & 0 \\ B_{12} & B_{22} & 0 & D_{12} & D_{22} & 0 \\ 0 & 0 & B_{66} & 0 & 0 & D_{66} \end{bmatrix}^{-1} \tag{6.59}$$

The stiffness matrices are calculated at the reference plane. However, as the laminate is not symmetrical, these needs to be modified to take into account the neutral plane. The elements of the compliance matrices $[\alpha]$, $[\beta]$ and $[\delta]$ at the neutral plane are calculated as

$$\alpha_{ij}^{\varrho} = \alpha_{ij} + \varrho(\beta_{ij} + \beta_{ij}) + \varrho^2 \delta_{ij} \tag{6.60}$$

$$\beta_{ij}^{\varrho} = \beta_{ij} + \varrho \delta_{ij} \tag{6.61}$$

$$\delta_{ij}^{\varrho} = \delta_{ij} \tag{6.62}$$

where $\varrho$ is the distance between the reference plane and the neutral plane, and is obtained as

$$\hat{\varrho} = -\frac{\hat{\beta}_{11}^{MP}}{\hat{\delta}_{11}^{MP}} \tag{6.63}$$

where the $\hat{\beta}_{11}^{MP}$ and $\hat{\delta}_{11}^{MP}$ are calculated as

$$\hat{\beta}_{11}^{MP} = \left(\beta_{11} - \frac{\beta_{12}\delta_{12}}{\delta_{22}}\right) \tag{6.64}$$

$$\hat{\delta}_{11}^{MP} = \left(\delta_{11} - \frac{\delta_{12}^2}{\delta_{22}}\right) \tag{6.65}$$

#### 6.2.1.7 Beam

Finally, to calculate the bending stiffness $EI$ for a cross-section with orthotropic and unsymmetrical laminate, we have

$$\hat{EI}_{yy} = \hat{EI}_{zz} = \pi\left(R^3 \frac{1}{\alpha_{11}} + R\frac{1}{\delta_{11}}\right) \tag{6.66}$$

where, the $\alpha_{11}$ and $\delta_{11}$ are evaluated at the neutral plane $\tilde{\varrho}$ as

$$\tilde{\varrho} = -\frac{\beta_{11}^{MP}}{\delta_{11}^{MP}} \tag{6.67}$$

where $\beta_{11}^{MP}$ and $\delta_{11}^{MP}$ are elements of the compliance matrix evaluated at the midplane.

#### 6.2.1.8 Equivalent bending stiffness from composite model

In order to define the equivalent bending elastic modulus, Equation (6.66) is solved for $E$ by dividing the right hand side of the equation by the second moment of area for a thin cylinder as

$$I = \pi t R^3 \tag{6.68}$$

therefore,

$$E_{eq,c} = \frac{\hat{E} I_{yy}}{I} \tag{6.69}$$

#### 6.2.1.9 Sensitivity analysis of the input parameters

Sensitivity analysis was carried out to assess the impact of the input parameters in the composite material model. The parameters $v_b$, $D$, $t$, $E_1$, $E_2$, $G_{12}$ and $\rho_{12}$ were varied independently, and the variations in $E_{eq,c}$ were recorded. Table 6.6 presents the data used for the reference model, and the values were based on the literature. The fibre distribution was considered as presented in Figure 5.7. Table 6.7 presents the range of values used to vary each parameter, and the percentage difference measured of the impact of each of the parameters in the $E_{eq,c}$. Note that the only parameters that influence the results are $E_1$, $D$ and $t$ with $E_1$ influencing the results significantly. The impact of the rest of the parameters on $E_{eq,c}$ is not significant.

**Table 6.6:** Parameters of the reference model for sensitivity analysis

| parameter | value | units |
|---|---|---|
| $v_b$ | 0.40 | |
| Diameter, $D$ | 70 | mm |
| Thickness, $t$ | 8 | mm |
| $E_1$ | 16000 | N/mm$^2$ |
| $E_2$ | 398 | N/mm$^2$ |
| $G_{12}$ | 581 | N/mm$^2$ |
| $\nu_{12}$ | 0.30 | |

**Table 6.7:** Impact of parameters in the composite model

| | VF | D mm | t mm | $E_1$ N/mm$^2$ | $E_2$ N/mm$^2$ | $G_{12}$ N/mm$^2$ | $v_{12}$ |
|---|---|---|---|---|---|---|---|
| Lower bound | 0.20 | 30 | 3 | 3000 | 300 | 300 | 0.10 |
| Upper bound | 0.80 | 300 | 30 | 30000 | 3000 | 3000 | 0.50 |
| (%) diff | 5.86e-13 | 22.87 | 50.34 | 163.64 | 5.86e-13 | 0 | 5.86e-13 |

### 6.2.2 Bimodulus material model for bamboo

The model presented here assumes that the tensile and compressive behaviour of bamboo is different. See for example Figure 6.28, while there is a difference in the tensile and

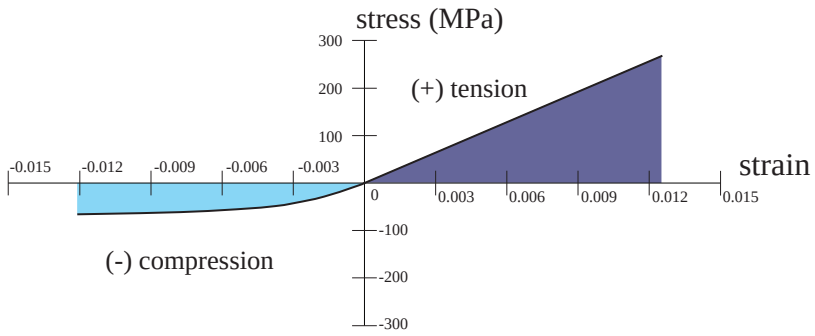


**Figure 6.28:** Stress-strain curve of bamboo in the compressive and tensile zones. The data plotted for the tensile quadrant was taken from the literature Arce-Villalobos (1993) and Shao et al. Shao et al. (2010). The curves from both references were graphically scaled and the plot showed in this graph corresponds to the average of these two. The data in the compressive quadrant is taken from Godina and Lorenzo (2015) and was presented in the preliminary tests.

compressive strengths, it is not clear whether the stiffness in tension and compression is the same. From the previous Subsection 6.1.3, and the data available in the literature (see Tables 2.4 and 2.5), we have that the flexural stiffness is usually higher than the compressive stiffness, and the flexural strength is significantly higher than the compressive strength. In this model, the differences in behaviour between a bamboo culm subjected to bending against one subjected to axial loads is attributed to the interaction between tension and compression occurring in the cross-section of bamboo under transverse loads, and to the high capacity of the fibres to sustain load.

In addition to the elastic modulus $E_{eq,b}$, this model is extended to analyse the maximum normal stresses (compressive $f_{c,m}$ and tensile $f_{t,m}$), and maximum shear stresses $f_{v,m}$, developed in the cross-section with the aim of identifying possible failure mechanisms.

The model is linear elastic and consists of an equivalent section to represent the bimodulus behaviour. The fundamental idea is that the stress-strain behaviour of bamboo, and hence the strength and stiffness, is different in tension and compression, therefore

$$E_t \neq E_c \tag{6.70}$$

and

$$\sigma_t \neq \sigma_c \tag{6.71}$$

It is considered that the fibres are the only constituent capable of carrying tensile loads. Therefore, we assume that the tensile forces are acting only on the area corresponding to the fibres. This area is equivalent to the volume fraction, as calculated in Equation (5.25). In addition, we take the elastic modulus of the fibre $E_f$ as the tensile elastic modulus $E_t$ to account for the reduction of area. The compressive loads are assumed to be acting on the whole area of the cross-section.

The neutral axis of a section made up with bi-modulus material do not coincide with the centroid axis. Figure 6.29 depicts the equivalent cross-section where the neutral axis is shifted from the centroid axis (see also Table 6.8). As it is considered to be a linear

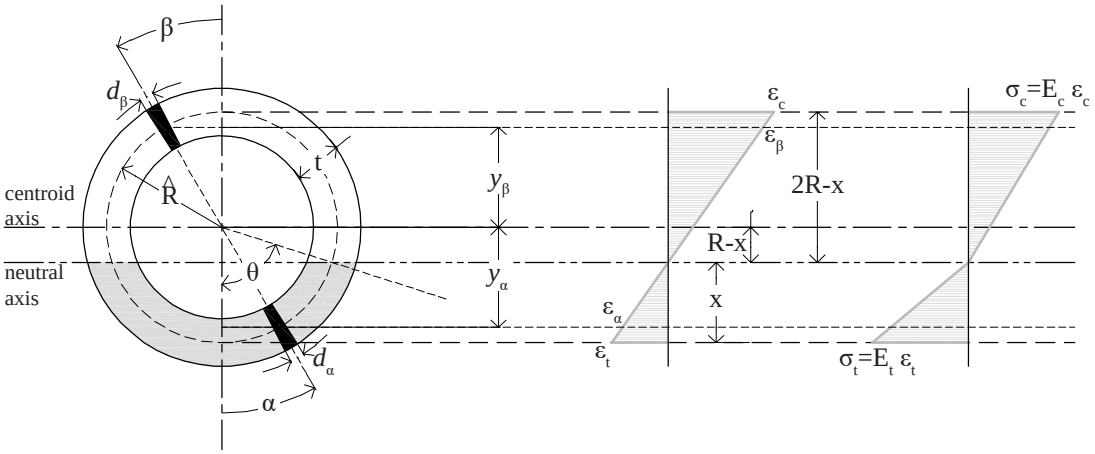


**Figure 6.29:** Notation and distribution of stress and strain in the cross-section.

**Table 6.8:** The cross-section properties and vertical distances of the equivalent section.

| Area, $A$ | Second moment of area, $I$ | Vertical distances, $y$ |
|---|---|---|
| $dA_t = t\hat{R}d_\alpha$ | $dI_t = y_\alpha^2 dA$ | $y_\alpha = \hat{R}\cos\alpha$ |
| $dA_c = t\hat{R}d_\beta$ | $dI_c = y_\beta^2 dA$ | $y_\beta = \hat{R}\cos\beta$ |
| $A = \int_0^{2\pi} t\hat{R}d_\alpha$ | $I = \int_0^{2\pi} \hat{R}^2\cos^2\alpha(t\hat{R}d_\alpha)$ | $x = \hat{R} - \hat{R}\cos\theta$ |
| $A = 2\pi\hat{R}t$ | $I = t\hat{R}^3\left[\frac{1}{2}(\alpha + \frac{\sin 2\alpha}{2})\right]_0^{2\pi}$ | $x = \hat{R}(1-\cos\theta)$ |
| | $I = \pi t\hat{R}^3$ | |

material, the strains vary linearly throughout the cross-section and are zero at the neutral axis. The tensile and compressive stresses at the bottom and top edge of the beam cross-section are not equal. However, they also vary linearly throughout the cross-section but only from the neutral axis.

Below the assumptions of the model are provided followed by a brief outline of the relevant equations to describe the compatibility of deformations, equilibrium conditions and bending moments, as well as the equations to estimate the equivalent bending stiffness. In addition, the equations to estimate the maximum bending and shear stresses developed in the cross-section are provided.

This model was developed by Dr. Rodolfo Lorenzo, and the full mathematical derivation is presented in Appendix C.

#### 6.2.2.1 Model assumptions

In accordance to the Euler-Bernoulli beam theory (Borg, 1962; MacLeod, 2005; Hibbeler, 2011; Young et al., 2012), the model assumes small deformations of the cross-section under the application of transverse loads, and that cross-sections remain plane and normal to the deformed axis after deformations. The cross-section is assumed to be that of a cylindrical tube (see Figure 6.29). The assumptions of the model are described below.

**b.1** The cross-section remains plane after deformation.

**b.2** The tensile and compressive elastic modulus of bamboo are different.

**b.3** The tensile forces are acting only in the area corresponding to the $v_f$.

**b.4** The elastic modulus of the fibre $E_f$ is considered as the tensile elastic modulus $E_t$.

**b.5** The shape of the cross-section is assumed to be that of a hollow circular tube.

#### 6.2.2.2 Compatibility of deformations

Assuming deformation compatibility and that the beam cross-section in Figure 6.29 is sagging, the maximum compressive and tensile strains at the top and bottom edge of the cross-section are proportional to the distance from the neutral axis

$$\frac{\epsilon_t}{x} = \frac{\epsilon_c}{2\hat{R} - x} \tag{6.72}$$

where $\epsilon_t$ and $\epsilon_c$ denote the tensile and compressive strains respectively, $x$ represents the distance from the neutral plane to the bottom edge of the beam cross-section, and $\hat{R}$ refers to the radius at the midplane of the cross-section thickness $t$ (refer to Figure 6.29 and Table 6.8). The respective tensile and compressive strains for a portion $d_\alpha$ and $d_\beta$ are

$$\epsilon_\alpha = \frac{\epsilon_t\Big[\hat{R}(\cos\alpha - 1) + x\Big]}{x} \tag{6.73}$$

$$\epsilon_\beta = \frac{\epsilon_t\Big[\hat{R}(\cos\beta + 1) - x\Big]}{x} \tag{6.74}$$

#### 6.2.2.3 Equilibrium conditions

To satisfy the equilibrium conditions, the tensile and compressive forces acting in the cross-section are equated

$$F_t = F_c \tag{6.75}$$

and according to Hooke's law for a linear elastic material, the tensile forces acting in the cross-section area located below the neutral axis are

$$F_t = \frac{2E_t\epsilon_t}{x} t\hat{R}[(x - \hat{R})\theta + \hat{R}\sin\theta] \tag{6.76}$$

To obtain the compressive forces as a function of the tensile elastic modulus $E_t$ and tensile strain $\epsilon_t$, the ratio of compressive elastic modulus $E_c$ to tensile elastic modulus $E_t$ is introduced as

$$n = \frac{E_c}{E_t} \tag{6.77}$$

Therefore, the compressive forces acting in the cross-section area located above the neutral axis are

$$F_c = \frac{2nE_t\epsilon_t}{x} t\hat{R}[(\hat{R} - x)(\pi - \theta) + \hat{R}\sin\theta] \tag{6.78}$$

Now substituting Equations (6.76) and (6.78) into Equation (6.75), setting the equation to zero, and after further simplifications we have

$$(1-n)[(x-\hat{R})\theta+\hat{R}\sin\theta]+n\pi(x-\hat{R})=0 \tag{6.79}$$

Solving Equation (6.79) gives the vertical position $x$, and the angle $\theta$ that defines the position of the neutral axis in the cross-section.

#### 6.2.2.4 Bending moments

The internal moments acting in the cross-section correspond to the sum of the moments on the tensile and compressive zones as

$$M=M_\alpha+M_\beta \tag{6.80}$$

where

$$M_\alpha=\frac{2E_t\epsilon_t}{x}t\hat{R}^2\Big[(x-\hat{R})\sin\theta+\frac{\hat{R}}{2}\Big(\theta+\frac{\sin 2\theta}{2}\Big)\Big] \tag{6.81}$$

$$M_\beta=\frac{2nE_t\epsilon_t}{x}t\hat{R}^2\left[(\hat{R}-x)\sin\theta+\frac{\hat{R}}{2}\Big[(\pi-\theta)+\frac{\sin 2\theta}{2}\Big]\right] \tag{6.82}$$

Now, substituting Equations (6.81) and (6.82) into Equation (6.80) and simplifying and cancelling out equal terms at both sides of the equation, we have

$$M=\frac{E_t\epsilon_t t\hat{R}^2}{x}\left[(1-n)\hat{R}\theta+2(1-n)(x-\hat{R})\sin\theta+\frac{1}{2}(1-n)\hat{R}\sin 2\theta+n\pi\hat{R}\right] \tag{6.83}$$

#### 6.2.2.5 Equivalent bending stiffness of the bimodulus model

The flexural stiffness is estimated from the moment curvature relationship of the general bending theory. Considering the bending governing equation, the strains of the beam cross-section at the distance $x$ from the neutral axis, and solving for $EI$ we have

$$EI=\frac{M}{\epsilon_t/x} \tag{6.84}$$

Substituting Equations (6.83), (6.73) and $x$ from Table 6.8 into Equation (6.84), we have

$$EI=E_t t\hat{R}^2\Big[(1-n)\hat{R}\theta+2(1-n)(x-\hat{R})\sin\theta+\frac{1}{2}(1-n)\hat{R}\sin 2\theta+n\pi\hat{R}\Big] \tag{6.85}$$

To estimate the equivalent bending elastic modulus $E_{eq,b}$ as a ratio of $E_c$, Equation (6.68) is substituted into Equation (6.85) and the right hand side of the equation is multiplied by the inverse of ratio $E_c$ to $E_t$ as in Equation (6.77), and after rearranging and

simplifying we have

$$\frac{E_{eq,b}}{E_c} = \frac{1}{\pi n \hat{R}}\Big[(1-n)[\hat{R}\theta + 2(x-\hat{R})\sin\theta + 1/2\hat{R}\sin 2\theta]\Big] + 1 \tag{6.86}$$

From assumption **b.3**, we have that the tensile forces are acting only in the area corresponding to the $\mathrm{v}_f$ of the cross-section calculated from Section 5.3 as in Equation (5.25). Then, the area for an element in the tensile zone is multiplied by the $\mathrm{v}_f$ as

$$dA_t = \mathrm{v}_f t \hat{R} d_\alpha \tag{6.87}$$

Therefore, the term $(1-n)$ is replaced by $(\mathrm{v}_f - n)$ in all the equations.

The equivalent bending stiffness $E_{eq,b}$ is obtained by multiplying Equation (6.86) by the compressive elastic modulus as

$$E_{eq,b} = \frac{E_{eq,b}}{E_c} E_c \tag{6.88}$$

#### 6.2.2.6 Bending stresses

Next, the maximum normal stresses at the top and bottom edge of the beam cross-section are calculated. According to Hooke's law

$$\sigma_t = E_t \epsilon_t \tag{6.89}$$

In order to substitute $E_t$ and $\epsilon_t$ into Equation (6.89), we rearrange Equation (6.83) to solve for $E_t$, and Equation (6.73) to solve for $\epsilon_t$, and after simplifying and multiplying both sides of the equation by $t$ and dividing both sides of the equation by $M$ we have

$$\frac{t\sigma_t}{M} = \frac{tE_t\epsilon_t}{M} = \frac{x}{\hat{R}}K \tag{6.90}$$

where

$$K = \left[\frac{1}{\hat{R}\Big[(\mathrm{v}_f - n)[\hat{R}\theta + 2(x-\hat{R})\sin\theta + \frac{1}{2}\hat{R}\sin 2\theta] + n\pi\hat{R}\Big]}\right] \tag{6.91}$$

Similar relationships can be obtained for the maximum tensile and compressive stresses located at $\gamma = 0°$ and $\gamma = 180°$ respectively (see Figure 6.30) and are given by

$$\frac{t\sigma_\alpha}{M} = \frac{\hat{R}(\cos\gamma - 1) + x}{\hat{R}}K \tag{6.92}$$

$$\frac{t\sigma_\beta}{M} = \frac{n\Big[\hat{R}[\cos(\pi-\gamma)+1] - x\Big]}{\hat{R}}K \tag{6.93}$$

Using Equations (6.92) and (6.93) and solving for the tensile bending stresses $\sigma_\alpha$ (for

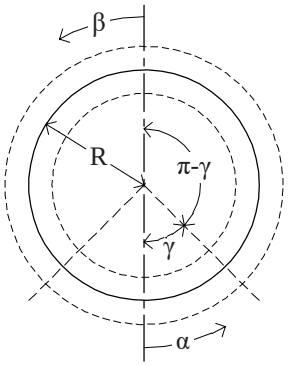


**Figure 6.30:** Location for calculating bending stresses in the cross-section.

$\gamma \leq \theta$) , and the compressive bending stresses $\sigma_\beta$ (for $\gamma > \theta$) we have

$$\sigma_\alpha = \frac{t\sigma_\alpha}{M}\frac{M}{t} \tag{6.94}$$

$$\sigma_\beta = \frac{t\sigma_\beta}{M}\frac{M}{t} \tag{6.95}$$

#### 6.2.2.7 Horizontal force equilibrium

Assuming a small element in equilibrium of length $\Delta z$ and subjected to a force $\Delta F_t$ as shown in Figure 6.31, the forces satisfy

$$\Delta F_t = F_{tB} - F_{tA} \tag{6.96}$$

From Equation (6.76) we can calculate the tensile forces (for $\gamma \leq \theta$ ), and dividing both sides of the Equation (6.76) by the moment from Equation (6.83), and simplifying we have

$$\frac{F_t}{M} = \Big[2\mathrm{v}_f[(x-\hat{R})\gamma + \hat{R}\sin\gamma]\Big]K \tag{6.97}$$

Similarly, dividing each of the terms of the right hand side of Equation (6.96) by the

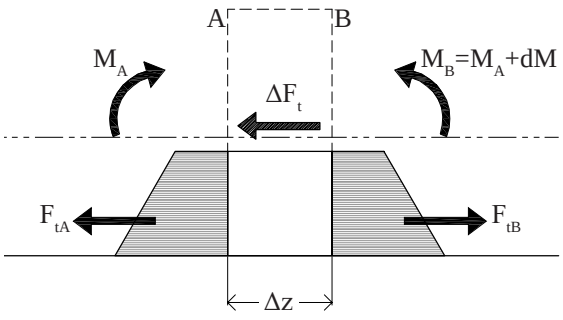


**Figure 6.31:** Horizontal forces in the beam cross-section.

moment, solving for each and substituting into Equation (6.96) we have

$$\Delta F_t = \frac{F_{tB}}{M_B} M_B - \frac{F_{tA}}{M_A} M_A = \frac{F_t}{M}(M_B - M_A) \tag{6.98}$$

where

$$M_B - M_A = \frac{dM}{dz}\Delta z \tag{6.99}$$

Note that the right hand side of the equation is the internal (vertical) shear force $V$, and $dz$ is the length of the infinitesimal element represented in Figure 6.31, thus

$$V = \frac{dM}{dz} \tag{6.100}$$

Now substituting Equation 6.100 into Equation (6.98) we have

$$\Delta F_t = \frac{F_t}{M} V \Delta z \tag{6.101}$$

By definition, the shear flow is the force per unit length in the longitudinal direction of the beam, therefore

$$q = \frac{\Delta F_t}{\Delta z} \tag{6.102}$$

Now, by substituting Equation (6.101) into Equation (6.102) we have

$$q = \frac{F_t}{M} V \tag{6.103}$$

The shear stresses can be calculated as a function of the shear flow as

$$\tau = \frac{q}{t} \tag{6.104}$$

The maximum shear stresses at the neutral plane are calculated by substituting Equation (6.103) into Equation (6.104) as

$$\tau = \frac{F_t}{M}\frac{V}{t} \tag{6.105}$$

#### 6.2.2.8 Calibration of the input parameters for the model

The input parameters for the bimodulus model are $E_c$, $E_t$, $\mathrm{v}_f$, diameter and thickness. The geometric properties are obtained as described in Chapter 4, $\mathrm{v}_f$ is calculated by image analysis as described in Section 5.3, and $E_c$ is obtained through mechanical testing. In this methodology, $E_t$ is estimated for each of the species used and the rationale is explained below.

The longitudinal modulus of elasticity of the fibres cell wall has been found to be constant in the radial direction of the culm wall (Yu et al., 2007). This property is highly dependent on the microfibril angle which was also found to be constant, about 9° for several samples taken at different heights (Yu et al., 2007). This suggests that the mechanical

properties of the fibre do not change within a culm. In this study, we assume that the $E_f$ is constant across and along the culm. The value of $E_f$ measured from tensile tests has been reported as $E_f$= 46,000 N/mm$^2$ (Amada et al., 1996, 1997).

The tensile elastic modulus for each of the species was estimated by minimising the different values between $E_b$ and $E_{eq,b}$ as

$$\text{Minimise:} \quad f(E_f) = \frac{1}{N}\sum_{i=1}^{N}\left|1 - E_{eq,b_i}/E_{b_i}\right| \tag{6.106}$$

where $i$ refers to the index of summation, and $N$ is the upper limit of the summation which is equal to the total number of bamboo culms for the species investigated. The $E_f$ (considered as $E_t$ in the bimodulus model) is related to $E_{eq,b}$ in the bimodulus model (refer to Equation (6.85)). The estimation of the fibre stiffness is carried out iteratively, by updating each time the equilibrium using Equation (6.79) to determine $E_{eq,b}$, until the right hand side of Equation (6.106) is constant. Recall from assumption **b.4** that the tensile elastic modulus is taken as the fibre elastic modulus, thus

$$E_t = E_f \tag{6.107}$$

### 6.2.3 Test methods

The developed models presented in Subsections 6.2.1 and 6.2.2 require experimental input obtained through small sample testing. The properties to measure are the elastic compressive modulus $E_c$, density $\rho$, and moisture content $w$. In addition to these, the volume fraction and its radial distribution across the culm wall thickness are quantified and used as input for the material models. Finally, the axial compressive strength $f_c$, and shear strength $f_v$ are determined to investigate if these properties can be used as indicators to predict the failure of bamboo in bending. Note that the physical properties are also included given the dependence of the mechanical response of bamboo on its hygroscopic properties and the microstructure of the material.

Figure 6.32 shows the flowchart of the processes required for determining the physical and mechanical properties for the SBD. The process starts after collecting the end sections for each of the culms, from which two coupons per property are fabricated for each section (see Figure 6.33). The end sections are approximately 500 mm in length and contain at least one node. From these, the samples are fabricated based on the required material properties. Two fabrication methods for these small coupons were explored and are presented in Appendix D. The first consists of a manual method, to gain confidence in cutting the material and the second method is based on automated fabrication.

To minimise the number of samples required, we calculate the density and volume fraction from the test samples for compressive strength. Therefore, in total only three different types of samples are required, one for each of the mechanical properties tested (see Figure 6.32). Once the samples are fabricated, the images for volume fraction analysis

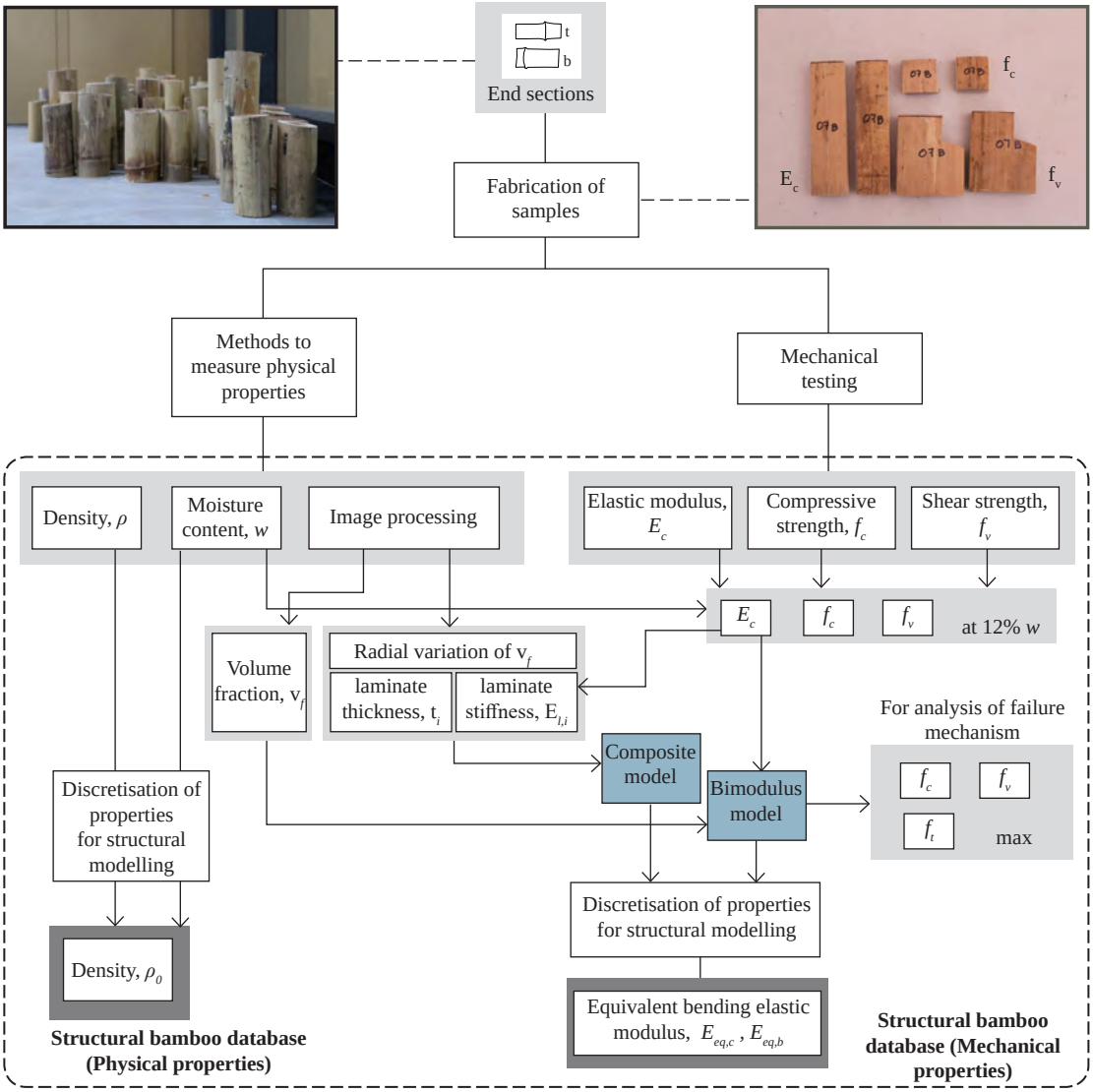


**Figure 6.32:** Flowchart of the methodology for determination of physical and mechanical properties for the SBD.

are taken, and the density is determined. The moisture content for each of the samples is measured right after the mechanical testing, and it is used for the correction of these properties to 12 % moisture content so that all the values are calibrated to the same moisture content.

The tests to determine ($E_c$, $f_c$ and $f_v$) are carried out according to JG/T-199 (2007). The test methods were described in Subsection 6.1.2. For $E_c$, an axial clip-on gauge extensometer of 10 mm gauge length was used to measure the strains. The readings are the same as for the strain gauges; however the axial clip-on gauge minimises costs and eliminates the time required for the installation of the strain gauges. A special jig was fabricated for the measurement of $f_v$; it was designed based on simple drawings provided in JG/T-199 (2007) (see Figure 6.17b).

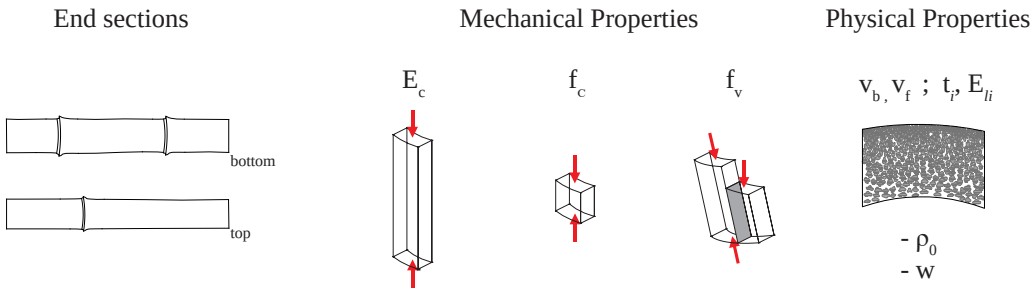


**Figure 6.33:** Physical and mechanical properties determined from small coupons taken from bamboo end sections.

#### 6.2.3.1 Correction factors for moisture content

The $E_c$, $f_c$ and $f_v$ were adjusted to the 12 % moisture content according to the standard JG/T-199 (2007) as

$$K_{E_c,w} = \frac{1}{0.89 + 0.36e^{-0.1w}} \tag{6.108}$$

$$K_{f_c,w} = \frac{1}{0.79 + 1.5e^{-0.16w}} \tag{6.109}$$

$$K_{f_v,w} = \frac{1}{0.67 + 0.77e^{-0.07w}} \tag{6.110}$$

where $K_{E_c,w}$, $K_{f_c,w}$ and $K_{f_v,w}$ are the correction factors for the elastic modulus, compressive strength and shear strength respectively. These equations are applicable for tested samples with moisture content between 5 and 30%. The influence that moisture content has in each of these properties is depicted in Figure 6.34. It is evident that the compressive strength $f_c$ is the most affected by moisture content, followed by the shear strength $f_v$.

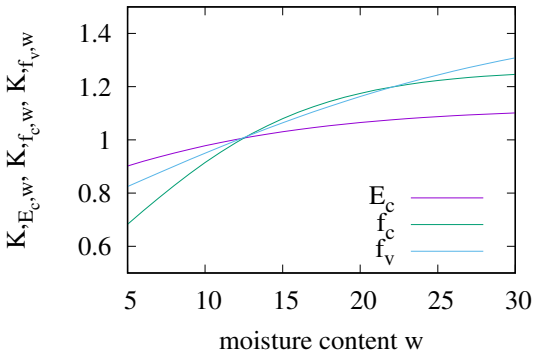


**Figure 6.34:** Influence of moisture content on mechanical properties for small coupons.

#### 6.2.3.2 Tolerances of samples

One of the most important aspects of the fabrication of the samples are the tolerances. The dimensional tolerances defined by the JG/T-199 (2007) for small coupons are depicted in Figure 6.35. These were measured with a vernier of 0.01 mm accuracy.

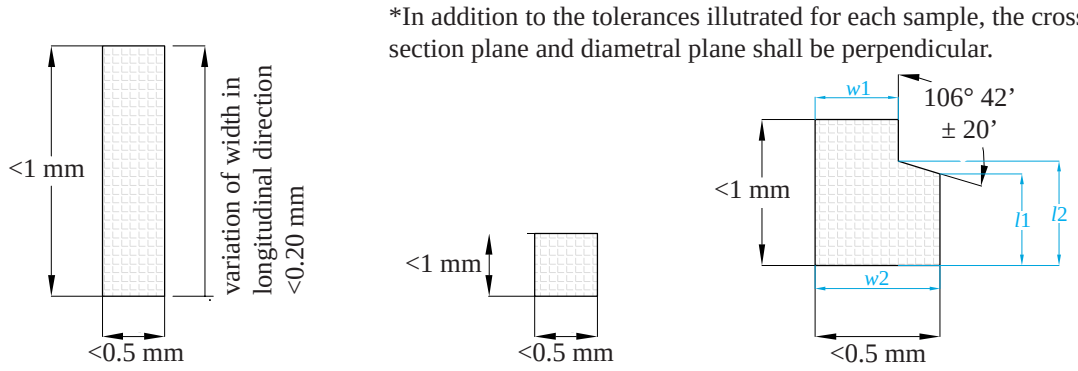


**Figure 6.35:** Tolerances for the small coupons as specified in the standard JG/T-199 (2007).

The angle of the tilted plane for the shear sample was calculated using the Equation (6.111) derived from the available measurements (for nomenclature of dimensions of shear sample Figure 6.35) as

$$\zeta = \arctan\left(\frac{l_2 - l_1}{w_2 - w_1}\right) \tag{6.111}$$

In addition, a flexible aluminium sheet with the shape of the shear sample was fabricated to visually evaluate the cut of the tilted plane just after fabrication.

### 6.2.4 Summary

This section outlined the methodology for determining the mechanical properties of bamboo culms. It provides two material models for the estimation of the equivalent bending elastic modulus from small coupons subjected to axial compressive loads. The next section will present a series of experimental tests to compare the results obtained from this methodology against results determined from full culm bending tests.

## 6.3 Experimental programme for the validation of the methodology

This section presents an experimental programme for the validation of the methodology described in the previous Section 6.2. This is done by comparing the results of the mechanical properties obtained through small coupon testing and the material models against the results obtained from full culm tests.

### 6.3.1 Materials

Two different species were used, guadua (*Guadua angustifolia Kunth*), and oldhamii (*Bambusa oldhamii*).

The experimental programme for determination of flexural properties of full culms, was carried out by different researchers following their own research methods, but they both were based on the ISO (2004b) standard. Guadua culms were tested at Coventry University and oldhamii bamboos at UNAM. The test details and set up for the guadua species are available in Trujillo et al. (2017).

#### 6.3.1.1 Guadua

The end sections for guadua, were obtained from Coventry University after the culms were subjected to transverse loads for the determination of flexural properties (Trujillo et al., 2017; Trujillo and Jangra, 2016). These culms were obtained from Caicedonia, Colombia (Trujillo et al., 2017). The culms were dried and of age between 2 to 5 years. They had a perforation in the node, which is usually done while leaching bamboos, a preservation process that consists of submerging bamboo culms in water, usually containing a chemical treatment such as boric acid and borax. The total length of the culms was about 12 m, and culms were cut into three samples of about 4 m in length. About 200 culms were tested in full scale under transverse loads. From these, 30 culms whose failure was classified as failure by bending rather than by shear were selected (Trujillo et al., 2017). End sections of about 450 mm in length from both ends were collected from each culm. The 60 sections were transported to UCL, where they were stored in a laboratory for approximately 8 months. During that time the moisture content of the pieces decreased on average from 12% at the time of the full culm bending test to 7.5% at the time of the fabrication of the small samples for testing. The average diameter of the culms was 92 mm.

The samples were fabricated from a total of 47 sections. Some of the sections were damaged, and therefore fabrication of the samples using this method was not possible. In addition, there were 5 bamboo culms from which no data was recorded from the full culm tests for the calculation of the elastic modulus, and one from which no bending strength was recorded. Therefore, the physical and mechanical properties as described from the SBD (refer to Subsection 6.2.3) were collected for a total of 13 bamboo culms including bottom and top. In total, 89 $E_c$ coupons, 94 $f_c$ and $f_v$ samples, and images from 93 samples for volume fraction analysis were prepared and tested.

#### 6.3.1.2 Oldhamii

The experimental tests carried out with oldhamii bamboo were taken from the same batch described in Chapter 4 for determining the geometrical properties. In addition to these, 15 oldhamii bamboos obtained from the same distributor were tested under transverse loads at the National Autonomous University of Mexico UNAM, under the research of Dr. Magdalena Trujillo. From these culms, a total of 9 culms were selected just after the

bending tests were carried out for cutting of the end sections and start the preparation for the fabrication of the samples. The small coupons were obtained from a total of 68 end sections (18 end sections were from the culms tested in bending and 50 end sections from the culms described in Chapter 4). The total number of samples was 148 coupons for $E_c$, $f_c$ and $f_v$, and images from 100 samples for volume fraction analysis. The samples were fabricated at UNAM and tested at UCL.

#### 6.3.1.3 Fabrication of samples and tolerances

The tolerances of the samples for the guadua and oldhamii bamboos are provided in Tables 6.9 and 6.10. These were fabricated according to the methods described in Appendix D.

Overall, the out-of-tolerance in length for all the samples was negligible. The maximum out-of-tolerance was in the compressive strength samples with the manual fabrication method with approximately 0.3 mm off. However, this dimension was probably taken by the kerf (width of the removed material) as the thickness of the blade was 0.5 mm.

On average the out-of-tolerance for the width of the samples was between 0.13 and 0.56 mm for the manual method and between 0.34 and 0.94 mm for the automated method. During the manual cutting, it was observed that low clamping force allows the culm to rotate by the force applied with the japanese saw during cutting. In contrast, with a high clamping force, the blade was jammed between the culm wall during longitudinal cuts. However, for the automated method, this can be attributed to the calibration of the set-up, vibrations occurring during cutting or the tolerances due to the milling bit used.

The most critical measurement was the angle for the shear strength sample. The out-of-tolerance was measured using Equation 6.111 derived from the available measurements to achieve ±20'. An aluminium sheet with the shape of the shear sample was used for the visual assessment of the tilted planes.

After fabrication, the samples with dimensions out-of-tolerances were sanded to achieve the required standards. A total of 5 $E_c$ samples from the guadua species were discarded as the width of the sample was out-of-tolerance and the extensometer could not be properly installed. Nevertheless, from these series of tests, we can conclude that it is not advisable to sand the samples as this can introduce uneven surfaces. Some of the samples were sanded in order to prepare the cross-section for image analysis, or in order to achieve tolerances. However, it is crucial that the end sections are flat, in particular for the $E_c$ and $\sigma_c$. As seen in the previous Subsection 6.1.1, the $E_c$ sample is very sensitive to the applied loads. Therefore, having a non-flat or curved surface can be detrimental to the tests, because the steel plate will not make full contact with the entire cross-section of the sample. In similar manner, for the $f_c$, if the samples are not flat the steel plate will not make contact with the sample. This can lead to rotation of the sample due to instabilities or delamination due to the concentration of stresses on one side of the sample.

**Table 6.9:** Tolerances of samples for guadua species fabricated with the automated method.

| property | dimension | units | differences in dimensions | | Percentage of samples of out tolerance |
|---|---|---|---|---|---|
| | | | (avg) | (std) | |
| $E_c$ | l | (mm) | 0.3 | 0.15 | 0 |
| | w | (mm) | 0.28 | 0.19 | 14.5 |
| | w (var) | (mm) | 0.13 | 0.17 | 16.9 |
| $f_c$ | l | (mm) | 0.28 | 0.17 | 0 |
| | w | (mm) | 0.25 | 0.15 | 6.4 |
| $f_v$ | l | (mm) | 0.34 | 0.4 | 1.1 |
| | w | (mm) | 0.56 | 0.9 | 43.6 |
| | angle | (deg) | 2.23 | 2.64 | 92.6 |

**Table 6.10:** Tolerances of samples for oldhamii species fabricated manually.

| property | dimension | units | differences in dimensions | | Percentage of samples of out tolerance |
|---|---|---|---|---|---|
| | | | (avg) | (std) | |
| $E_c$ | l | (mm) | 0.76 | 3.33 | 1.2 |
| | w | (mm) | 0.94 | 2.91 | 23.6 |
| | w (var) | (mm) | 0.34 | 0.37 | 51.4 |
| $f_c$ | l | (mm) | 0.31 | 0.26 | 2.1 |
| | w | (mm) | 0.46 | 0.41 | 32.4 |
| $f_v$ | l | (mm) | 0.33 | 0.26 | 1.4 |
| | w | (mm) | 0.56 | 0.45 | 45.1 |
| | angle | (deg) | 2.35 | 1.84 | 91.6 |

### 6.3.2 Results and discussion

#### 6.3.2.1 Geometrical properties of culms subjected to transverse loads

In general, the dimensions for both species tend to decrease towards the top of the culm. The diameter, thickness and shape factor are provided in Appendix E. The inherent geometric variability is evident. For some guadua culms, the variation in diameter was observed to be very small, null or even opposite to what was expected, similar to the diameters in the oldhamii samples in Subsection 4.3.2. Again, this is in contrast with the general assumption that these properties decrease with height (10% of the guadua culms have higher diameter at the top). For the oldhamii bamboo tested in bending only the average diameter was available. Interestingly, unlike the oldhamii species presented in Chapter 4, some guadua bamboos show a slight decrease in $\Phi$ towards the top of the culm. This means that although the thickness and diameter decrease in size towards the top, the bamboo becomes thicker in proportions. However, it is important to mention that some guadua culms have their nodes at the ends, which influence the measurements in diameter but mostly in thickness.

The change in thickness under and above the intranode is very high for some culms, particularly of the guadua species. It has been previously reported that the variation in thickness along the culm is higher at the bottom (Grosser and Liese, 1971). Figure 6.36, shows a cross-section corresponding to the bottom part of one culm of the guadua species. The thickness at internode changes abruptly under and above the intranode. The

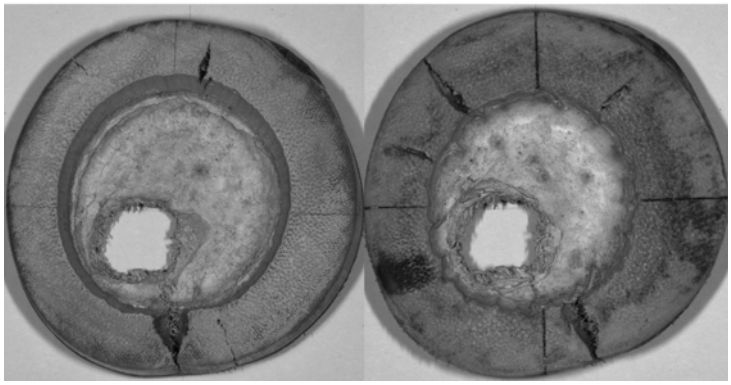

**Figure 6.36:** Cross-section of the bottom and top part of the intranode for a guadua bamboo.

difference in thickness is 4.1 mm in average over a length of only 46 mm. This can impact the results (i.e. bending elastic modulus and strength) when extrapolating the thickness from bottom to top or averaging the dimensions. It was noted that the thickness measured from the small coupons taken from the end sections differed considerably from those taken from the full culm. In Figure 10 (refer to Appendix E), the maximum thickness is 23.5 mm, whereas the maximum thickness measured from small coupons was 10.2 mm. This shows the abrupt change of thickness from one internode to another, and highlights the need to investigate the pattern of variation along the culm, and to establish specific locations for measurements. It is crucial that for all future tests, the dimensions are taken from the middle part of the internode when possible, avoiding measurements close to the node.

#### 6.3.2.2 Volume fraction

Representative images used for measurement of the volume fraction $v_b$ are presented in Figure 6.37 for both species. The images belong to samples at the bottom part of the

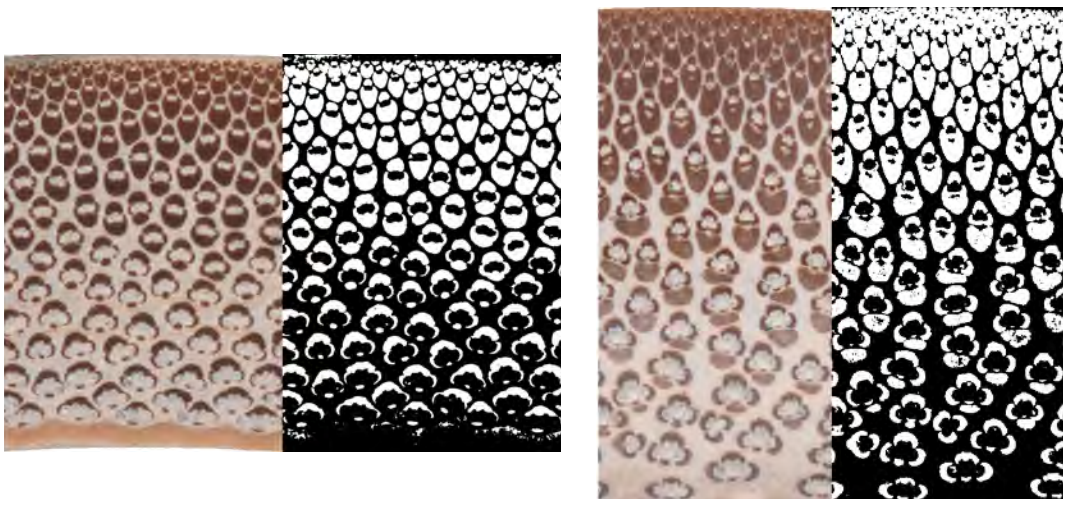

(a) (b)

**Figure 6.37:** Volume fraction $v_b$ analysis for (a) guadua, and (b) oldhamii species.

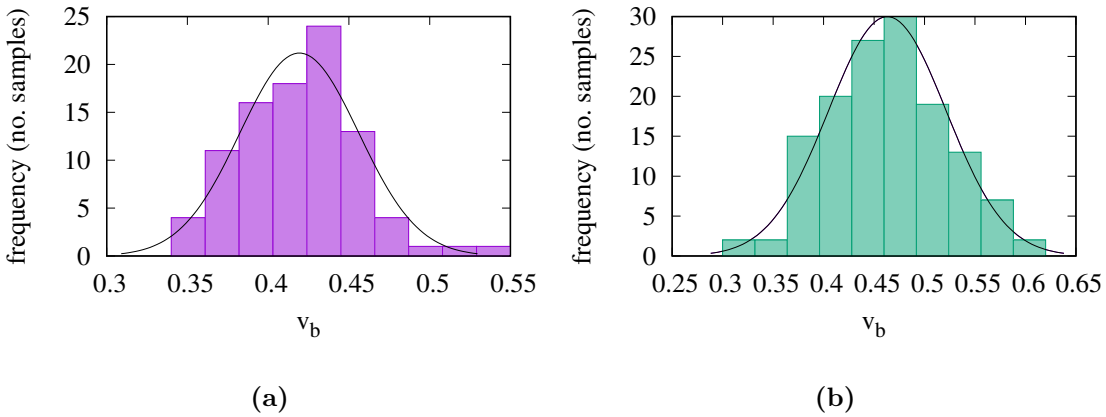


**Figure 6.38:** Frequency distribution of $v_b$ for the (a) guadua and (b) oldhamii species.

culm. The inner and outer layers of the culm are more pronounced for the guadua species. For oldhamii species these layers are almost absent, similar to the moso species presented in Subsection 5.3. Both species show an increase of fibres at the outer side of the culm. Overall, the oldhamii species have a higher volume fraction. Figure 6.38 shows the frequency distributions of $v_b$ for both species. Appendix F provides the mean, standard deviation and coefficient of variation for both species.

#### 6.3.2.3 Small coupons

Figure 6.39 depicts the typical stress-strain curve for determining $E_c$ and the load-displacement curves for $f_c$ and $f_v$. The compression behaviour is similar to that described previously for the elastic regime and until failure respectively (see Subsection 6.1.2). The load-displacement curve from the shear tests (see Figure 6.39c) shows a softer behaviour followed by a linear response and a brittle failure. The initial softer behaviour was associated with the loading plate adjusting to the specimen.

The results (mean, standard deviation and coefficient of variation) of the small coupons from the bottom and top are provided in Appendix F. In general, no strong differences were found between the bottom and top for all the mechanical properties tested. This shows that there are no significant changes of values in mechanical properties over a length of 4 and 5 metres for the guadua and oldhamii species respectively. The physical properties ($v_b$ and $\rho$) were constant along the culm for the guadua species, whereas for the oldhamii species $v_b$ increases by 11% and $\rho$ increases by 8% towards the top. We know that the pattern of variation can be different for different species (Chung and Yu, 2002). For the guadua species, Correal and Arbeláez (2010) reported almost constant values for the compressive and bending stiffness, and compressive and shear strength over culm lengths between 20 to 30 metres. However, they reported an increase of density and modulus of rupture, around 15 and 17% respectively, over the same length. For the oldhamii species, no data reporting the longitudinal variations was found in the literature.

The frequency distribution of $E_c$, $f_c$ and $f_v$ for both species is shown from Figures 6.40

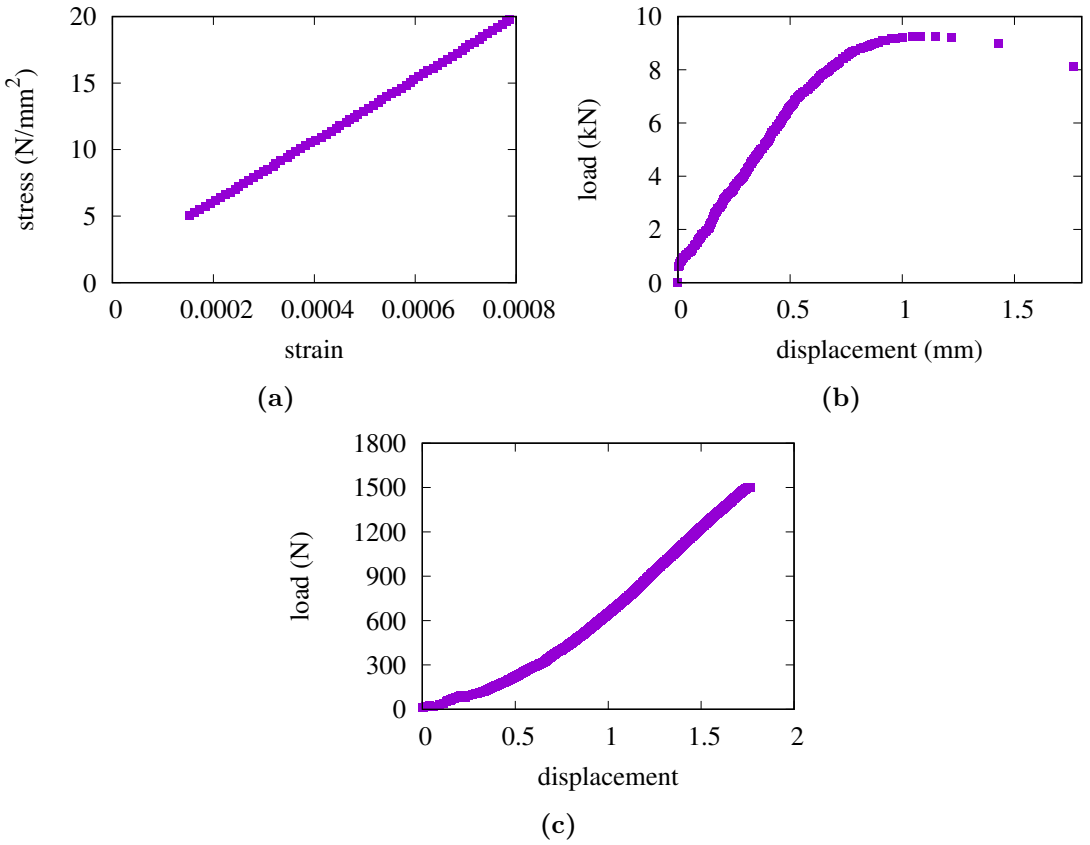


**Figure 6.39:** (a) Typical stress-strain curve for determining $E_c$. Typical load-deflection curve for determining (b) $f_c$ and (c) $f_v$.

to 6.42. The oldhamii species presented higher values for all the mechanical properties studied. The data corresponds to the values from all the small coupons tested corrected to 12 % moisture content (see Equations from (6.108) to (6.110)). The average moisture content measured for guadua and oldhamii was of 8.0 and 8.2% respectively. As mentioned, the moisture content has higher impact for $f_c$ than for $f_v$ and $E_c$. For the same moisture content (e.g. 8 %), $f_c$ is reduced by 17%, while $f_v$ and $E_c$ are reduced by 10 and 5% respectively. This indicates that the moisture content is more critical for the failure of the culm than for the elastic properties.

The relationship between volume fraction and density is depicted in Figure 6.43. Unlike previous findings (Dixon and Gibson, 2014), showing a linear relationship (with $R^2 = 0.80$) between volume fraction of vascular bundles and density taken from samples at different positions in the radial direction, the relationship in this study was not strong.

The plots between mechanical properties against physical and geometric properties are provided in Appendix F. In general the data was scattered and no strong relationships were found among these properties. A number of studies have found a linear relationship between the tensile elastic modulus and the volume fraction (Chuma et al., 1990; Amada et al., 1996, 1997; Shao et al., 2010; Zhou et al., 2012). However, there are fewer studies for compressive behaviour. Lo et al. (2008) reported an increase of compressive strength with

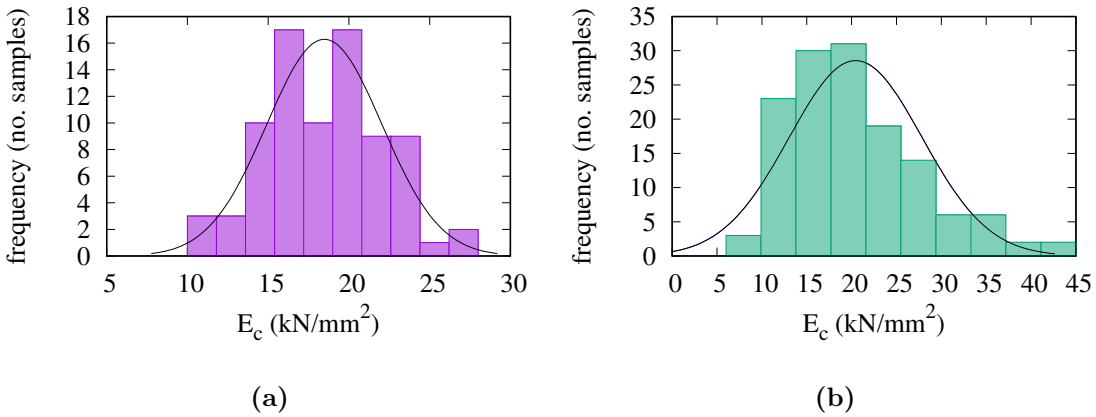


**Figure 6.40:** Frequency distribution of $E_c$ for the (a) guadua and (b) oldhamii species.

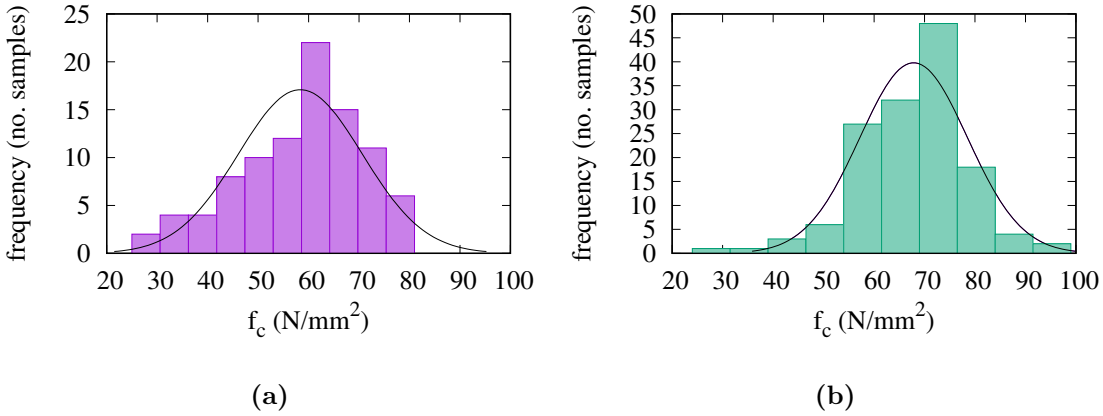


**Figure 6.41:** Frequency distribution of $f_c$ for the (a) guadua and (b) oldhamii species.

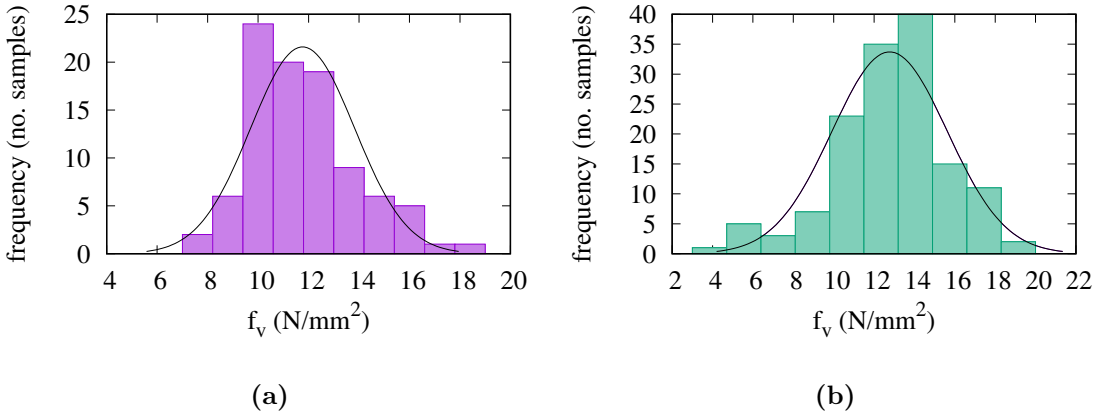


**Figure 6.42:** Frequency distribution of $f_v$ for the (a) guadua and (b) oldhamii species.

the number of vascular bundles, and Dixon and Gibson (2014) found a linear relationship between the axial compressive strength and density.

It is important to highlight that the studies where a relationship between $E_t$ and $v_b$ was reported were concerned with samples taken across the radial direction (i.e. thickness), and therefore quantified the whole variation in the radial direction. However, in this study,

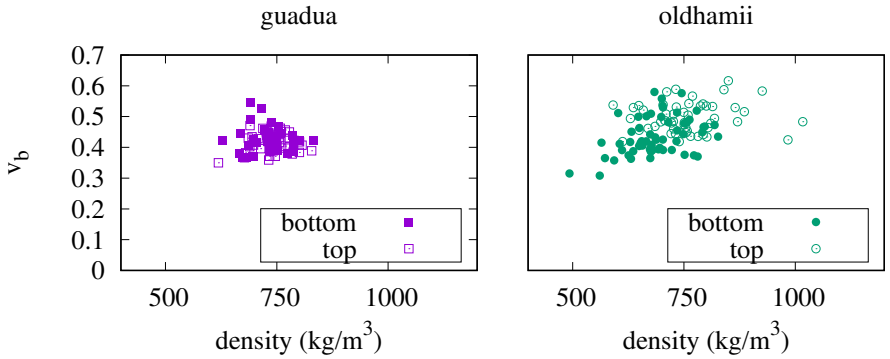


**Figure 6.43:** Relationship between volume fraction and density.

we are concerned with values at two different positions along the length of the culm (i.e. bottom and top), and therefore quantified only a small portion of the overall length of the culms. From the literature (refer to Subsection 2.2.3 and Figure 2.10) we know that the variations in physical and mechanical properties are higher in the radial than in the longitudinal direction. Therefore, it is reasonable to expect less strong correlation for $E_c$ and $v_b$ in this study as is found.

Assuming a linear relationship between $E_c$ and $v_b$, the compressive elastic modulus of the fibre $E_f$ and matrix $E_m$ can be estimated by applying the rule of mixtures. The linear models for the guadua and oldhamii species from linear regression are

$$E_{c,g} = 26194 v_b + 8531 \quad \text{N/mm}^2 \tag{6.112}$$

$$E_{c,o} = 16365 v_b + 11739 \quad \text{N/mm}^2 \tag{6.113}$$

From these models, using the rule of mixtures, $E_f$ for guadua and oldhamii are $E_{f,g}$= 34725 N/mm$^2$ and $E_{f,o}$= 28104 N/mm$^2$ respectively, and those for the matrix are $E_{m,g}$= 8531 N/mm$^2$ and $E_{m,o}$= 11739 N/mm$^2$. The values of $E_m$ are very high in comparison with the resulting values using the tensile elastic modulus $E_{t,m}$ which $\leq$ 2000 N/mm$^2$ (Amada et al., 1996; Shao et al., 2010). This could be due to the function of the matrix when the composite is subjected to compressive forces. However, this aspect is not further analysed in this study.

#### 6.3.2.4 Equivalent elastic modulus $E_{eq}$

Herein, the equivalent elastic modulus from the composite $E_{eq,c}$ and bimodulus models $E_{eq,b}$, are investigated, and these are compared against results obtained from full culm tests under transverse loads.

Figure 6.44 illustrates an idealised portion of the culm wall cross-section for the composite model. The thickness and elastic modulus for each lamina are estimated from Equations (5.31) and (5.36) respectively. The equivalent bending elastic modulus $E_{eq,c}$ from the composite model is estimated from Equation (6.69) assuming a hollow circular

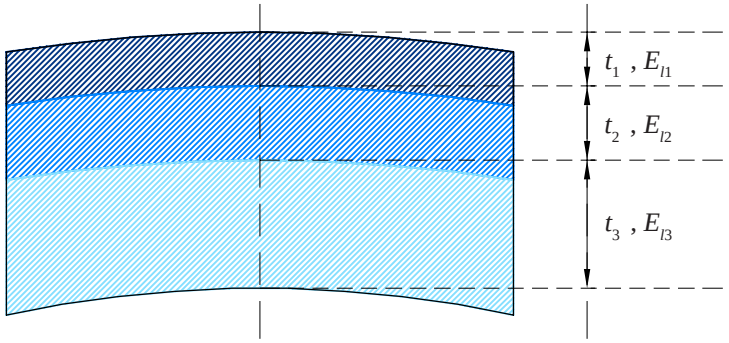


**Figure 6.44:** Bamboo culm thickness idealised as a laminate of three layers.

cross-section.

For the bimodulus model, the values for $E_t$ are estimated as described in Subsection 6.2.2.8 using Equations (6.106) and (6.107). The elastic modulus of the fibre estimated for the guadua and oldhamii species are $E_f$= 46,113 and 43,436 N/mm$^2$ respectively, according to the calibrated values obtained from Equation (6.106). The $v_f$ is calculated using Equation (5.25). The equivalent stiffness $E_{eq,b}$ is estimated from Equation (6.88) and depends on the $v_f$ and the ratio compressive to tensile stiffness $n$ from Equation (6.77).

Figure 6.45 presents the comparison between $E_b$ from full culm tests, and the equivalent

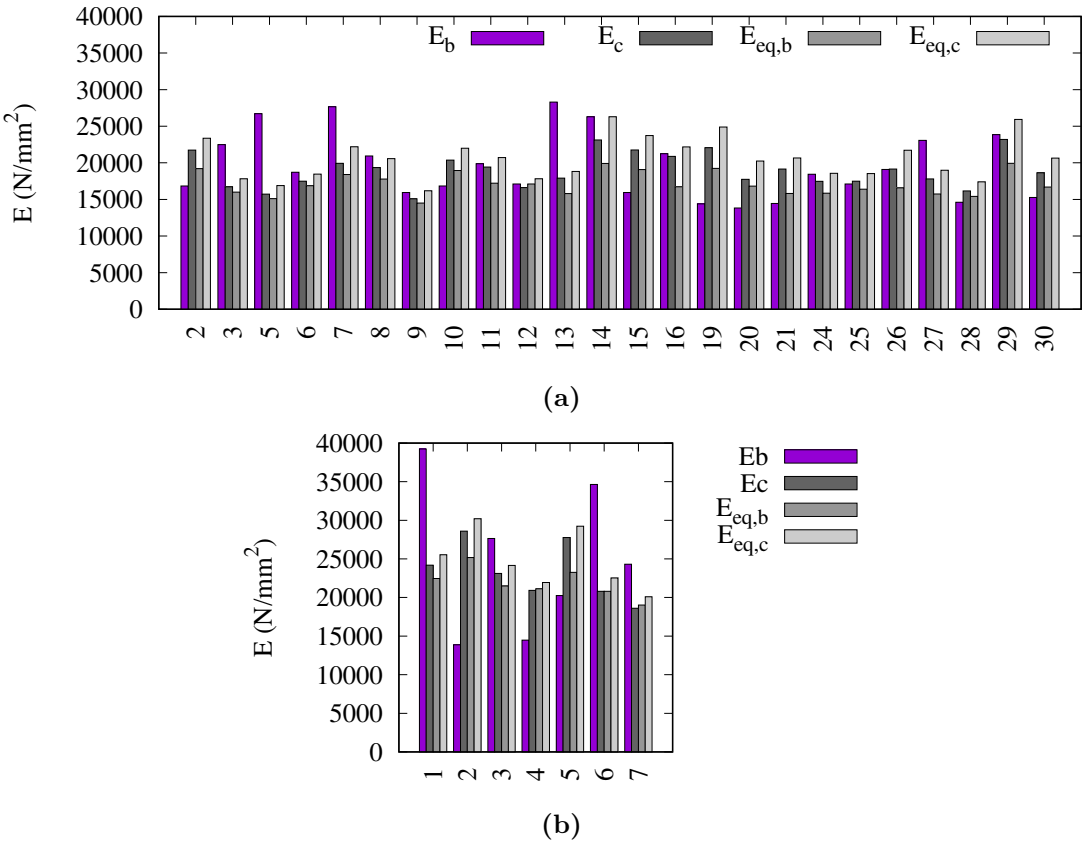


**Figure 6.45:** Comparison of $E_b$ against $E_{eq,b}$ and $E_{eq,c}$ for (a) Guadua, and (b) Oldhamii bamboos.

elastic modulus from the composite $E_{eq,c}$ and bimodulus $E_{eq,b}$ models. In order to make an accurate comparison between properties, the results from the small coupons were corrected to the moisture content measured at the time of the full culm bending tests. The correction factors presented from Equation (6.108) to (6.110) were used for this purpose. The values obtained for the ratio $E_{eq,b}$ to $E_c$ as from Equation (6.86) were 1.01 and 0.94 for the guadua and oldhamii species respectively, with a standard deviation of 0.075.

For the guadua species, there were three culms where $E_b$ is clearly significantly higher than the rest of the culms. Similarly, $E_b$ of two oldhamii culms is significantly higher than the rest, and one that is considerably lower. If we consider these culms as outliers, on average, the percentage error between $E_b$ and $E_{eq,b}$ is 16% and between $E_b$ and $E_{eq,c}$ is 20% for the guadua species, and 26 and 32% for the oldhamii species respectively.

The percentage error quantified is comparable to the variations that arise from samples taken from the same cross-section. The percentage difference between samples of the small coupons tested taken from the same cross-section is 20 and 34% for the guadua and oldhamii species respectively. Also, it is similar to the coefficient of variation in other natural materials such as timber, which varies between 10 and 30% (Dinwoodie, 2000).

The relationship between $E_c$ and the $E_{eq}$ is depicted in Figure 6.46. The solid line represents the slope of one. The composite material model tends to estimate an equivalent modulus higher than that predicted from the bimodulus model.

Furthermore, for all $E_{eq,b}$, approximately two-thirds of all the samples are lower than $E_b$, whereas for $E_{eq,c}$ about two-thirds of the samples are higher than $E_b$. No significant differences were found between $E_{eq,b}$ and $E_{eq,c}$ against $E_b$, and between $E_c$ against $E_b$. Nonetheless, $E_{eq,b}$ is a better approximation to $E_b$ by 4 and 6% for the guadua and oldhamii species respectively, and thus can be considered as a conservative estimate.

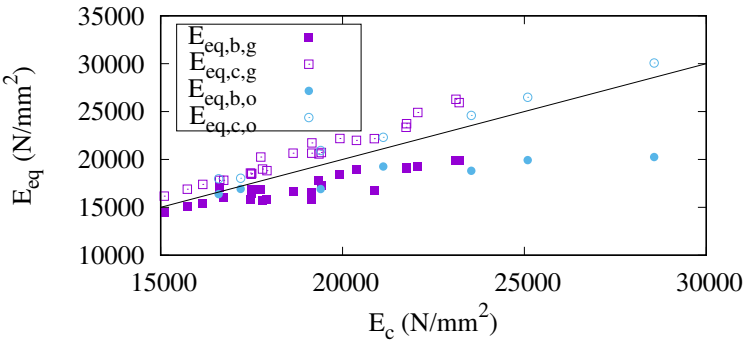


**Figure 6.46:** Relationship between $E_c$ and $E_{eq}$.

#### 6.3.2.5 Failure

Figure 6.47 depicts the distribution of the maximum values for tensile $f_{t,m}$, compressive $f_{c,m}$ and shear $f_{v,m}$ stresses in the cross-section of bamboo calculated from the bimodulus model. The neutral plane shifted from the centroid to the tensile or compressive zones is

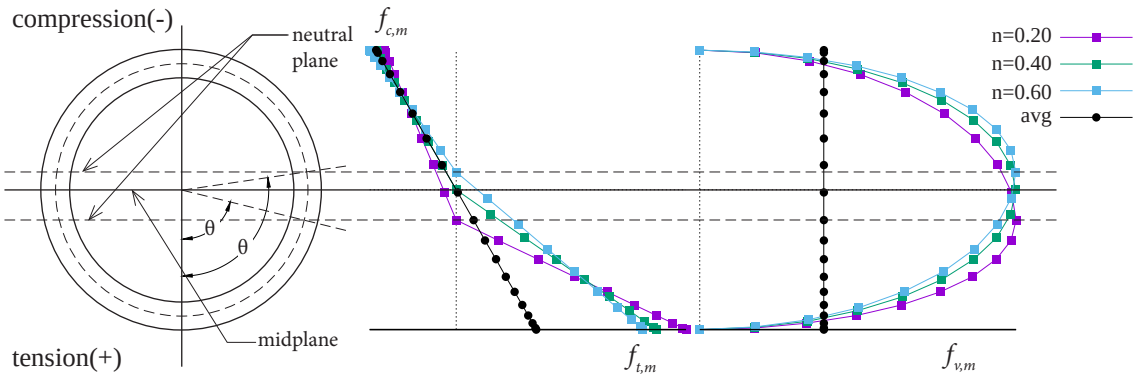


**Figure 6.47:** Distribution of normal and shear stresses for a section with a constant $v_f$ of 0.40, for different ratio $n$, and of average values for a uniform section.

illustrated to show the effect that the model has in the distribution of stresses throughout the cross-section. The maximum tensile, compressive and shear stresses are calculated according to Equations 6.94, 6.95 and 6.105. Except for one guadua culm, the neutral plane for all the culms was shifted towards the compressive zone. While $f_{t,m}$ and $f_{v,m}$ are generally underestimated if we take their average values, $f_{c,m}$ is almost the same as the average values. Table 6.11 provides the percentage difference between the maximum and average stresses calculated at the cross-section.

Figures 6.48 - 6.50 show the difference in values between the estimated maximum tensile, compressive and shear stresses in the cross-section using the bimodulus model, and the compressive and shear strength measured from small coupons. The tensile strength was estimated using the rule of mixtures according to Amada et al. (1997) as

$$f_t = \sigma_f v_b + \sigma_m (1 - v_b) \tag{6.114}$$

where $\sigma_f$ and $\sigma_m$ are the fibre and matrix tensile strength ($\sigma_f = 610$ MPa, $\sigma_m = 50$ MPa).

The percentage difference between the maximum stresses calculated using the bimodulus model and the capacity of the bamboo to sustain compressive $f_c$, tensile $f_t$ and shear $f_v$ forces is significant (see Table 6.12).

Table 6.13 presents the number of culms that show any of the failure types described above. For the majority of the culms, $f_c$ is lower than the value calculated from the bimodulus model at the moment of failure. In contrast, for approximately 40% of the guadua culms and 70% of the oldhamii culms the maximum tensile stresses from the bimodulus model were lower than $f_t$. Finally, for most of the culms, $f_v$ is higher than the

**Table 6.11:** Percentage difference between maximum and average stresses in the cross-section.

| species | Percentage difference | | |
|---|---|---|---|
| | $\Delta f_{c,m}$- $f_{c,avg}$ | $\Delta f_{t,m}$- $f_{t,avg}$ | $\Delta f_{v,m}$- $f_{v,avg}$ |
| guadua | 3.6 % | 96.3 % | 87.2 % |
| oldhamii | 4.5 % | 89.0 % | 87.2 % |

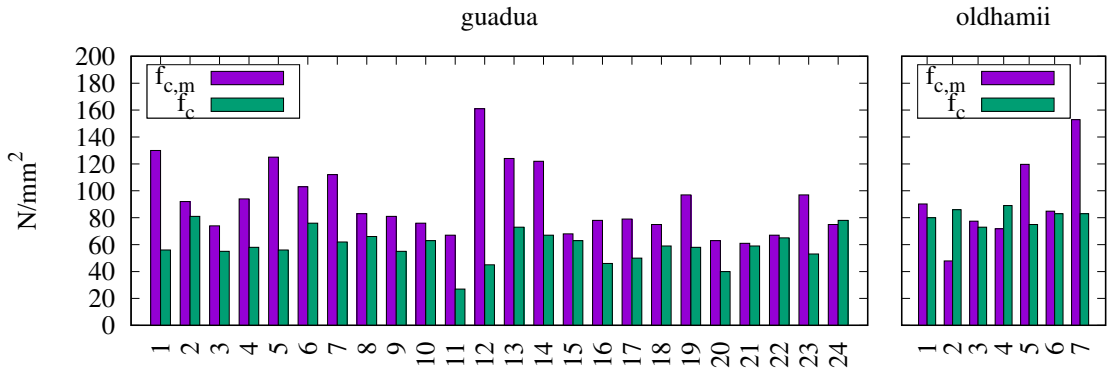


**Figure 6.48:** Comparison between maximum compressive stresses, $f_{c,m}$, from bimodulus model and compressive strength, $f_c$, from small coupons.

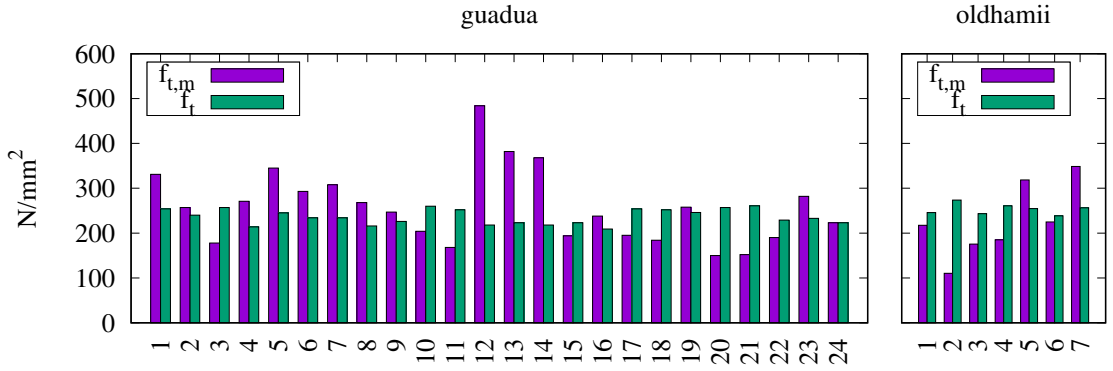


**Figure 6.49:** Comparison between maximum tensile stresses, $f_{t,m}$, from bimodulus model and tensile strength, $f_t$, from small coupons.

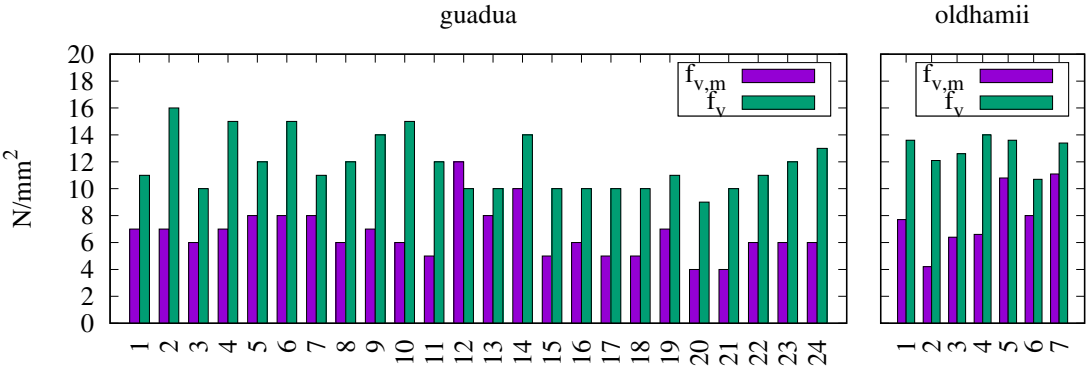


**Figure 6.50:** Comparison between maximum shear stresses, $f_{v,m}$, from bimodulus model and shear strength, $f_v$, from small coupons.

calculated maximum shear stresses developed in the cross-section. Interestingly, the culm with higher shape factor ($\Phi$=6.4, see Figure 10 in Appendix E), corresponding to the one

**Table 6.12:** Percentage difference between the stresses developed in the cross-section from the bimodulus model and the capacity of bamboo.

| species | Percentage difference | | |
|---|---|---|---|
| | $\Delta f_{c,m}$- $f_c$ | $\Delta f_{t,m}$- $f_t$ | $\Delta f_{v,m}$- $f_v$ |
| guadua | 41 % | 29 % | 60 % |
| oldhamii | 29 % | 32 % | 52 % |

**Table 6.13:** Number of culms exceeding $f_c$, $f_t$ and $f_v$ for guadua and olhdamii bamboos to investigate failure mechanisms, the total number of culms is 24 and 7 respectively.

| Failure Type | Guadua | Oldhamii |
|---|---|---|
| $f_c$ | 23 | 5 |
| $f_t$ | 15 | 2 |
| $f_v$ | 1 | 0 |

with thinner section, was the only one that exceeded $f_v$. There was no more data recorded for thin sections that might aid to identify a pattern.

These results suggest that while some culms failed after reaching the maximum compressive and tensile stresses, there is another mechanism triggering the failure of the rest of the culms. Nevertheless, the question of how does the cross-section resist normal stresses higher than the compressive strength arises. Firstly, the bimodulus model is linear elastic, and as such the tensile and compressive stresses are estimated under this assumption. However, we know that the bending behaviour of bamboo is linear elastic followed by a ductile behaviour prior to failure (see Figure 6.19). In addition, recall from Subsection 6.1.3 that for some timbers ($f_t > f_c$) once the compressive strength is reached, the neutral axis is shifted towards the tensile zone, causing tensile failure. A similar mechanism might be occurring in bamboo culms, but this requires further investigation.

It is important to highlight some aspects related to the compressive tests. First, recall that the end sections from the guadua and oldhamii culms were cut after the bending tests. Although these were taken from the ends of the beam, and not from the area of the maximum moments and shear forces occurs, no measurements were taken to quantify if the end sections were damaged during the test. Therefore, the end sections of the culms might have been damaged during the bending tests, influencing the results of the small coupon testing. Furthermore, recall from Subsection 6.1.2 that the compressive strength measured from small coupons was found to be approximately 9.6% lower than that measured from the full culm specimens. In addition, for the guadua species, some sampls were extremely dried when tested for $f_c$ and thus had a very low density (see Figure 11 in Appendix F). All the samples with $< 500$ kg/m$^3$ failed due to delamination. Finally, some of the samples were sanded for preparation of volume fraction analysis or for tolerance purposes. As mentioned, sanding can be detrimental to the sample due to the uneven surfaces. The JG/T-199 (2007) do not specify any equipment for the appropriate alignment of samples. Nevertheless, the special alignment equipment (Bodig and Jayne, 1982) might be beneficial as this test is susceptible to misalignments as well as end restraints due to

the radial gradient distribution as discussed in Subsection 6.1.1.

### 6.3.3 Summary

This section presented and carried out the experimental programme to validate the methodology for determining the mechanical properties of bamboo culms by comparing the results from this methodology against the results from full culm bending tests. Guadua and oldhamii bamboo species were used for this purpose.

The average volume fraction calculated for guadua and oldhamii bamboo was found to be 0.34 and 0.38 respectively. The guadua species has an inner and outer layer greater than for the oldhamii species. The influence of this aspect for the calculation of the area of the sample or the volume fraction is not considered. In this study, the area of both layers is considered as part of the matrix. However, further analysis is required to determine how to consider these layers in a bamboo species that have this feature more intensified such as the guadua species.

Overall, the results from the mechanical testing of small coupons do not show a significant variation from bottom to top, suggesting that the mechanical properties along a culm of approximately 5 m, do not change significantly.

Unlike the relationships reported between the tensile properties of bamboo and volume fraction and density, the relationships between compressive properties and $v_b$ and density are not strong. Two different causes are identified to explain this behaviour. The first is the role of the matrix in the compressive behaviour of bamboo. Although both behaviours depend on the composite action between the fibres and matrix, the function of the matrix in the compressive behaviour is crucial. The tensile properties are directly related to the properties of the fibre and the matrix only helps to distribute the load among them, whereas under compressive loads, the matrix prevents buckling of the fibres and thus improving the capacity of the fibres to sustain compressive forces. The second is the direction and scale at which these properties were collected. Usually, the relationship between tensile strength and stiffness against volume fraction are made from samples taken from a single cross-section. However, in this study the samples used to make these relationships correspond to two discrete points along the culm for a batch of multiple culms. In addition, we know from the literature that variations are higher in the radial than in the longitudinal direction. For these reasons, is reasonable to expect lower correlations in the longitudinal direction.

The percentage error calculated from the results obtained of the equivalent bending modulus $E_{eq,b}$ and $E_{eq,c}$ from both material models was found to be similar to the percentage error between samples of the same cross-section. The percentage error between the $E_b$ and $E_{eq,b}$ and $E_{eq,c}$ is 16 and 20% for the guadua species, and 26 and 32% for the oldhamii. Although both models can predict the bending elastic modulus within similar ranges, the $E_{eq,b}$ is a better approximation to $E_b$ by approximately 5%. However, the data used for this validation is limited in number, and further tests are required to gain better

understanding on the relationship between $E_b$ and $E_{eq}$.

In general, the bimodulus model has higher effect for the analysis of the stresses than the elastic modulus. For example, the average values for the ratio $E_{eq,b}$ to $E_c$ were 1.01 and 0.94 for the guadua and oldhamii respectively, about 1 and 6% difference, whereas the percentage difference for the stresses is about 4, 93 and 87% for the compressive, tensile and shear stresses (see Table 6.11). $f_c$ is significantly lower than $f_{c,m}$. Possible aspects that might be influencing these results were highlighted. For some culms, $f_t$ was higher than $f_{t,m}$. On the contrary, $f_v$ was significantly higher than $f_{v,m}$. In addition, only one culm exceeded $f_v$, corresponding to the culm with the thinnest cross-section. This can possible be related to the high shear stresses in thin sections. This was the only example with thin sections. Further tests to identify possible failure mechanisms associated with the proportions of the cross-section (i.e. thin or thick sections according to the shape factor) are recommended as in thick sections the stresses across the culm wall are different (Young et al., 2012). However, both models explored here consider a cross-section with a thin culm wall.

## 6.4 Discretisation of mechanical properties for SBD

This section presents the discretisation of the mechanical properties for the SBD. Table 6.14 presents the mechanical properties obtained for the SBD. From Section 4.4, we know that the discretised properties can include or not the coordinates at the internode. For representation, here we will consider that both, the node and internode coordinates are used for structural modelling (see Figure 6.51).

**Table 6.14:** Mechanical properties for the SBD.

| Strength | | Stiffness |
|---|---|---|
| $f_c$ | $f_v$ | $E_c$ |

Since coordinates are taken at the middle of the internodes, every two segments have

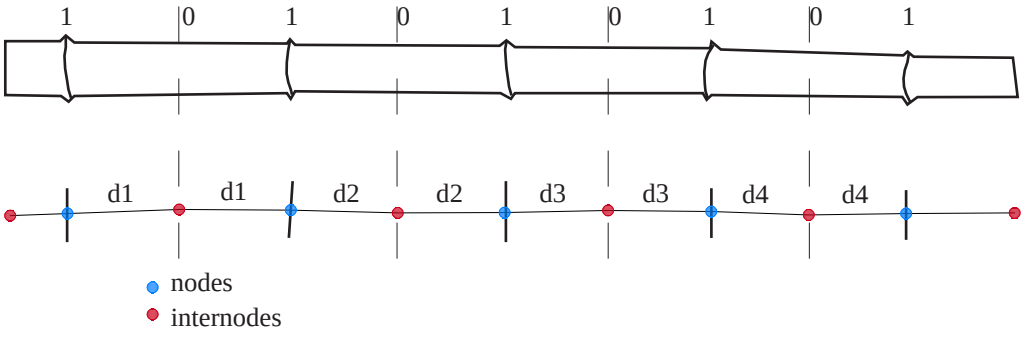


**Figure 6.51:** Discretised bamboo culm at nodes and internodes. The $d$ refers to the data used for the structural modelling.

the same section properties, and each segment is denoted as $d_1, d_2, ..., d_q$, where $q$ is the total number of internodes. The mechanical properties for each of the segments in the structural model are estimated from the discretised geometry and mechanical properties at both ends. A linear interpolation of the elastic modulus $E_{eq,b}$ against the diameters is then used to estimate the $E_{eq,b}$ for each internode. The coefficients $a$ and $b$ of the linear interpolation from the bottom and top are obtained as:

$$a = \frac{\sum_{i=1}^{n}(D_i - D_{avg})(E_i - E_{avg})}{\sum_{i=1}^{n}(D_i - D_{avg})^2} \tag{6.115}$$

$$b = E_{avg} - aD_{avg} \tag{6.116}$$

where $n$ is the upper bound of the summation referring to the number of data points which is usually 2, corresponding to the bottom and top samples, but can be greater if the culm is cut into sections, and $i$ represents the index of the summation. $D_i$ corresponds to the diameters at the bottom and top, $D_{avg}$ to the average diameter, $E_i$ (i.e. $E_i = E_{eq,b}$) to the elastic modulus from the bottom and top and $E_{avg}$ to the average elastic modulus. The elastic modulus at each internode is estimated using these coefficients as a function of the diameter using the relationship

$$E_j = aD_j + b \tag{6.117}$$

## 6.5 Summary

This chapter presented the development of the methodology for the determination of mechanical properties of bamboo culms to use for the global linear elastic analysis of bamboo structures. Table 6.14 presents the discretised mechanical properties for the SBD. This was achieved by a combination of numerical and experimental methods. In addition, the methodology was extended to investigate the failure of bamboo.

Preliminary tests were carried out in Section 6.1 to gain insight into the suitable methods to use for this methodology that meets the principles of the design framework presented in Chapter 3. The main findings that informed the development of the methodology were: (a) the test methods (including end conditions), tolerances of the samples and the radial fibre distribution influences the response of the bamboo sample when subjected to compressive loads; (b) the stress-strain relationship of small coupons and full culms is the same for low stresses; (c) it was suggested that the iteration between the axial tensile and compressive behaviour in the cross-section was crucial for the estimation of bending properties.

The methodology was developed based on these findings, the literature review and the rationale presented in Chapter 3. It consists of experimental tests on small coupons and two different material models used to derive the equivalent bending elastic modulus $E_b$. One of the material models is based on composite material theory, and models the radial gradient as a laminate of three different layers with varying properties. The other

is a bimodulus model, where the main assumption is that the tensile and compressive behaviour of bamboo culms are different.

An experimental programme to validate the methodology was presented using oldhamii and guadua bamboo species. This was done by comparing the results from the equivalent modulus against those from full culm bending tests used as benchmark. It was found that the results obtained from the bimodulus model $E_{eq,b}$ was the best approximation to $E_b$. The difference between the results from full culm tests and the predicted $E_{eq,b}$ from small coupons under compressive load was approximately 11%. Further test methods are required to identify the failure mechanism of the culm. It was interesting to note that the only culm that developed stresses higher than the shear strength was the culm with the thinnest section. There was no more data to support a possible relationship between the thickness of the culm wall in the cross-section and failure by shear stresses. It is recommended that future tests incorporate higher numbers of culms, but also thin and thick sections to identify possible failure mechanisms associated with the shape factor of the cross-section.

Finally, the discretisation of the mechanical properties for the SBD was presented, and the method to derive the equivalent bending elastic modulus $E_{eq}$ for each element in structural modelling was provided. This method will be used in next Chapters 7 and 9, for the automatic selection of bamboo culms and the structural modelling of bamboo reciprocal systems.

# Part III

# Incorporation of SBD into the design process

# Chapter 7

# Structural morphology of bamboo reciprocal structures

This chapter concerns the geometry of reciprocal structures. The objectives of the chapter are described below.

- To define a method for the generation of the geometry of reciprocal structures considering the variation of diameters of bamboo culms.
- To propose methods for the optimal selection, position and incorporation of the discretised geometry of bamboo culms in the structural model.

Reciprocal structures can be described as self-supported structures where for each element there is at least one element that acts as a support and another that is supported. The simplest case is presented with three elements in Figure 7.1a. The concept of reciprocity has been used since ancient times as a building technique to build primitive dwellings (see Figure 7.1b) and where the span required to cover is greater than individual elements Popovic (2008). A historical and contemporary review of reciprocal structures is given by Popovic (2008) and Pugnale and Sassone (2014).

Although these structures have been used for hundred of years, it is not clear where and when reciprocal structures has its origins. In fact, there are many terms used to refer to these type of structures, including reciprocal frame (Chilton and Choo, 1992; Popovic, 2008), nexorades (Baverel, 2000), reciprocal frameworks (Thönnissen, 2015), mutually supported elements (Rizzuto and Hulse, 2007; Rizzuto, 2008), reciprocal systems (Baverel and Pugnale, 2014), reciprocal structures (Thönnissen, 2014; Parigi and Kirkegaard, 2014) and many others (Pugnale and Sassone, 2014). The common idea that link up all these terms into the same definition but with different names is, as described by Chilton (Chilton and Choo, 1992), the type of arrangement of elements in which each element supports and is supported by other elements in the structure.

One of the main aspects of reciprocal structures is the type of joints. Traditionally, these have been jointed by simply overlapping and lashing together timber elements (Popovic, 1996). However, there are other types such pinned, clamped or notched joints (see

**(a)** **(b)**

**Figure 7.1:** (a) Basic reciprocal structure of three elements. (b) Ancient Hogan dwelling (Thönnissen, 2015).

Figure 7.2). The type of joint to use in reciprocal structures is crucial, as this determines the structural behaviour and can help to prevent progressive collapse of the structure (Chilton and Choo, 1992). Figure 7.3 shows a general classification for these joints, from which each of them can have several variations. Herein, we refer to these type of structures as *reciprocal structures* with mechanical connectors.

The key geometric parameters of reciprocal systems are illustrated for a three element reciprocal unit in Figure 7.4. The eccentricity is the perpendicular distance between each

(a) (b) (c)

**Figure 7.2:** Types of connections. (a) Notched (Popovic, 2008), (b) bolted (Rizzuto and Larsen, 2010) and (c) clamped (Sénéchal et al., 2011).

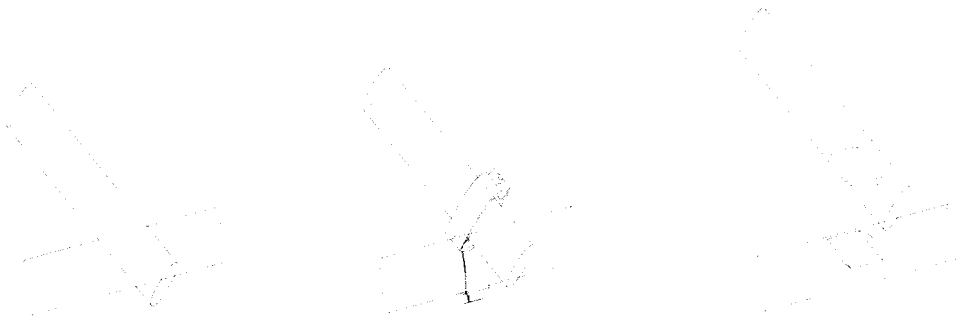

(a) (b) (c)

**Figure 7.3:** Classification of joints for reciprocal structures proposed by Thönnissen (2015), (a) contact bearing, (b) addition and (c) subtraction.

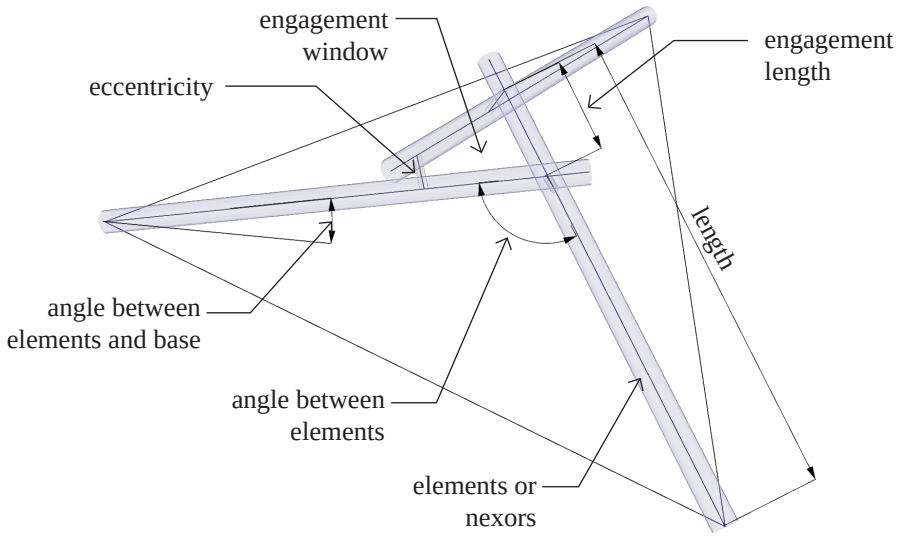


**Figure 7.4:** Illustration of geometric parameters of reciprocal systems according to Baverel (2000), for a three-element module.

pair of contacting elements and will be defined below. This is a fundamental parameter directly related to the geometry of bamboo culms, as the eccentricity needs to accommodate the diameter of both culms that are connected. Based on these parameters, Baverel (2000) proposed three different procedures based on analytical geometry to define the reciprocal configuration, namely translation, rotations and extended translation. Other definitions, including genetic algorithms (Baverel et al., 2004), dynamic relaxation (Douthe and Baverel, 2013), and parametric methods (Anastas et al., 2016) have been proposed.

One of the most challenging aspects regarding the form-finding methods for reciprocal structures with double curved surface (i.e. not plane reciprocal systems) is the generation of the eccentricities between elements. There is currently no systematic method to generate specific eccentricities so that the different diameter of bamboo culms can be taken into consideration. Song et al. (2013) proposed an optimisation strategy for the definition of the eccentricities. However, after optimisation, there are at least a few elements that do not converge (i.e. some eccentricities are very small or very large after optimisation). Furthermore, Goto et al. (2011) developed a tool that provides a numerical solution solved by the Newton-Raphson method. More recently, Anastas et al. (2016) employed the Live Physics engine Kangaroo for Grasshopper in order to define the required eccentricities. This is a powerful and interactive method accessible to designers with little or no experience of optimisation methods. However, this method can also result in non-convergence in some situations. All these tools, although very powerful cannot guarantee convergence, as some geometries simply cannot comply with all the geometrical constraints imposed, particularly, in surface areas with high curvature, as highlighted by Song et al. (2013).

## 7.1 Definition of the geometry

The two main methods identified for the generation of the geometry of reciprocal structures are rotations and translations, as described above. In this thesis, a rotational method that allows accommodating the variable geometry of bamboo culms is proposed.

Figure 7.5 illustrates an overview of the main steps to generate the geometry of reciprocal systems. The first step takes any arbitrary smooth surface with double curvature tessellated with a triangular mesh. Tessellation refers to the tiling of the arbitrary surface using closed polygons. The next step consists of rotating the edges to create the reciprocal configuration of the system. Since the edges of the mesh are lying in different planes, these rotations will generate eccentricities among the edges. In this context, eccentricity is defined as the orthogonal distance between two edges. This distance should be sufficient to accommodate the diameters of the bamboo culms that are going to be connected. However, it is unlikely that the eccentricities coincide with the required dimensions to accommodate the bamboo culms. Therefore, the last step consists of adjusting the eccentricities in the reciprocal system to the diameters of the bamboo culms to be used.

The arbitrary underlying surface is taken as a fixed input together with the given tessellation. The tessellations explored in this thesis are limited to triangular grids of degree 6, the number of edges incident on a vertex (see Figure 7.6). Interestingly, the dual of this tessellation is a hexagonal grid of degree 3 (see Figure 7.6). Therefore, the final

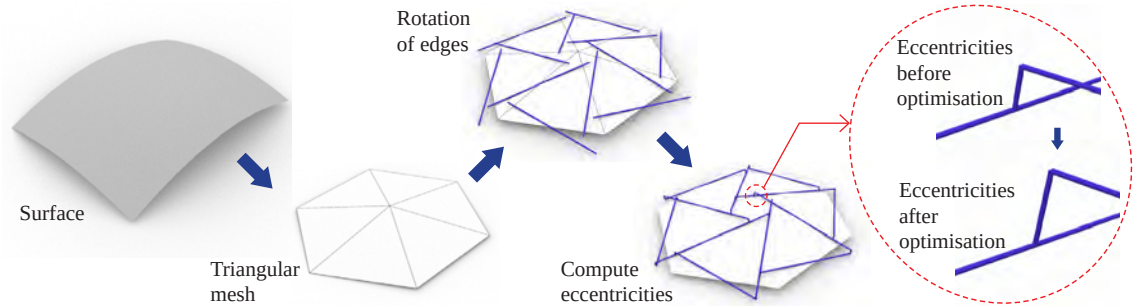


**Figure 7.5:** Overview of the general steps to generate the geometry of reciprocal systems.

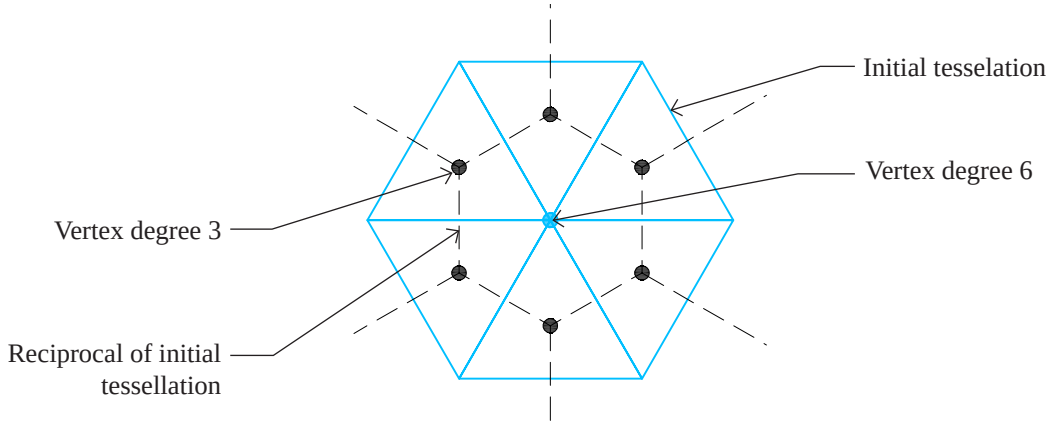


**Figure 7.6:** Triangular tessellation and its reciprocal shown in a flat plane.

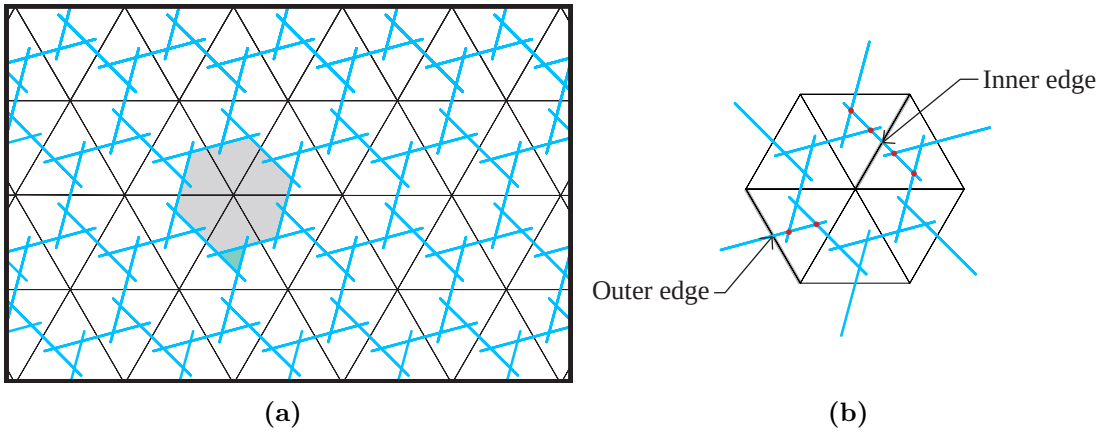


**Figure 7.7:** (a) Reciprocal configuration for a triangular tessellation of degree 6. (b) Connecting points for inner and outer edges.

reciprocal geometry will consist of a grid pattern of triangles and hexagons. Figure 7.7a illustrates this grid in two dimensions. Note that the inner edges have four connecting points, whereas boundary edges have only two connecting points (see Figure 7.7b).

### 7.1.1 Reciprocal configuration

The reciprocal configuration is described here using five steps. We start by organising the mesh objects (i.e. faces, edges and vertices) obtained from the tessellated surface to define the connectivity among the edges. For example, for each edge, which other edges are connected to it? Next, we define the axis of rotation for each edge and the angles to use for the rotations. Once this data is established, the rotations are performed, and then the orthogonal distance (i.e. the eccentricities) between the two edges in each connecting point are computed.

#### 7.1.1.1 Mesh objects

The initial input is a triangular mesh, similar to the one depicted in Figure 7.8. For the sake of clarity, the mesh is represented for now as a plane mesh. The vertices are enumerated, and the boundary vertices are distinguished from the rest. Similarly, the edges are enumerated, and the boundary edges are identified from the rest. The faces are labelled 0 or 1. For each face 0, their adjacent faces are 1, creating a 0-1 pattern resembling a chequerboard as in Figure 7.9. The label of the first face is chosen arbitrarily. Note that this chequerboard pattern is possible as the triangular tessellation is of degree 6. The direction of the set of edges defining faces 0 are clockwise, and those defining faces 1 are anticlockwise, as shown in Figure 7.9. From this, a sequence of steps is made for each edge in order to identify the edges that are to be connected with it. The total number of eccentricities in the system is also the total number of connecting points and is equal to twice the number of inner edges plus the number of boundary edges.

Figure 7.10 illustrates the selection of the edges, for each inner and outer edges re-

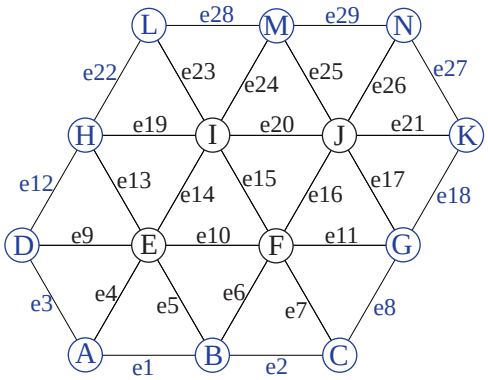


**Figure 7.8:** Nomenclature of the mesh vertices and edges. The boundary vertices and edges are distinguished from the inner ones by the colour purple.

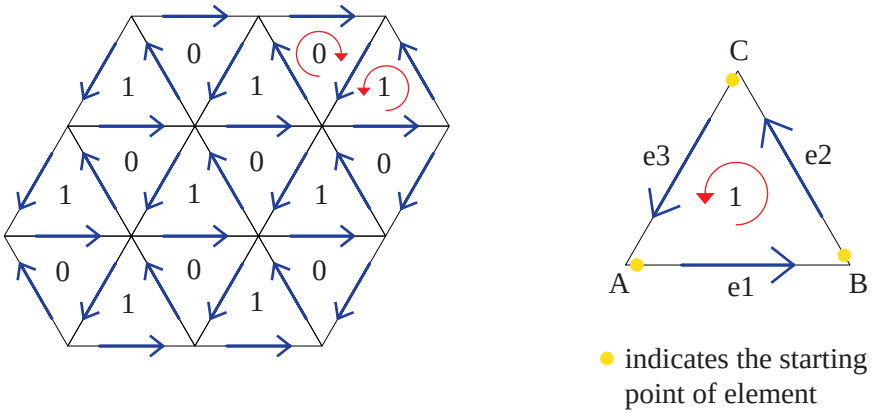


**Figure 7.9:** Nomenclature of faces 0 and 1 and edges direction.

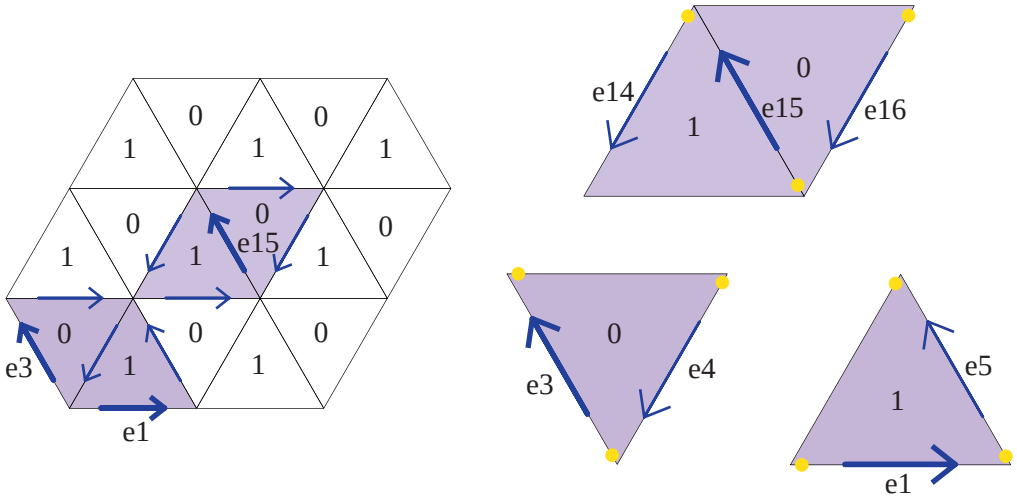


**Figure 7.10:** Selection of edges to find connecting points.

spectively to find the connecting points. For each inner edge, two edges are selected, each one taken from the adjacent faces respectively. Therefore, these two selected edges do not share a common vertex. The routine for the inner edges is depicted in Figure 7.10 with an edge labelled as edge *e15*. It can be described in three steps: a) For the inner edge *e15*, the

two adjacent faces are selected. These faces shall be 0 and 1 respectively. b) The first edge corresponds to the one from the adjacent face 0 that ends at the starting point of the inner edge *e15*. c) The second edge corresponds to the one from the adjacent face 1 that starts at the endpoint of the inner edge *e15*. The routine for the boundary edges is illustrated in Figure 7.10 with the edges labelled as *e3* and *e1* for edges corresponding to faces 0 and 1 respectively. For each boundary edge, the selected edge shall be taken from the same face; the routine is described as follows: a) For each boundary edge lying in face 0, take the edge ending at the start point of the boundary edge. b) For each boundary edge lying in face 1, take the edge starting at the endpoint of the boundary edge. By performing these operations in all the inner and boundary edges, the total number of connecting points are found.

#### 7.1.1.2 Rotation vector

So far, all the diagrams are presented in two dimensions. In order to define the rotational vector $\overrightarrow{p}$ for the reciprocal configuration, triangular faces from a faceted surface in three dimensions are used (see Figure 7.11). Similar to the previous step, the inner and boundary edges are considered separately. The rotation vector for the inner edges is defined by the dihedral angle ($\alpha$), the angle between the two flat faces, as depicted in Figure 7.11 for faces $f_1$ and $f_2$. The rotation vector lies at $\alpha/2$ and is defined by the sum of the two vectors normal to the faces $\overrightarrow{n}$. Since the length of the vector is not relevant, the rotation vector is unitised. For the boundary edges, the rotation vector is considered simply as the vector normal to the face adjacent to the boundary edge.

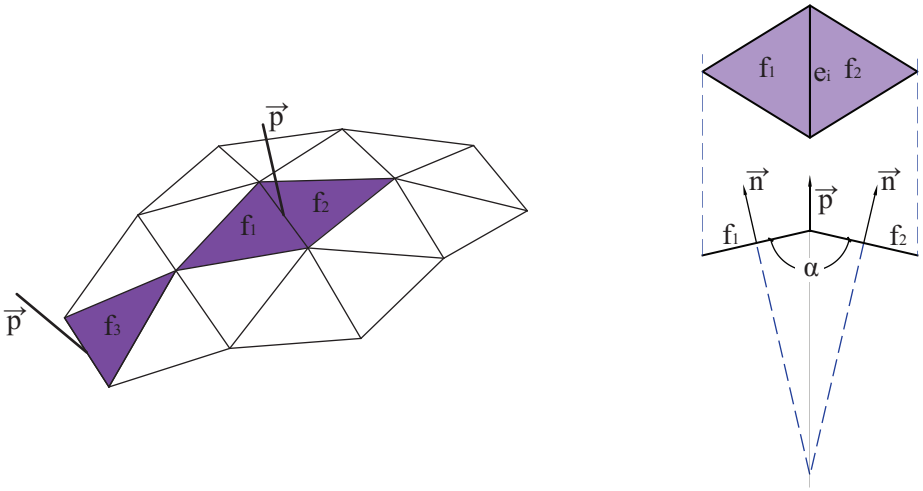


**Figure 7.11:** The rotation vector.

#### 7.1.1.3 Normalisation of rotations

This step is introduced to derive a factor to rotate the edges proportionally to their dual, taking into account how regular or irregular the tessellation is local. A regular tessellation

is defined as a tessellation with polygons with all edges and angles equal. For a regular tessellation in two dimensions, the dual of a triangular mesh of degree 6 is 90° (see Figure 7.12a). However, this is not usually the case for irregular tessellations, and most double curved surfaces are characterised by irregular tessellations. See for example Figure 7.12b, if we rotate the edges 90° in the irregular tessellation, some edges tend to have the connecting points very close to other connecting points. Therefore, minimising the space available to install physical connections and practically eliminating one edge reducing it to a minimal length. To prevent this, a factor to normalise the rotations to their dual is introduced.

The angle $\beta$ between the edges and their duals (see Figure 7.13) is used to derive the angle for the normalised rotations. For an inner edge, its dual is the line passing through the centroids of the two adjacent faces, whereas for a boundary edge the dual is the line between the midpoint of the edge and the centroid of the adjacent face. The angle $\beta$ is measured for each edge and the normalised angle $\lambda$ is defined as

$$\lambda = \frac{\eta}{(1/\beta)} \tag{7.1}$$

where $\eta$ is value from 0 to 1, such that for 0 the edge is in its initial position, and for 1 the edges are parallel to their dual and is defined during the design process. Thus, for a regular tessellation $\eta = 0 = 0°$ and $\eta = 1 = 90°$.

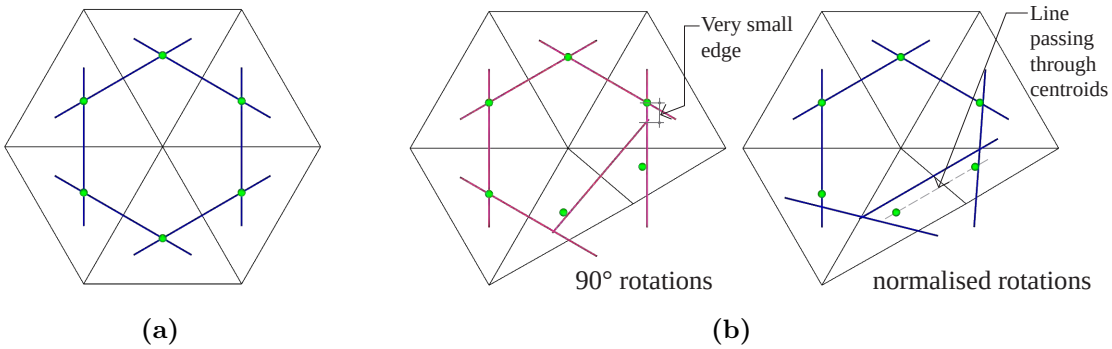


**Figure 7.12:** Rotations in (a) regular and (b) irregular tessellations.

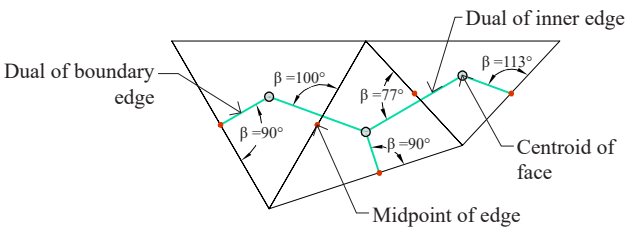


**Figure 7.13:** Angle $\beta$ between the edges and their duals.

#### 7.1.1.4 Rotations

The fundamental idea of the rotation of the edges is depicted in Figure 7.14. The edges are rotated about the axis defined by the rotation vector $\overrightarrow{p}$, using the midpoint of the edge as the centre of rotation by an amount defined by the normalised angle $\lambda$.

The rotations of the edges are depicted in Figure 7.15 for three different angles for clockwise and anticlockwise directions. Note that after rotations, the edges are in contact with the underlying surface at the midpoint of the edges, and thus following the shape of the input surface as close as possible. Also, note that for different rotations, the opening and the engagement length changes.

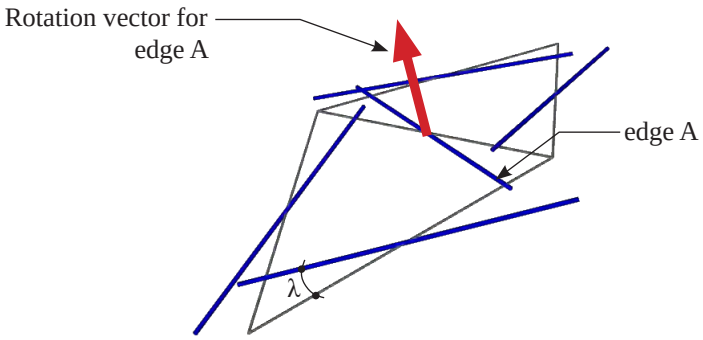


**Figure 7.14:** Rotations of the edges by $\lambda$ to create a reciprocal configuration.

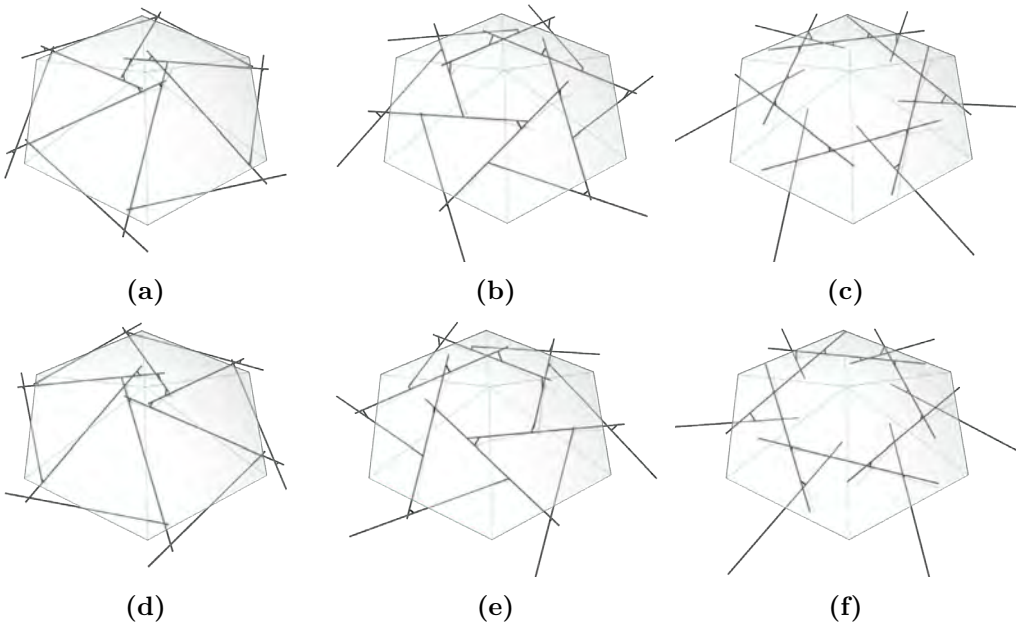


**Figure 7.15:** Rotations in clockwise (a) 15°, (b) 45°, (c) 75°, and anticlockwise (d) 15°, (e) 45°, (f) 75° directions.

#### 7.1.1.5 Eccentricities

After the rotations, the eccentricities are defined for each connecting point, by computing the orthogonal line between both edges. This is computed for each of the connecting points defined in the previous step of the organisation of the mesh objects. Assuming that the equations of the two lines are

$$a = a_0 + (a_1 - a_0)\mathrm{s} \tag{7.2}$$

$$b = b_0 + (b_1 - b_0)\mathrm{t} \tag{7.3}$$

where $a_0$ and $a_1$ are the endpoints of one edge (i.e. line), and $b_0$ and $b_1$ are the endpoints of the other edge, and $s$ and $t$ are the scalar parameters. Then, the distance between the two lines is obtained by computing the dot product of the unit vector perpendicular to both edges, and is expressed as follows

$$u = \frac{|(b_0 - a_0) \cdot [(a_1 - a_0) \times (b_1 - b_0)]|}{|(a_1 - a_0) \times (b_1 - b_0)|} \tag{7.4}$$

where $u$ denotes the eccentricity.

### 7.1.2 Definition of eccentricities

This subsection presents the method for modifying the eccentricities in a reciprocal structure to account for the diameter of the elements. It consists of a mathematical optimisation problem to perform geometric transformations in the edges until reaching the target eccentricities. The definition of target eccentricities depends on the type of connection system, some requiring uniform eccentricities throughout the structure and others varying eccentricities to accommodate the differences in diameter of bamboo culms. This method solves the eccentricities for both types of connection systems.

The method consists of an iterative process that subdivides the edges into groups and solves a maximum of two eccentricities per edge at each iteration. Figure 7.16 depicts some examples where a series of edges are solved with a maximum of two eccentricities per edge. The edges are free to rotate and translate in the out-of-plane direction as shown

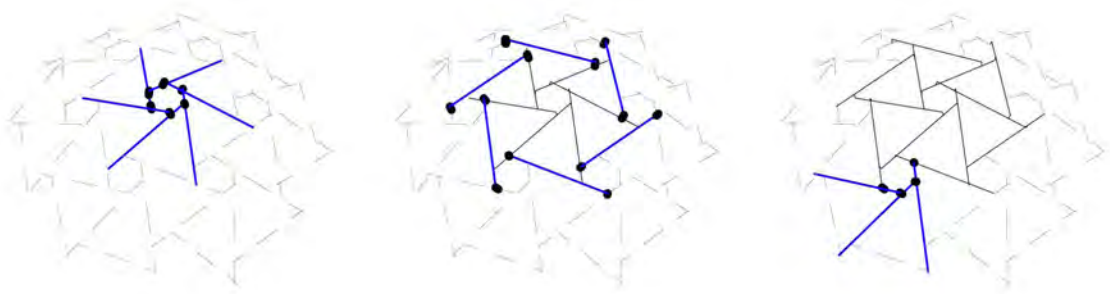

**Figure 7.16:** Example of edges used to solve eccentricities per iteration. Note that for each edge, only 2 eccentricities per each iteration are to be solved.

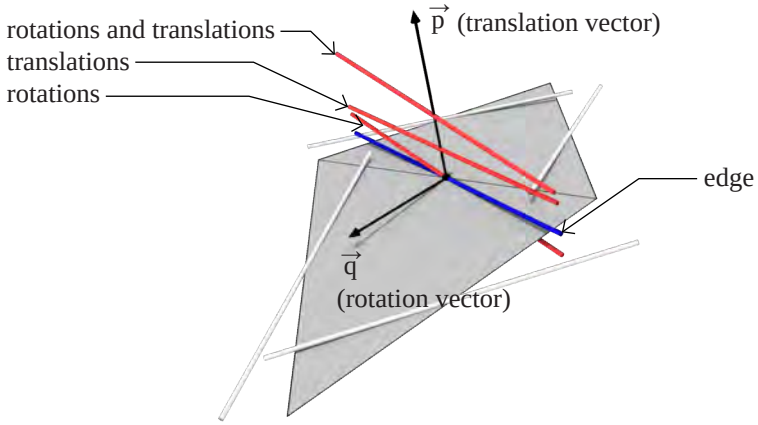


**Figure 7.17:** Geometric transformations of the edges indicating the rotation and translation vectors.

in Figure 7.17 until a position where the eccentricities equal the target eccentricities within the given range is found. Unlike previous methods, this method simplifies the problem of finding the eccentricities in an entire structure simultaneously, thereby eliminating the issue of finding target eccentricities at four points for all the inner edges.

The problem consists of minimising the sum squared difference between the eccentricities $u$ and the target eccentricities $u_c$, by finding the set of angles $\hat{\gamma}$ and distances $d$ for the rotations and translations respectively. These are subjected to two inequality constraints that are to be satisfied. The first states that the eccentricities shall lie between the given tolerances. The second is a constraint imposed to keep the topology arrangement of the edges unchanged (e.g. if an edge is on the top of another edge, do not change it underneath). It is important to highlight that the second constraint is conditional. Therefore, the method searches first for solutions that satisfy all the constraints, but if no solution is found the second constraint is eliminated to increase the solution space. Prior to presenting the formulation of the mathematical optimisation problem, the geometric transformations for the objective function and the constraints are defined.

The design variable is a matrix $\boldsymbol{X}$ of two columns and a number of rows equal to the number of edges, used for the geometric transformations, and to calculate the eccentricities $u$ for the objective function. The first column $\boldsymbol{x}_1$ of $\boldsymbol{X}$ corresponds to the collection of angles $\hat{\gamma}$ in radians in the range $-\pi < \hat{\gamma} < \pi$. The second column $\boldsymbol{x}_2$ of $\boldsymbol{X}$ contains the distances $d$. Below, the procedure to rotate and translate the endpoints of the edges is presented.

The rotations of each edge are performed about the axis $\overrightarrow{q}$ corresponding to the vector perpendicular to the rotation vector $\overrightarrow{p}$ (refer to 7.1.1.2), and the unit vector in the direction of the edge $\overrightarrow{e}$, and using the midpoint of the edge as centre of rotation. The vector $\overrightarrow{q}$ is defined by

$$\overrightarrow{q} = \overrightarrow{p} \times \overrightarrow{e} \tag{7.5}$$

which is the cross product of vectors $\overrightarrow{p}$ and $\overrightarrow{e}$. To rotate an edge (i.e. a line) in three-

dimensions, we first need to compute a series of preliminary geometric transformations to translate the centre of rotation to the origin, and also align the rotation vector to the $z$ axis. Once these transformations are computed, the required rotations are performed about the $z$ axis using the angle defined by $\hat{\gamma}$. Finally, the inverse of the preliminary geometric transformations is calculated to return the geometry to its original position.

To translate the geometry to the origin, we use the translation matrix

$$\boldsymbol{T} = \begin{pmatrix} 1 & 0 & 0 & n_x \\ 0 & 1 & 0 & n_y \\ 0 & 0 & 1 & n_z \\ 0 & 0 & 0 & 1 \end{pmatrix} \tag{7.6}$$

where $n_x$, $n_y$ and $n_z$ are the components of the vector used to translate the geometry to the origin.

Next, to align the rotation vector to the $z$ axis, we perform rotations about the $x$ and $y$ axes, using the transformation matrices for rotations as follows

$$\boldsymbol{R_x}(\hat{\boldsymbol{\alpha}}) = \begin{pmatrix} 1 & 0 & 0 \\ 0 & \cos\hat{\alpha} & \sin\hat{\alpha} \\ 0 & -\sin\hat{\alpha} & \cos\hat{\alpha} \end{pmatrix} \quad , \quad \boldsymbol{R_y}(\hat{\boldsymbol{\beta}}) = \begin{pmatrix} \cos\hat{\beta} & 0 & -\sin\hat{\beta} \\ 0 & 1 & 0 \\ \sin\hat{\beta} & 0 & \cos\hat{\beta} \end{pmatrix} \tag{7.7}$$

where $\hat{\alpha}$ and $\hat{\beta}$ are the angles between the projection of the rotation vector to the $yz$ plane and the $z$ axis, and the $xz$ plane and the $z$ axis respectively.

Now, the required rotations are performed about the $z$ axis, using the transformation matrix

$$\boldsymbol{R_z}(\hat{\boldsymbol{\gamma}}) = \begin{pmatrix} \cos\hat{\gamma} & \sin\hat{\gamma} & 0 \\ -\sin\hat{\gamma} & \cos\hat{\gamma} & 0 \\ 0 & 0 & 1 \end{pmatrix} \tag{7.8}$$

where $\hat{\gamma}$ is the rotation angle in radians for the geometric transformation of the edge.

To compute the rotations of the edges about the $\overrightarrow{q}$ axis , we multiply all the preliminary geometric transformations matrices and their respective inverses to return the geometry to its original position after the rotations about the $z$ axis, equivalent to the rotations about the $\overrightarrow{q}$. This is computed as follows

$$\begin{pmatrix} x' \\ y' \\ z' \\ 1 \end{pmatrix} = \boldsymbol{T}^{-1}\boldsymbol{R}_x^{-1}\boldsymbol{R}_y^{-1}\boldsymbol{R}_z\boldsymbol{R}_y\boldsymbol{R}_x\boldsymbol{T} \begin{pmatrix} x \\ y \\ z \\ 1 \end{pmatrix} \tag{7.9}$$

where $x$, $y$ and $z$, and $x'$, $y'$ and $z'$ denotes the coordinates of the geometry before and after transformations and can be replaced by the coordinates of the starting $p_0$ and ending $p_1$ points of the edges.

Next, the translations of the edge along the $\overrightarrow{p}$ axis by the distance $d$ are defined by vector $m$ as follows

$$m = \overrightarrow{p} \times d \tag{7.10}$$

and the translation matrix as

$$M = \begin{pmatrix} 1 & 0 & 0 & m_x \\ 0 & 1 & 0 & m_y \\ 0 & 0 & 1 & m_z \\ 0 & 0 & 0 & 1 \end{pmatrix} \tag{7.11}$$

where the $m_x$, $m_y$ and $m_z$ are the components of the translation vector. Note that as the edge is translated out-of-plane, it keeps the shape of the reciprocal configuration as close as possible as defined in Subsection 7.1.1.

Finally, the endpoints of the each translated edge are obtained as follows

$$M \times p_{0_{(x,y,z)}} \quad , \quad M \times p_{1_{(x,y,z)}} \tag{7.12}$$

The eccentricities $u$ after geometric transformations are calculated by Equation (7.4), using the endpoints obtained from Equation (7.12).

Now, the two inequality $g$ constraints for the tolerances added to the target eccentricities $u_c$ and the topology configuration are introduced. The following inequality constraint provides the clearance added to the target eccentricities $u_c$

$$\mid u - u_c \mid - \omega \leq 0 \tag{7.13}$$

where $\omega = 1$ in order to provide a tolerance of 1 mm. The topology arrangement of edges refers to the relative position between each two edges. Figure 7.18a shows the topology between two edges, where edge A is on the top of edge B and where edge A' is underneath edge B'. The target topology is considered as the topology obtained after rotations as specified in the last Subsection 7.1.1. Therefore, the inequality constraint will check that the topology arrangement between elements is the same as the target topology. This is accomplished by evaluating the direction of the eccentricities as shown in Figure 7.18b.

The general formulation of the minimisation problem is stated as follows:

$$\begin{aligned} \text{Minimise:} \quad & f(\boldsymbol{X}) = \sum_{i=1}^{k} (u_i - u_{c,i})^2 \\ \text{Subject to:} \quad & g_1(\boldsymbol{X}) = \min(\Delta z) \quad \leq 0 \quad , \quad \text{for} \quad i = 1, ..., k \\ & \text{where} \quad \Delta z = \max\Big\{(u_{c,i} - \omega) - u_i \quad , \quad u_i - (u_{c,i} + \omega)\Big\} \\ & g_2(\boldsymbol{X}) = A \cdot B > 0 \end{aligned} \tag{7.14}$$

where $k$ refers to the number of eccentricities to solve in the structure, and the $A$ and $B$ are the directional vectors for the eccentricities before and after optimisation respectively.

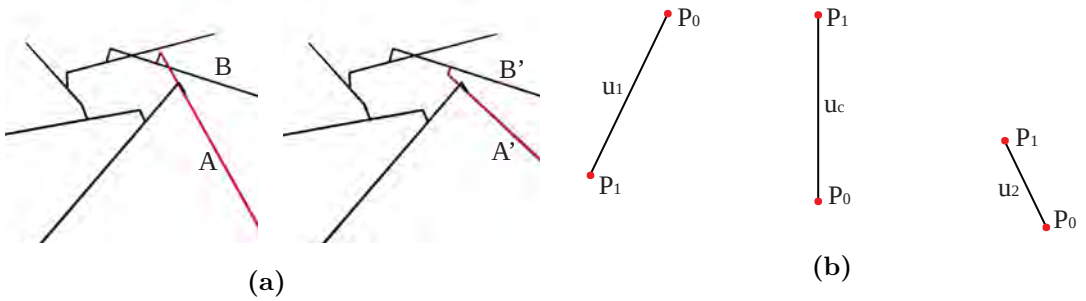


**Figure 7.18:** (a)Topology arrangement between edges in reciprocal configuration. Edges AB are arranged top/bottom and edges A'B' bottom/top. (b) Target eccentricity $u_c$ with endpoints $P_0$ and $P_1$, and different eccentricity solutions found $u_1$ and $u_2$, where $u_2$ has the same topology arrangement as $u_c$.

Note that if the inequality constraint $g_2$ imposed to keep the topology arrangement fixed is not satisfied, there will be no solution. However, there will be cases in which the edges cannot maintain the same connectivity among them. Therefore, for these cases where no solution is found, this constraint is eliminated from Equation (7.14), and the minimisation problem becomes

$$\begin{aligned} \text{Minimise:} \quad & f(\boldsymbol{X}) = \sum_{i=1}^{k} (u_i - u_{c,i})^2 \\ \text{Subject to:} \quad & g_1(\boldsymbol{X}) = \min(\Delta z) \quad \leq 0 \quad , \quad \text{for} \quad i = 1, ..., k \\ & \text{where} \quad \Delta z = \max\Big\{(u_{c,i} - \omega) - u_i \quad , \quad u_i - (u_{c,i} + \omega)\Big\} \end{aligned} \tag{7.15}$$

Therefore, the conditions imposed to the topology arrangement are

$$\begin{cases} \text{if} \quad A \cdot B > 0 & \rightarrow \text{Equation (7.14)} \\ \text{else} & \rightarrow \text{Equation (7.15)} \end{cases} \tag{7.16}$$

Additional bounds are introduced to take into account different set up of the series of edges at each iteration. In Figure 7.16, different cases of set up are presented. For some edges, the eccentricities to solve are located at the ends, whereas others have the eccentricities concentrated towards one side of the edge, see Figure 7.19. The last case can cause the edge to shift disproportionately out-of-plane by a considerable amount from one side only, as depicted in Figure 7.20, which results in a non optimal topology. For those edges where the eccentricities are concentrated towards one side of the edge, a set of lower and upper bound values are imposed to the design variables

$$L_{B1} \leq x_1 \leq U_{B1} \quad ; \quad L_{B2} \leq x_2 \leq U_{B2} \tag{7.17}$$

where $L_{B1}$ and $U_{B1}$ are the lower and upper bound for the design variable of the angle of rotations and are $-\frac{\pi}{5}$ and $\frac{\pi}{5}$ respectively, and $L_{B2}$ and $U_{B2}$ are the lower and upper bound of the design variables of the distances for translations, which are $-\Gamma u_c$ and $\Gamma u_c$

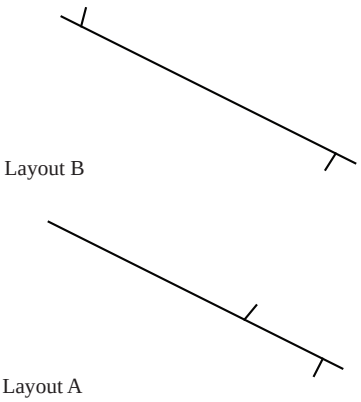


**Figure 7.19:** Set-up of edges with respect the position of eccentricities to be solved per iteration. Layout A eccentricities concentrated on one side, and Layout B eccentricities at both ends.

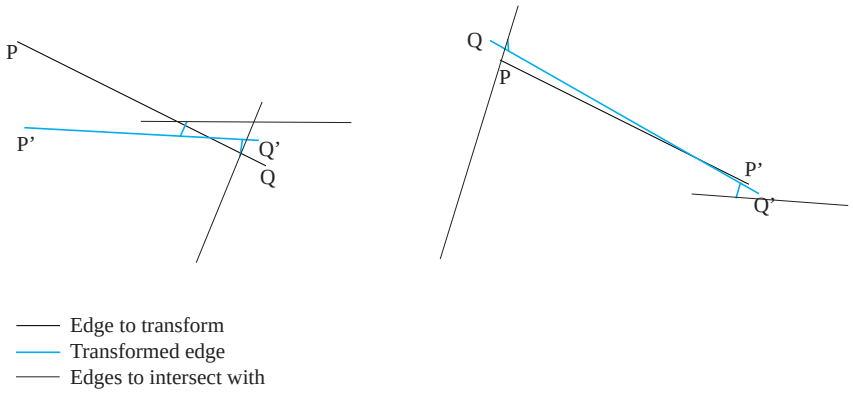


**Figure 7.20:** Layout of edges to solve for rotations and translations

respectively. The default value used for $\Gamma$ is 2.5.

#### 7.1.2.1 Hinge method for edges where no solution is found

In addition, the method can be decomposed into smaller steps if no solution is found for a series of edges simultaneously.

For example, assuming that there is no solution for the three edges (A, B and C) in Figure 7.21, the method is simplified by finding first single eccentricities for those edges that intersect with fixed edges. That is edges A and C intersects with edges A' and C', which are said to be fixed because their matrix $\boldsymbol{X}$ of the design variable is already defined. Once the eccentricities are defined, they are used as hinges to allow for rotations of the edges A and C along A' and C' respectively (see Figure 7.21). Note that in this case, the rotations occur from the position of the eccentricity instead of from the midpoint of the edges. In this way, edges A and C rotate using the hinge method, while edge B is free to rotate and translate according to the general formulation until a solution is found. By doing so, the eccentricities in edges A and C will not change, and only the eccentricities for edge B are to be solved, as depicted in Figure 7.21.

The hinge method uses the same formulation of the optimisation problem as in Equa-

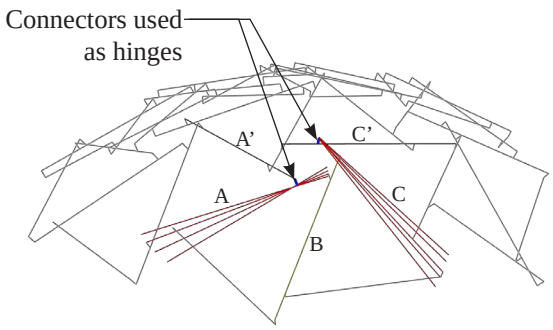


**Figure 7.21:** Rotation of individual edges to find eccentricities. In this example the edges in blue are fixed to their adjacent edges and are allow to rotate along them. Therefore, keeping the eccentricities at that point while finding the optimal eccentricities required.

tions (7.14) to (7.17). However, the second column of the design variable $\boldsymbol{x}_2$ is zero for those edges solved using the hinge method (e.g. edges A and C from Figure 7.21).

#### 7.1.2.2 Iterative method

The optimisation problem presented above is performed iteratively in each of the set of edges. The subdivision of edges is depicted in Figure 7.22. It starts with the definition of a seed vertex, where the first set of edges to be optimised are selected. This can be one of the middle vertices of the entire structure. In this figure, the seed vertex corresponds to the vertex 1, and the first set of edges are the six edges incident on the vertices. Note that in order to solve the eccentricities among the first six edges, only two eccentricities per edge are to be solved. Next, for the second set, all the edges around the first six edges, corresponding to the edges in red in Figure 7.22, are selected. Similarly, only two eccentricities per edge are to be solved. The subdivision of the edges is continued likewise iteratively. The next set of edges corresponds to the ones incident in the six vertices around the first seed vertex, and then to the edges around all the edges incident in these six vertices. Note that in general, the subdivision is grouped into two different set types, those sets of edges incident in the vertex, and those around it. For each iteration, the problem is divided into two following this subdivision.

The flowchart of the whole iterative process is presented in Figure 7.23. In order to provide an organised system for the vertices and set of edges for each iteration, a series of lists and tables are introduced and described below.

The list $V_j$ contains the vertices for each iteration and is defined as

$$V_j = \{v_1, ..., v_n\}$$

where the indices $j$ and $n$ refer to the number iterations and the number of vertices per

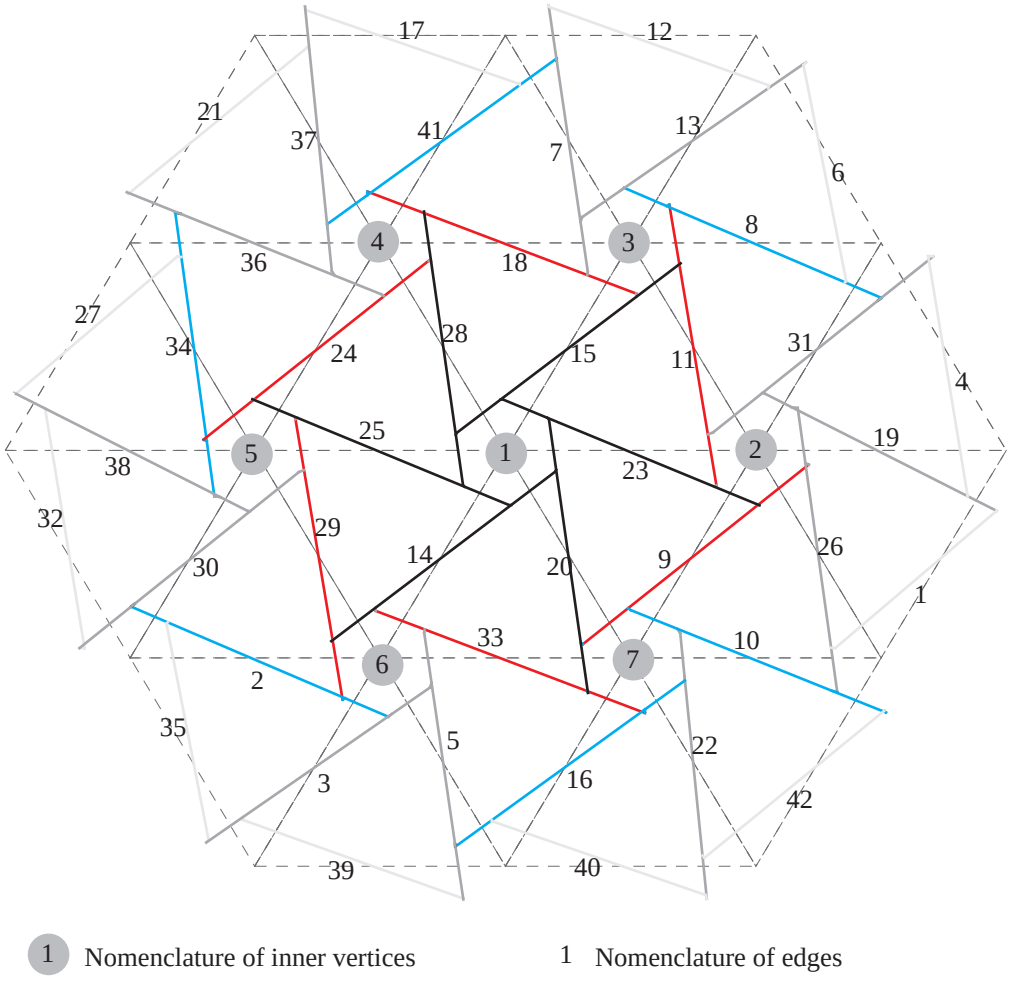


**Figure 7.22:** Subdivision of edges for iterations.

iteration respectively. The table $C_j$ for the edges of the first set type is defined as

$$C_j = \begin{Bmatrix} e_{1,1}, ..., e_{1,r} \\ ... \\ e_{n,1}, ..., e_{n,r} \end{Bmatrix}$$

where the index $r$ refers to the maximum number of edges per each vertex per iteration. Finally, the list $E_j$ for the edges of the second set type is defined as

$$E_j = \{e_1, ..., e_s\}$$

where the index $s$ refers to the maximum number of edges per iteration.

As a demonstration, the lists and tables used for the subdivision of edges for each iteration for the structure shown in Figure 7.24 are presented below. The geometry of the structure was defined following the method presented in this section and was optimised for the eccentricities according to the culm diameters of the oldhamii species analysed in

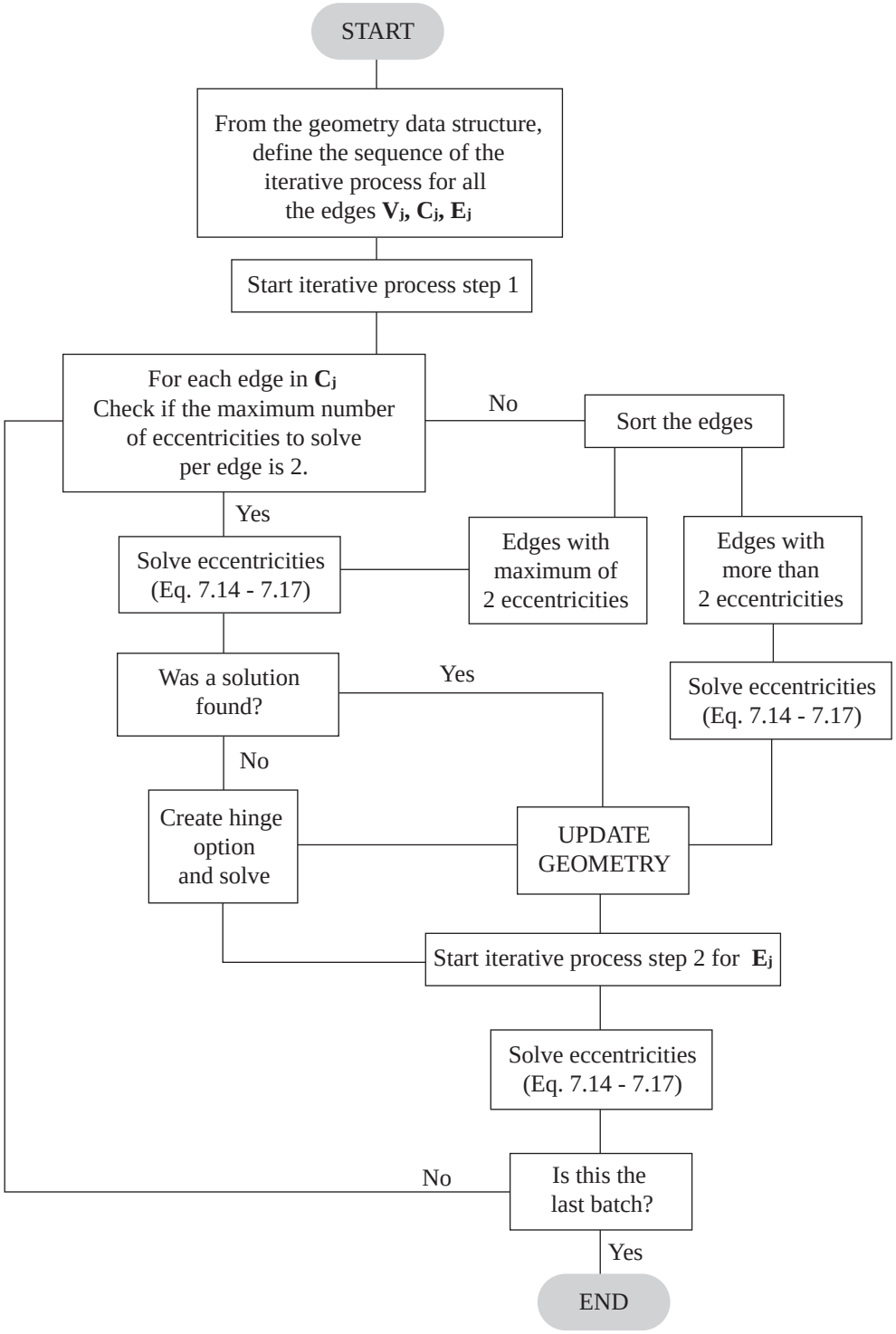


**Figure 7.23:** Flowchart of the iterative process for solving the eccentricities.

Chapter 4. This structure is later used in subsequent chapters as an example.

The $V_j$ lists for the vertices are

$$V_1 = \{v_1\} \quad , \quad V_2 = \{v_2, v_3, v_4, v_5, v_6, v_7\}$$

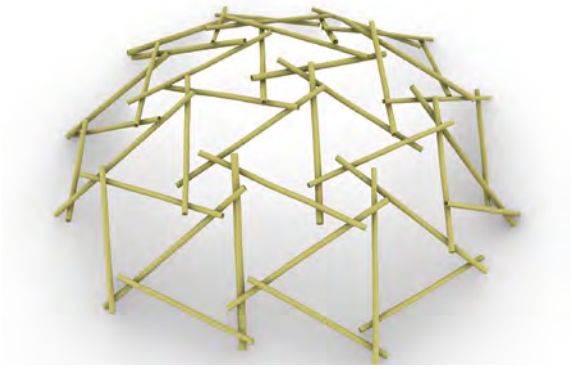

**Figure 7.24:** Reciprocal structure with optimised eccentricities.

The list and table $C_j$ for the edges of the first set type are

$$C_1 = \{e_{23}, e_{15}, e_{28}, e_{25}, e_{14}, e_{20}\} \quad , \quad C_2 = \begin{Bmatrix} e_{26} & e_{19} & e_{31} \\ e_{8} & e_{13} & e_{7} \\ e_{41} & e_{37} & e_{36} \\ e_{34} & e_{38} & e_{30} \\ e_{2} & e_{3} & e_{5} \\ e_{16} & e_{22} & e_{10} \end{Bmatrix}$$

Finally, the list $E_j$ of edges for the second set type are

$$E_1 = \{e_9, e_{11}, e_{18}, e_{24}, e_{29}, e_{33}\} \quad , \quad E_2 = \{e_1, e_4, e_6, e_{12}, e_{17}, e_{21}, e_{27}, e_{32}, e_{35}, e_{39}, e_{40}, e_{42}\}$$

These lists and tables represents the subdivision of the total number of edges of the structure in Figure 7.24 consisting in two general iterations.

## 7.2 SBD in structural morphology

This section presents the methods developed to select the bamboo culms for each of the elements in a structure and to incorporate the discretised geometric properties of bamboo culms into the digital structural model.

The first method consists of an optimisation problem for the selection of bamboo culms for each element in the structure, including their positions along the element. The problem is based on two main criteria for the optimal position on the longitudinal and transverse directions. Figure 7.25 illustrates the flowchart for the overall procedure. The first criterion is the relative positions between the connections in the elements and the nodes in the culms to prevent clashing while at the same time installing the connection close to the node.

The second criterion considers the relationship between the eccentricities and the diameters in the transverse direction. The mathematical formulation of the optimisation problem is set up based on these two main geometric criteria. Furthermore, a basic math-

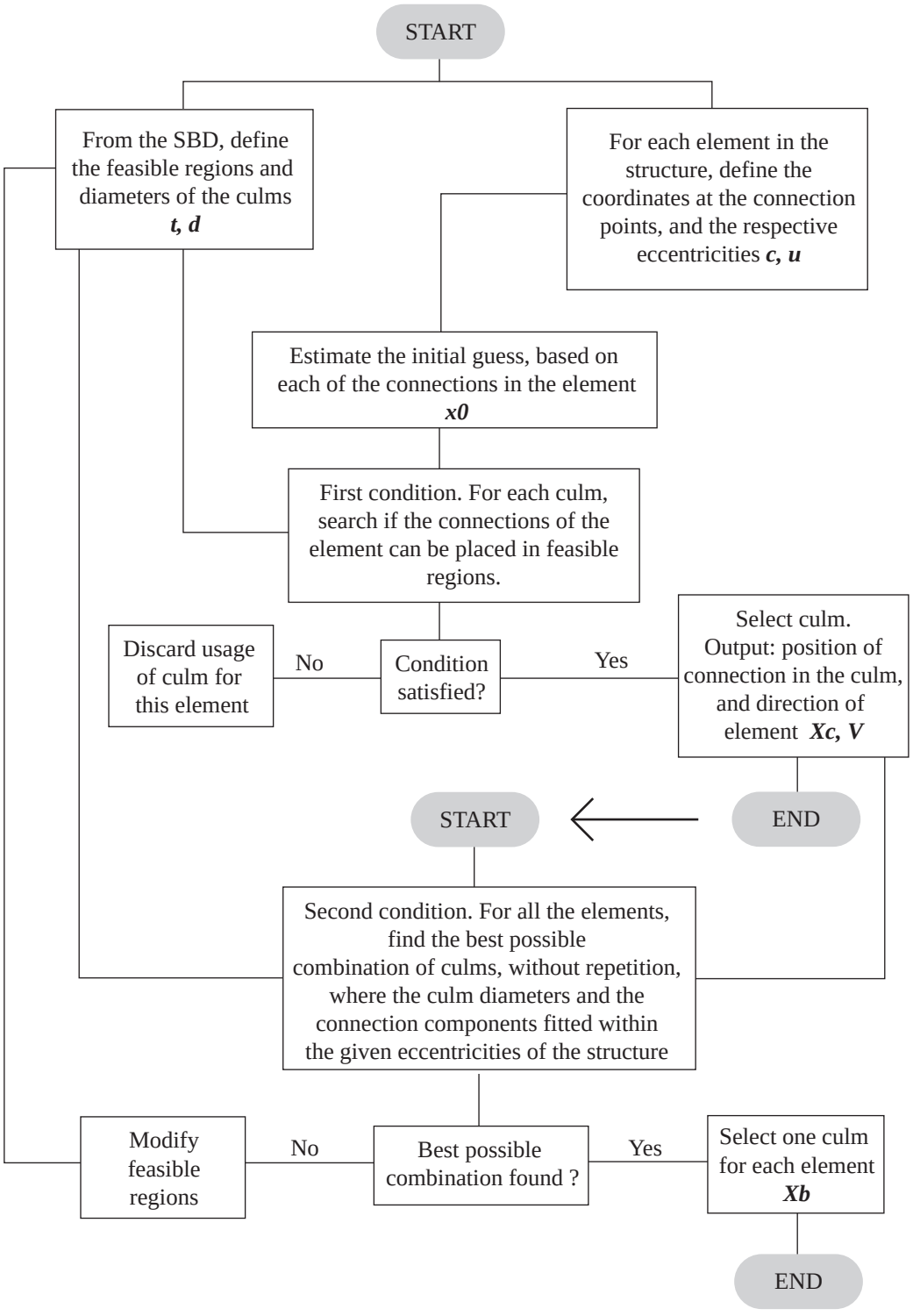


**Figure 7.25:** Flowchart of the two steps optimisation problem for the selection and position of the culms for each of the elements of a given structure.

ematical formulation is set up considering the mechanical properties of bamboo culms and the overall displacements of the elements in the structure, with the aim of assessing the feasibility to extend the method further to account for the deflections of the structure.

The section finalises with the criterion used to incorporate the discretised geometric properties for each of the selected bamboo culms to use for each element.

Prior to define the constraints criteria, the proposed connections for bamboo culms are briefly described as the definition of the optimal position of bamboo culms along the element depends on the type of connection. These connections are fully introduced in the next Chapter 8. There are two types of connection systems proposed (See Figure 7.26). One consists of a series of timber blocks to clamp the bamboo culms in position, and the other consists of a pair of vertical elements joined to the culms by steel bands clamped around the bamboo culms.

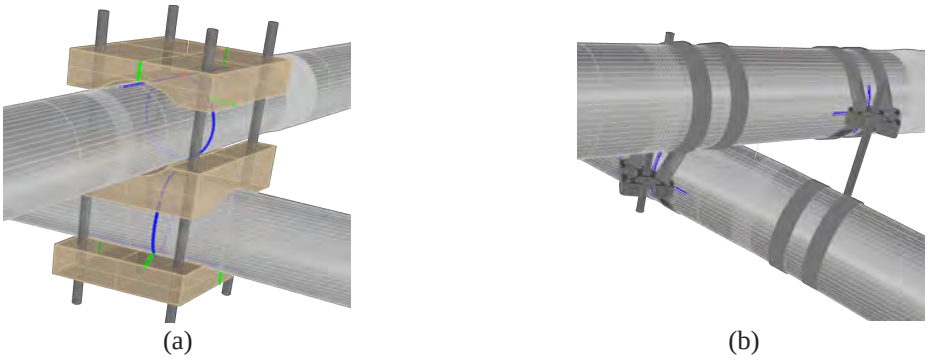


**Figure 7.26:** Connection systems for bamboo culms. (a) Timber and (b) aluminium connection to installed in bamboo culms.

In the subsections below, feasible areas along the culm will be defined, which indicates where along the culm the connections can be installed. This is to prevent clashing between the nodes in the bamboo culms and the connection components. In this case, the specific geometry of each connection is considered for the definition of the feasible areas. Note that the timber blocks of the first connection are fully in contact with the bamboo culm, whereas the aluminium connections are only in contact with the connection components at the location of the steel bands. The selection of the type of connection system for a bamboo structure is independent of these methods. These methods are adapted to the required type of connection system by changing the feasible areas. These methods can be used for any type of connection system and the two proposed bamboo connection system are used only to illustrate the procedure of selection and position of bamboo culms in the structure.

### 7.2.1 Constraint criterion for the longitudinal direction

This subsection defines the constraint vector $\boldsymbol{t}$ for the longitudinal direction for the two connection systems presented in Chapter 8. Figure 7.27 depicts the feasible regions $F$ for the timber connection system, which represent the zones where all the points satisfy the

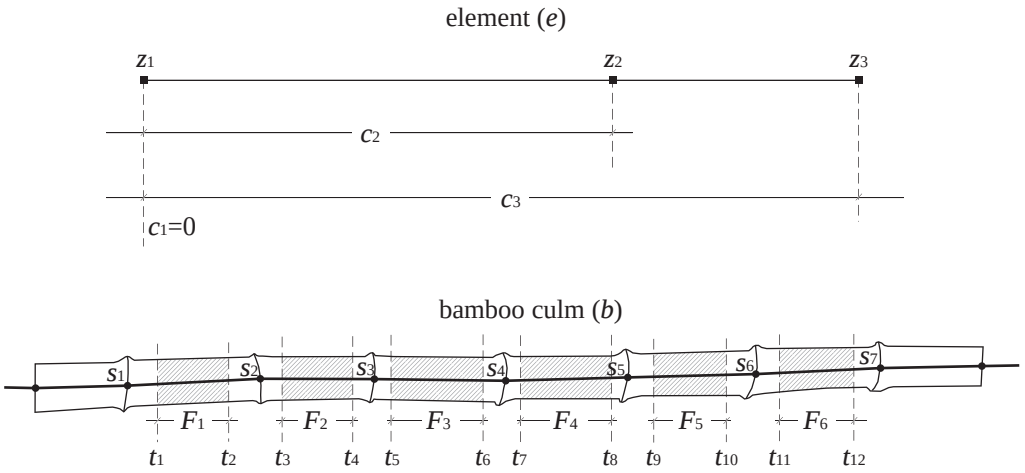


**Figure 7.27:** Geometric constraints in the longitudinal direction. The element $e$ is represented as a line element with its respective connections $z$. The feasible regions $F$ are indicated along the bamboo culm with a dashed hatch, where the coordinates $t$ represents the lower and upper bounds for each feasible region respectively, and $s$ are the node coordinates. Assuming that the $z_1$ is used as the initial guess for the search, the distances between $z_1$ and the rest of the connections $z$ is given by $c$.

constraints. These are defined by the coordinates $t$ located along the axis and are calculated for each culm taking into consideration the type of connection, and the width node coordinates ($xt$ coordinates from the SBD as in Table 4.7). The coordinates $t$ represents the lower and upper bound for each feasible region. Below, the definition of the feasible regions for the timber and the aluminium connections are presented.

#### 7.2.1.1 Feasible regions for installation of timber connections

From Figure 7.27 we can see that the feasible regions are defined at each internode. To define the $t$ coordinates, the lower and upper bound for each feasible region is determined as the closest possible position of the timber connection to the node. The objective is to prevent clamping the node within the timber blocks. These coordinates are established based on the geometry of the timber connection.

Figure 7.28, depicts feasible regions for a timber connection. The view of the figure corresponds to a plane (e.g. $xy$) perpendicular to the axis of the eccentricities and parallel to both elements that are being connected. The location of the timber connection in Figure 7.28, represents the optimal position. The coordinates of the connections are denoted by $z$ and are considered to be at the centroid of each connection. Note that in this example the connection is in the same position as the coordinate $t_u$. Therefore, the distance between $z_1$ and $t_u$ is zero, which is equivalent to the best position. The subscripts $u$ and $l$ in the $t$ coordinates refer to the lower and upper bound of each feasible region.

The distance A in the Figure 7.28 corresponds to the distance from the $xt$ coordinates to the coordinates of the connection. However, when no solution is found, the feasible regions are modified to increase the possible solutions. The distances $B$, $C$ and $D$ in the

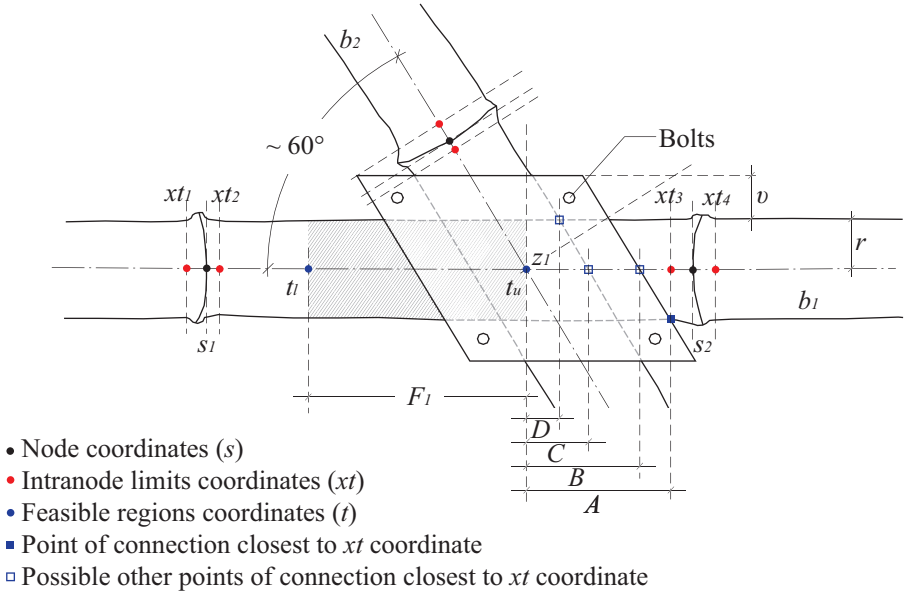


**Figure 7.28:** Feasible regions $F$ on the culm for determination of the position of timber connections.

figure correspond to the reduction of the optimal distance $A$. These solutions allow the node to be inside the timber blocks at different positions.

The position of the $t$ coordinates depends on the angle of intersection between the two elements. Herein, to simplify the calculation, and avoid recalculating the coordinates at each iteration, the angle is considered fixed. For roughly regular triangular tessellations of degree 6, where the angle between the elements is $\approx 60°$, the calculation of $A$, $B$, $C$ and $D$ are given by

$$A = \frac{r+\upsilon}{\cos 30°} + r\tan 30° \quad , \quad B = \frac{r+\upsilon}{\cos 30°} \quad , \quad C = \frac{r}{\cos 30°} \quad , \quad D = r\tan 30° \tag{7.18}$$

where $r$ is the radius of the culm at the internode (equivalent radius as in Chapter 4), and $\upsilon$ is the distance between the culm outer surface and the edge of the timber block. Thus, the $t$ coordinates for each node of the bamboo culms for the timber connections are

$$\boldsymbol{t} = \begin{pmatrix} t_u \\ t_l \end{pmatrix} = \begin{pmatrix} xt_k - A_k \\ xt_{k+1} + A_{k+1} \end{pmatrix} \tag{7.19}$$

where the index $k$ indicates the number of $xt$ coordinates. If no solution is found, $A$ can be replaced by $B$, $C$ or $D$ in order to increase the feasible regions.

#### 7.2.1.2 Feasible regions for installation of aluminium connections

The typical case for the aluminium connections is depicted in Figure 7.29. In this connection system, the $z$ coordinate of the connection is placed in the centroid of the overall connection where there are no physical components. Contrary to the constraint conditions

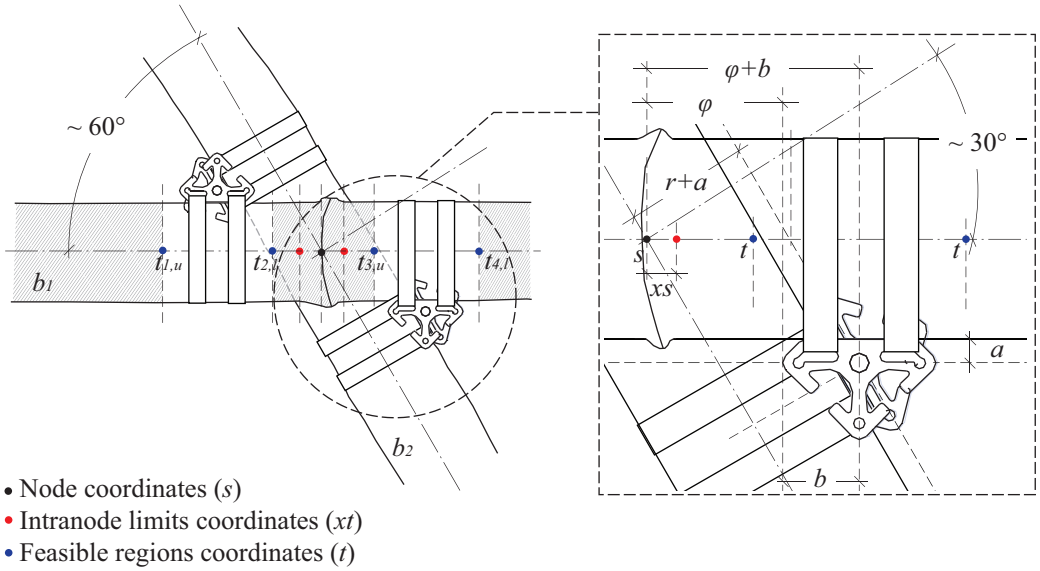


**Figure 7.29:** Feasible regions $F$ on the culm for determination of the position of aluminium connections.

for the timber connection, in this connection, the optimal point is where the $z$ coordinate is exactly in a node coordinate $s$. Thus the feasible regions are defined to avoid installing the aluminium components against the node, to prevent difficulties in the fitting of the connection components. In addition to the feasible regions in the internode, this connection system also has feasible regions in the nodes. The number of $t$ coordinates for this case is four per node, as shown in Figure 7.29, and are denoted by $t_{1,u}$, $t_{2,l}$, $t_{3,u}$ and $t_{4,l}$.

The position of the feasible regions for this connection system depends on the particular aluminium components. The dimensions $a$ and $b$ correspond to the distances from the edge of the aluminium component and the hole clearance and half width of the component respectively (see Figure 7.29).

In similar manner, the geometry of the connections is considered for roughly regular triangular tessellations of degree 6, with elements joined at $\approx 60°$. The location of the $t$ coordinates at both sides of the nodes is given by the distance $\varphi$ plus the distance $xs$ between the nodes and the respective $xt$ coordinates, as shown in Figure 7.29. The calculation of $\varphi$ is given by

$$\varphi = \frac{r+a}{\cos 30°} + \Big(r + a\tan 30°\Big) - b \tag{7.20}$$

where $a$ is 8.3 mm and $b$ is 26.8 mm for this aluminium component. Thus, the respective $t$ coordinates for each node of the bamboo culms for the aluminium connections are defined by

$$\boldsymbol{t} = \begin{pmatrix} t_{1,u} \\ t_{2,l} \\ t_{3,u} \\ t_{4,l} \end{pmatrix} = \begin{pmatrix} xt_k - (\varphi + 2b) \\ xt_{k+1} - \varphi \\ xt_{k+2} + \varphi \\ xt_{k+3} + (\varphi + 2b) \end{pmatrix} \tag{7.21}$$

To clarify, note that Equations (7.19) and (7.21) both define the feasible regions. However, they refer to feasible regions of different connection systems, and thus shall not be used for the same problem.

### 7.2.2 Constraint criterion for the transverse direction

This subsection defines the constraint vector $\boldsymbol{u_c}$ that represent the target eccentricities, for the transverse direction for the two connection systems presented in Chapter 8. Figure 7.30 depicts the target eccentricities $u_c$ required in the elements, and the total eccentricities $u$ resulting from the diameters of the culms meeting at each connection, plus additional connection components if applicable.

In this step, the criterion for both connection systems differs in that for the timber connection the thickness of the middle timber block is included as part of the material to be within the eccentricities, whereas for the aluminium connection the condition is set up only by the diameters of the culms. As the overall process of the selection of the culms can be iterative, the geometry of the reciprocal system can be updated at each iteration, and then the eccentricities and the target eccentricities for this step shall be updated based on the new geometry. However, at the very first iteration, the target eccentricities shall be defined based on the dimensions of the culms available to use, and herein we defined the target eccentricities for this case.

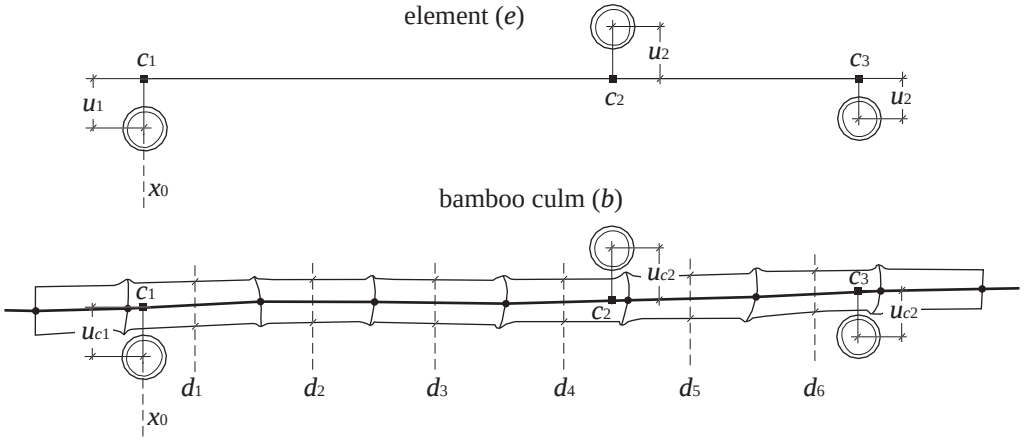


**Figure 7.30:** Geometrical constraints in the transverse direction. The eccentricities $u$ are depicted in the element $e$ at each connection $c$ point. The total eccentricity $U_c$ is illustrated with bamboo culms at each connection point $c$. Note that for purposes of representation, the elements and direction of eccentricities are presented in an orthogonal plane. However, in three dimensional reciprocal structures, these do not lie in the same plane.

#### 7.2.2.1 Target eccentricities for timber connections

The constraints for the second step are defined by the diameter of the culms and the components of the connection systems (e.g. timber blocks).

Figure 7.31 depicts the transverse arrangement of elements. The combination of the radius of culms $r_1$ and $r_2$, together with the thickness of timber in the middle block $\mu$, results in a target eccentricity $u_c$ defined by

$$u_c = r_1 + r_2 + \mu \tag{7.22}$$

where $r_1$ and $r_2$ correspond to the radius of both culms respectively. The target eccentricities are computed for all the connections in the structure as in Equation 7.22. For solutions where $u_c < u$, the thickness $\mu$ needs to take the difference and increase in size. However, when $u_c > u$ there is no solution.

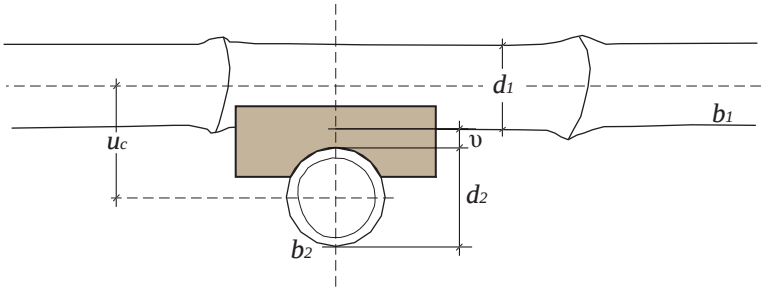


**Figure 7.31:** Arrangement of components in the transverse direction for the timber connection.

#### 7.2.2.2 Target eccentricities for aluminium connections

Figure 7.32 shows a transverse section of the aluminium connection. In this connection, the value of distance $\mu$ represents the space in between the two culms. However, this distance is not necessary and is not considered for the estimation of the target eccentricities. The radius of both culms defines the target eccentricities as

$$u_c = r_1 + r_2 \tag{7.23}$$

Note that Equations (7.22) and (7.23) defined the same parameter but for different connection system. For solutions where $u_c < u$, the space between the culms is increased together with the vertical components of the connection located at opposite sides, where $u_c > u$ there is no solution.

### 7.2.3 Formulation of the optimisation problem

Once the constraint vectors $\boldsymbol{t}$ and $\boldsymbol{u_c}$ are defined, the formulation of the two-step optimisation problem can be set up in general for the two connection systems. Below, the

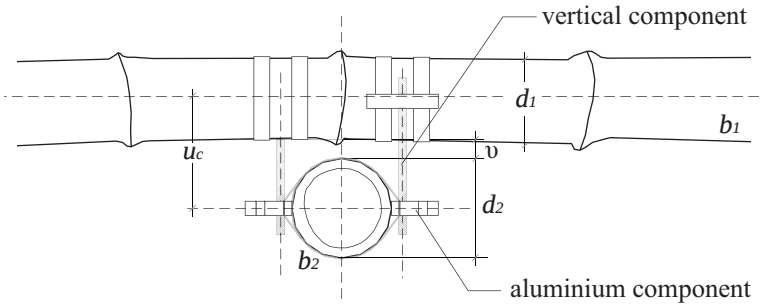


**Figure 7.32:** Constraints for the aluminium connection in the transverse direction.

mathematical formulation of the two steps is provided, followed by a formulation set up to minimise the displacements of the reciprocal system.

#### 7.2.3.1 First step optimisation problem

The first step consists of an iterative process for each element. It searches for all the possible culms where all the connections of an element are within feasible regions $F$ (see solutions A, B and C in Figure 7.33). The feasible regions are defined by the $t$ coordinates $\{t_1, t_2, ..., t_n\}$, where $n$ is the number of $t$ coordinates in each culm. The position of the connections are determined by the distances $c$, and thus $\{c_1, c_2, ..., c_m\}$, where $m$ refers to the number of connections in each element and can vary between two to four. Because the first connection is used as the design variable to search for the optimal position, the value of $c_1$ is always zero.

The objective function in this step aims to minimise the squared of the mismatch distances between the position of the connections $z_j$ and the $t$ coordinates. The position of each of the connections is defined by

$$z_j = z_1 + c_j \tag{7.24}$$

where $j$ denotes the index of each of the connections as $j = 1, ..., m$. The design variable is a matrix $\boldsymbol{S}$ of size $p \times q$, where $p$ is the number of culms available for the search and $q$ is the

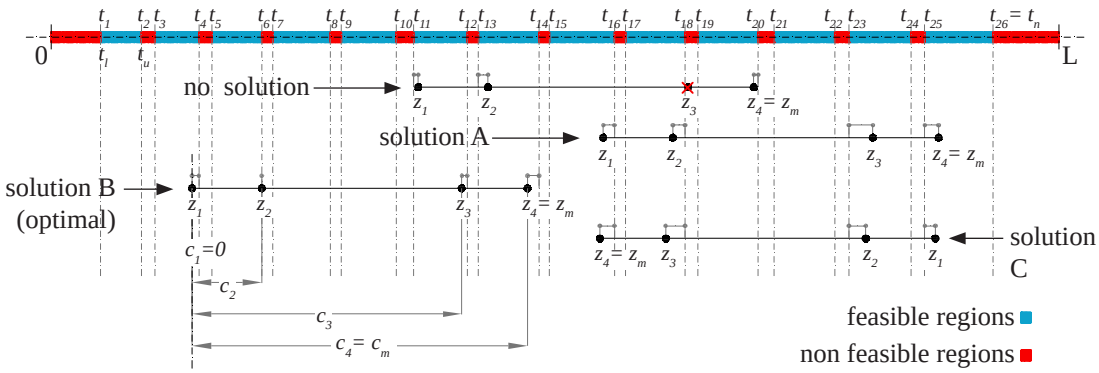


**Figure 7.33:** Example of solutions for optimisation problem.

number of elements. The matrix provides the coordinate position of the connections used for the search, from which the rest of the coordinates corresponding to each connection are calculated as in Equation (7.24). In addition, a matrix $\boldsymbol{D}$ indicating the direction of the elements in the connection is provided. This specifies whether the solution was found from bottom to top or vice versa (see for example solution C in Figure 7.33).

The problem is subject to an inequality constraint to guarantee that the connections are lying within feasible regions (see Figure 7.33). For all the culms that meet the longitudinal constraints of the elements, the position of all the connections in the culms is determined. Figure 7.33 shows an element with the connections located where no solution is found.

Due to the nature of the problem, a nonlinear algorithm is selected for setting up this first step. In addition, it allows defining nonlinear constraints function as the minimum of the constraint functions, which are set up as the several feasible regions $F$ along the culm defined by the coordinates $t$. The nonlinear problem statement is written as

$$\begin{aligned} S_{\min} &= \min_{z_1 \in [0, L-c_m]} S(z_1) \\ \text{where} \quad S(z_1) &= \sum_{j=1}^{m} \min_{i} (z_1 + c_j - t_i)^2 \\ \text{Subject to:} \quad g(z_j) &= \min(\Delta y) \quad \leq 0 \quad \text{for} \quad j = 1, ..., m \\ \text{where} \quad \Delta y &= \max\{t_i - z_j \quad , \quad z_j - t_{i+1}\} \end{aligned} \tag{7.25}$$

where $\boldsymbol{S}$ is a matrix where each of the elements is a scalar that represents the $x$ coordinate of the connection $c_1$ along the culms, which is used as a design variable for the search. The index $i$ refers to the $t$ coordinates as $i = 1, ..., n$.

The inequality constraint is set up such that the solution is negative if a feasible point is found in $\Delta y$ for each pair of $t$ coordinates corresponding to each feasible region. Therefore, the maximum value of the set of functions $\Delta y$ for each connection, which iterates through all the feasible regions, results in zero or a negative number when a solution is found.

For each culm, the search is done using each of the connections in the elements as design variables. This is done because the nonlinear constraints are not smooth. In general, the solver searches for a local minimum within the nearest $t$ coordinate, but there is no guarantee that it will continue the search through the rest of the feasible regions if no optimal point is found. By running the search through each connection (i.e. $z_j$) the possibility to find the global minima is significantly increased. The optimisation problem described above represents the computation for each element, which iterates through each culm.

#### 7.2.3.2 Second step optimisation problem

The second step begins by taking the matrix of the design variable $\boldsymbol{S}$ generated in the previous step. It searches for the best combination of culms that can be used for all the elements. Contrary to the previous step, this step requires the search of several variables

simultaneously, where the number of variables is the total number of elements, and for all the elements, the best combination of culms is selected.

The objective function is set up to minimise the squared distance between $u_c$ and $u$ for all the connections of the entire structure. In this step a solution is found when at least one culm is linked to each of the elements, without repeating the culms, and where $u_c$ is smaller than $u$. If no solution is found, the feasible regions are to be modified to allow for a more flexible search (see Figure 7.25). For a small number of elements, this can be solved using combinations without repetitions. However, this becomes impractical for problems with a large number of elements. Instead, a genetic algorithm is adopted as it can solve for integer optimisation problems, where the bamboo culms can be treated as integer variables.

The statement of the optimisation problem is written as

$$\begin{aligned} \text{Minimise:} \quad & f(\boldsymbol{x}) = \sum_{k=1}^{h} \Big(u_k - u_{c,k}\Big)^2 \\ \text{Subject to:} \quad & g_k = u_{c,k} - u_k \quad \leq 0 \end{aligned} \tag{7.26}$$

where $\boldsymbol{x}$ is a design variable and is a vector containing the bamboo culms selected for each element in the structure (including the geometry, connectivity and diameters), $h$ denotes the number of connections in the entire structure. The inequality constraint is set up so that the function $g_k$ is negative or equal to zero when a solution is found. In addition, none of the elements in vector $\boldsymbol{x}$ shall be repeated.

#### 7.2.3.3 Formulation of the optimisation problem for mechanical constraints

Until now, the optimisation problem considers only geometric constraints. Herein, a simple method that takes into consideration the mechanical properties of bamboo culms, determined in Chapter 6, and the overall behaviour of the structure, to minimise the displacements is presented. The objective of this formulation is to asses the effect of incorporating these parameters as part of the selection and position of the culms with the aim of improving the overall structural performance of the system.

This method starts with the selection of the bamboo culms to fit the longitudinal requirements of each element as described in Equation (7.25), the second step to the selection of the bamboo culm to use for each element in the structure is defined to minimise the deflections of each element in the structure. Additionally, the eccentricities shall be within a given range. The method described here is to replace the problem statement of Equation (7.26).

The maximum bending moments $M_{yy}$ and $M_{zz}$ for each segment of the structural elements are obtained from the linear static analysis. As the cross-section is assumed to be symmetrical, only the highest moment from $M_{yy}$ and $M_{zz}$ is considered. The stiffness of the elements is maximised by maximising the radius of curvature of the elastic curve.

From the moment curvature relationship (Young et al., 2012), we have

$$\frac{1}{\rho} = \frac{M}{EI} \tag{7.27}$$

where $\rho$ is the radius of curvature, and $EI$ is the flexural stiffness of each of the sections in the elements. To set up the optimisation problem as a minimisation function, then the inverse of the radius of curvature $\frac{1}{\rho}$ is taken. The problem statement takes the matrix $\boldsymbol{S}$ as starting point, and is written as

$$\begin{aligned} \text{Minimise:} \quad & f(\boldsymbol{x}) = \sum_{i=1}^{b} \left(1/\rho_i\right)^2 \\ \text{Subject to:} \quad & g_k = u_{c,k} - u_k \quad \leq 0 \end{aligned} \tag{7.28}$$

where the $\boldsymbol{x}$ is the design variable corresponding to the culm selected for each element. The index $b$ refers to the number of bamboo culms in the structure, $f(\boldsymbol{x})$ is the sum of the inverse of radius of curvature squared.

### 7.2.4 Incorporation of discretised bamboo geometry in structural model

Once the selection of bamboo culms for each element in the structure, and the lengthwise position are defined, the next step is to incorporate the discretised bamboo culms geometry into the structural skeleton. As the discretised geometry for a single culm is not a straight line, is not possible to make the four connecting points in the bamboo culms incident to the four connecting points of the straight lines in the structural model.

To incorporate the discretised geometry, the two connecting points at the extremes, are used as reference to align the discretised elements in the structural model. Figure 7.34 depicts this process. After this process is applied to all elements, the eccentricities will slightly change depending on the out-of-straightness of the bamboo culms at each connecting point. Note that for each connection, one of the end nodes will change and the other remains fixed. Therefore, all the connectors shall be computed again to account for

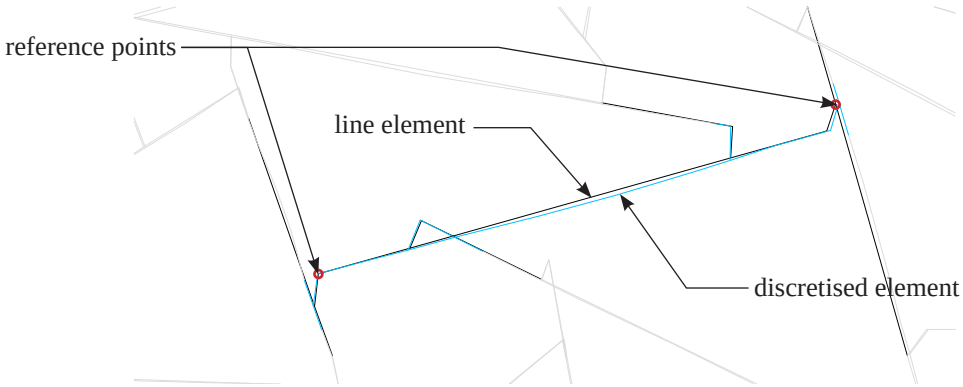


**Figure 7.34:** Alignment of discretised elements to line elements in structural skeleton.

these changes. For those elements with two connections (i.e. boundary elements), these two connecting points are used as the reference to align the discretised elements.

## 7.3 Summary

This chapter introduced the methods concerned with the geometry of the reciprocal systems in view of using varying eccentricities to accommodate the diameters of bamboo culms and the incorporation of the discretised bamboo geometry from the SBD into the structural model.

A novel method to optimise the geometry of reciprocal systems to accommodate the variations in diameter of bamboo culms was developed. It is based on a rotational method, but it takes into consideration how regular or irregular is the tessellation to perform rotations normalised to their dual. The full connectivity between elements to identify the connections was provided. It demonstrated the possibility to create complex reciprocal geometries using the diameter of bamboos as a parameter to allow for the installation of appropriate connection systems and prevent the existence of very small or very large eccentricities. Although the method is limited to triangular tessellations of degree 6, the basis of each of the steps can be extended to a more generalised method to consider other types of tessellations.

Section 7.2 introduced the optimisation problems formulated for selecting the bamboo culms to use for each element in the structure and to find its optimal position based on geometric constraints. This method addressed the problem of installing the connections close to the nodes. Although several authors have recommended this to prevent splitting (refer to Chapter 1), there was no method proposed to address this. The method is based on simple geometric constraints. However, a formulation of the same problem was given to minimise the deflections of the reciprocal system. Chapter 9 will evaluate and discuss the incorporation of discretised geometric properties of bamboo using these methods.

Finally, the criterion to incorporate the discretised geometric properties of bamboo into the digital structural model was introduced.

# Chapter 8

# Connection systems for bamboo reciprocal structures

This chapter discusses the process of developing two different connection systems for bamboo culms in reciprocal structures. The main aim is to gain insight into their structural performance and feasibility for fabrication for the further development of appropriate bamboo connection systems. These are designed considering the forces and moments required to transfer by the connectors, and the criterion defined in Section 3.2. The specific objectives are listed below.

- To review the main challenges with designing connection systems for bamboo.
- To develop connection systems at the conceptual design stage and analyse their load-transfer mechanism.
- To carry out experimental tests to gain insight into the structural behaviour of the proposed connection systems arranged in reciprocal configuration.
- To evaluate the geometric error measured between the digital and physical models.

The connection systems are classified into two categories, timber and aluminium connections. Figure 8.1 provides the view normal to the eccentricity which is used to describe the geometry of the connections.

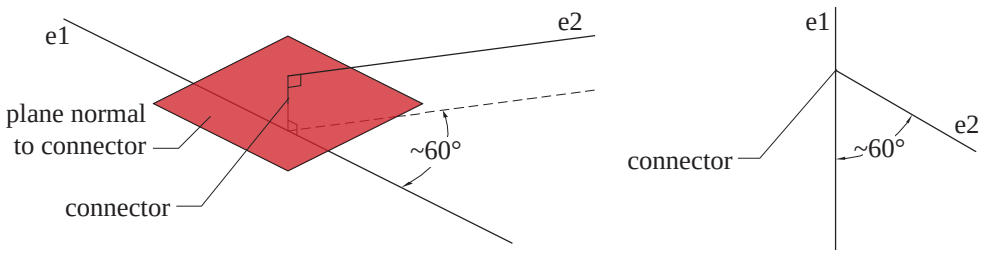


**Figure 8.1:** Direction of eccentricity and shared plane in which both elements lie.

## 8.1 Challenges with bamboo connections

One of the most critical aspects of bamboo constructions are the connections. The Colombian code NTC-5407 (2006) provides guidance on the requirements for the fabrication of bamboo joints, many of which are bolted connections designed for trusses. Similarly, the National Building Code of India IS-6874 (2008b) provides guidance of jointing techniques for round bamboo culms, classified as traditional and modern practices. Furtheremore, López (1981) provides the first practical guide for the design of traditional bamboo connections and the workability of the material. A key aspect highlighted is the position of nodes in elements to avoid splitting or crushing of the culm when loaded in the transverse direction.

The ISO (2004a) standard does not cover the design of jointing techniques. Nevertheless, it specifies that joints shall be based on experience from previous generations, reports on evaluations made after disasters, full-scale tests of the connection, tests on the capacity of each component of the connection or based on design principles. A visual review of the most commonly used connection systems is provided by Dunkelberg (1985), López (1981) and Minke (2012). There is very little data available regarding the strength and stiffness of the connections.

Figure 8.2 shows some jointing techniques used in bamboo constructions to highlight key challenges. The connections can be classified in either type of joint (e.g. orthogonal, diagonal, parallel, multiple elements in one point, in-plane or out-of-plane), or jointing method (e.g. lashing, mechanical fasteners, grouting and metallic or wood pieces). Lashing connections are mostly used in temporary structures such as scaffolding (see Figure 8.2a,b,c). However, strength (Trujillo, 2007) and stiffness are relatively low, and slip is one of the critical issues besides splitting of the rope (Chung and Chan, 2002). A combination of lashing with pins and holes is also found in multiple structures such as housing, but the holes can damage the ropes in the edge of the drill holes (Dunkelberg, 1985). Lashing connections with pins usually require a curve cut (called fish mouth and shown in Figure 8.2c, or flute tip) to provide full contact of the cross-section (Minke, 2012). In some cases, the use of the rope in pin connections is provided to resist tensile forces (Janssen, 1995). The issues with these connections lie in the fact that the culms need to fit accurately to prevent concentration of stresses. Therefore the cuts shall be very precise (Janssen, 1995), but this relies mainly on the workmanship. Additionally, there should be no movement between the pin and the hole to prevent splitting (Dunkelberg, 1985).

A typical connection using horns (mortise and tenon type) is shown in Figure 8.2d. Besides the fact that these also require very good workmanship and fitting between components, the strength of this connection has been reported to be low (Janssen, 1995). Dowel-type connectors including bolts and nails can take many different forms (see for example Figures 8.2e,f,g). The main issue with these connections is the susceptibility of splitting, which is triggered by the perforation of the culm, or shear caused by the absence of nodes or the location of the connection close to the end, as shown in Figure 8.2f.

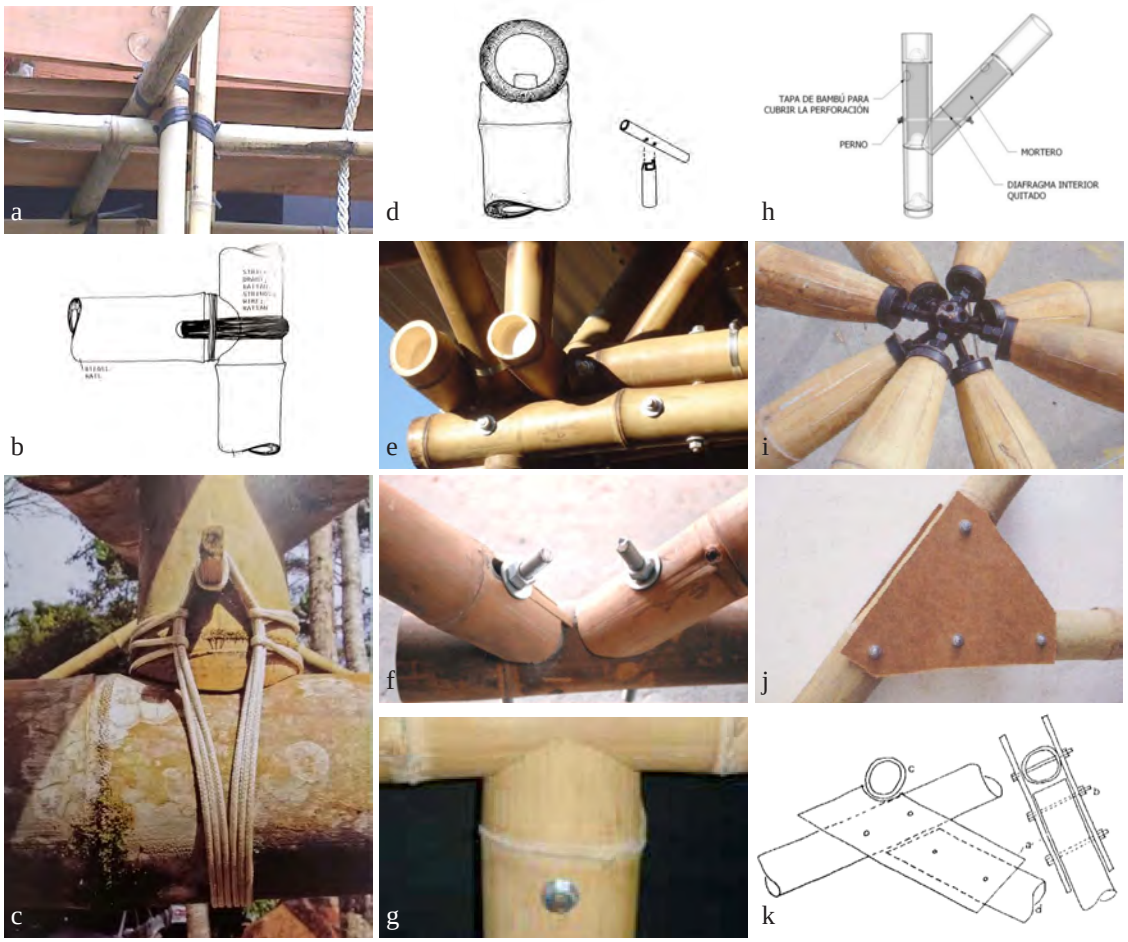


**Figure 8.2:** Jointing techniques for bamboo culms. (a) Lashing connection (Chung and Chan, 2002). (b) Lashing with holes (Dunkelberg, 1985). (c) Lashing with pins (Minke, 2012). (d) Mortise and tenon type (Dunkelberg, 1985). (e-g) Different variations of steel bolted connections by Vahanvati and Vahanvati (2018), Tam (2004) and Ubidia (2015). (h) Steel-bolted with grouting (ICG, 2012). (i) Conical end connection for axial loads designed by Jörg Stamm (Minke, 2012). (j) Wood plates bolted connection (Minke, 2012). (k) Wood plates bolted connection for purlins (Janssen, 1995).

A combination of steel bolted with grouting is a typical type of joint particularly used in Colombia. This provides a significant increase in the strength of the connection about three to five times higher than if no grouting is considered (Trujillo, 2007). However, the consistency of the grout together with the moisture content of the bamboos is critical due to the shrinkage of bamboo (Trujillo, 2007). Another connection using the inside of the internode is shown in Figure 8.2i for the transfer of axial loads. It is a combination of a conical ending connection with steel threaded rod. However, the fabrication and time off-site for the preparation must be taken into account. Finally, although the connectors using wood pieces such as the ones depicted in Figures 8.2j,k have the advantage of pre-fabrication, and are strong and stiff (Janssen, 1995), the culms must be roughly the same diameter to fit, and they also rely on perforation of the culms.

Some of the recommendations for the design of bamboo connections given by Arce

(Arce-Villalobos, 1993; Janssen, 1995) are to prevent the penetration of the culm using nails, screws or bolts, to avoid open ends, to consider the non-uniform geometry of the culm and to maximise the axial strength. He also highlight the need to design connections that prevent large deformations and maximise the strength of the bamboo culms while, at the same time, can be cost effective and allow prefabrication.

## 8.2 Timber connection

The timber connection is based on bespoke fabrication and seeks to provide arguably a more adequate sustainable solution by using natural materials for the connection of bamboo culms. The material selected for the connections in this study was softwood as it is widely available and more cost effective than hardwood due to its relatively fast grow rate in comparison with the latter. Solid sawn lumber was obtained and dressed as appropriate. The softwood grade C16 used has bending strength of 16 $N/mm^2$ and compressive strength of 17 and 2.2 $N/mm^2$ for the longitudinal and transverse directions respectively, and elastic modulus of 8.0 and 0.27 $N/mm^2$ for the longitudinal and transverse directions respectively and a mean density of 370 $kg/m^2$.

Figure 8.3 depicts the design of the timber connection. It consists of three timber blocks that clamp the two bamboo culms together. These timber blocks have a groove fabricated to allow a more evenly distribution of forces to the culm in the transverse direction (refer to Subsection 8.2.2.1). The fabrication methods tested for this connection are presented in Appendix G. Overall, it was found that the use of automated methods such as CNC, can be efficiently used to create the groove in the timber blocks as the fabrication consists of a simple linear milling process. Further automated methods including robotic fabrication are encouraged to explore this as a potential viable method to systematically fabricate multiple timber blocks.

The timber blocks are referred to as bottom, middle and top timber blocks. These are fixed by four steel threaded rods located at each corner. A thin steel plate was installed over the top and bottom timber blocks in order to apply more uniformly distributed loads throughout the timber blocks, which are acting as packing to transfer the loads to the

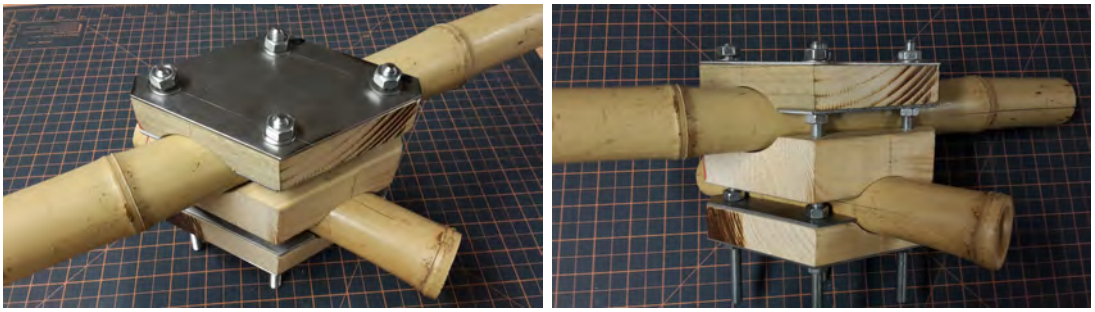

**(a)** **(b)**

**Figure 8.3:** (a) Prototype of the timber connection (b) Transverse view of the timber connection.

bamboo culms. In the interface between the bamboo culms and the timber blocks a thin neoprene sheet is installed in order to provide friction and to allow for small adjustments between the shape of the bamboo culm and the timber components. The total thickness of the neoprene is 3 mm, and based on experimental observations, a total of 1 mm was considered as possible to compress to allow for tolerances required due to irregularities in the cross-section shape.

### 8.2.1 Connection geometry

The geometric parameters of the connection are illustrated in Figure 8.4. These parameters are defined assuming that the cross-section of the culm is a circle. The key parameters that define the overall geometry and dimensions of the timber blocks are: (a) diameter of the culms $D$, (b) angle $\beta$ between the two bamboo culms, (c) angle $\theta$ that defines the depth of the groove, (d) the diameter $\varnothing$ of the steel threaded rods, (e) the end distance for the installation of the steel threaded rods, and (f) the clearance between bamboo culm and steel threaded rod defined as 5 mm to prevent clashing and denoted as $c$ (see Figure 8.4). The angle $\beta$ is obtained from the structural morphology, and for triangular tessellations of degree 6, is approximately 60°. The angle $\theta$ that defines the depth of the groove and therefore the contact area between the timber block and the bamboo culm is empirically defined for the purposes of the connection design based on the dimensions of the material available. The reciprocal modules tested in Subsection 8.4 considers angles between 63° and 47° and the differences in structural performance are discussed below. The steel threaded rods used were M8, for the connections fabricated of culms between 40 and 72 mm in diameter. The minimum end distance for fasteners, including bolts is of 2D for the parallel and perpendicular direction (McMullin and Price, 2017).

The timber blocks fabricated for this research were obtained from timber planks of

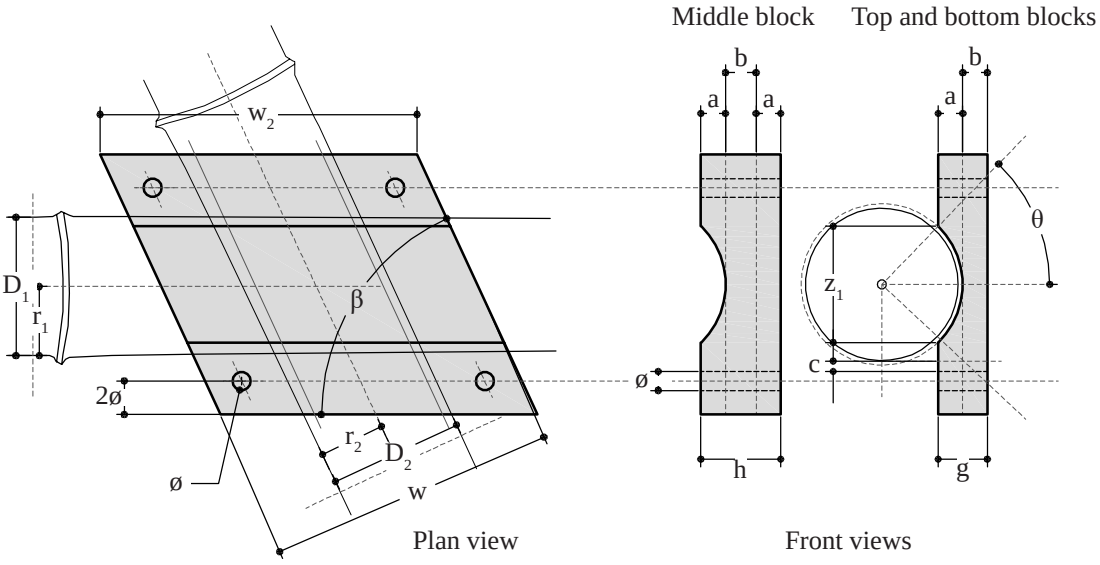


**Figure 8.4:** Geometric parameters of timber connection

sawn timber. Therefore it was important that the standard sizes of the timber planks available in the market can be used for the most common bamboo dimensions. Table 2.1 provides a range of average diameters of different bamboo species considered suitable for construction. The width and thickness of common sawn timber range from 100 to 225 mm and from 47 to 75 mm respectively. These can be used for the fabrication of timber connections for bamboo culms of diameters between 50 and 150 mm.

The calculation of the rest of the parameters dependent on the key parameters is provided below. The minimum width of the connection in the direction perpendicular to the culms is equal to $w$ and given by

$$w = D + 2(2\varnothing + c) \tag{8.1}$$

The depth and chord dimensions for the groove in the timber block are equal to $a$ and $z_1$ and are define as follows

$$a = r - r\cos\theta \tag{8.2}$$

$$z_1 = 2(r\sin\theta) \tag{8.3}$$

where $r$ refers to the radius of the groove and is equal to $r = r_1 + 2$ mm allowance for the neoprene material. Note that $r_1$ corresponds to the radius of the culm to be used for that particular groove. For a single timber connection, the radius of the bottom and top culms might differ.

The thickness of the timber block for the middle and end parts (i.e. top and bottom) are equal to $h$ and $g$ respectively and given by

$$h = 2a + b \tag{8.4}$$

$$g = a + b \tag{8.5}$$

where $b$ is the thickness of the timber blocks that will be transferring the compressive forces to the outer cross-section of the culm. Finally the length of the timber planks equal to $w_2$ is obtain as

$$w_2 = \frac{w}{\cos(90 + \beta)} \tag{8.6}$$

To provide standardised sizes for the fabrication of the grooves in the timber blocks, a set of ranges was defined. This set of ranges was based on the clearance provided by the neoprene material. Figure 8.5 shows the main idea for setting these ranges. The neoprene is a thin sheet of 3 mm thickness that has two purposes, one is to provide greater friction between the bamboo culms and the timber block and the other is to provide a clearance between the timber blocks and bamboo culms to allow for accommodating different bamboo sizes within the same groove size. The value of ranges was set based on the perpendicular distance between the two circles representing the diameters of the culm at the angle $\theta$ (see Figure 8.5). This allows for ranges of 5 mm to be created, based on

the outer diameter of bamboo culms. It is assumed that the maximum compression that the bamboo culm and timber block will produce in the neoprene is 1 mm. For a given range, the whole neoprene pad is compressed 1 mm for the largest size, whereas for the smallest size the neoprene area at the edges of the groove are less compressed as shown in Figure 8.6. For bamboo culms in dimensions between 50 and 150 mm, the perpendicular distance ranges between 0.75 and 0.79 mm. This will allow to fabricate the same groove for diameters within 5 mm in range.

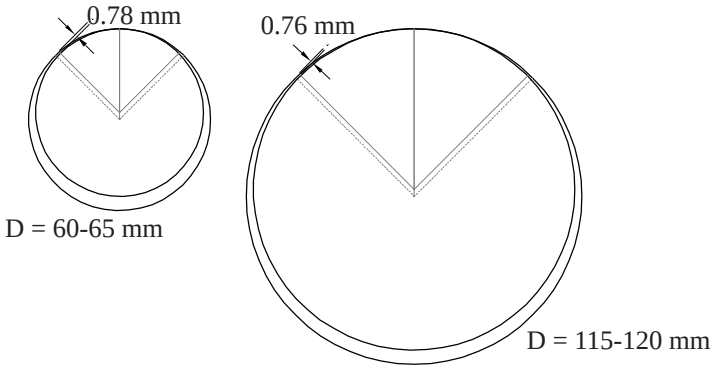


**Figure 8.5:** Tangent distance between two circles for different ranges.

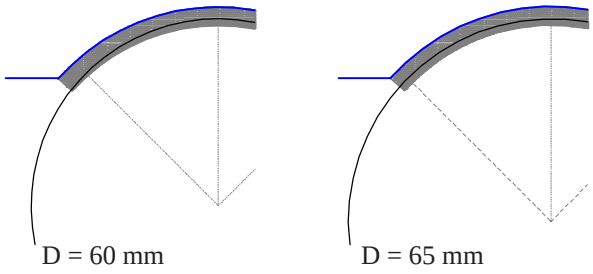


**Figure 8.6:** Arrangement of components to illustrate the use of neoprene for fitting different bamboo diameters within the timber blocks to allow for tolerances.

### 8.2.2 Structural behaviour

The study of the mechanical behaviour presented here is done in parallel to a series of connection prototypes (see Subsection 8.4) assembled in three and five-element modules with the aim of developing understanding on the structural behaviour of the connection system.

The main load transfer mechanism of the timber connection is depicted in Figure 8.7. This connection is designed to transfer the loads between the culms through bearing pressure. The torque applied to the nuts cause tension to the steel threaded rods and hence compression in all the components that are within the four nuts at the top and bottom part of the connection. Figure 8.7a shows the applied forces and the resulting compressive reactions that the culms applied to the timber blocks. This is idealised as

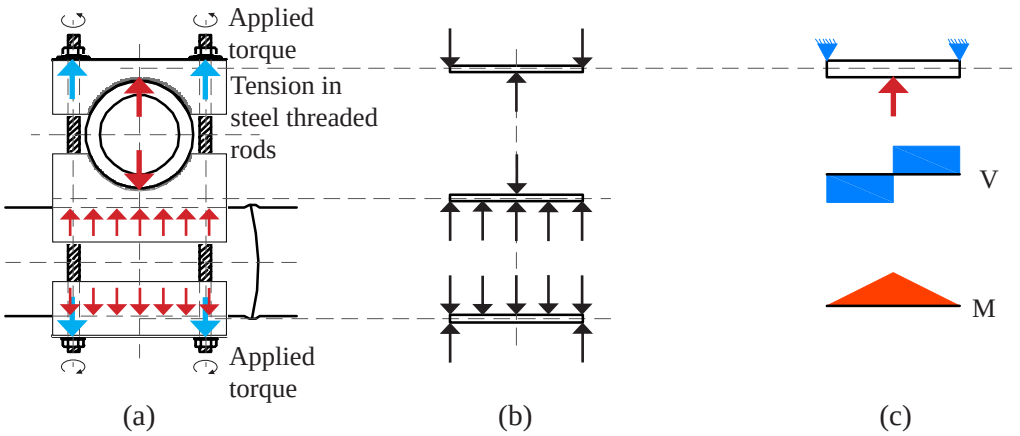


**Figure 8.7:** Load transfer mechanism of timber connection.

three simple supported beams in Figure 8.7b for the top, middle and bottom blocks. For representation, the top culm is oriented normal to the longitudinal axis and the bottom culm perpendicular to it. Assuming that the forces of the top culm can be represented by its resultant and that this lie in the centre of the culm cross-section, the top part of the timber connection can be idealised as a simply supported beam. Therefore, the maximum bending moment and deflections occur at the middle part (see Figure 8.7).

The forces are transferred from the nuts to the timber blocks, through all the components in between, namely the washers and the steel plate. The timber blocks are acting as a continuous beam providing bearing pressure to the steel plate. Therefore, the timber blocks are subjected to a combination of bending moments and bearing pressure. The forces are transferred from the timber block to the bamboo culms by bearing pressure while compressing the neoprene interface.

As seen from the previous Subsection 9.2.1, the connection needs to transfer moments in the $x$, $y$ and $z$ directions. To understand the load transfer mechanism of the connection under external applied loads, it is assumed that a vertical load is applied to the upper node of the connector element as shown in Figure 8.8. Because the direction of the connectors is perpendicular to both elements that are joined at that particular connection, the majority

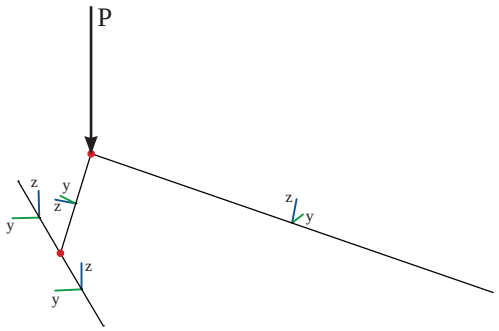


**Figure 8.8:** Vertical load applied to the reciprocal structure through the connector.

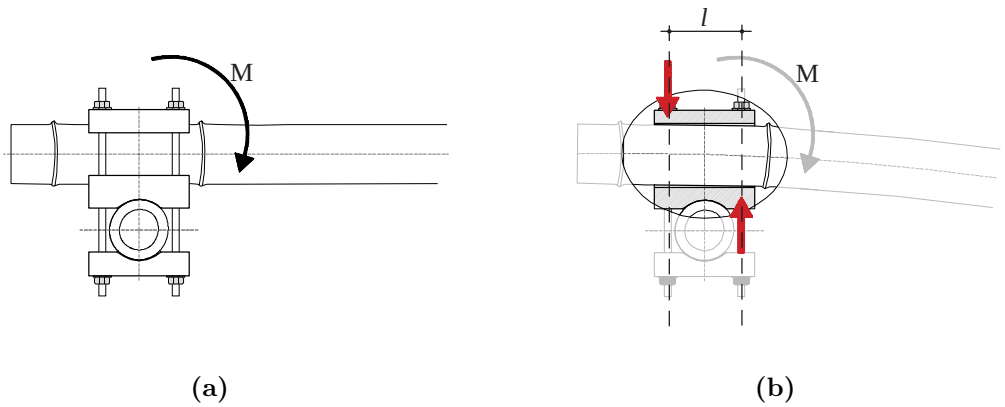


**Figure 8.9:** (a) Moments in the vertical direction. (b) Deformation of the culm and critical points in the culm caused by the moments in the vertical direction.

of the connectors will not have the applied loads normal to the direction of the eccentricity, unless the components supporting the envelope or cladding are designed to do so. This will cause load components in the longitudinal and transverse direction of the connector axis. These forces are eventually transferred to the element at the bottom end of the connector, causing also eccentric moments owing to the connectors length.

Figure 8.9 shows a moment applied to the top element. If the connection is capable of resisting the moments produced by the beam element in this direction, then the angle between the connector and the bamboo element will not change. This moment capacity in the vertical axis of the connection is provided by the push-pull of the steel threaded rods located at opposite sides as depicted in Figure 8.9.

In similar manner, the moments generated in the horizontal direction (i.e. normal to the triangle in the reciprocal system) have to be resisted by the connection (see Figure 8.10a). It might be tempting to assume that due to the triangular geometry there are no moments in the elements creating the triangular shape. However, recall that the elements are not in the same plane and the connectors generate eccentric moments that are trans-

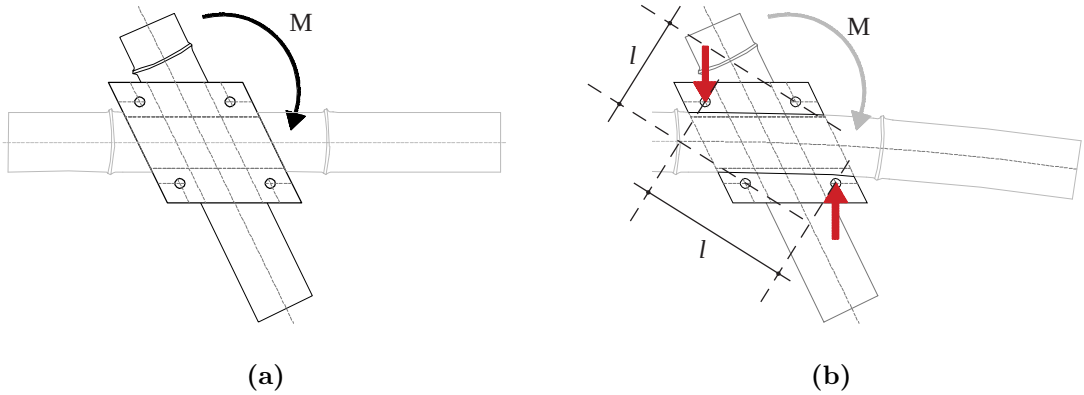


**Figure 8.10:** (a) Moments in the horizontal direction. (b) Deformation of the culm and critical points in the culm caused by the moments in the horizontal direction.

ferred to the elements joined by the connectors. In structures with double curved surface, the structural stability is provided by the in-plane shear stiffness (Harris et al., 2008). The shear stiffness is provided to the structural system by preventing rotations between the elements in the plane that is normal to the surface at that particular point where the two elements are connected. To prevent a change in angle between bamboo elements, the connection needs to be capable of resisting rotational moments in the $x$ direction of the connector. This is provided by the steel threaded rods at two opposite directions, as depicted in Figure 8.10b, causing a push-pull that prevents rotations in this plane.

#### 8.2.2.1 Influence of the means of transferring transverse compressive forces to bamboo culms

Experimental tests on the transverse compressive capacity were carried out to compare the influence between the direct applied load and the load applied using timber blocks with circular groove. The angle $\theta$ that defines the depth of the groove of the timber block was arbitrary (in this case >63°), however, when the load was applied, only the very top and bottom part of the culm cross-section was in contact with the timber blocks. Figure 8.11 shows the two different set-up.

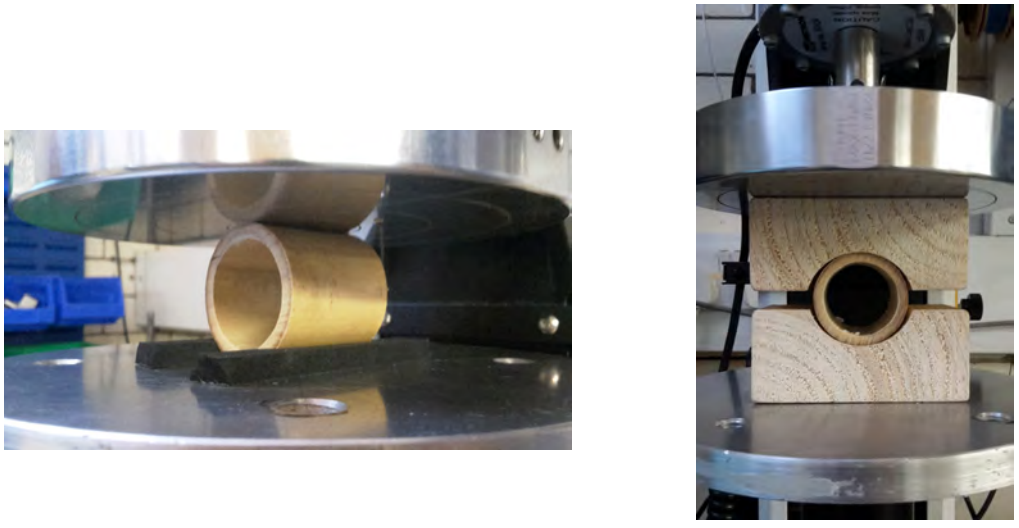

(a) (b)

**Figure 8.11:** Transverse compression tests. (a) Set-up 1. (b) Set-up 2.

To make a direct comparison, the loads of both set-up are idealised as two point loads at opposite sides as depicted in Figure 8.12. These point loads represents the worst-case scenario for the transverse loading of the bamboo culm. We can calculate the circumferential normal stress due to pure bending of a circular ring with two opposite point loads according to Young et al. (2012). This comparison can also be done using only analytical methods and different types of load distribution. However, the equations to calculate these stresses are for linear elastic analysis (Young et al., 2012), and bamboo is an orthotropic material and presents a nonlinear compressive behaviour in the transverse

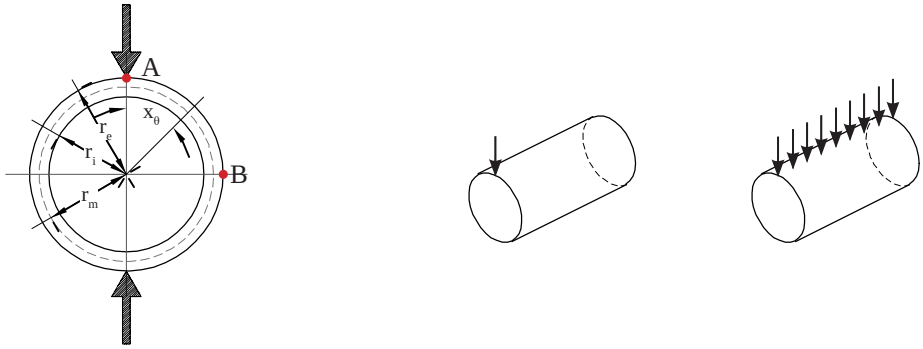


**(a)** **(b)**

**Figure 8.12:** (a)Idealisation of the two point load case on a thin ring. (b) Transverse load due to critical points and clamping force. Notation according to Young et al. (2012).

direction (Sharma et al., 2013). Therefore, experimental tests are more appropriate for this comparison. Below, the formulas for the calculation of the forces and moments and the circumferential stresses are presented according to Young et al. (2012) and following their notation.

Figure 8.13 shows the force normal to the cross-section $N$, the shear force in the radial direction $V$ and the bending moment in the plane of the curve $M$. The circumferential normal stresses are obtained as

$$\sigma_\theta = \frac{My}{Aer} \tag{8.7}$$

where $y$ is the distance from the neutral axis to the required stress measurement in the radial direction, $r$ is the radial distance from the required stress measurement to the centre of the ring, $A$ is the area of the cross-section and $e$ is the distance between the centroidal and the neutral axis, which for thin rings (where $\frac{R}{d} < 8$; and $d$ is the depth of the cross-section, i.e. thickness) is

$$e = R - r_n = R - \frac{A}{\int_A dA/r} \tag{8.8}$$

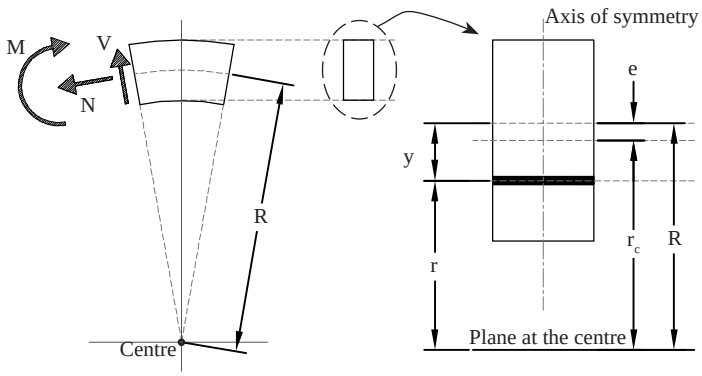


**Figure 8.13:** Forces and moments in circular ring, notation according to Young et al. (2012).

where $r_n$ is distance from the centre to the neutral axis. The general formula for the moment $M$ is given by

$$M = M_A - N_A R(1-u) + V_A Rz + LT_M \tag{8.9}$$

where $u = \cos x$, $z = \sin x$, and $LT_M$ is a load term given for the type of load. In this case, the equation can be simplified to

$$M = M_A + LT_M \tag{8.10}$$

as for this given load case $N_A$ and $V_A$ are equal to zero. The internal moment at A and the load term are given by

$$M_A = \frac{WRk_2}{\pi} \tag{8.11}$$

$$LT_M = \frac{-WRz}{2} \tag{8.12}$$

where $W$ is the applied load in N, $k_2 = 1 - \alpha$, and $\alpha$ is the hoop stress deformation factor, which for thin and thick rings is $\alpha = I/AR^2$ and $\alpha = e/R$ respectively, and $I$ is the second moment of area of the cross-section (Young et al., 2012).

The set-up 1 of the test was prepared in a similar way to that presented by Sharma et al. (2013). The set-up 2 introduces the bottom and top timber blocks with a groove that is placed against the bamboo culm, similar to those used for the connection systems (see Figure 8.11). The neoprene interface was not used to prevent the influence of the results by the compression of the neoprene, and allows a more direct comparison with the results of the test with set-up 1. Two samples taken from a moso bamboo were obtained from the same internode. The tests were carried out in a testing machine Instron 3345 with a load cell of 5 kN capacity, at a load rate of 1.00 mm/min. The length of the element was equal to the diameter.

The samples dimensions and circumferential stresses for points A and B are presented in Table 8.1. The load-displacement curves for both test methods are shown in Figure 8.14a. During the test, ovalisation of the cross-section with both set-up was observed by the naked eye. The ultimate transverse load that can be applied to the bamboo samples increases by 30% when applying the transverse load through the timber blocks using the set-up 2. Figure 8.14b depicts the calculated distribution of stresses from the top at point A to the side at point B in the cross-section view (see Figure 8.12a). The stresses change from compression to tension at approximately 40° by considering the load case of 2 point loads at opposite sides.

Based on the results for the set-up 2 with timber blocks, Figure 8.15 provides the failure load for a range of cross-sections. The values are calculated in N for a unit length. The failure load increases proportional to the area for the same shape factor $\Phi$ (see Figure 8.2). Note that as the length of the cross-section is taken as a unit, the area is equal to the thickness.

**Table 8.1:** Dimensions and circumferential stresses for the edge bearing tests.

| | D (mm) | t (mm) | L (mm) | $\sigma_A$ (N/mm$^2$) | $\sigma_B$ (N/mm$^2$) |
|---|---|---|---|---|---|
| Set-up 1 | 38.76 | 4.15 | 39.4 | 30.01 | -17.36 |
| Set-up 2 | 39.04 | 4.29 | 39.4 | 40.47 | -23.43 |

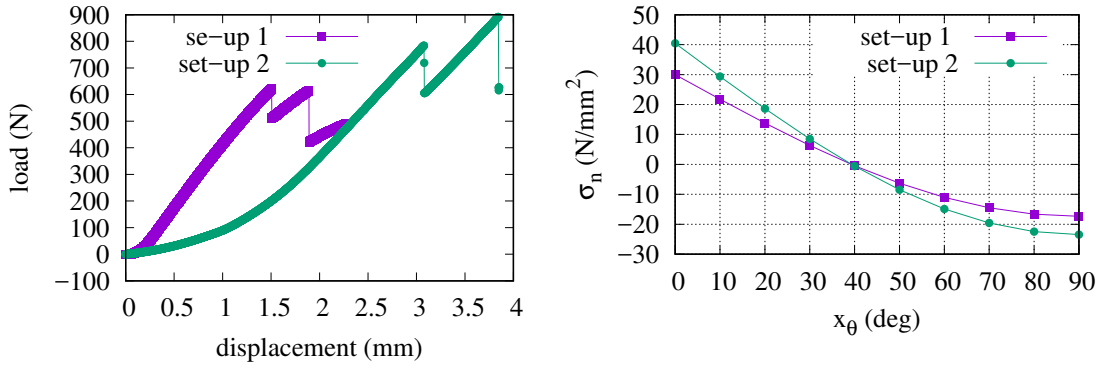


(a) (b)

**Figure 8.14:** (a) Load-displacement curves for the transverse compression tests. (b) Calculated distribution of stresses from point A (0°) to point B (90°) at failure of the bamboo samples.

| D (mm) | t (mm) | Φ | Area (mm) | W (N) |
|---|---|---|---|---|
| 40 | 4 | 4.5 | 4 | 18.9 |
| 80 | 8 | 4.5 | 8 | 37.9 |
| 120 | 12 | 4.5 | 12 | 56.9 |
| 40 | 8 | 2 | 8 | 88 |
| 80 | 16 | 2 | 16 | 176 |
| 120 | 24 | 2 | 24 | 264 |

**Table 8.2:** Failure load under transverse force.

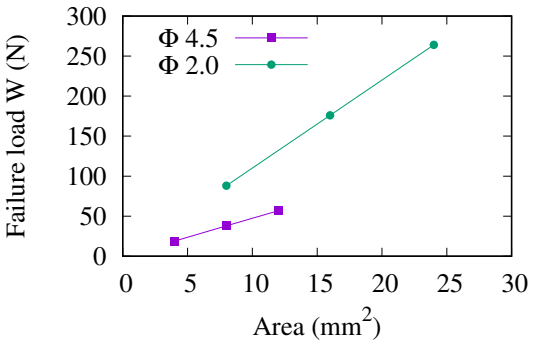


**Figure 8.15:** Failure load to area relationship.

This is relevant because having the linear relationship for different shape factors Φ, the failure load can be estimated based on the area of the sample, which can significantly simplified the determination of the transverse capacity of the culm.

## 8.3 Aluminium connection

This section presents the process for developing a connection system feasible to fabricate with components available in the market. The design of the connection presented here was proposed by Dr. Rodolfo Lorenzo, and all the experimental tests and analyses were carried out by the author of this thesis.

Figure 8.16 depicts the connection system. It consists of two vertical components, the

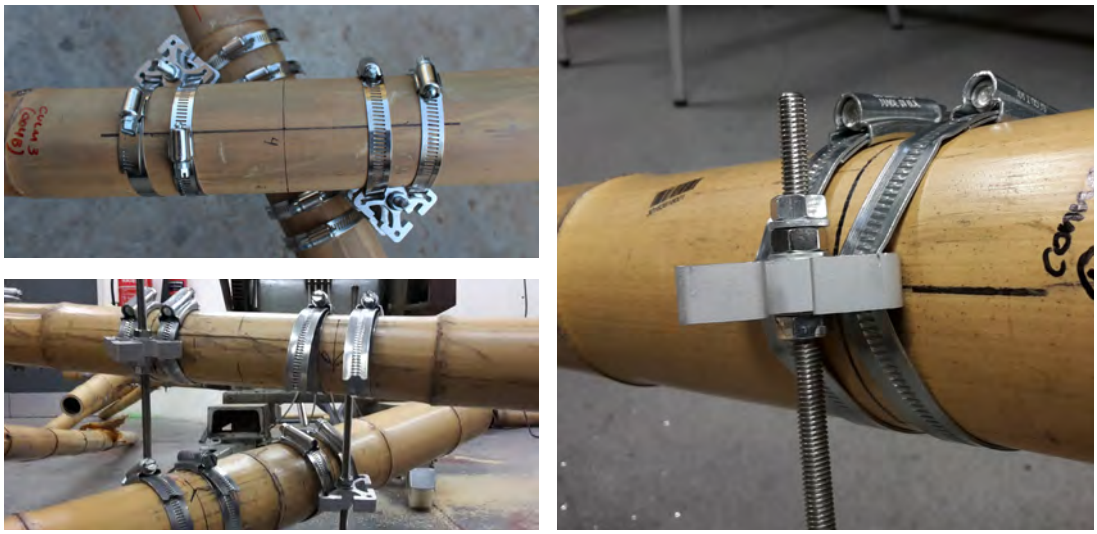

**Figure 8.16:** Aluminium connection assembled to assess fitting of components.

aluminium components and the metal bands clamping the bamboo culms. It is important to mention that this connection was assembled with the aim of assessing the overall geometry and the fitting of the components. Therefore, simply steel threaded rods were used as vertical components. However, the design of the vertical components is thoroughly considered to ensure structural stability of the whole system.

These vertical components are attached to the culm through an aluminium component, which is fastened against the culm surface with two metal hose clips installed around the bamboo culm. The aluminium components are edge profiles of 40 x 40 mm obtained from Paletti Profilsysteme (Paletti-Profilsysteme, 2012). The cross-section of the aluminium profiles has several gaps from which the vertical components and the metal hose clip can be installed across. This connection system simplifies the fabrication of the components, as the only process required is to cut the vertical components and the aluminium components to the required length and width respectively based on the dimensions of the connectors and the diameters of the culms. The rest is done by assembling all the components.

### 8.3.1 Connection geometry

Figure 8.17 presents the geometric parameters of the connection. The length of the vertical components is driven by the length of the eccentricity. The length of the aluminium component was defined so that the metal hose clips were easily assembled through the gaps and around the outer surface of the culm, this is further discussed below. The position of the aluminium component with respect to the eccentricity is calculated as

$$s_1 = \frac{r_2 + p}{\cos\beta} + \frac{r_1 + p}{\tan\alpha}, \qquad s_2 = \frac{r_1 + p}{\cos\beta} + \frac{r_2 + p}{\tan\beta} \tag{8.13}$$

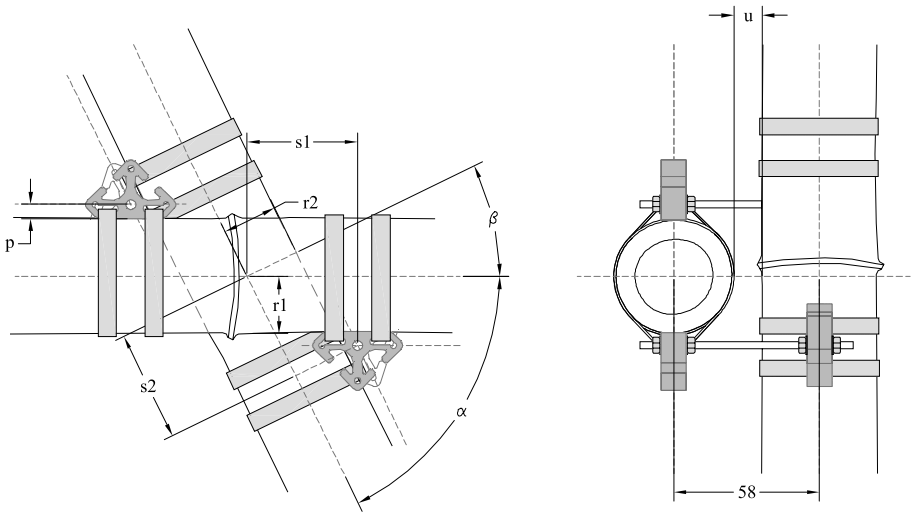


**Figure 8.17:** Geometric parameters of aluminium connection.

where the $r_1$ and $r_2$ refer to the radius of the top and bottom culms respectively, $p$ is the distance from the hole in the aluminium component to the outer edge surface, which is equal to 8.2 mm, the angle $\beta$ is the angle between the longitudinal axis of one culm and the axis perpendicular to the longitudinal axis of the other culm, and $\alpha$ is $90°-\beta$. When both culms have the same diameter then $s_1 = s_2$. These distances are used to mark the position of the connection components directly in the culm surface as described in Appendix H.

The structural stability of the connection is provided by the vertical components and the clamping force of the metal bands. Next Subsection 8.3.2 analyses the structural stability of the vertical components. For this study, these components consist of steel threaded rods packed with aluminium components as shown in Figure 8.18.

The metal bands provide shear stiffness to the connection. The metal hose clips (e.g. jubilee clips) were found to be more suitable for connecting bamboos than the steel band clamps installed with a special tool, which were more easily loosened. In addition, the metal hose clips can be installed using a common hose clip screwdriver and are easy to undo or clamp more if required.

The main purpose of the aluminium components (i.e. Paletti Profilsysteme) is to provide a connection between the metal bands and the vertical components so that the loads can be transferred. The use of this particular aluminium section was mainly due to the adaptability to connect the vertical components and the metal hose clips using the openings of the cross-section. However, some of the material of the aluminium component is not structurally utilised (see hatched area in Figure 8.19a). This should be considered in future design iterations to increase the percentage of utilisation.

One of the parameters to determine for this connection was the width of the aluminium component. One of the concerns was the bearing of the aluminium component against the

**Figure 8.18:** Vertical components of aluminium connection.

culm and the possible penetration of the culm wall thickness. However, no issues regarding the aluminium component embedded in the culm wall was observed. Figure 8.19b shows different sections and the width to diameter ratio. A large aluminium section means that the metal band has less contact area with the outer surface of the bamboo culm. Therefore, it was seek to use the smallest possible width for the aluminium component that provides enough material to connect the metal band with the vertical components, but also that prevents rotations of the component around the bamboo culm. Several aluminium component widths were tested during the assembly of many of the modules, and a ratio of 0.15 was empirically proposed as a suitable ratio. The connections used in Section 8.4.3 were fabricated using this ratio.

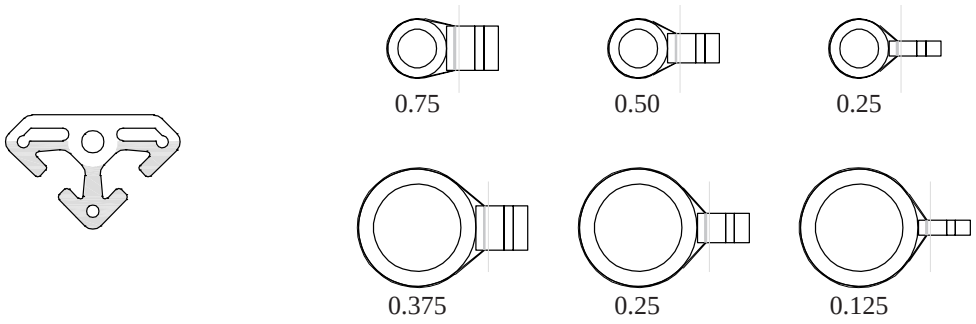


**Figure 8.19:** (a) Cross-section of Paletti Profilsysteme indicating area which is not loaded or used in this connection system. (b) Width of aluminium components with respect the diameter of bamboo. The ratio width to diameter is indicated for each example.

### 8.3.2 Structural behaviour

The performance of the aluminium connection relies on the capacity of the metal hose clip to fix the aluminium component into position and prevent movement along the outer surface of the culm. Once this is achieved, there are two main aspects to consider. The first refers to the shear stiffness of the connection in the plane that passes through the four points where the aluminium components and the bamboo culms are joined at each connection (see Figure 8.20). Shear distortion due to change of angles in this plane shall be prevented to provide shear stiffness to the system. The second refers to the stability of the connection in the out-of-plane direction of this particular plane. A single connection alone has no capacity to resit out-of-plane loading. To provide this, vertical components shall be installed at the four sides of the connection rather than only at opposite sides. Nevertheless, this stability is achieved by the interaction of all the bamboo elements and the connection components in a three-element module.

The behaviour of a single connection is similar to the behaviour of a single frame where the vertical elements are the vertical components and the horizontal beam element is the bamboo culm between the two aluminium components. The push and pull action of the vertical components parallel to the eccentricity is only achieved when at least three bamboo elements are connected together with three connection systems. As the connections between the vertical components and the culms can be considered as pinned, the frame alone is a mechanism and it only achieved stability when the three elements are connected.

Figure 8.21a depicts the aluminium connection under a vertical load that is parallel to the eccentricity direction. It is assumed that the total load $P$ applied to the connection is distributed at each rod as a vertical load $p$. The free body diagram shown in Figure 8.21a considers that the loads are applied at the principal axis of the elements. Additional to the axial, we can also take into consideration the moment ($M = pe$) generated by the eccentric load, by considering the distance $e$, as shown in Figure 8.21. This eccentricity corresponds to the radius of the culm plus the distance from the outer culm surface to the axis of the rod. Note that these moments occurred about different axes, as the aluminium components connects bamboo culms oriented at different directions.

Figure 8.21b depicts the forces between the aluminium component and the outer culm

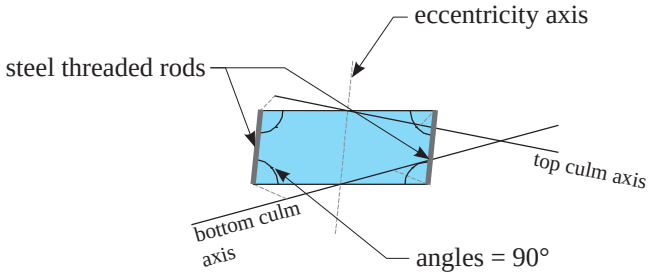


**Figure 8.20:** Direction of the eccentricities and vertical components with respect the culms axes.

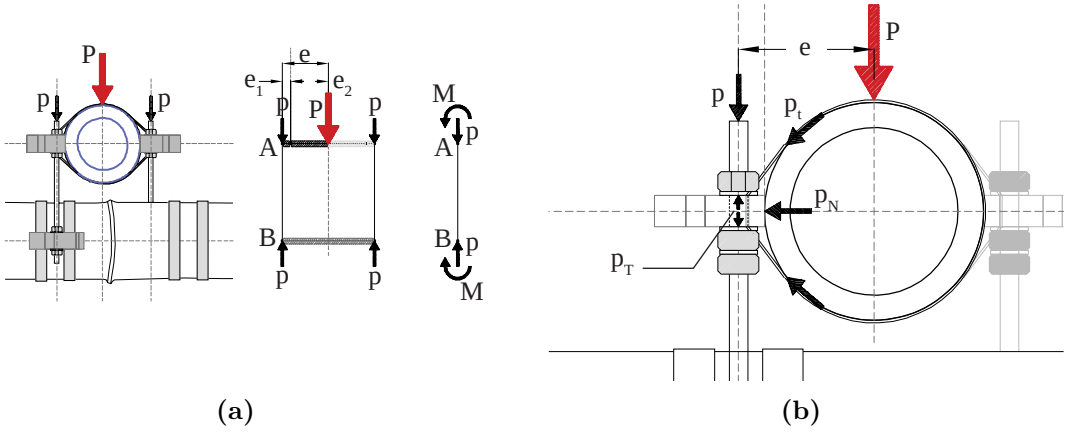


**Figure 8.21:** (a) Free body diagram of a single connection in the plane of the eccentricity. (b) Idealisation of the vertical components of the connection as a column pinned at both ends, and free body diagram in a single connection in three-dimensions.

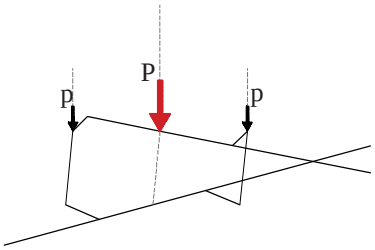


**Figure 8.22:** Vertical load applied to the aluminium connection system.

surface, which is subjected to tangential forces $p_t$ transferred through the metal hose clip. At the same time, these forces produce a frictional force $p_N$ between the aluminium component and the outer culm surface of the culm. The forces between the aluminium component and the steel threaded rod are transferred by fixing the aluminium components into position along the length of the steel threaded rod using washers and nuts. The torque applied through the nuts produces friction between the steel threaded rods and the nuts and tension to the steel threaded rod $p_T$, which keeps the aluminium components fixed in position relative to the length of the steel threaded rods.

A more realistic situation of how the loads are applied to the connection is depicted in Figure 8.22 where the elements in the structure have different orientations (see also Figure 8.8). In reciprocal structures with double curvature, the connections in the surface will be oriented at different angles from that of the vertical axis. In this case, the vertical components which are parallel to the eccentricity will be subjected to forces and moments generated by the components of the applied load in the three directions of the local axis of the vertical components. Therefore, we can consider that the performance of the vertical components is governed by the forces and moments induced by the vertical and horizontal

components of the applied load $P$.

To illustrate this, the moments and forces of three connections (0 to 2) from module C presented in Section 8.4.3 are considered. Table 8.3 provides the moments and forces obtained from the structural analysis under the total load of 1.5 kN. It is assumed that the total moments and forces of the connector are shared equally by the two vertical components. Therefore the total moments and forces in Table 8.3 correspond to half the total value for the connectors. As the vertical components for that module was installed with packing in between the aluminium components, the total area considered for the analysis is that of the area defined by the nut, which is taken as 10 mm for a steel threaded rod of 6 mm. The length of each of the connectors is different due to the differences in diameters of the culms. The most critical case, is that of connector 2, which is the longest connector. The maximum stresses developed in the cross-section are those of bending stresses. Considering the maximum elastic stress of the vertical components as 250 N/mm$^2$, none of these exceed the capacity.

To analyse the stability of the vertical components, we can idealise this as an element pinned at both ends and calculate the buckling capacity of the vertical components (see Figure 8.23a). However, note that the idealised supports are not supports at the ground but those between the bamboo and the vertical components. The vertical components are pinned to the aluminium component which is attached to the culm. Nevertheless, this culm is free to rotate and translate under the applied loads, and these rotations and translations are not the same for the bottom and the top culms. Taking this into account, we can consider that the connection is fixed at one end and free at the other end as shown in Figure 8.23b. The critical load for these boundary conditions is (Hibbeler, 2011)

$$P_{cr,ff} = \frac{\pi^2 EI}{4L^2} \tag{8.14}$$

Now, considering the vertical and horizontal components of the applied load, we can assume that vertical and horizontal forces are applied at the free end of the element. To simplify this behaviour and understand the moments and forces governing the behaviour of this connection system, we can assume that the bamboo culm at the bottom is fixed and the upper culm is free to rotate and translate. The horizontal force component will translate the bamboo culm, which in turn will deform the vertical component by an amount equal to the maximum deflection of a cantilever beam (Hibbeler, 2011) as:

**Table 8.3:** Stresses and critical loads in vertical components.

| | D (mm) | L (mm) | Fx (N) | Fyz (N) | Mxy (Nmm) | A (N/mm$^2$) | $\tau$ (N/mm$^2$) | $\sigma$max (N/mm$^2$) | $P_{cr,ff}$ (kN) | $P_{cr,fe}$ (kN) |
|---|---|---|---|---|---|---|---|---|---|---|
| 0 | 10 | 89 | 165 | 83 | 3792 | 2.10 | 1.06 | 38.62 | 31.12 | 15.36 |
| 1 | 10 | 91 | 357 | 117 | 8930 | 4.54 | 1.49 | 90.96 | 29.77 | 13.09 |
| 2 | 10 | 95 | 300 | 260 | 16560 | 3.82 | 3.31 | 168.68 | 27.27 | 9.30 |

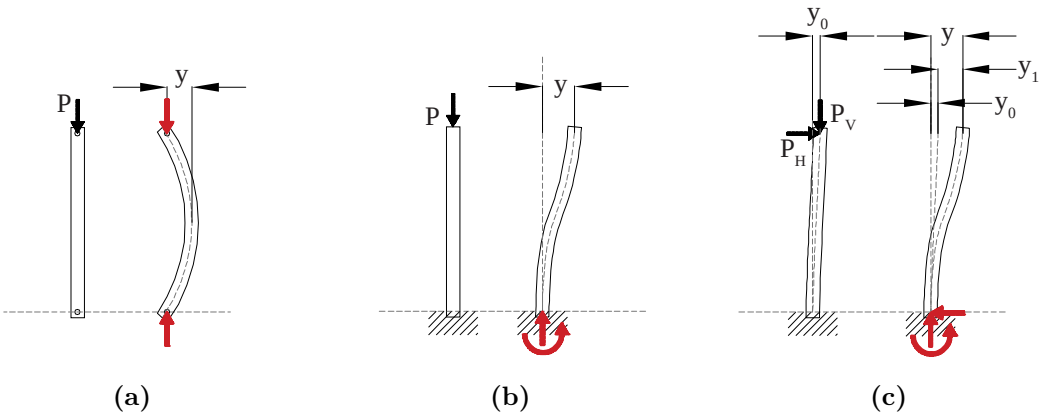


**Figure 8.23:** Idealisation of vertical components of connection system (e.g. steel threaded rod) (a) Pinned at both ends. (b) Fixed at one end and free to translate and rotate at the other end. (c) Fixed at one end with initial $y_0$ deformation due to horizontal force component.

$$v_{max} = \frac{PL^3}{3EI} \tag{8.15}$$

where $v_{max}$ is the deflection at the free end of the vertical component due to the horizontal component force. Now we can consider that the amount of that deflection $v_{max}$ will cause a moment at the free end of the vertical component when analysing the behaviour under the vertical load in the axial direction. We can calculate this assuming that the vertical component is not straight due to the deformations owing to the horizontal forces. As a result, eccentric moments are generated in the vertical component. The critical load $P_{cr,fe}$ is calculated using the secant formula (Hibbeler, 2011) for the maximum compressive stress $\sigma_{max}$ in the column as:

$$\sigma_{max} = \frac{P}{A}\left[1 + \frac{ec}{r^2}\sec\left(\frac{L}{2r}\sqrt{\frac{P}{EI}\frac{L}{2}}\right)\right] \tag{8.16}$$

where $e$ is taken as the initial deflection $v_{max}$ due to the horizontal force, $c$ refers to the distance from the centroid of the section to the outermost fibre of the column and $r$ is the radius of gyration

$$r = \sqrt{I/A} \tag{8.17}$$

solving for $P$ the critical load $P_{cr,fe}$ is obtained.

Table 8.3 provides the failure load $P_{cr,ff}$ due to fixed-free support conditions, and $P_{cr,fe}$ considering the eccentric moment. The critical load $P_{cr,ff}$ is relatively high. However, the $P_{cr,fe}$ becomes more significant (twice or more the value of $P_{cr,ff}$) especially for longer elements. Note that here the moments and forces were equally distributed for the purpose of this analysis. However, the axial load taken by each of the two vertical components is going to depend on the geometry dimensions and orientations, as well as the direction of the load applied.

## 8.4 Experimental prototypes

This section provides the experimental tests for three different prototypes assembled with timber and aluminium connections in reciprocal modules. The aim was to gain insight into the behaviour of these proposed connections in reciprocal structures at conceptual design stage, rather than quantifying the strength and stiffness for design purposes. Therefore, in this stage, the structural behaviour of at least a single reciprocal unit was sough rather than tests in individual connection systems. In this way, we can evaluate the mechanical behaviour of the connections under the complex load distribution in elements arranged in reciprocal configuration. The specific objectives are: i) to investigate the behaviour of bamboo reciprocal modules using the timber and aluminium connections, ii) to identify critical parameters and weaknesses in order to improve the designs in further iterations, and iii) to evaluate the feasibility to further developed these connections.

The first prototype (module A) consists of a three-element reciprocal unit assembled with timber connections. This prototype was loaded until failure. The second prototype (module B) is also a three-element reciprocal unit assembled with timber connections. For this module, the design of connection systems was improved. This prototype was also loaded until failure. The last prototype (module C) is a five-element reciprocal module so that one of the elements represents an inner element in reciprocal structures. This prototype was assembled with both connection systems using the same bamboo culms for comparison. For the timber connection, some geometric parameters were modified to assess the effect in the overall structural behaviour. This prototype is the first to incorporate all the aspects of the SBD into the design process (i.e. geometrical, physical and mechanical properties). The modules C assembled with both connection systems were loaded in the elastic regime.

### 8.4.1 Reciprocal module A

Table 8.4 and Figure 8.24 provides the average diameters and thickness for each of the culms, and the geometry of the reciprocal module respectively. The bamboo species used for this module was moso bamboo. The total length of the elements was approximately 970 mm. Unlike the final design, this connection have only two steel bolts located at opposite sides, as shown in Figure 8.25.

#### 8.4.1.1 Experimental test

Figure 8.25 shows the prototype tested. The supports at the end of the legs were free to rotate in all directions, free to translate in the horizontal plane and restrained to translate in the vertical direction. The test set-up is depicted in Figure 8.26. The module was loaded through an upper plate designed with the aim of transferring the loads uniformly to each of the elements. The plate is a plane surface supported by three timber legs cut normal to the direction of the timber connections ( see Figure 8.25d). Steel test weights

| Bamboo | Diameter (mm) | Thickness (mm) |
|---|---|---|
| Culm 1 | 38.5 | 3.8 |
| Culm 2 | 41.0 | 7.5 |
| Culm 3 | 42.6 | 4.3 |

**Table 8.4:** Bamboo culms average dimensions.

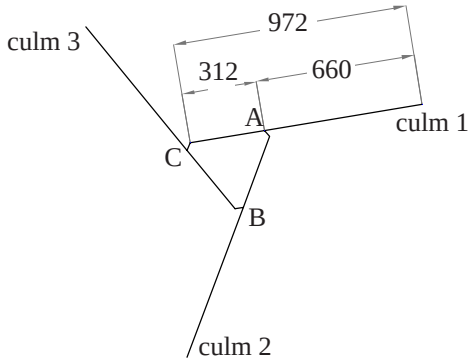


**Figure 8.24:** Geometry of the reciprocal module and nomenclature. Units are in mm.

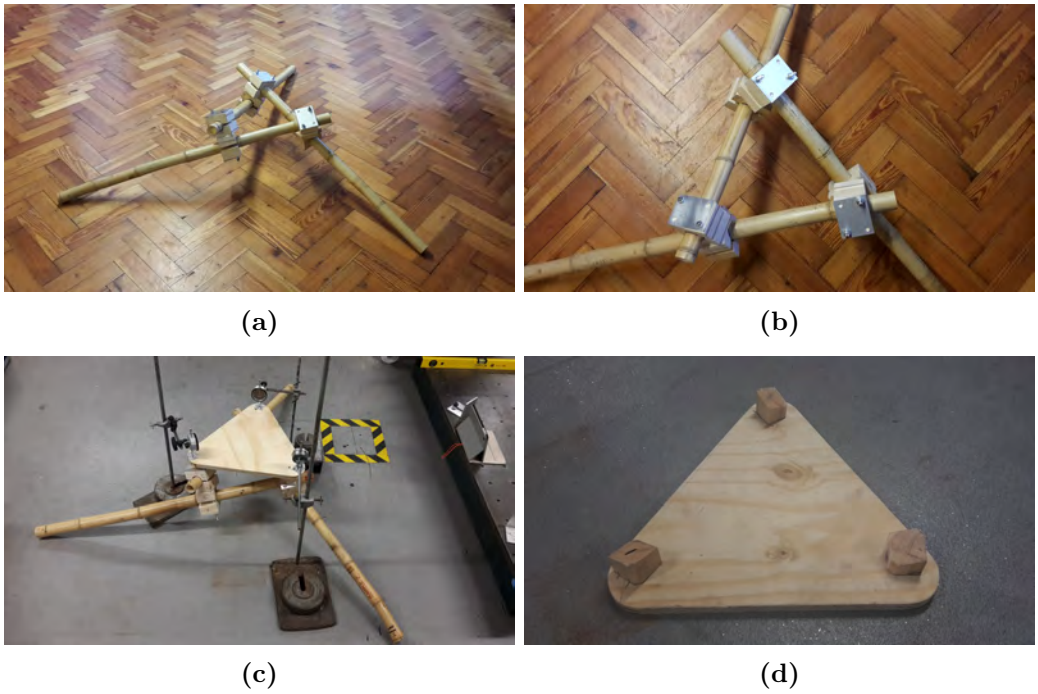

**(a)** **(b)**

**(c)** **(d)**

**Figure 8.25:** (a,b) Prototype of the reciprocal module test. (c) Test set-up. (d) Timber plate to transfer loads to three timber connections.

were used for loading the module. The displacements were measured at the three corners of the loading plate using analogue dial gauges with an accuracy of 0.01 mm. The tests were carried out by placing the steel test weights one at a time on the top of the timber plate and measuring the displacements.

The maximum displacement recorded at a load of 1.74 kN was of 59.9 mm. The failure load of the module was 1.84 kN. However, the module collapsed prior to the recording of the displacement at this loading. The load-displacement relationship is shown in Figure 8.27. The behaviour of the module is linear at the beginning of the test and started to yield prior to failure.

Figure 8.28 shows the collapse of the module. As expected, the collapse of the module

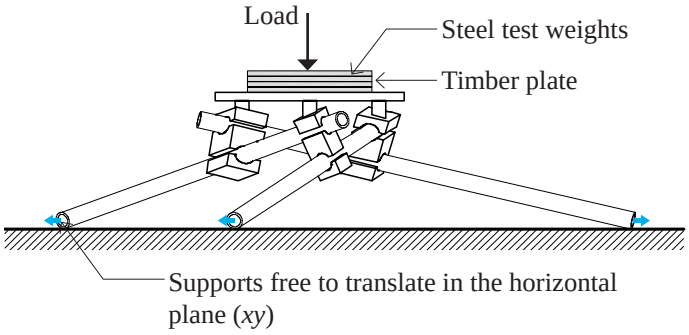


**Figure 8.26:** Set-up of experimental test in reciprocal module.

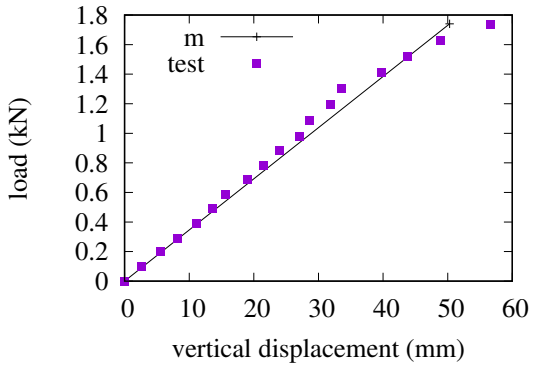


**Figure 8.27:** Load-displacement curve of the reciprocal module from structural analysis (m) and experimental test (test).

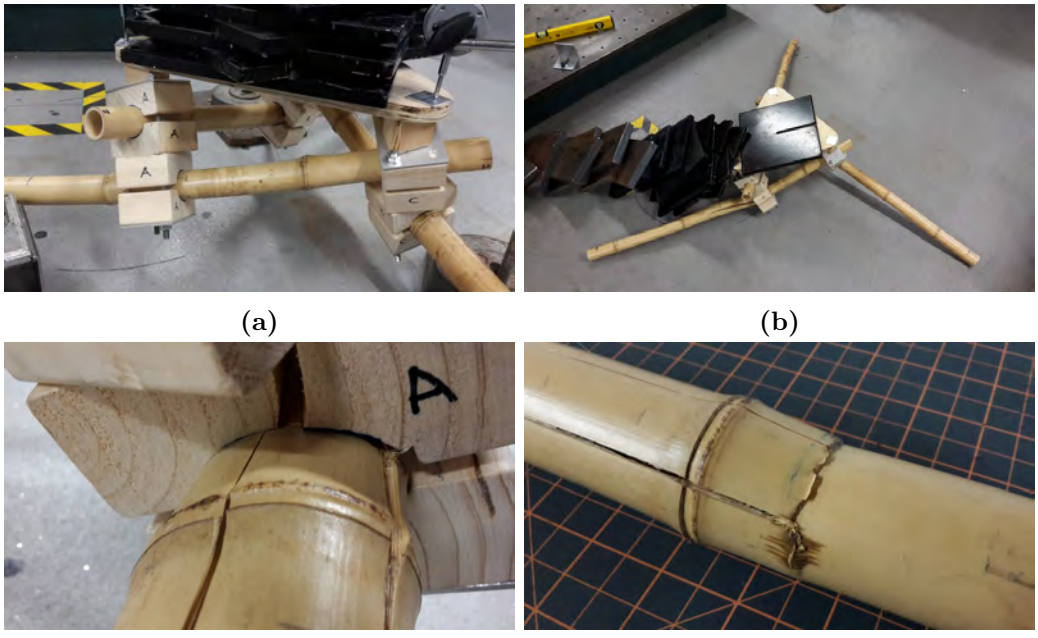


**Figure 8.28:** (a) Deflected shape of bamboo culm under loading of the module. (b) Collapse of the module. (c) Longitudinal splitting of failed culm. (d) Indentation and splitting of failed culm.

occurred due to failure of culm 1, which has the smallest dimensions (see Table 8.4). The failure was very sudden and loud due to the splitting of the failed culm. During the test, the sound generated by the cracks were also heard. However, the sound was low and no visible splits were observed during this time. Figures 8.28c and 8.28d show the failed culm with two longitudinal splits located at the top part of the culm, as well as a small indentation located at the position where the timber blocks were clamped. The middle timber block of connection A, which corresponds to the position of failure, splitted in two parts. After collapse occurred, the whole structure was kept together as locked, since the other two connections and culms have not failed.

A relative slip between bamboo culms and timber blocks was observed in one of the connections. A slip of approximately 7.50 mm was measured in connection B. The rest of the connections did not show any relative movement from its initial position when assembled. This is possibly attributed to the fact that steel bolts were only provided in two sides of the timber blocks and the friction between the bamboo culm and the timber blocks was no enough to prevent slip. The horizontal displacement at the ends of the culm was measured at the load of 0.98 kN. The displacements recorded in the horizontal direction of culms 1, 2 and 3 are 7.5, 6.0 and 7.5 mm respectively. These were measured with a metal ruler with the smallest graduation of 1 mm.

#### 8.4.1.2 Numerical analysis

The structural model was developed as described in Section 9.1. For this test no digital data of the geometry or mechanical properties of the culms were obtained. The model was loaded at the three upper nodes of the connectors with a total load of 1.74 kN applied in the vertical direction. The supports were considered free to translate in the xy plane. To prevent numerical instabilities, an upper node was fixed to rotate in the three directions and fixed to translate in the xy plane. Figure 8.29 shows the model used for the structural analysis.

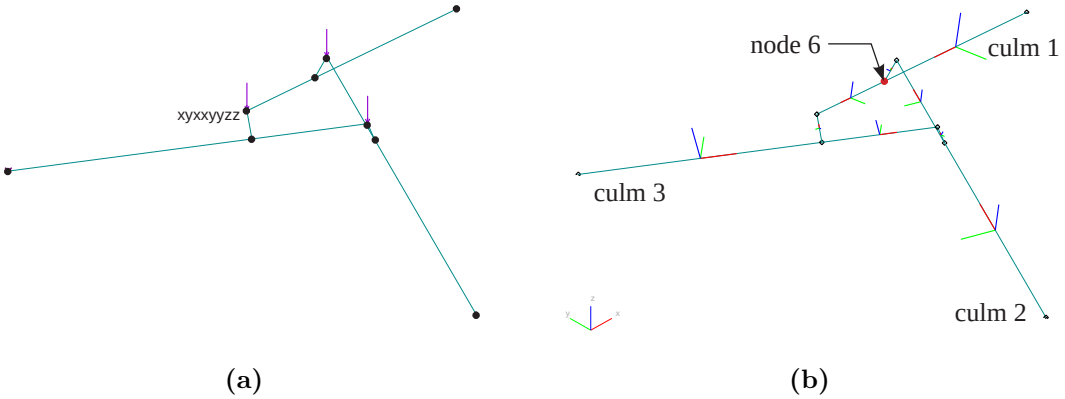


**Figure 8.29:** (a) Structural modelling of reciprocal module A, with spring supports to provide translational resistance in the xy directions, and an upper node fixed to rotate and translate in the xy directions. (b) Elements local axes.

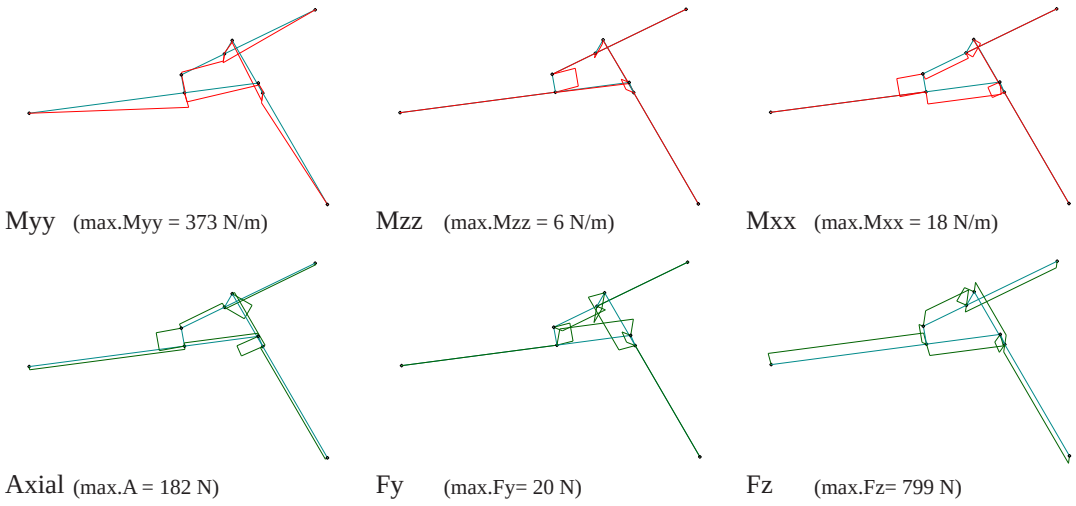


**Figure 8.30:** Moments and forces in reciprocal module A indicating the maximum value on average for the three culms.

The bending moments and forces of the elements are depicted in Figure 8.30. The critical moments are in the $y$ direction. These are located along the elements just below the eccentricities. As the supports are free to translate in the $xy$ plane, no moments are generated in the $z$ direction. Similarly, the axial forces in the elements are not significant. The elements of the engagement length are subjected to torsion and shear forces mostly in the $z$ direction. The shear forces in the $y$ direction were not significant. The deformed shape of the module do not tend to twist as in the module in Section 9.2, as this is free to translate in the $xy$ plane.

Due to the orientation of the eccentricities, and the overall geometry of the system, the connectors are subjected to axial, shear, torsion and bending moments. The axial forces are transferred by the timber blocks to the bamboo culms. The moments and shear forces are taken by the connection and particularly by the four steel threaded rods. The capacity of the connectors to resist bending moments and shear forces is provided by preventing the change of angle between the connector and both bamboo culms joined at that point (top and bottom). Whereas the capacity of the connector to resist torsional moments is provided by preventing a change of angle between elements.

The displacements measured from the physical test are higher than those calculated numerically (see Figure 8.27). However, the numerical model run was linear static analysis. Therefore, the yield of the module prior to failure cannot be recorded. Nonetheless, the linear regime of the load-displacement curve are in good agreement with those measured from the physical test (see plot m in Figure 8.27). The horizontal displacement of the module was 11.8 mm in average. This is higher than those measured from the physical test, however, the friction generated between the floor and the culms at the supports is not considered.

Considering the bending moments in the $y$ direction at the location of below the

connector as shown for node 6 in Figure 8.29b, the bending stresses in culm 1 are 114 N/mm$^2$. Now, considering the shear forces in the $z$ direction for the bamboo culms in the location of the engagement length, the magnitude of the shear stresses is 1.9 N/mm$^2$. A moso bamboo culm of similar dimensions and from the same batch was tested under transverse loads to calculate the bending strength and the shear stresses developed on the culm at the moment of failure. The test was carried out according to ISO (2004b) and following the same procedure as in the test presented in Subsection 6.1.3. The ultimate bending strength $\sigma_u$ calculated was 101.7 N/mm$^2$, and the shear stresses at failure point was 2.03 N/mm$^2$. Although the results of both culms are not directly comparable as each bamboo is different, the magnitude of bending and shear stresses developed in culm 1 are similar to the stresses calculated from the culm tested until failure, suggesting that collapse of the module was caused by material failure.

### 8.4.2 Reciprocal module B

For this module, the geometry of the culms was determined by 3D scanning. The timber connection is depicted in Figure 8.31. There were three main changes from the connection of the reciprocal module A. These were: i) only three block components, the middle block is shared by both culms, ii) steel bolts were provided at the four corners of the timber blocks, and iii) an intermediate layer of neoprene was added in order to provide more friction to the interface between the bamboo culm and the timber blocks. The bamboo culms used were of the moso species with an average length of 800 mm.

#### 8.4.2.1 Geometry of module

The dimensions of the culms and geometry of the module are provided in Table 8.5 and Figure 8.32 respectively. The out-of-straightness measured for each of the culms was of 5.1, 2.6 and 2.5 mm for the culm 1, 2 and 3 respectively.

The assembly of this module was done using the marking jig method and assembly system for timber connections described in Appendices H and I. The geometric error between the physical and the digital modules was evaluated by measuring the eccentricities.

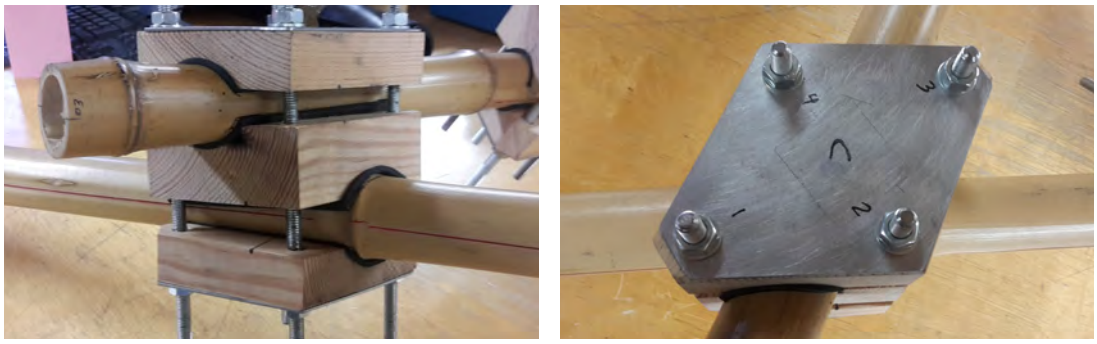


**Figure 8.31:** Improved timber connection design.

| Bamboo | Diameter (mm) | Thickness (mm) |
|---|---|---|
| Culm 1 | 40.3 | 5.0 |
| Culm 2 | 40.1 | 4.3 |
| Culm 3 | 40.1 | 4.4 |

**Table 8.5:** Bamboo culms average dimensions.

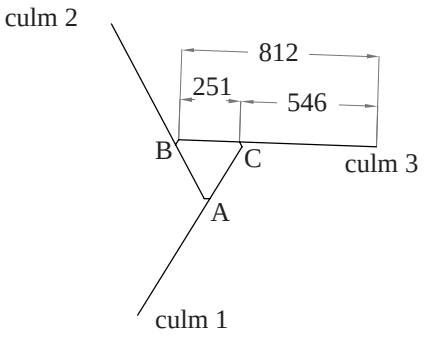


**Figure 8.32:** Geometry of the reciprocal module and nomenclature.

**Table 8.6:** Eccentricities

| | Connection A | | Connection B | | Connection C | |
|---|---|---|---|---|---|---|
| | e (mm) | diff (mm) | e (mm) | diff (mm) | e (mm) | diff (mm) |
| side 1 | 56.8 | 1.2 | 56.7 | 1.3 | 58.1 | -0.1 |
| side 2 | 57.3 | 0.7 | 57.4 | 0.6 | 58.8 | -0.8 |
| side 3 | 58.2 | -0.2 | 56.6 | 1.4 | 58.5 | -0.5 |
| side 4 | 57.7 | 0.3 | 56.7 | 1.3 | 58.6 | -0.6 |
| average | 57.5 | 0.5 | 56.9 | 1.1 | 58.5 | -0.5 |

The eccentricities for the three connections in the digital model were 58 mm. Table 8.6 provides the differences from the measurements taken directly from the physical model using a digital vernier (measures to the nearest 0.01 mm) and those from the digital model for the three connections measured at the four corners. Connection B has the higher difference with 1.1 mm against the dimensions in the digital model. Overall, the average percentage error for the three connections was 1.2%. This error also represents the culm geometry measured through 3D scanning. This is important to consider since in larger structures composed by more than three elements, cumulative errors might arise. From Table 4.4, we know that the error of the geometric properties of the culms obtained through scanning was 1.2% (approx. 0.45 mm), which could be influencing and causing the differences in measurements from the digital and physical models in this module.

#### 8.4.2.2 Experimental test

The reciprocal module was loaded with two different set-up to take into account the boundary conditions at the supports (see Figures 8.33 and 8.34). For the first set-up the supports were free to rotate in all directions and free to move in the horizontal plane, but restrained in the vertical direction, similar to the previous test on module A. For the second set-up, horizontal restrain was provided at the supports by adding timber props

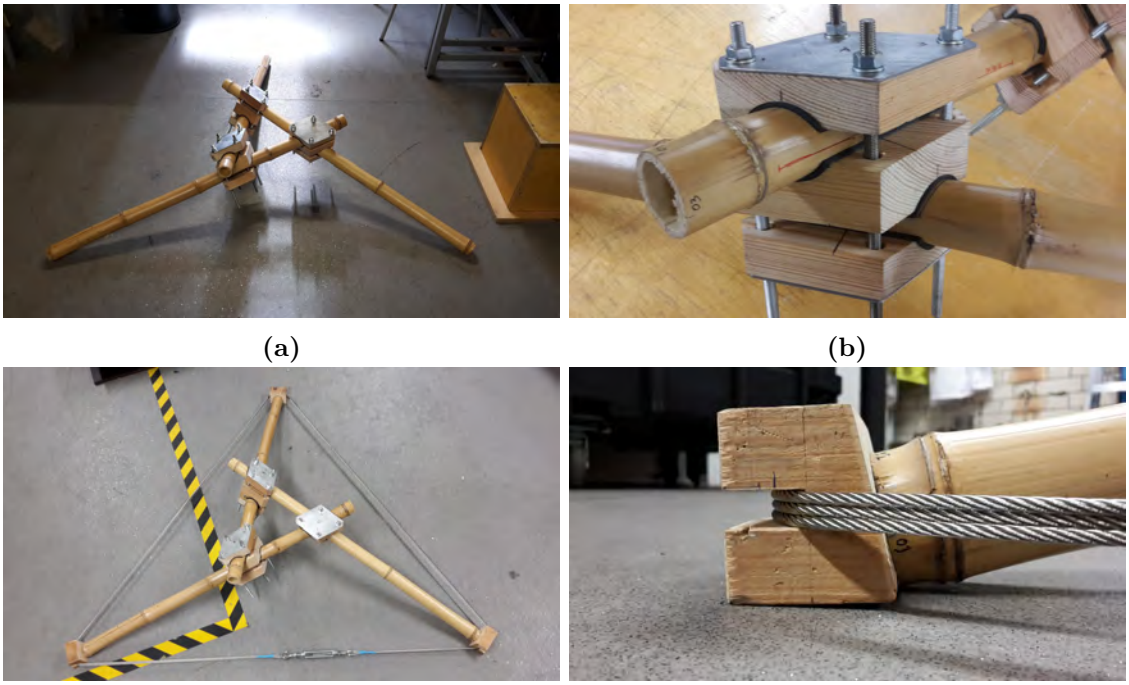

**(a)** **(b)**

**(c)** **(d)**

**Figure 8.33:** (a) Prototype of the reciprocal module with modified connection system. (b) Modified connection. (c) Boundary conditions for the second loading test. (d) Detail of support condition.


**(a)** **(b)**

**Figure 8.34:** (a) Set-up of loading test 1. (b) Set-up of loading test 2.

connected with a stainless steel wire rope among them. The timber props were machined with one of the faces cut normal to the longitudinal axis of the culms so that it provides full contact surface for the cross-section of the culm. In addition, a groove was machined to allow for the installation of the wire rope. The wire rope used was 3 mm 7 x 19 stainless steel, installed with three laps and fixed with a turnbuckle using copper ferrules at the ends to crimp the wire.

The first set-up was loaded in the elastic region only, and the second set-up was loaded until failure. The load-displacement curves of both tests are provided in Figure 8.35. The first test was loaded up to 883 N and unloaded. A linear elastic behaviour was observed. However, a maximum residual displacement of 2 mm was registered after unloading the

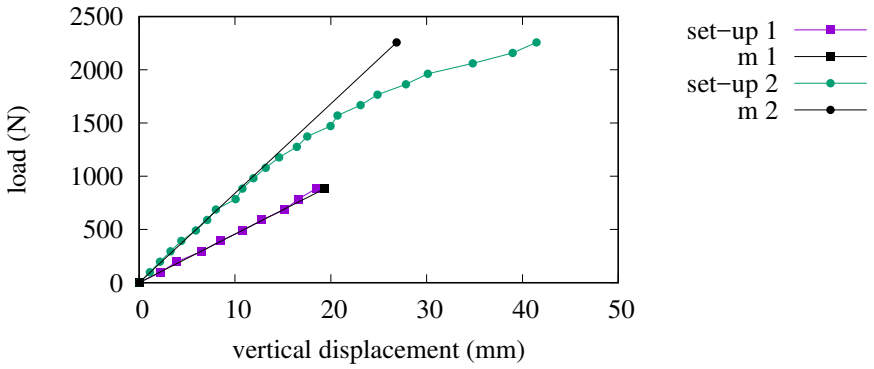


**Figure 8.35:** Load displacement plot for reciprocal module B with two set-up. (a) Set-up 1, free support conditions. (b) Set-up 2, restrained support conditions.

module. This residual displacement is assumed to be due to the settling of the timber connections and friction of the legs on the floor. The maximum displacements in the horizontal plane measured before the unloading of the physical module were 2.3, 4.3 and 1.8 mm for culms 1, 2 and 3 respectively. The second set-up was loaded until failure, which was recorded at a load of 2256 N. As expected, the boundary conditions significantly affect the stiffness of the module (see Figure 8.35). Since in a real scenario the three legs will be jointed to other elements to form a larger structure, the behaviour will be that of a combination of both test set-up. If we consider three inner elements of a large reciprocal structure, the three ends of the elements are connected to their adjacent elements so they are not free to translate. However, these will be affected by the deformation of the elements to which they are connected.

Figure 8.36 shows the collapse of the module. Similar to the previous test on module A, the collapse was caused by the failure of the culm with the smallest dimensions (i.e. culm 2, see Table 8.5). No visible damage was observed from the rest of the culms and the connections. The failure of this culm was characterised by several cracks and indentations. Figure 8.37 shows the location of the cracks and indentations due to the timber blocks around the cross-section. The cracks located at orthogonal positions (i.e. top, bottom and sides) are longitudinal cracks prolonged along the culm in the direction of the fibre. However, the cracks produced by the indentations located between the edge of the timber block grooves and the culm are directed towards the cracks generated at the sides. This suggests that the indentation of the timber blocks in the bamboo culm was not the cause of failure of the culm, but instead a secondary effect caused after the failure of the culm. In this scenario, the cracks created at these points were deviated towards the sides, which were already cracked, as these were the fastest path for the stresses to be released.

#### 8.4.2.3 Numerical analysis

The structural model was made as described in Section 9.1 and using the discretised geometry from the SBD. As the deviation of the internodes was null for these culms, the discretisation of the model was done at each node only, therefore each segment correspond

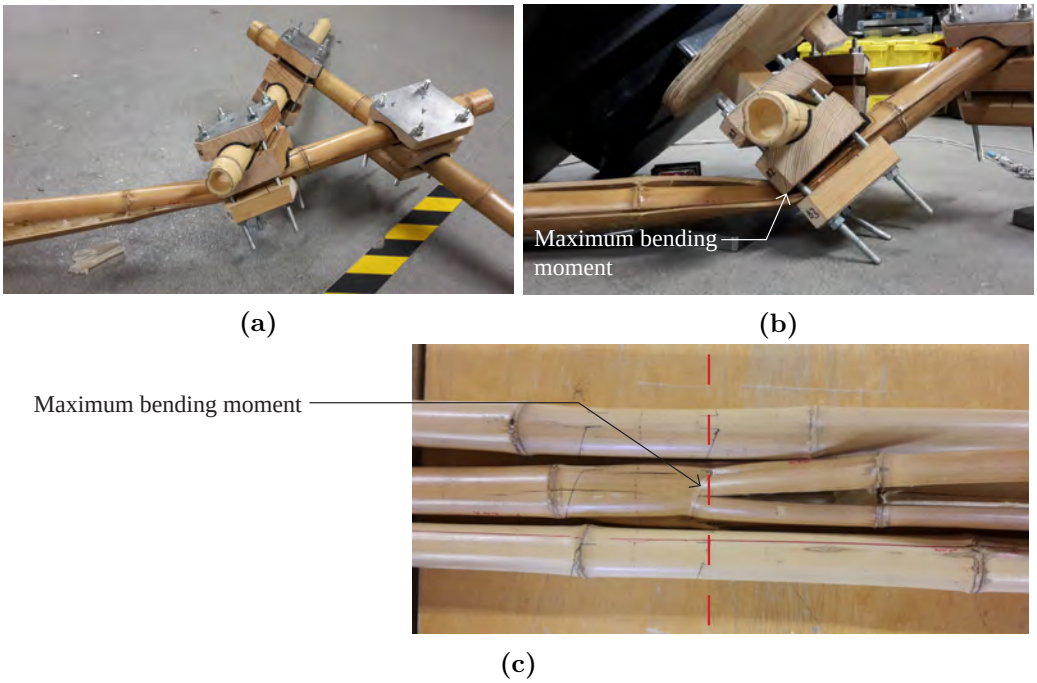


**Figure 8.36:** Failure of module b. (a) Location of failed culm. (b) Side view of failed culm and location of maximum bending moment. (c) Location of failure along the culm at bottom part of timber connection indicating the maximum bending moment.

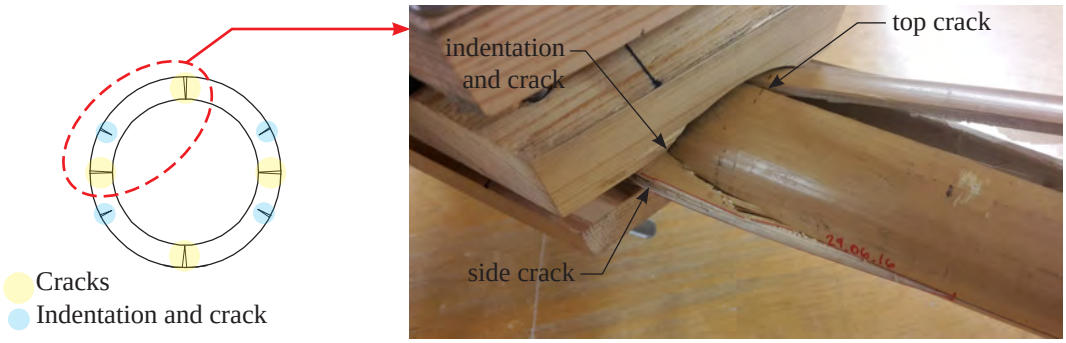


**Figure 8.37:** Position of cracks and indentation of failed culm.

to one internode. Figure 8.38 depicts the reciprocal unit with line elements, and with the superposed discretised elements incorporated to the structural skeleton according to the method described in Subsection 7.2.4. The bamboo elements are slightly shifted from the support legs, as shown in Figure 8.38b.

The support conditions for both set-up were considered differently. For the first set-up, the supports were free to translate in the $xy$ plane, as in the previous module A. For the second set-up, the action of the cable was considered for modelling the support conditions. During the test, horizontal displacements were recorded at the supports. This horizontal movement was caused by the elastic stretch of the wire rope. The support stiffness was estimated from the components of the set-up. The cables, linked at the three supports, were providing partial restraint to the horizontal translation in the $xy$ plane. Therefore,

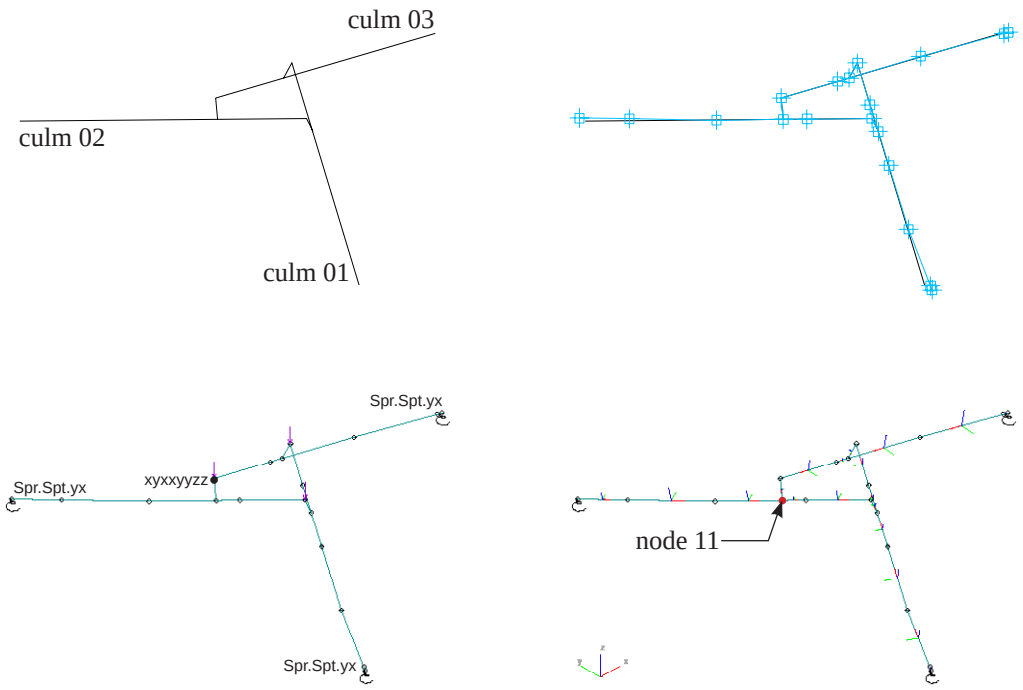


**Figure 8.38:** (a) Reciprocal unit with line elements. (b) Reciprocal unit with line elements and discretised elements superposed. (c) Structural model of reciprocal unit. (d) Local axes of discretised elements in structural model.

the axial stiffness was considered as

$$K_{xy} = \frac{AE}{L} \tag{8.18}$$

where $A$ is the area of the cable, $E$ is the elastic modulus of the cable, and $L$ is the length of the cable (distance between supports). Recall that the cable was installed with 3 laps, therefore the area shall be multiplied by 3, and there are 2 sets of cables incident in each each support, then the total stiffness at each support is considered as $2K_{xy}$. The calculated stiffness for each support was 373100 Nm.

The total load was applied at the upper node of each connector and was distributed equally. For the first and second models a total load of 883 and 2256 N was applied respectively in the z direction.

The vertical displacements obtained from the structural models for both set-up are shown together with the load-displacement curves of the experimental tests (see Figure 8.35). The results for the model with the set-up 1 are in good agreement with the results from the experimental tests. Similarly, the results of the model for the set-up 2 accurately represents the elastic regime observed from the measurements in the physical test. Recall from Subsection 9.1.4 that the connectors (i.e. the eccentricities) are modelled fixed at both ends. Therefore, we assume that there are no relatively movements between the connector and the two elements jointed at the ends in any of the three main orthogonal

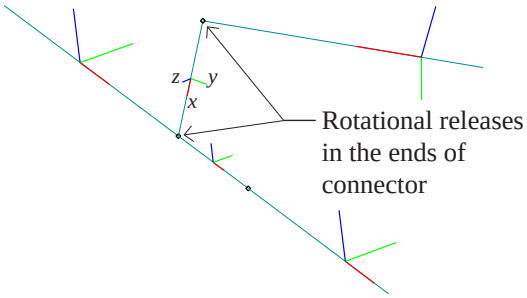


**Figure 8.39:** Connector axes and releases at the ends.

directions ($x$, $y$ and $z$).

From the load-displacement curve (see Figure 8.35), we know that the rotational stiffness provided by the timber connection is sufficient to consider its behaviour as rotationally rigid. Table 8.7 provides the estimated rotational stiffness of the connections for set-up 1 and 2. These were estimated by modifying the rotational stiffness of the connectors until the vertical displacements of the module matched with those measured from the experimental tests within the linear regime. For this, the ratio of the forces acting in the connector in the $x$, $y$ and $z$ directions were used to modify the rotational stiffness. Figure 8.39 shows the local axes of the connectors. Note that the rotational stiffness provided in Table 8.7 are equivalent values that does not represent the rotational stiffness of the connection, but the stiffness of the connector for each set-up with the given loads and support conditions. To accurately calculate the rotational stiffness of the connection, experimental tests on a single connection are required. It is evident that the support conditions, and thus the force distribution, will determine the amount of stiffness required for each specific case. As expected, the rotation stiffness required is higher for the set-up 1 since the module is free to translate in the horizontal plane and thus the elements are not capable to transfer axial forces and moments in the $z$ axis.

The moments and forces from the second test set-up are depicted in Figure 8.40. Table 8.8 provides the results of the experimental tests and numerical analysis of key measurements. The critical moments occurred in the y direction, in the elements below the eccentricity. Unlike the previous module A, moments in the z direction are developed in the elements close to the connections, which is more similar to how the elements will behave in a structure as they will be connected to other elements. The highest torsional moment are created in the connectors and the elements of the engagement window. However, some

**Table 8.7:** Equivalent rotational stiffness of the connections in module B with both test set-up.

| Set-up | Rotational stiffness | | |
|---|---|---|---|
| | $x$-axis (kNm/rad) | $y$-axis (kNm/rad) | $z$-axis (kNm/rad) |
| Set-up 1 | fixed | 88.5 | fixed |
| Set-up 2 | 28 | 24 | 9.1 |

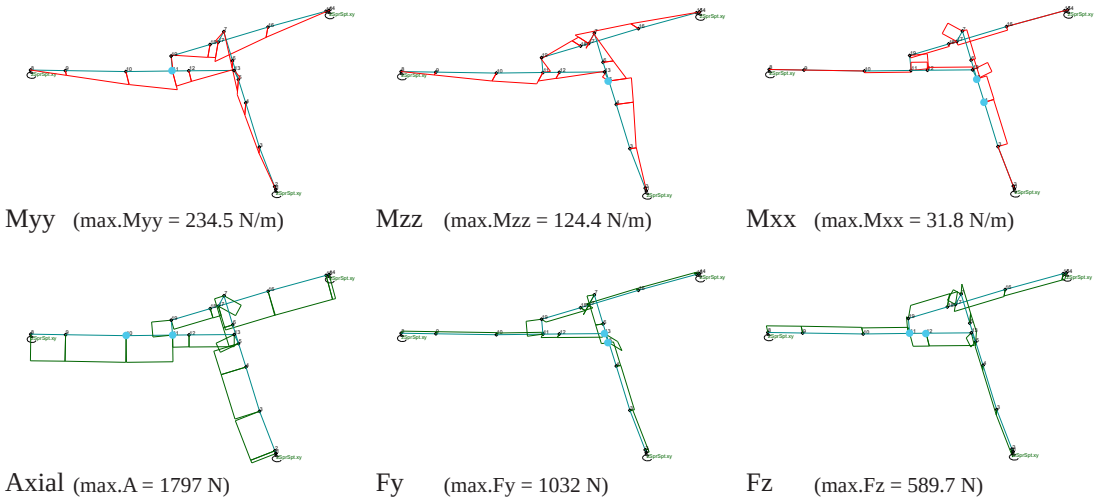


**Figure 8.40:** Moments and forces of module B

**Table 8.8:** Results of reciprocal module B.

| Culm | Test | Numerical model | | | | | | | | |
|---|---|---|---|---|---|---|---|---|---|---|
| | Uz (mm) | Uz (mm) | Myy (N/m) | By (N/mm$^2$) | Mzz (N/m) | Bz (N/mm$^2$) | Fy (N) | Sy (N/mm$^2$) | Fz (N) | Sz (N/mm$^2$) |
| Culm 1 | 42.9 | 26.9 | 232 | 54.9 | 124 | 29.4 | 401 | 1.6 | 547 | 2.2 |
| Culm 2 | - | 26.9 | 235 | 59.5 | 112 | 28.4 | 383 | 1.7 | 590 | 2.6 |
| Culm 3 | 40.0 | 26.9 | 231 | 59.0 | 108 | 27.7 | 338 | 1.5 | 564 | 2.5 |

torsion was also observed in culm 1, which has the higher out-of-straightness values (5.1 mm). The shear stresses in the $z$ direction are relatively high considering the values of shear stress obtained from full culm moso bamboo under transverse loads (see Table 6.5). The deformations of the module are similar to the deformations studied in Section 9.2 with an anticlockwise twist.

The maximum bending and shear stresses are located at the culm 2 that failed during the test. It is worth noting that although the maximum bending moments are located below the connector in the structural model, the location of the actual maximum bending model is shifted by the amount equal to the length of the timber connection. See for example Figure 8.36c indicating the location of the maximum bending moment. Because the connectors are idealised as a single element in the direction of the eccentricity, this feature is not captured in the structural model.

### 8.4.3 Reciprocal module C

Reciprocal module C was the first to fully incorporate the SBD using the data from the oldhamii bamboo culms presented from Chapters 4 to 6. This module was assembled with the timber and aluminium connections (see Figure 8.41) using the same bamboo culms, in order to compare the structural performance. The angle $\theta$ that defines the depth of

**(a)** **(b)**

**Figure 8.41:** Five element reciprocal modules. (a) Timber connections. (b) Aluminium connections.

the groove of the timber connection was modified in order to evaluate the effect of this geometric parameter in the connection stiffness.

#### 8.4.3.1 Geometry of module

The average dimensions of the culms and the geometry of the module are provided in Table 8.9 and Figure 8.42 respectively. The selection and position of the bamboo culms for each of the elements was carried out according to the method presented in Section 7.2, using only the geometrical constraints. The selection of the culms was performed based on the timber constraints and the same positions were used for the aluminium connections.

This module was assembled using the marking blocks method presented in Appendix H and the assembly methods for both connection systems as in Appendix I. The geometric error of the module was measured using a laser point Leica DISTO S910 (Leica-Geosystems, 2015) that captures points in three-dimensions (see Figure 8.43). The points were exported to DXF files and further imported to Rhinoceros. The accuracy of the laser is of $\pm 1.0$ and 2.0 mm for favourable and unfavourable conditions. These tolerances apply in a range between 0.05 to 10 m with 95% of confidence level. It was considered that the conditions were unfavourable as no white targets were used and the illumination was not regulated because this was carried out outdoors.

Figure 8.43 shows the target points used to measure the geometry of the culms using a laser point. The average geometric error between the marking points in the culms and

| Bamboo | Diameter (mm) | Thickness (mm) |
|---|---|---|
| Culm 0 | 72.2 | 7.9 |
| Culm 1 | 70.3 | 6.7 |
| Culm 2 | 72.3 | 8.0 |
| Culm 3 | 75.3 | 7.7 |
| Culm 4 | 69.6 | 8.4 |

**Table 8.9:** Bamboo culms average dimensions.

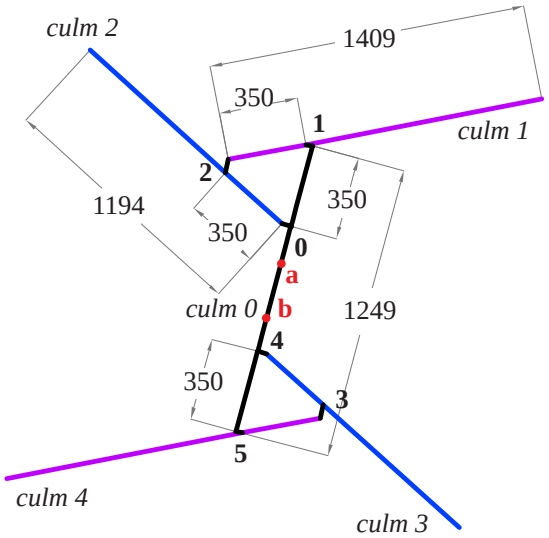


**Figure 8.42:** Geometry and nomenclature of module. The point a and b correspond to the points used for measuring the displacements.

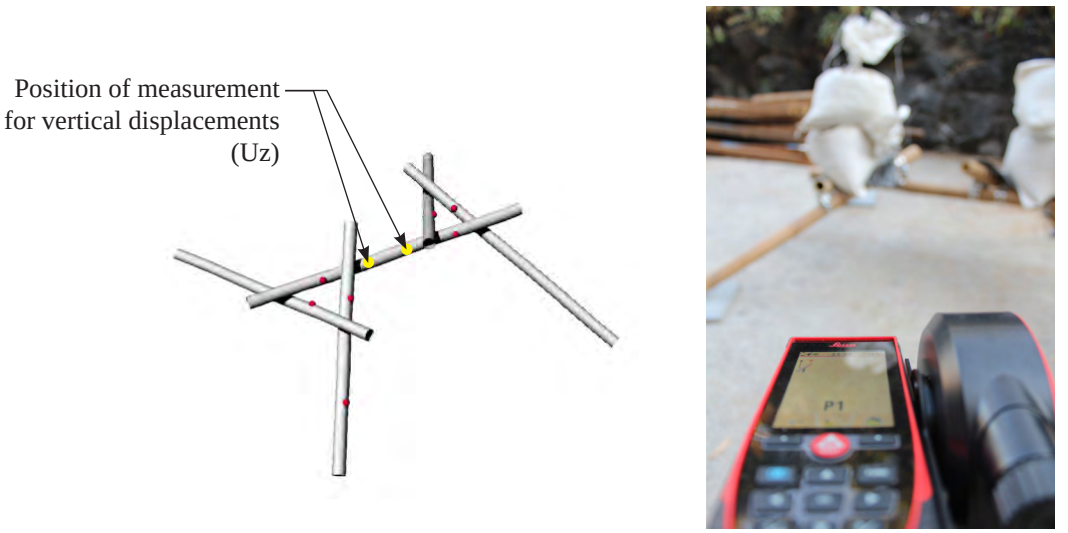


**Figure 8.43:** Position for measurements of geometry and vertical displacements, and laser point Leica.

the 3D points measured with the laser for the modules assembled with both connection systems is provided in Table 8.10. There is not significant difference between the reciprocal geometry obtained assembled with timber and aluminium connections. However, the error in geometry is higher than with the previous method. Although, a larger error was expected as the number of culms is higher than with the previous method, the differences can be due to different reasons. Throughout the process, there are four aspects to consider: a) the accuracy of the scanned geometry of the culms, b) the accuracy of the marking system, c) the accuracy of the assembly method, and d) the accuracy of the measuring method. In this case, the marking system and the measuring method used is different

**Table 8.10:** Geometry error of the physical module with timber and aluminium connections.

| | timber | aluminium |
|---|---|---|
| mean (mm) | 7.0 | 6.1 |
| % error | 3.0 | 2.7 |

than those used in the previous module B. The accuracy of the measuring method from the previous marking system is 0.01 mm using a digital vernier, while the accuracy of the laser point is up to 2.0 mm.

#### 8.4.3.2 Experimental test

The set-up for the module assembled with both connection systems is depicted in Figure 8.44. Concrete slabs were placed underneath each support with the aim of providing a smoother surface, as the concrete floor of the test area was very rough. It was considered that the legs were free to translate in the horizontal plane. The timber blocks located at the supports (see Figure 8.44), were used only as reference for the measurements of the horizontal displacement, therefore they do not affect the support conditions. The module was loaded using sand bags. A total of 1468 N was applied using four sand bags, two at each side on the inner triangles. Neoprene sheets were provided on the elements forming the triangle to prevent the steel threaded rods of the connections to pierce the sand bags.

The load-displacement curves are presented in Figure 8.45. The vertical displacements were measured using the laser point described above. The target points used to measure the displacements are depicted in Figure 8.43. These were located at the middle section of the horizontal element. The module assembled with the timber connections presents a stiffer behaviour of about 7 % higher than that of the aluminium connections. Both modules presented a linear elastic behaviour under the applied load.

**Figure 8.44:** Test set-up and loading of module C.

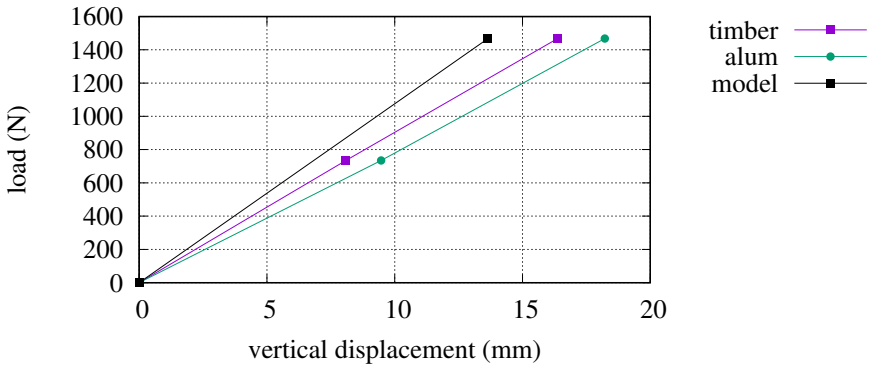


**Figure 8.45:** Load-displacement curves for module assembled with timber and aluminium connections, where *timber* and *alum* refer to the experimental tests respectively, and *model* refers to the results from the structural model.

#### 8.4.3.3 Numerical analysis

The structural model for the modules of both connection systems was considered to be equal. The modelling was as described in Section 9.1, using the SBD and assuming rigid connections at the six connecting points. The supports in the model were considered as free to rotate in the three directions, and free to translate in the xy plane. An upper node was fixed to rotate in the three directions and prevented to translate in the xy plane to avoid numerical instabilities in the model, due to unrestrained degrees of freedom. The total load was divided by six and the loads were applied to the upper node of each connector.

Figure 8.46 depicts the sequence of steps of the modelling and analysis process including the incorporation of the geometry of bamboo culms as the discretised elements in the structure. In addition to this model using discretised elements, a model using line elements was developed to evaluate the effect of incorporating the SBD into the design process.

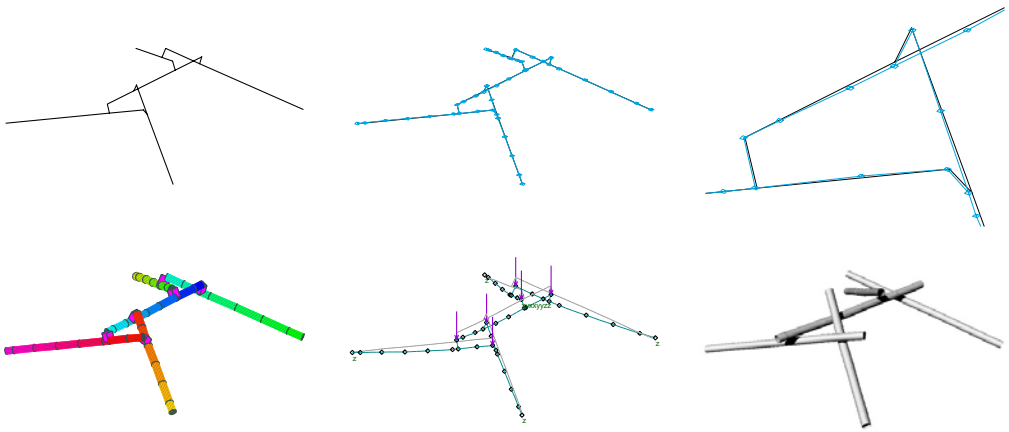

**Figure 8.46:** Modelling sequence of the reciprocal module. (a) line elements. (b) bamboo elements. (c) eccentricities in bamboo elements. (d) structural model with with gradient properties. (e) deformations. (f) model.

**Table 8.11:** Equivalent rotational stiffness of both type of connection systems in module C.

| Connection type | Rotational stiffness | | |
|---|---|---|---|
| | $x$-axis (kNm/rad) | $y$-axis (kNm/rad) | $z$-axis (kNm/rad) |
| Timber connections | 8.5 | 1.2 | 5.5 |
| Aluminium connections | 4.2 | 0.6 | 2.7 |

The vertical displacements obtained from the structural model (using discretised elements) is presented together with the results of the experimental tests in Figure 8.45. From previous modules (module A and B) we know that modelling the connections as rigid connections accurately predicts the behaviour of the modules with timber connections in the elastic regime. However, in this module C, the structural model underestimates the displacements from that of the physical modules assembled with timber and aluminium connections. Table 8.11 presents the estimated equivalent rotational stiffness for both connection systems in this module C. Note that the rotational stiffness estimated from this module is significantly lower than that estimated for module B (see Table 8.7).

There are certain differences in the geometric design of the timber blocks for this module C with respect the previous modules A and B. The angle $\theta$ defining the depth of the groove (see Figure 8.47) is smaller for module C, which in turns decreases the contact area between the bamboo and the timber blocks. As mention in Subsection 8.2.1, this angle was empirically defined as the effect (forces and moments) of the connections in the element are very complex and therefore the most feasible method to determine an optimal value for this angle is by testing. The results suggests that the loss of stiffness of the system was caused by the depth of the groove resisting shear forces and moments and in the horizontal direction (see Figure 8.10). From these observations, we can see that the optimal value lies between these two angles (i.e. 47° and 63°).

During the loading test assembled with aluminium connections, deformation of the vertical components was observed (see Figure 8.48). This can be caused by the interaction between buckling and bending in the steel threaded elements packed with aluminum components as studied in Section 8.3. As mentioned, overall the stiffness of the aluminium

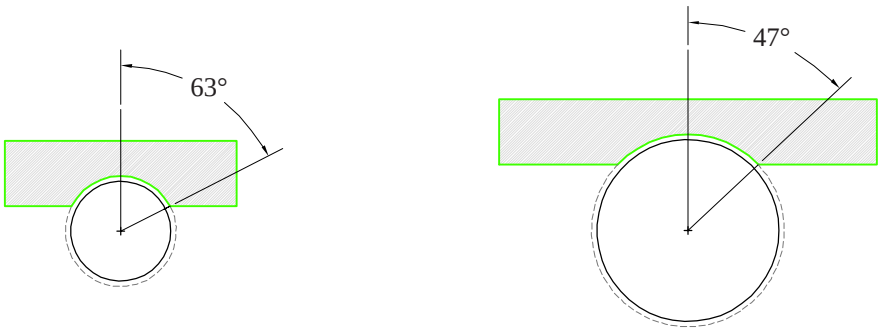


**Figure 8.47:** Timber groove depth for module B and C.

(a) (b)

**Figure 8.48:** Deformations of the vertical components in aluminium connection under vertical load. (a) Loaded connection. (b) Unloaded connection.

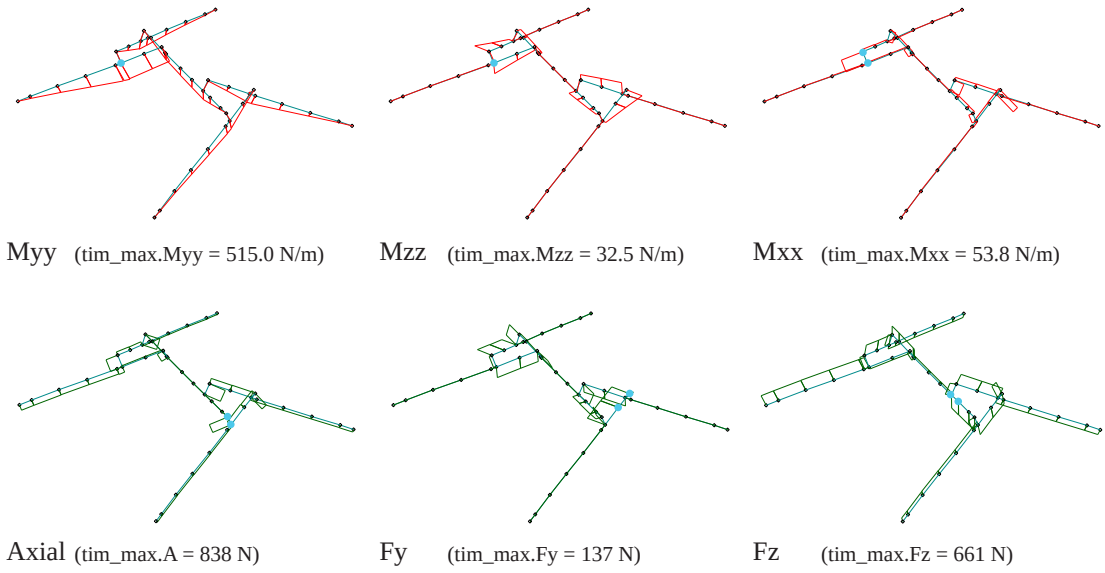


**Figure 8.49:** Moments and forces of module C.

connections is lower than that of the timber connections. This highlights the need to provide rotational stiffness in both directions of the local axes of the connections.

The distribution of moments and forces for both models are presented in Figure 8.49 for the discretised elements. The bending moments in the $y$ direction, and the shear forces in the $z$ direction are distributed in inner and boundary elements. Whereas the moments in the $z$ direction, torsion and shear forces in the $y$ direction are concentrated towards the elements in the triangle and in the connectors. The middle element corresponding to culm 0 is subjected to bending moments in the $y$ direction and torsion.

Sensitivity analysis was carried out to investigate the influence of using discretised elements against using line elements. This was assessed by comparing the results from two elements in the module (one inner and one boundary element) and one connector. Figure

**Table 8.12:** Results of key elements for module C modelled with rigid connections.

| | Elements | | | | | | Connectors | | |
|---|---|---|---|---|---|---|---|---|---|
| | Boundary element | | | Inner element | | | | | |
| | Line | Discretised | % diff | Line | Discretised | % diff | Line | Discretised | % diff |
| $U_z$ (mm) | 11.28 | 13.65 | 19.0 | | | | | | |
| $U_{xy}$ (mm) | 4.87 | 5.80 | 17.4 | | | | | | |
| $R_{xyz}$ (rad) | 0.017 | 0.020 | 15.9 | | | | | | |
| $Fx$ (N) | 219 | 253 | 14.6 | 64 | 136 | 71.8 | 557 | 536 | -7.4 |
| $Fy$ (N) | 0 | 0 | - | 129 | 141 | 8.8 | 203 | 242 | 17.6 |
| $Fz$ (N) | 513 | 560 | 8.8 | 255 | 178 | -35.2 | 504 | 482 | -4.6 |
| $M_{xx}$ (Nm) | 0 | 2 | - | 31 | 1 | -187.5 | 72 | 60 | -17.9 |
| $M_{yy}$ (Nm) | 432 | 480 | 10.4 | 316 | 381 | 18.6 | 33 | 51 | 41.3 |
| $M_{zz}$ (Nm) | 0 | 1 | - | 56 | 34 | -48.4 | 110 | 84 | -26.5 |
| $F_{yz}$ (N) | 513 | 560 | 8.8 | 285 | 227 | -22.7 | 543 | 539 | -0.8 |
| $M_{yz}$ (Nm) | 432 | 480 | 10.4 | 316 | 381 | 18.6 | 110 | 84 | -26.9 |
| $A_x$ (N/mm$^2$) | 0.15 | 0.17 | 15.9 | 0.04 | 0.09 | 72.9 | 0.60 | 0.56 | -7.4 |
| $S_y$ (N/mm$^2$) | 0 | 0 | - | 0.17 | 0.19 | 9.9 | 0.23 | 0.28 | 17.6 |
| $S_z$ (N/mm$^2$) | 0.68 | 0.75 | 10.1 | 0.34 | 0.24 | -34.0 | 0.58 | 0.56 | -4.6 |
| $B_y$ (N/mm$^2$) | 20.35 | 21.87 | 7.2 | 14.87 | 17.34 | 15.3 | 7.94 | 12.08 | 41.3 |
| $B_z$ (N/mm$^2$) | 0 | 0.04 | - | 2.65 | 1.56 | -51.4 | 26.02 | 19.94 | -26.5 |

Figure 8.50 shows the boundary, inner and connector elements used for the moments, forces and stresses presented in this table. The displacements and rotations correspond to the maximum values of the entire model.

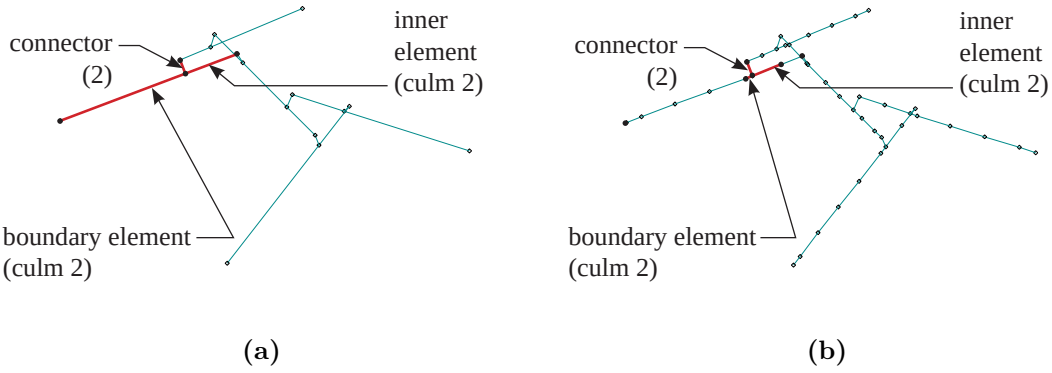


**(a)** **(b)**

**Figure 8.50:** Position of the (a) line and (b) discretised elements for the measurements of moments, forces, stresses and displacements.

8.50 indicates the elements and connector used for this analysis. Table 8.12 presents the results of the structural models with line and discretised elements.

Overall the vertical displacements are underestimated by 19.0% by using the line element model if we consider the connections to be rigid. Table 8.13 provides the percentage difference of the vertical displacements $U_z$ between the line and discretised models if we consider the connections to be semi-rigid. For this we used the estimated stiffness from Table 8.11 for modelling the behaviour of both connection systems. The percentage difference is 14.7% for the timber module and 11.7% for the aluminium module.

**Table 8.13:** Vertical displacements $U_z$ of module modelled with semi-rigid connections.

| Model semi-rigid connection | Line (mm) | Discretised (mm) | % diff |
|---|---|---|---|
| timber | 14.1 | 16.4 | 14.7 |
| aluminium | 16.2 | 18.2 | 11.7 |

## 8.5 Summary

This chapter presented the development of two different connection systems for bamboo culms at the conceptual design stage. It discussed the structural behaviour of the connections concerning the moments and forces that these need to transfer according to the studies in Chapter 9. Both systems rely on the clamping force of the components in the transverse direction of the bamboo culms. Therefore, these are avoiding perforations in the cross-section, which have been associated with the splitting of the culms.

The first connection is made up of timber blocks. The capacity of this connection to resist the forces and moments in the $x$, $y$ and $z$ directions is provided by the four steel threaded rods located at opposite orthogonal sides in the corners of the timber blocks. Although the connection is capable of resisting moments in the $y$ and $z$ directions and torsional moment in the $x$ direction, it is likely not fully fixed but partially fixed. From the experimental tests of module C, we know that the vertical displacements measured from the physical module are higher than those estimated from the structural analysis. This was associated with the geometry of the connection, which has a smaller angle $\theta$ than the timber connections of modules A and B. The importance of this angle is that it defines the depth of the groove, and thus it influences the rotational stiffness of the connection since the contact area of the timber connection decreases with a decrease of angle. While the structural model of this connector is conservative for the calculation of stresses, it is non-conservative for the estimation of displacements. This is because the higher moments attracted by the connector in the structural model, as the model of the connector is stiffer than the physical connection. The angle $\theta$ is a key parameter for the stiffness of the connection, and as such, further tests are required to investigate the influence of this angle in the rotational stiffness of the connection to consider this in the estimation of deflections and to define optimal values for the geometric parameter of this connection.

The influence of the application of transverse load using the timber block with a groove against using a flat surface was also investigated. It was found that the transverse capacity of bamboo can increase up to 30% using the timber block with a groove. In addition, a relationship between failure load and area (thickness if a unit length is considered) was found for culms of the same shape factor $\Phi$. This can potentially be used for estimating the transverse capacity of the culms without the need for experimental tests. Further tests are recommended for the population of a database that can be used to test the feasibility of using this relationship.

Overall, the behaviour of the reciprocal modules assembled with timber connection was found to be linear elastic. During unloading of module B a small residual displacement was observed, which was associated with the settling of the timber components. From modules A and B tested until failure, yielding before failure was observed from the load-displacement curves. Failure occurs due to the strength of the material rather than the failure of the connection. Therefore, this connection allows to take full advantage of the capacity of the bamboo culms. The failure of the culms occurred at the location of the maximum moment, which agrees with the behaviour observed in the structural model. The critical stresses for modules A and B were shear stresses and these were associated with the geometry of the modules. It was observed that once the module collapsed, the whole structure remains locked, suggesting that the redundancy of the structure can prevent disproportionate collapse, and thus allow for the replacement of elements. In the first module A, slip of the connection was observed. This was prevented in module B by the application of neoprene in the interface between the timber blocks and the bamboo culms, as well as using four steel threaded rods instead of two. Furthermore, indentation of the timber blocks in the failed culm of module B were observed. However, observations of the cracks in the culms suggested that the indentations were generated once the culm has failed.

The other connection consists of aluminium components. Unlike the timber connection, this connection only provides two vertical components at opposite sides. Therefore, the rotational capacity of the two principal orthogonal directions is different. Nevertheless, the structural stability of the connection is provided when the reciprocal systems are assembled. Therefore, like for the timber connection, we can consider that the connection is partially fixed. We confirmed that with the experimental test in module C, which did not show any disproportionate sway of the connections in any particular direction, as would happen with a connection with moments releases in either $y$ or $z$ directions. From the load-displacement curve, we deduce that the displacements measured from the physical module with aluminium connections are higher than those estimated from the structural model. This agrees with the behaviour observed from the same module assembled with timber connections. However, the displacements are higher for the aluminium connection, suggesting that the rotational stiffness of the partially fixed aluminium connection is lower than that of the timber connection.

During the experimental test of module C, deformation of the vertical component was observed. The stability analysis of the vertical components was carried out considering that a vertical component is free to rotate and translate in one end and that it has an eccentric moment caused by the deformations due to the horizontal forces. Besides the fact that there were only two vertical components, the deformation found in the vertical element might be associated with the vertical component itself, which was a combination of steel threaded rods and packing rather than a single component. Further design iterations, should consider this aspect. The rationale behind the design of this connection was to provide a design that uses standardised components. However, it is recommended

to explore other alternatives to minimise material that is not structurally working (e.g. aluminium components) and to provide a single element for the vertical components.

Overall, the timber connection provides a structurally sound solution for the assembling reciprocal structures. However, some aspects needs to be carefully studied; for example, the influence of the angle that defines the depth of the groove. More tests are required to evaluate the influence of angle $\theta$ in the rotational stiffness of the connection. Also, the fabrication of the timber blocks shall be evaluated based on the direction of the applied load through the steel threaded rods, to prevent splitting of the timber blocks during assembly. In addition, further tests to analyse the transverse compressive strength of bamboo using edge bearing tests with suitable set-up (e.g. with timber blocks) are recommended. Besides gathering data to assess the relationship between $\Phi$, area and failure load, this will allow the quantification of the maximum load that can be applied to the timber blocks, and therefore, the analysis of the connection based on the capacity of the each of the components.

For the aluminium connection, although stability is achieved in a three element module, the stiffness of the system is lower than that estimated. Therefore, a further iteration of the design of this connection with four vertical components is sought to assess the stiffness and also investigate possible failure mechanisms with the aluminium connection. Four vertical components at the two opposite locations are recommended to further developed this connection into a robust design, and to assess the stiffness of this connection.

Furthermore, it was found that modelling module C with line elements can underestimate the deflections of the system by 19%. In line with the previous chapter, this highlighted the influence of using the SBD and discretised elements in structural analysis for the safe design of bamboo structures.

Finally, the geometric error measured between the digital and the physical modules assembled was evaluated. For the reciprocal module B the average percentage error was 1.2% with a maximum difference of 1.1 mm measured. The geometric error for reciprocal module C assembled with timber and aluminium connections was 3.0 and 2.7% (i.e. 7.0 and 6.1 mm respectively). While there were two aspects (the marking system and the measuring method) identified that influenced the difference of geometric error between both reciprocal modules (modules B and C), the error was not significant. The percentage error measured for the geometry assembled using the jig and block methods is 1 and 3% on average respectively, corresponding to 1 and 6.5 mm respectively, as the models used were of different dimensions. In addition, the geometric error measured for a larger structure (as shown in Appendix I) was 1%, corresponding to approximately 12.8 mm.

There are no guidelines for tolerances on erection methods for bamboo culms. In comparison with other structural materials, the tolerances measured here are not considered to be excessive. The allowable positional tolerances for rough lumber is $\pm 6$ mm (Ballast, 2007), and for the position of steel columns at the base it is 10 mm (Taylor, 2008). Although these are not directly related because the geometry of reciprocal systems is very complex in comparison to conventional frame systems, the magnitude of the tolerances is

expected to be comparable, and thus within the same range.

The design and structural performance of both connection systems differ significantly. The main differences between both connection systems are the fabrication methods and structural performance. Whereas the timber connection relies on bespoke fabrication, the aluminium connection can be more easily fabricated as it is based on components currently available in the market. The selection of one single connection system will ultimately depend on the requirements and context of the structure to be built. As highlighted by Follet and Jayanetti (2008), the development, research and improvement of bamboo connections is paramount for the acceptance and usage of the material in construction as a main load-bearing element.

# Chapter 9

# Structural behaviour of bamboo reciprocal structures

This chapter presents a series of structural analyses carried out for developing an understanding of the global structural behaviour of bamboo reciprocal structures. The specific objectives are described below.

- To define the structural modelling of bamboo elements using the discretised properties from the SBD and assess the difference between this approach and modelling bamboo with uniform properties.
- To gain insight into the load-transfer mechanism of bamboo reciprocal systems including the role of the connections, and to evaluate the effect of key geometric parameters in the structural performance.

The behaviour of reciprocal systems has been characterised by bending (Baverel, 2000; Rizzuto and Larsen, 2010), and axial and shear stresses (Anastas et al., 2016). The governing behaviour is affected by the geometry of the reciprocal system (Baverel, 2000; Douthe and O.Baverel, 2009), as well as the cross-section of the elements. Baverel (2000) investigated the behaviour in circular sections, Anastas et al. (2016) investigated the behaviour using thin rectangular sections.

There is no analysis in the literature of the influence of the eccentricity on the structural behaviour in plane or doubly curved structures. Szabadszállási et al. (2004) concluded that plane reciprocal structures are not suitable for long span structures. However, based on investigations for doubly curved reciprocal structures in three dimensions, Douthe and Baverel (2013) suggested that there are two types of reciprocal systems. One for reciprocal structures of a single layer, in which the structure behaves like a thin shell governed by membrane forces, and another for double layer in the structure acts as a spatial structure, very much like a thick shell with high bending stiffness. In this thesis, we are concerned with the design of reciprocal structures of double curvature with one layer.

## 9.1 Structural modelling

The numerical analyses presented in this thesis were carried out in the commercial structural software Oasys-GSA (2017a). The type of analysis run in this study is linear static analysis, and the requirements of the model are to obtain as outcome the displacements and rotations at the nodes, the reactions at the restrained nodes, and the forces and moments in the beam elements.

### 9.1.1 Geometry

The modelling of all the elements, including connections, was done using beam type elements with six degrees of freedom at each node (MacLeod, 2005). For the purpose of clarity, in the modelling process the terms *line element* and *discretised element* are introduced to distinguished between the modelling of bamboo culms as straight line elements with uniform properties and as discretised elements defined by a series of segments to account for the variable properties respectively. Likewise, the term *connector* is used to refer to the element representing the connections in the direction of the eccentricities. The connectors are represented as rigid links that joints the two elements. Figure 9.1 shows the structural models for the line and discretised elements.

The geometry of the discretised elements is defined from the SBD as presented in Section 4.4, using the end node coordinates for each discretised element and the respective diameter and thickness for each. Recall that each of the segments corresponds to half an internode to take into consideration the deviation of the internodes. The selection and position of bamboo culms for each element in the structure is determined by some predefined criteria (see Section 7.2), and the discretised elements were incorporated to the structural skeleton as described in Subsection 7.2.4.

The local axes of the elements are defined within the structural software when imported from Rhinoceros (McNeel, 2017). As these are non-vertical elements, the $x$ axis is defined by the direction of the element (using the direction cosines), the $z$ axis is defined in the

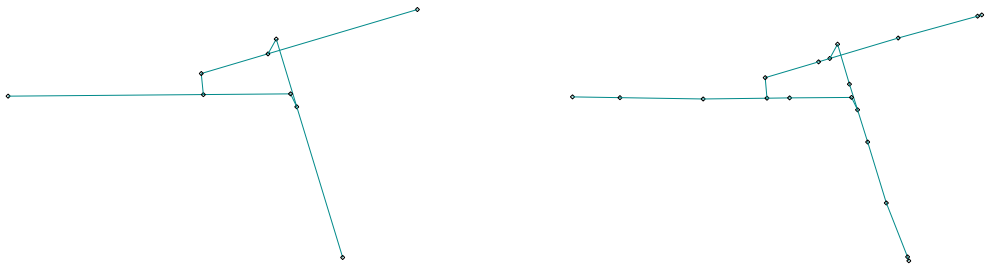

**(a)** **(b)**

**Figure 9.1:** Model with (a) line elements and (b) discretised elements.

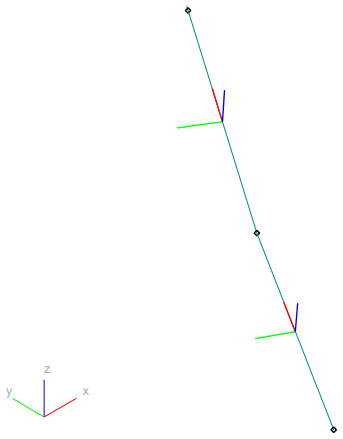


**Figure 9.2:** Local axes of elements.

vertical plane and orthogonal to the $x$ axis, and the $y$ axis is defined as orthogonal to the $x$-$z$ plane (Oasys-GSA, 2017b). Figure 9.2 shows the local axes of the elements with respect the global axes of the model.

### 9.1.2 Material model

The material model considered for the analysis is isotropic linear elastic. Table 9.1 presents a typical example of the definition of the material model for a bamboo element. Note that the elastic modulus $E$, and density $\rho$ changes for the discretised elements according to the data from the SBD for each segment as described in the previous Part II in Tables 5.3 and 6.14. The typical values used for the elastic modulus $E$, and density $\rho$ are taken from Figures 6.14a and 6.15. As the Poisson's ratio $\nu$ is not a critical parameter (as seen from the sensitivity analysis in Subsection 6.2.1.9), the average value of 0.30 was considered. Furthermore, previous investigations (Zhou et al., 2012; García et al., 2012) and preliminary tests (see Subsection 6.1.2) have shown that $\nu$ lies within the range of 0.12 and 0.43.

**Table 9.1:** Typical material model definition for bamboo culms. The parameters in bold changes for the discretised elements.

| Parameter | value | units |
|---|---|---|
| Material model | isotropic linear elastic | |
| **Elastic modulus**, $E$ | 16000 | $N/mm^2$ |
| Poisson ratio, $\nu$ | 0.30 | |
| Shear modulus, $G$ | $E/2(1+\nu)$ | $N/mm^2$ |
| **Density**, $\rho$ | 700 | $kg/m^3$ |

### 9.1.3 Section properties

From Section 4.3 we know that the section properties of bamboo are non-symmetrical, and as such, these can impact the second moment of area with respect to two orthogonal


**(a)** **(b)**

**Figure 9.3:** Principal axes of (a) irregular and (b) regular cross-section shapes.

directions. Also, the principal axes do not coincide with the geometric axes as shown in Figure 9.3a. Nevertheless, in order to simplify the modelling of each of the discretised sections, the cross-section of bamboo for line and discretised elements are considered as hollow circular sections with double symmetry (see Figure 9.3b). For the line elements, the average diameter and thickness are used for the entire culm, while for the discretised elements the diameter and thickness change between segments along the culm according to the discretised properties from the SBD.

### 9.1.4 Connectivity

The support conditions for the structural models analysed in this chapter are considered as pinned, free to rotate in the $x$, $y$ and $z$ directions and fixed to translate in the $x$, $y$ and $z$ directions. Therefore, the supports are not capable to transfer moments.

The modelling process of the connectors was carried out together with Section 9.2 where the stiffness of the connectors was studied. It was assumed that the connections are rigid, therefore the two ends of the connectors are defined as fixed (i.e. zero degrees of freedom). It is considered that the deformations of the connector are very small or negligible in comparison with the deformations of the bamboo element. Therefore, the properties of the connector are at least an order of magnitude greater than the flexural stiffness of the bamboo element.

### 9.1.5 Load discretisation

The loads were applied at the top node of the connector in the vertical direction at the $z$ axis of the global coordinate system, as shown in Figure 9.4.

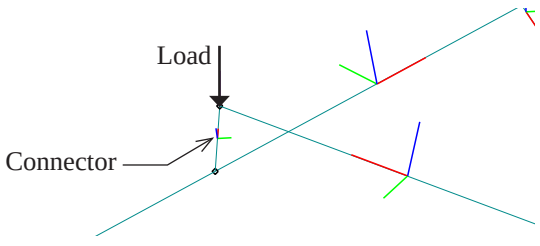


**Figure 9.4:** Load discretisation.

## 9.2 Bamboo reciprocal modules

This section investigates the behaviour of a three-element module to study the force transfer mechanism, the rotational releases in the connectors, the effect of the eccentricities and the engagement length ratio in reciprocal systems.

Figure 9.5 shows the structural model of a three-element reciprocal module modelled and loaded as described in Section 9.1. The length of the elements and the engagement length is similar to the modules presented in Chapter 8. The total length of the elements is 1.2 m and the eccentricities length is 66 mm for the three connectors. The connectors were modelled with no rotational or translational degrees of freedom in the first place. However, the effect of the rotational releases in the connector are investigated in Section 9.2.1. The focus of this subsection is concerned with understanding the structural behaviour of the system rather than with the exact values of forces, moments and displacements resulted from the structural analysis.

The forces and moments are presented from Figures 9.6 to 9.8. The governing behaviour of each of the elements in the reciprocal systems is similar to that of a simply supported beam. The maximum bending moments are concentrated towards the element outside the engagement length, at the location below the connectors. These are oriented in an arbitrary direction that mainly depends on the direction of the applied load and the direction of the connectors. The shear forces are generated along the whole culm but are higher at the elements located in the engagement window. Also, the different orientation of the connectors, and therefore of the forces, causes torsion in the elements located in the engagement window. As here the support conditions are considered pinned, there is no torsion in the elements outside the engagement window. All the moments and forces are transferred between the elements by the connectors, which are mostly subjected to torsion moments and shear forces, but also to bending moments.

The deformed shape of the system is shown in Figure 9.9. Note that besides the deformations in the direction of the applied load (in the $z$ direction), the whole system tends to rotate from the centre in an anticlockwise direction. This twist is caused by the inherent geometric configuration of the reciprocal system and the direction of the elements. When one of the culms (made up of two elements) deflects in the $z$ direction, it also displaces in the horizontal direction, causing horizontal forces in the elements which

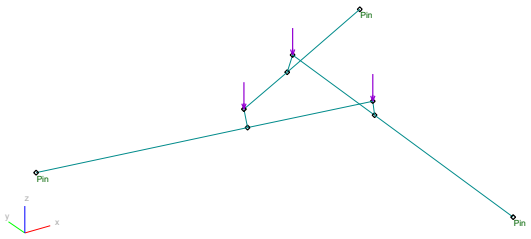


**Figure 9.5:** Idealised model of a three-element reciprocal unit.

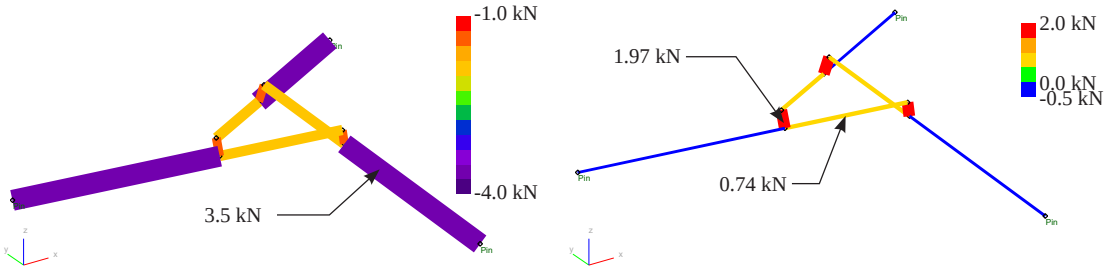


(a) (b)

**Figure 9.6:** (a) Axial forces, $F_x$. (b) Shear forces, $F_y$.

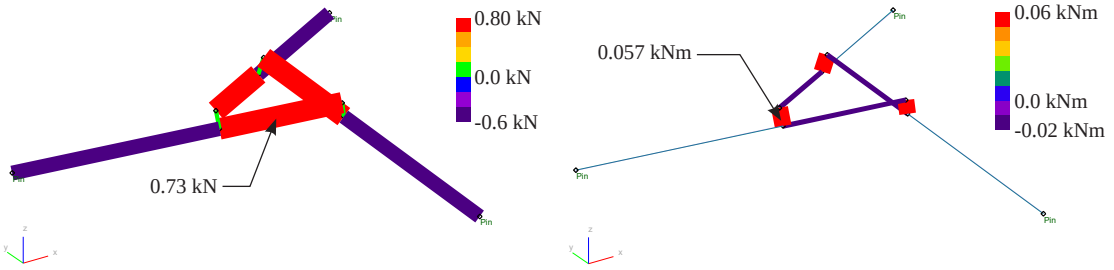


(a) (b)

**Figure 9.7:** (a) Shear forces, $F_z$. (b) Torsion, $M_{xx}$.

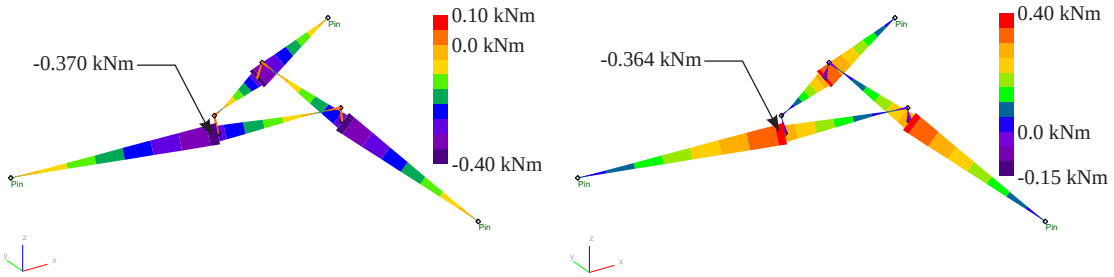


(a) (b)

**Figure 9.8:** (a) Moments in the $y$ direction, $M_{yy}$. (b) Moments in the $z$ direction, $M_{zz}$.

are supporting the culm. Therefore, the direction of the elements define the direction of the rotations. See for example the deformations in Figure 9.10 for a system with the same dimensions, but with the elements arranged in the opposite direction. The twist deformation of the system occurred in the clockwise direction for this case.

### 9.2.1 Study of stiffness in connectors

This subsection investigates the influence of the stiffness of the connections, in the main orthogonal directions of the eccentricity, on the overall structural behaviour of a reciprocal unit. The purpose is to inform the connections designs by identifying the forces and moments that the connections should be capable of transferring.

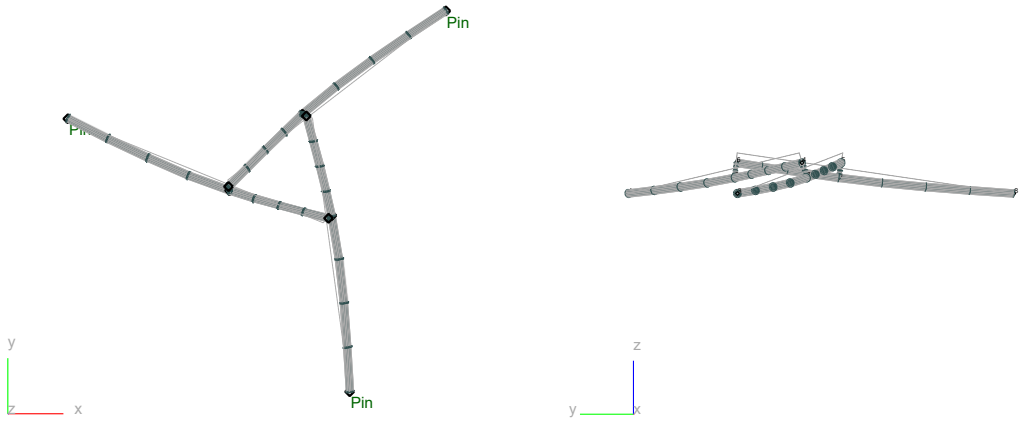


**Figure 9.9:** Deformed image of the reciprocal unit.

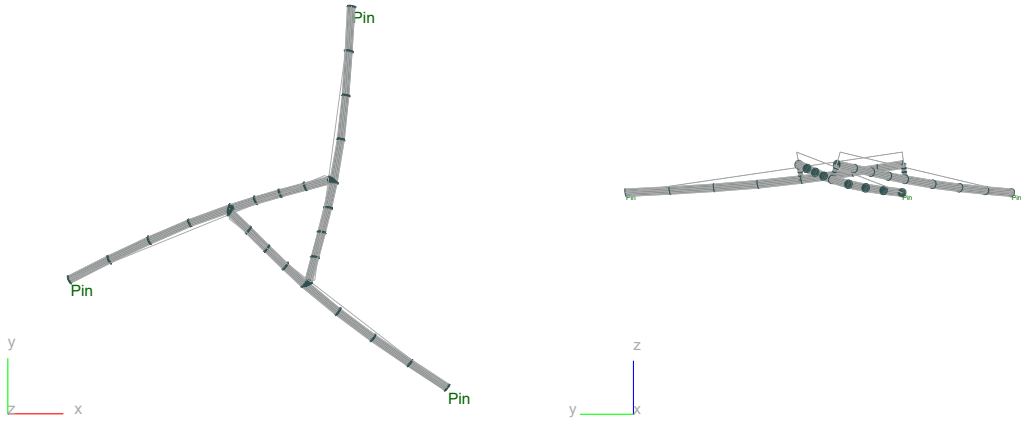


**Figure 9.10:** Deformed image of the reciprocal unit with rotations in opposite directions as previous module.

The structural stability of the reciprocal system depends in the capacity of the connectors to transfer moments and forces among the elements. Herein, we investigate the influence of the stiffness of the connectors by changing the rotational stiffness in the $x$, $y$ and $z$ directions to prevent the possibility to have a mechanism when there is loss of stiffness in the connections.

The study consists of analysing the behaviour of a three-element module while varying the degrees of freedom of the connector. The benchmark model was considered with fully fixed rotations and translations. It was assumed that the connector can transfer the same moments and forces at both ends. Therefore, the degrees of freedom were varied equally at both sides, except for the rotational releases in the $x$ direction which is only varied at one end to prevent instabilities. Because the end nodes of the connectors move freely under the applied loads, the behaviour of the system with rotational releases in the $x$ direction of the connector is very similar to the benchmark model. Furthermore, the connector cannot be released in the $y$ and $z$ directions simultaneously because the connection between element and connector becomes a hinge and as such is not capable of

transferring moments between elements. Therefore, the analysis is focused in the rotational releases for the $y$ and $z$ directions independently.

Figure 9.11 shows the direction of the $y$ and $z$ axes. Note that the $z$ axis is in line with the $x$ axis but orthogonal to it. For this analysis, the applied load is arbitrarily selected in the $z$ direction of the global axes.

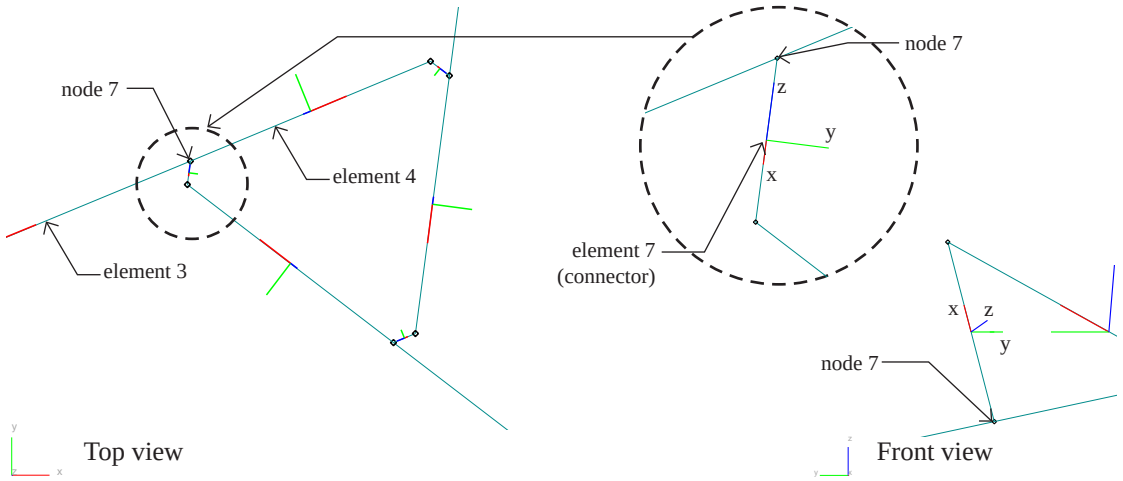


**Figure 9.11:** Local axes of connectors

First, we will analyse the rotational releases in the $y$ direction. Before inspecting the deformed shape, we first see how the connector is free to rotate in the $x$-$z$ plane. Figure 9.12, shows the elements inside the engagement window and the respective connectors orthogonal to them. Rotations with respect the $y$ axes will allow the connector to sway outwards, as shown in Figure 9.12, for different angles of $y$ rotation until the whole structure is lying in the same plane. This will cause torsion in the element of the engagement length. In addition, the displacements caused by the sway of the connector generates significant moments in the elements located below the connector. The deformed shape is presented in Figure 9.13, and the displacements are approximately five times higher than the benchmark model. Note that the deformed shape is different to that of a fully fixed system as the sway of the connectors prevent the twist of the module.

Figure 9.14 shows the rotations of the connectors in the $z$ direction for different angles

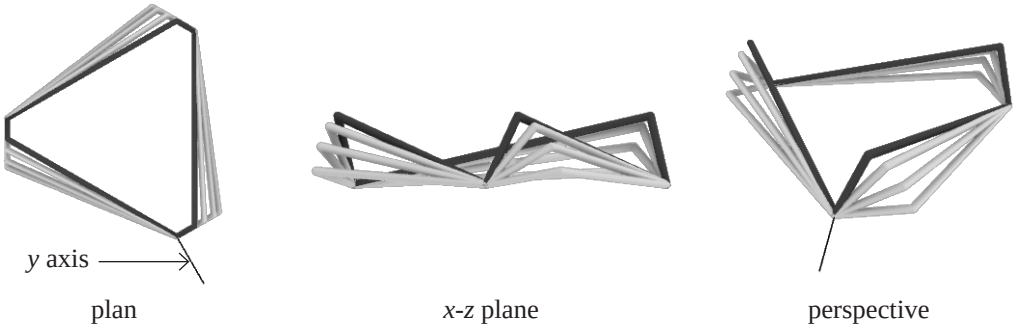


**Figure 9.12:** Rotations of connectors in $y$ axis.

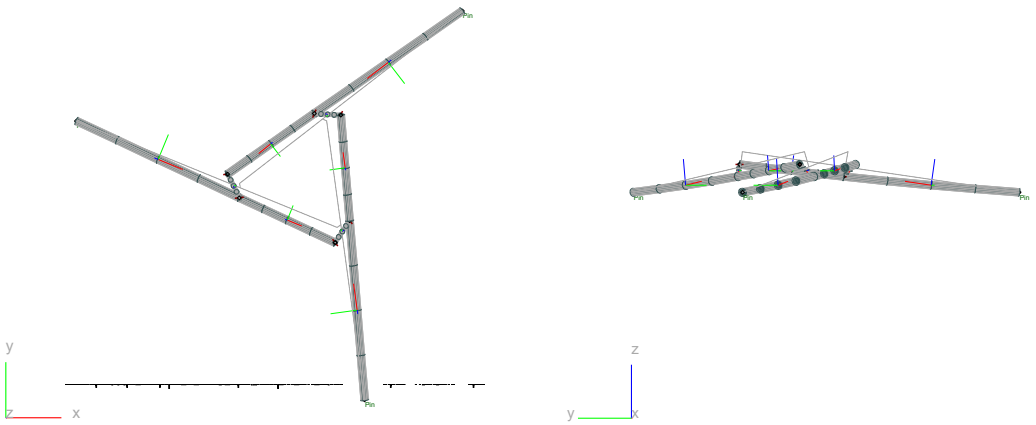

**Figure 9.13:** Deformed image for module with rotational releases in connectors in the $y$ direction.

of rotation. Note that unlike for the rotations in the $y$ direction, these rotations allow swaying but also to stretch the elements of the engagement length. This is caused by the direction of the rotations in the $x$-$y$ plane which tends to displace one end node of the connector to the inner side of the structure, and the other one to the outside of the structure. The deformed shape is shown in Figure 9.15, and the displacements in the direction of the applied load are twice those of the benchmark model. Similar to the releases in the $y$ direction, the deformed shape does not show twist of the module.

Figure 9.16 shows the comparison of the rotational releases in the connectors for both directions. We can observe that the elements in both cases tend to move away (or outwards) from the centre of the structure after rotations. However, the rotations in the $y$ direction allow sway of the elements further away from the centroid and change of the angle between elements about 25 times higher than that of the benchmark model (approximately 25° in this model). The combination of releases in the $x-y$ and $x-z$ directions is very similar to the previously described models.

From these observations we can conclude that the connectors of reciprocal systems require a transfer of rotational stiffness in the three directions in order to prevent having a system affected by large deformations. The structure becomes a mechanism only if no rotational stiffness is provided in the two axes orthogonal to the direction of the

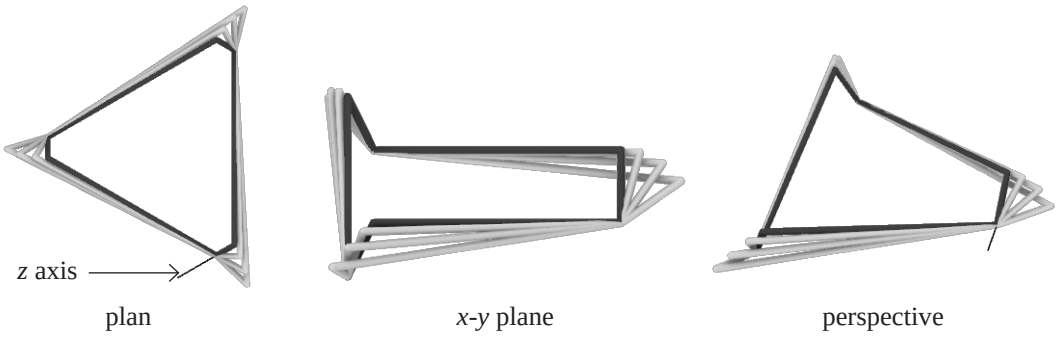


**Figure 9.14:** Rotations of connectors in $z$ axis.

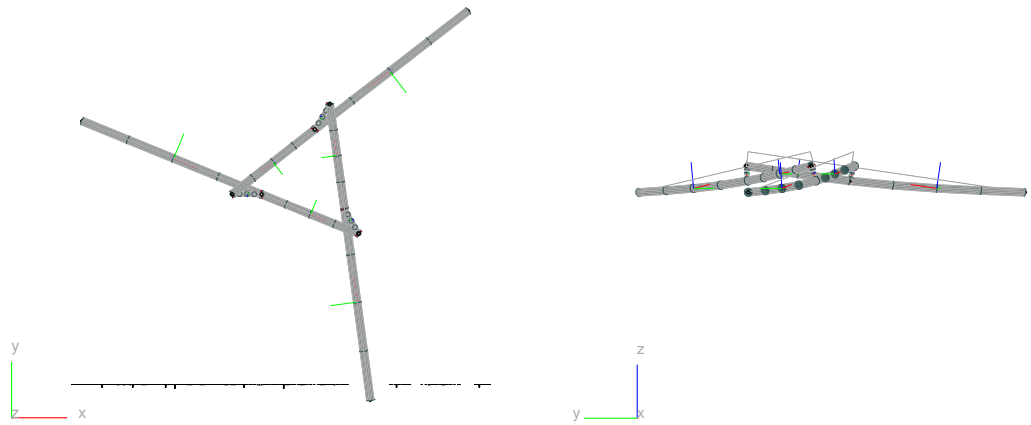

**Figure 9.15:** Deformed image for module with rotational releases in connectors in the $z$ direction.

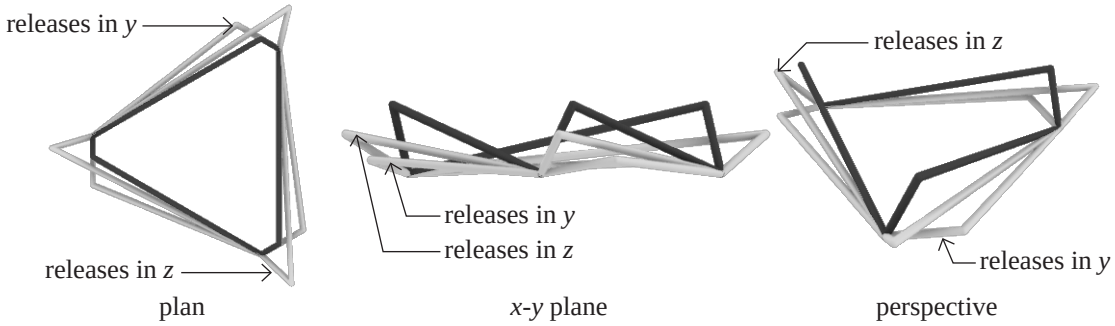


**Figure 9.16:** Comparison of rotations of connectors in $y$ and $z$ axis.

eccentricities (i.e. the $y$ and $z$ axes). However, rotational stiffness is required in the three directions in order to provide stability and stiffness to the whole reciprocal system and to prevent very large deformations.

### 9.2.2 Effect of engagement length ratio

Herein we will analyse the effect of the engagement length ratio in the overall bending stiffness of the system. This study is carried out in modules of three and six-elements, as in reciprocal systems of triangular tessellations of degree 6, the engagement window (see Figure 7.4) has the shape of an hexagon, which cannot be achieved using a three element module.

Figure 9.17 shows the relationship between different engagement length ratios that generate varying openings of the engagement window and their respective eccentricity and engagement length for both type of modules. In both cases, the maximum eccentricities are located at 0.5 engagement length ratio, but for the engagement length, it differs. In a three-element module, the minimum engagement length is when the elements are orthogonal to their initial position, whereas for the six-element module, the orthogonal position generates the larger opening of the engagement window. Therefore, to compare both models, we can consider the second half of the three-element module (from 90° to

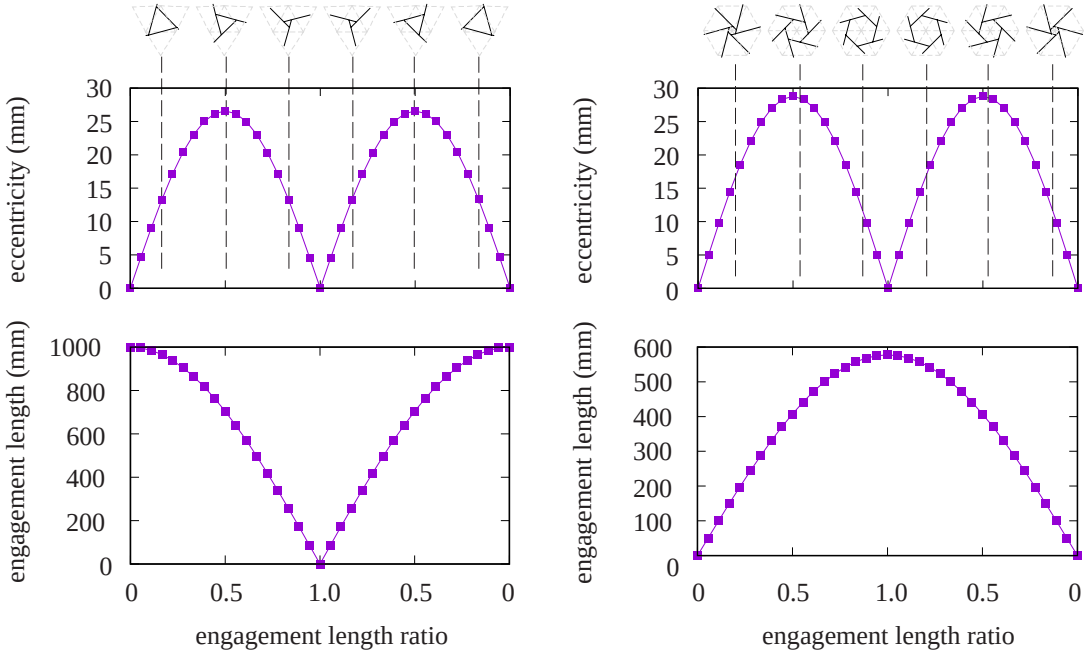


**Figure 9.17:** Relationship between engagement length ratio against eccentricities and engagement length.

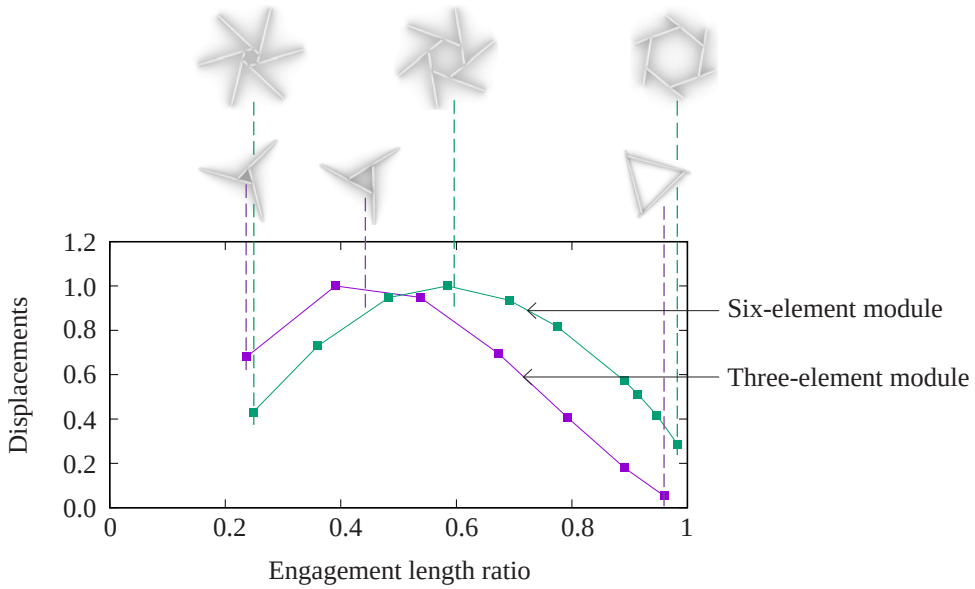


**Figure 9.18:** Relationship between engagement length and displacements normalised to their maximum values.

180°) and the first half of the six-element module (from 0° to 90°). Note that 1.0 of engagement length ratio corresponds to the geometric configuration where the element is perpendicular to its initial position. Thus, the angles between the initial and final elements for an engagement length ratio of 1.0 and 0.5 is 90° and 45° respectively.

Figure 9.18 shows the relationship between engagement length ratio and the overall displacements normalised to its maximum value. It was found that the rotations at the

nodes increase together with the increase of displacements. We can observe that the compliance of the system regarding the engagement length ratio is different for both models. In general, the three-element module presents higher displacements at approximately 0.45 of engagement length ratio, while the six-element module shows higher displacements at approximately 0.60 of engagement length ratio (see Figure 9.18). This is equivalent to an angle of approximately 62° and 37° from the initial configuration for three and six-element modules respectively. In both models the displacements decrease when the elements are either in their initial configuration or perpendicular to it.

This and the last Subsection 9.2.3 provide insight into the influence of the geometric parameters in the overall stiffness of the system and can be used as guidelines to further manipulate the geometry of reciprocal systems to improve the structural performance.

### 9.2.3 Effect of eccentricities

The effect of the eccentricities is also analysed based on the bending stiffness of the overall system. The study of the effect of the eccentricities in reciprocal systems is not straightforward. This is because all the geometric parameters are related, and therefore it is not possible to change only the eccentricity while keeping the rest of the parameters fixed. Here, we will seek the study of this parameter by considering changes in eccentricities while keeping the rest of the geometry as close as possible to the initial geometry.

In Chapter 7, the method presented for the optimisation of eccentricities consists of two main geometric transformations. One is the rotation of the elements out-of-plane, which is equivalent to modification of the dihedral angle between the faces. However, this will result in modules with different height, see for example Figure 9.19. Although the modules have similar engagement length, the eccentricities increase with the height of the module. For these modules the deflections decrease with an increase of eccentricity. Therefore the first module with an almost flat geometry is less stiff. Nevertheless, the geometry between modules changes considerably, and thus we can assume that we are comparing different structures. Note that the structural model of this module was done as described in Section 9.1.

The other method is the translation out of the plane, which can be achieved by moving the elements along the translation vector $\overrightarrow{p}$ as defined in Subsection 7.1.2. This will

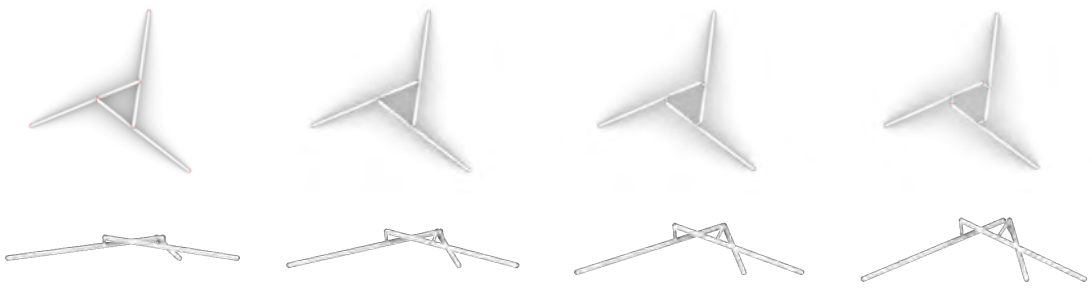

**Figure 9.19:** Reciprocal modules with different height and eccentricities (rotation method).

allow keeping the direction of the elements equal and very similar engagement length as shown in Figure 9.20. From Figure 9.21, we can see that the deflection of the system increases proportionally with the eccentricity. The relevance of this is for the design of the connection systems and the definition of target eccentricities for the optimisation method in Subsection 7.1.2. In principle, the minimum required eccentricities shall be sought to prevent greater compliance of the system.

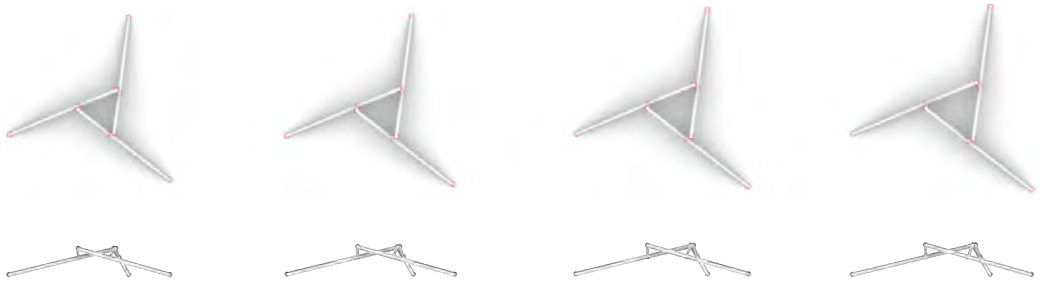

**Figure 9.20:** Reciprocal modules with different eccentricities (translation method).

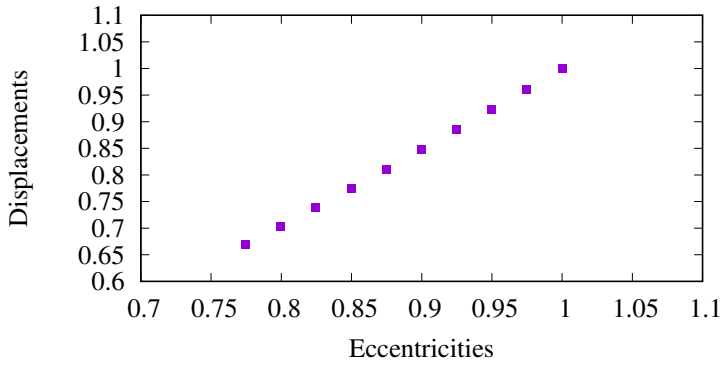


**Figure 9.21:** Relationship between eccentricities and displacements normalised to the maximum value of each.

## 9.3 Bamboo reciprocal system

This subsection investigates the behaviour of bamboo reciprocal systems using as case study the structure defined in the previous Chapter 7. In addition, a series of analyses to evaluate the effect of different parameters, namely the engagement length ratio, the eccentricities, the use of the SBD and the optimisation processes for the selection of bamboo culms are presented. The different structural models developed to evaluate these parameters are described below.

A total of six models were made. This finite set of models can be considered as benchmark models to investigate some of the best and worst possible scenarios for this specific structure. Table 9.2 provides a description of each of the models. When the properties from the SBD are considered, the properties from the oldhamii species analysed

from Chapters 4 to 6 are used.

**Table 9.2:** Description of the different structural models used.

| Model | Element type | Eccentricities | Material / section prop. | Description |
|---|---|---|---|---|
| model 0 | line | random* | average ‡ | Original model |
| model 1 | line | equal** | average ‡ | |
| model 2 | line | variable*** | average ‡ | |
| model 3 | line | variable*** | low ‡‡ | |
| model 4 | discretised | variable*** | SBD | Selection of culms (geometric constraints) |
| model 5 | discretised | variable*** | SBD | Selection of culms (mechanical constraints) |

* Random eccentricities as obtained directly from the definition of the geometry in Section 7.1 prior to the optimisation of the eccentricities.
** Equal eccentricities in the whole structure obtained from optimisation of eccentricities as described in Subsection 7.1.2.
*** Variable eccentricities according to the diameters of the bamboo culms to use in each element obtained from optimisation of eccentricities as described in Subsection 7.1.2.
Material and section properties: three different models were considered, where SBD is provided, the structural model was modelled using the discretised data obtained from the SBD. The other models considered the average data and the lowest values to account for when no data is provided.
‡Average value from all the culms averaged from the bottom and top properties, refer to Table 9.3.
‡‡Lowest value from all the culms averaged from the bottom and top properties, refer to Table 9.3.

**Table 9.3:** Material and section properties of equivalent models with line elements.

| model | E ($N/mm^2$) | D (mm) | t (mm) |
|---|---|---|---|
| average | 20,513 | 63.71 | 7.92 |
| low | 20,207 | 56.91 | 5.70 |

### 9.3.1 Structural behaviour

The geometry and overall dimensions of the structural system are depicted in Figure 9.22. The modelling of the structure was carried out as described in Section 9.1. Figure 9.23a shows the structural model with pinned support conditions around the boundaries and the applied loads at each connector. The total area of the reciprocal structure covers 20.8

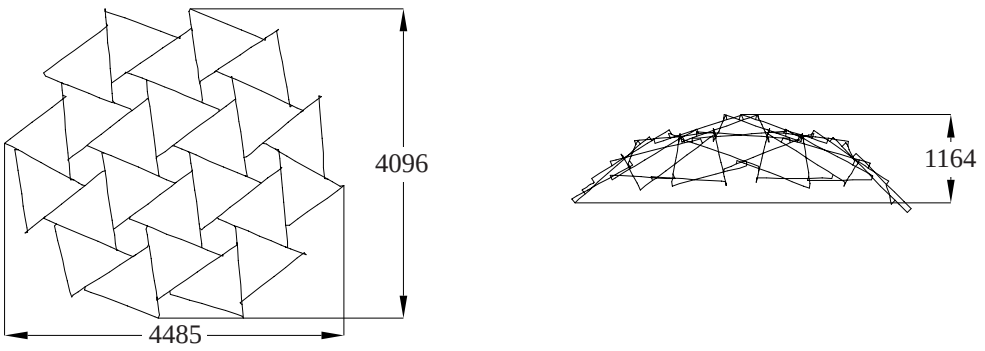


**Figure 9.22:** Geometry and dimensions of reciprocal structure.

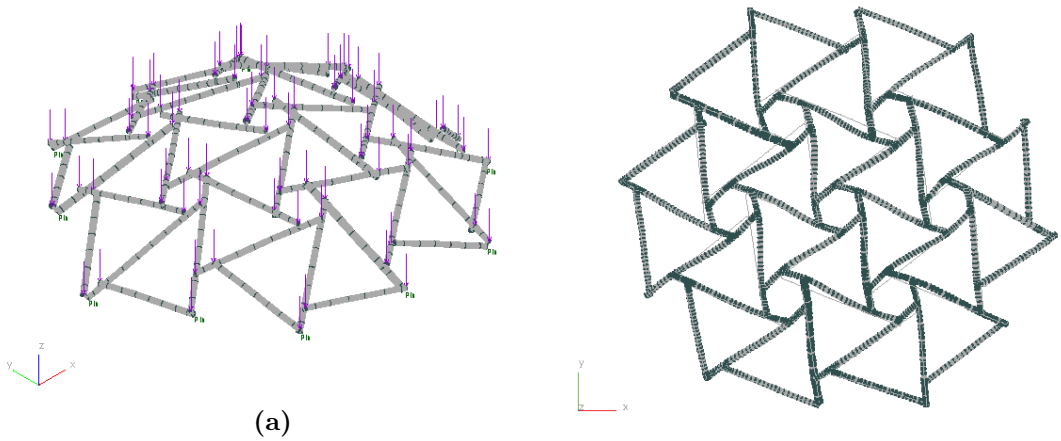

(a) (b)

**Figure 9.23:** (a) Structural model with applied loads. (b) Shape of the deformed structure.

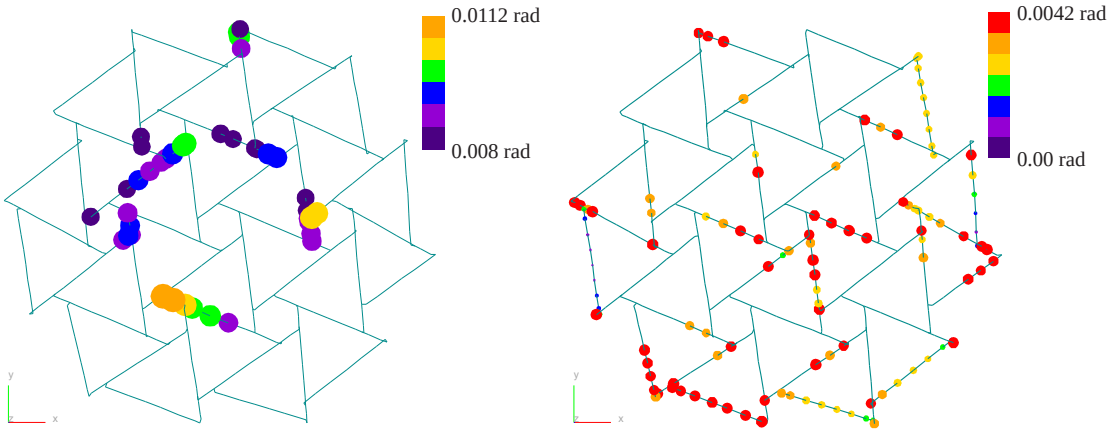


(a) (b)

**Figure 9.24:** (a) Location of maximum rotations at nodes. (b) Location of minimum rotations at nodes.

$m^2$ and consists of 42 elements with 72 connectors.

For this analysis, module 4 is considered (see Table 9.2). However, the overall behaviour can be described in similar way for the rest of the modules. The deformed shape of the system is depicted in Figure 9.23b. Similar to the rotations observed in a three-element module, each individual engagement window is twisted in an anticlockwise direction. The higher rotations occurred towards the centre of the structure, but not in the nodes at the inner engagement window (see Figure 9.24).

The distribution of forces and moments in the structure are depicted from Figures 9.25 to 9.27. The axial forces are mostly concentrated towards the boundary of the structure, indicating that the horizontal trust is mainly taken by the elements close to the boundaries. Note that these forces are mostly concentrated in those elements perpendicular to the boundary, and not those that are almost parallel to the boundary of the structure.

The shear forces are mostly concentrated in the middle of the structure and are higher

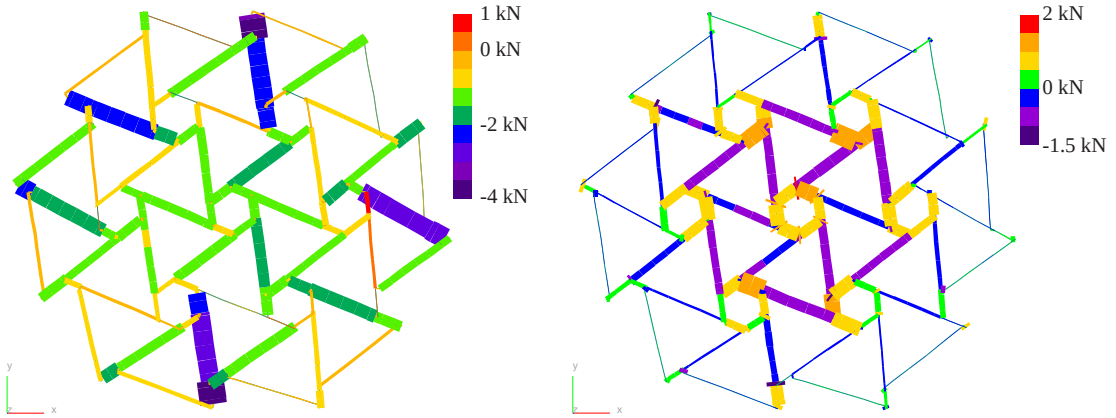


**(a)** **(b)**

**Figure 9.25:** (a) Axial forces $Fx$. (b) Shear forces $Fy$.

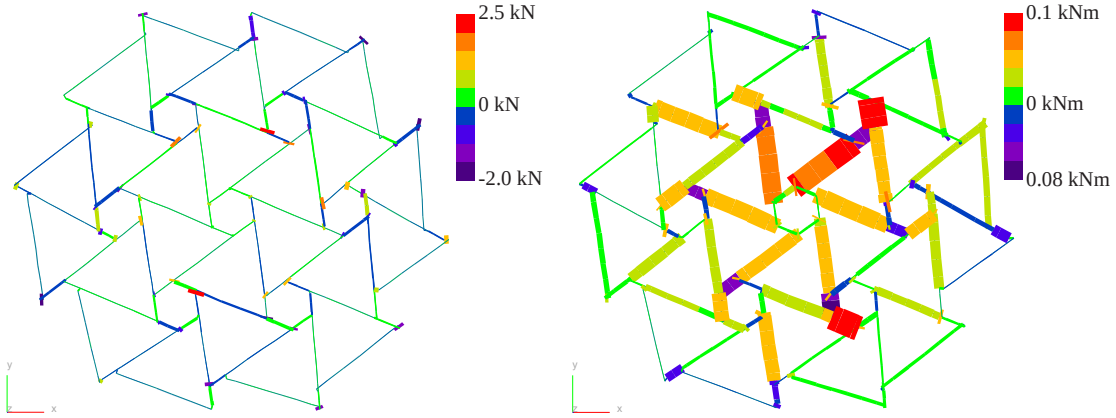


**(a)** **(b)**

**Figure 9.26:** (a) Shear forces $Fz$. (b) Torsion $Mxx$.

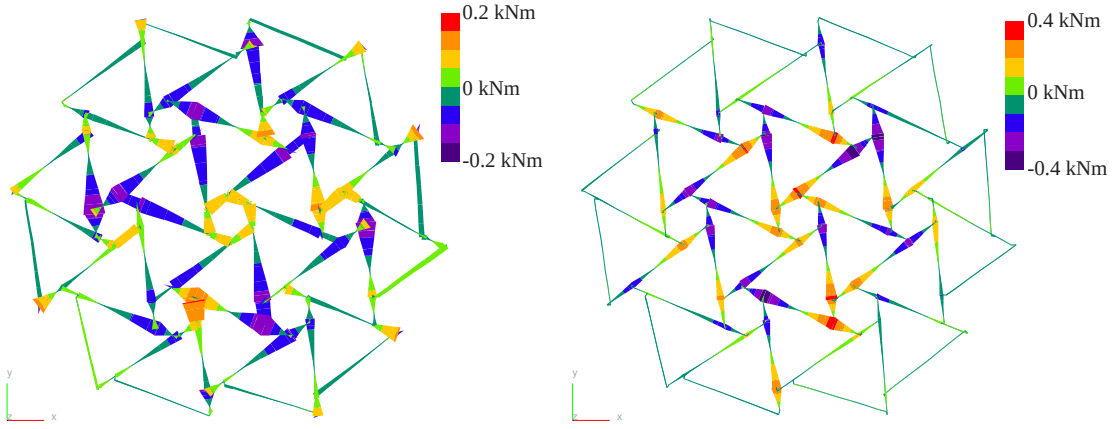


**(a)** **(b)**

**Figure 9.27:** (a) Moments $Myy$ in the $y$ direction. (b) Moments $Mzz$ in the $z$ direction.

in the elements located at the engagement window. These coincides with the location of the maximum torsional moments, suggesting that the different direction of the shear forces along one culm, produces torsion in the elements. Note that the shear forces in the $y$ direction are caused by the vertically applied loads, whereas the horizontal movement causes the shear forces in the $z$ direction. These $F_z$ forces coincide with the location of the maximum rotations.

Similarly, the bending moments are concentrated towards the centre of the structure and are gradually decreasing towards the boundaries. However, these are higher in the elements outside the engagement window, just below the connectors.

### 9.3.2 Effect of engagement length ratio in reciprocal structure

The observations of the previous subsection are particular for the structure used as case study. However, different behaviour is expected for reciprocal structures with different geometric parameters (e.g. engagement window, density, eccentricities, etc.). Assuming that the surface and tessellation are fixed inputs, the engagement window is the geometric parameter that mostly affects the shape of the whole system.

Figure 9.28 shows the influence of the displacements, maximum bending moments and shear forces for the structure with different engagement length ratios for model 0. The higher displacements occur in the structure with engagement length ratio of approximately 0.5. This value lies between the opening reported for the three and six-element modules from Figure 9.18. The maximum bending moments occur at similar engagement length ratios. This coincides with the minimum value of the shear forces, which is caused by the beam type behaviour of the overall system.

### 9.3.3 Effect of eccentricities in reciprocal structure

Table 9.4 provides the minimum and maximum eccentricities length for the first three models and the measured vertical displacements. In principle, the distribution of forces and moments under the same loading case should be almost the same. Small variations in the distribution of forces due to the differences in geometry were observed, however, these were negligible.

Overall, model 0 which has the smallest eccentricities presents a stiffer behaviour in comparison to that of the models with optimised eccentricities for equal or variable values respectively. Recall from Table 9.2 that the variable eccentricities refer to the optimised eccentricities according to the diameters of the bamboo culms to use. The percentage difference of vertical displacements between the original model and those optimised for the eccentricities is 11 and 14% for the equal and variable eccentricities respectively. This suggests that the compliance of a whole system increases with the increase of the eccentricities in a whole reciprocal structure, which agrees with the behaviour observed in the three-element module.

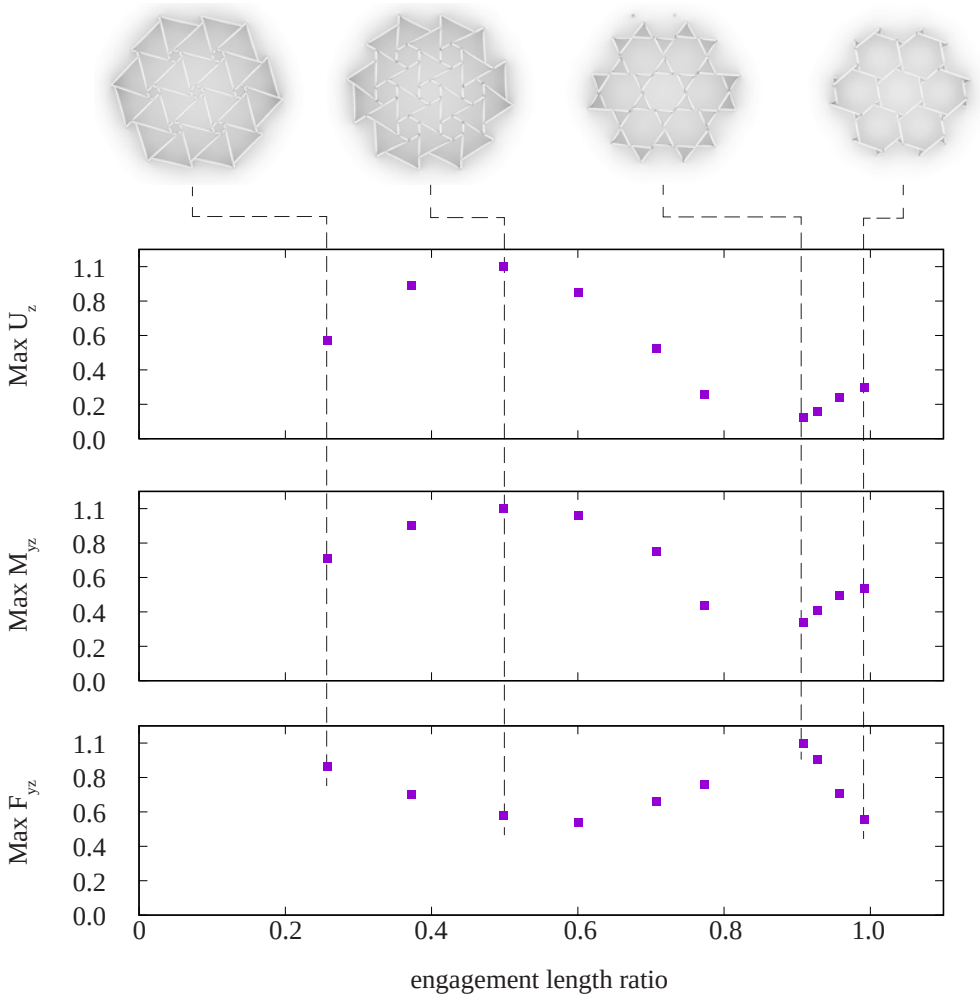


**Figure 9.28:** Maximum displacements, moments and shear forces for reciprocal structures with different engagement length.

**Table 9.4:** Range of eccentricities and maximum vertical displacements for each of the models.

| | model 0 | model 1 | model 2 |
|---|---|---|---|
| units | (mm) | (mm) | (mm) |
| Eccentricities (min) | 1.85 | 89.80 | 73.17 |
| Eccentricities (max) | 71.10 | 90.10 | 96.05 |
| $U_z$ | 8.77 | 9.77 | 10.07 |

### 9.3.4 Effect of SBD in structural modelling

This subsection evaluates the influence of using discretised elements incorporating the data from the SBD against using line elements with uniform properties. For this analysis, model 4 is considered as the benchmark model. This is compared against the models 2 and 3, which are modelled using line elements and with average and low value of properties respectively (refer to Table 9.2). These can potentially be used for estimating the stiffness and the maximum stresses respectively.

**Table 9.5:** Comparison of results between model using SBD and models with line elements and uniform properties.

| | SBD (discretised elements) | | Uniform models (line elements) | | | | | | | |
|---|---|---|---|---|---|---|---|---|---|---|
| | model 4 | | model 2 | | | | model 3 | | | |
| | avg value | max value | avg value | % diff | max value | % diff | avg value | % diff | max value | % diff |
| $U_z$ (mm) | - | 10.70 | - | - | 10.07 | -6.1 | - | - | 16.62 | 43.3 |
| $U_{xy}$ (mm) | - | 5.21 | - | - | 4.77 | -8.8 | - | - | 8.03 | 42.6 |
| $R_{xyz}$ (rad) | - | 0.0112 | - | - | 0.0104 | -7.4 | - | - | 0.0200 | 56.4 |
| $F_x$ (kN) | 1.05 | 3.65 | 1.09 | 3.7 | 3.65 | 0.0 | 1.09 | 3.7 | 3.87 | 5.9 |
| $F_y$ (kN) | 0.37 | 1.38 | 0.45 | 19.5 | 1.24 | -10.7 | 0.45 | 19.5 | 1.28 | -7.5 |
| $F_z$ (kN) | 0.15 | 0.56 | 0.19 | 23.5 | 0.57 | 1.8 | 0.19 | 23.5 | 0.57 | 1.8 |
| $M_{xx}$ (kNm) | 0.023 | 0.088 | 0.023 | 0.0 | 0.072 | -20.0 | 0.022 | -4.4 | 0.068 | -25.6 |
| $M_{yy}$ (kNm) | 0.041 | 0.161 | 0.055 | 29.2 | 0.152 | -5.8 | 0.055 | 29.2 | 0.149 | -7.7 |
| $M_{zz}$ (kNm) | 0.080 | 0.388 | 0.111 | 32.5 | 0.319 | -19.5 | 0.111 | 32.5 | 0.314 | -21.1 |
| $F_{yz}$ (kN) | 0.42 | 1.44 | 0.51 | 19.4 | 1.27 | -12.5 | 0.51 | 19.4 | 1.31 | -9.5 |
| $M_{yz}$ (kNm) | 0.096 | 0.404 | 0.132 | 31.6 | 0.335 | -18.7 | 0.132 | 31.6 | 0.334 | -19.0 |
| $A_x$ ($N/mm^2$) | 0.81 | 2.98 | 0.78 | -3.8 | 2.63 | -12.5 | 1.19 | 38.0 | 4.22 | 34.4 |
| $S_y$ ($N/mm^2$) | 0.56 | 2.07 | 0.65 | 14.9 | 1.79 | -14.5 | 0.98 | 54.5 | 2.78 | 29.3 |
| $S_z$ ($N/mm^2$) | 0.24 | 1.14 | 0.28 | 15.4 | 0.82 | -32.7 | 0.42 | 54.5 | 1.24 | 8.4 |
| $B_y$ ($N/mm^2$) | 2.57 | 14.31 | 3.21 | 22.1 | 8.80 | -47.7 | 5.16 | 67.0 | 13.95 | -2.5 |
| $B_z$ ($N/mm^2$) | 4.72 | 21.22 | 6.39 | 30.1 | 18.43 | -14.1 | 10.36 | 74.8 | 29.36 | 32.2 |

Table 9.5 presents the results and percentage difference for the displacements $U_z$ and $U_{xy}$ in the vertical and horizontal directions, the rotations $R_{xyz}$ at the nodes, the axial forces $f_x$, the shear forces $F_y$ and $F_z$, the moments $M_{xx}$, $M_{yy}$ and $M_{zz}$, the resultant shear forces $F_{yz}$, the resultant moments $M_{yz}$, the axial stresses $A_x$, the shear stresses $S_y$ and $S_z$ and the bending stresses $B_y$ and $B_z$. The $x$, $y$ and $z$ directions refer to the local axes (see Figure 9.2). See for example the results of the moments $M_{zz}$ in the Table 9.5 and also in Figure 31b in Appendix J. The average values of $M_{zz}$ are overestimated in the line element models. Although using line elements can be considered conservative based on the average values, the maximum moments $M_{zz}$ are underestimated in the line element models (see Figure 31b). This suggests that the model with discretised elements can capture the effect of the eccentric moments generated by the irregular geometry of bamboo culms (caused for example by the out-of-straightness of the culms). Therefore, highlighting the location of the highest forces and moments occurring in the structure, which are not identified from the models with line elements.

Similar behaviour was observed for all the moments and forces, which impacts the analysis of stresses. For example the maximum bending stresses $B_y$ are underestimated in the line element model 2 by 48%, which was expected as in model 2 the average properties are used. However, the stresses $B_y$ are also underestimated in model 3, modelled using the lower values, and thus was anticipated to be a conservative model for the analysis of stresses. While the stresses are underestimated only by 2.5%, these results emphasises the importance of considering the discretised geometry of bamboo culms for the analysis of stresses and the design of bamboo structures in general.

From Table 9.5 we have that using model 2 results in displacements with a percent-

age error of approximately 6% lower. This shows the impact of considering the irregular geometry in the models, which results in a more compliant system. Furthermore, using model 3 for the estimation of the vertical displacements is not realistic as it signification overestimate the deflection of the structure by 43%, which can lead to underuse the material.

The results from Table 9.5 were obtained from the structural models as described in Section 9.1, and thus we assumed that the connections are rigid. Similar to the findings from the previous modules A and B from Subsections 8.4.1 and 8.4.2. However, if we consider that the connections are semi-rigid if we found from module C, the overall displacements of the whole system changes. Table 9.6 provides the percentage difference of the same modules analysed in Table 9.5 but considering also the semi-rigid behaviour of the connections. The equivalent stiffness estimated for the timber connections was used for the modelling of the semi-rigid connections. Note that while the percentage difference between line and discretised models changes depending on the behaviour of the connection, the effect of the stiffness of the connection is higher than the effect of the SBD, highlighting the importance of the accurate modelling of the connection stiffness.

**Table 9.6:** Comparison of vertical displacements $U_z$ for reciprocal modules considering rigid and semi-rigid connections.

| | model 4 | model 2 | | model 3 | |
|---|---|---|---|---|---|
| | max value | max value | % diff | max value | % diff |
| rigid connections | 10.70 | 10.07 | -6.1 | 16.62 | 43.3 |
| semi-rigid (timber) | 41.16 | 45.61 | 10.3 | 58.3 | 34.5 |

### 9.3.5 Effect of selection and position of bamboo culms based on geometric and mechanical constraints

Two different criterion for the selection and position of the bamboo culms for each element in the structure were presented in Subsection 7.2.3. The first considers only geometric parameters to prevent clashing between connections and nodes in culms, and the second one aims to maximise the overall bending stiffness by taking into consideration the mechanical properties of the bamboo culms and the overall structural behaviour of the system.

Table 9.7 provides the results from these two analyses. For the same structure, selecting the culms using the second method can maximise the overall bending stiffness of the structure. It was found that the displacements decrease by 33 and 46% in the vertical and horizontal directions respectively, and the rotations decrease by 22%.

The procedure presented in the Subsection 7.2.3.3 consists in a simple formulation to study whether further methods that incorporate these properties can be useful for the design and overall performance of the structure. The significant improvement in the stiffness of the systems emphasises the potential to develop these.

**Table 9.7:** Comparison of results between discretised models.

| | | Discretised models (bamboo elements) | | | | | |
|---|---|---|---|---|---|---|---|
| | | model 04 | | model 05 | | | |
| | | avg value | max value | avg value | % diff | max value | % diff |
| $U_z$ | (mm) | - | 10.70 | - | - | 7.71 | -32.5 |
| $U_{xy}$ | (mm) | - | 5.21 | - | - | 3.26 | -46.0 |
| $R_{xyz}$ | (rad) | - | 0.0112 | - | - | 0.0090 | -21.8 |
| $F_x$ | (kN) | 1.05 | 3.65 | 0.95 | -10.0 | 3.38 | -7.7 |
| $F_y$ | (kN) | 0.37 | 1.38 | 0.32 | -14.5 | 1.37 | -0.7 |
| $F_z$ | (kN) | 0.15 | 0.56 | 0.14 | -6.9 | 0.57 | 1.8 |
| $M_{xx}$ | (kNm) | 0.023 | 0.088 | 0.022 | -4.4 | 0.102 | 14.7 |
| $M_{yy}$ | (kNm) | 0.041 | 0.161 | 0.043 | 4.8 | 0.185 | 13.9 |
| $M_{zz}$ | (kNm) | 0.080 | 0.388 | 0.072 | -10.5 | 0.380 | -2.1 |
| $F_{yz}$ | (kN) | 0.42 | 1.44 | 0.37 | -12.7 | 1.39 | -3.5 |
| $M_{yz}$ | (kNm) | 0.096 | 0.404 | 0.089 | -7.6 | 0.405 | 0.2 |
| $A_x$ | (N/mm2) | 0.81 | 2.98 | 0.69 | -16.0 | 2.6 | -13.6 |
| $S_y$ | (N/mm2) | 0.56 | 2.07 | 0.43 | -26.3 | 1.63 | -23.8 |
| $S_z$ | (N/mm2) | 0.24 | 1.14 | 0.18 | -28.6 | 1.04 | -9.2 |
| $B_y$ | (N/mm2) | 2.57 | 14.31 | 2.10 | -20.1 | 10.29 | -32.7 |
| $B_z$ | (N/mm2) | 4.72 | 21.22 | 3.31 | -35.1 | 17.80 | -17.5 |

## 9.4 Summary

This chapter investigates the structural behaviour of bamboo reciprocal systems using structural analyses. The structural modelling of the line and discretised elements and the connectors are defined. The discretised elements are modelled using the properties from the SBD. The section properties for each of the discretised elements is considered uniform and symmetrical. For bamboo culms with a high degree of ovalisation, the assumption is non-conservative as the second moment of area in the minor direction can decrease up to 79%, as seen from the oldhamii culms analysed in Subsection 4.3.6. Therefore, further methods to incorporate the irregularities into the cross-sectional shape are recommended.

The load-transfer mechanism for the elements in the reciprocal system is similar to that of a simply supported beam, with the difference that here the forces and moments are transferred in three directions. Bending moments and shear forces govern the behaviour of the system, however, shear forces $F_z$ generate also torsion. The deformed shape of the model in plan view tends to twist about the centre of each engagement window. The influence of the stiffness of the connectors on the overall stability of the system was evaluated. Overall, it was concluded that the connector should be capable of resisting moments in the two orthogonal directions normal to the eccentricities (i.e. $y$ and $z$) to prevent large deformations due to the sway of the connectors about the bamboo culm. These deformations change its initial form considerably, and thus are not acceptable as the structural stiffness of the system is lost.

The effect of the eccentricities and the engagement length was also investigated. It

was found that the deflections of the system increase with the increase of eccentricities for a three-element module and also in a whole structure. The effect of the engagement length ratio depends much on the geometry configuration (i.e. three-element, six-element and full structure). It was found that the maximum deflection (as well as the maximum bending moment) lies between 0.45, 0.60 and 0.50 of the total opening of the engagement window for the three, six-element and full structure. In addition, the maximum bending moments were found to be inversely related to the maximum shear forces.

This data can be used to manipulate the geometry for maximising stiffness or minimising shear forces. The analysis of the eccentricities and engagement length gives insight into the influence of the geometry in the structural behaviour. Further parametric analysis will aid to developed guidelines for the design of reciprocal systems at the early design stage. This is relevant, particularly for the stiffness of the system, as these structures are characterised by their flexibility. The aspects analysed here correspond only to the structure used as a case study to analyse the effect of some of the principal parameters. However, other aspects such as span to height ratio as well as the density of the tessellation (i.e. size of the polygons) are expected to have an impact and shall be taken into consideration in future analysis.

The main difference between using line and discretised elements (using the SBD) is that with line elements the maximum forces and moments generated in the system and caused by the non-uniform geometry cannot be identified. Furthermore, even when using low values of the section and material properties, the stresses estimated from the line element models can be underestimated. This is possibly caused by eccentric moments introduced by the irregular geometry of the discretised elements such as the out-of-straightness. The main issue is that this can lead to the design of unsafe structures.

Finally, the method developed in Subsection 7.2.3.3 for the incorporation of mechanical behaviour in the selection of the culms was evaluated. The overall vertical deflections (i.e. $z$ direction which is equal to the direction of the applied load) can be reduced by 33%, and 46% for the horizontal direction, by considering this method instead of using simple geometric constraints.

# Part IV

# Conclusions

# Chapter 10

# Conclusions and future work

## 10.1 Conclusions

The main aim of this thesis was to develop a new design approach for bamboo culms in construction to overcome the issues associated with its non-uniform properties. This was achieved by developing a novel design framework that enables the incorporation of the non-uniform properties of bamboo culms into the different steps of the design process. This framework consists of a methodology for determining the geometric, physical and mechanical properties of bamboo culms and the methods to incorporate the collected data into the design workflow. Several aspects were developed in parallel to the main framework in order to implement it in reciprocal systems. For this, two possible connection systems were investigated. These were developed at conceptual design stage and both relied on clamping methods. The experimental tests and analysis have shown promising results; however future research and development is needed if these are to be used as robust and reliable connection systems for bamboo structures.

The idea behind the framework was to place bamboo culms within the context of digital technologies, which are increasingly playing a pivotal role in the future of architecture, engineering and the construction practices. The work presented here attempts to assess the potential of considering the non-uniform properties of bamboo culms with the purpose of helping to overcome some of the greatest challenges as a building material. This research is part of a broader research project at University College London (Godina and Lorenzo, 2015; Lorenzo et al., 2017) to contribute to the use of bamboo culms as a sustainable building material. It constitutes the first step towards developing a robust design framework suitable to transfer to the bamboo industry. Due to the interdisciplinary nature of the research and the broad range of subjects, collaborations of different parts of the project have been made and specified within the text.

A summary of the main contributions of the thesis are described below based on the primary goals set out in Section 1.3.

### 10.1.1 Structural bamboo database (SBD)

This thesis presented the methods to establish the properties of bamboo culms referred to as *structural bamboo database* (SBD). The framework is project based and allows to systematically determine the geometric, physical and mechanical properties for a specific batch of bamboo culms. The specific methods are described below:

- A method for determining the geometric properties of bamboo culms was proposed using 3D scanning. This allows for a more accurate representation of the geometry of bamboo culms in the design process, including data for structural modelling (i.e. geometry and section properties) as well as an auxiliary data for different steps along the design process (e.g. architectural design and construction data). This represents the first method to systematically measure the geometric properties of bamboo culms. The importance of this for the bamboo industry is significant since many of the issues that arise in the construction practices, such as fitting of components, are associated with the non-uniform geometry of bamboo. In addition, the geometric properties a comprehensive dataset of oldhamii bamboo were analysed and contributes to the knowledge of the properties of the oldhamii species from which very little data is in the literature.

- Indirect methods were proposed for the estimation of the physical properties of bamboo culms, namely the moisture content and density. These methods minimise the time require to determine these properties by eliminating the need to oven-dry the samples. For the estimation of the moisture content, a hand-held moisture meter was calibrated to three different bamboo species (guadua, oldhamii and moso). This thesis provides the model to calculate the moisture content using BD-2100 Delmhorst moisture meter, and can possibly aid the monitoring of moisture content in the bamboo industry. Similarly, an equation was proposed for the indirect estimation of the dry density by simply measurements of the density at a given moisture content. Furthermore, a semi-automated method was developed in Matlab for the quantification of volume fraction of vascular bundles as well as its radial distribution by using image analysis of images taken with a digital camera. The quantification of these properties usually associated with sophisticated lab equipment is not affordable for its common use in the construction industry of bamboo structures. The method proposed here is intended to support the determination of these properties which are useful for the analysis of mechanical properties of bamboo culms.

- In this thesis a methodology for the estimation of an equivalent bending elastic modulus for bamboo culms by using numerical and experimental methods was proposed. While the dataset used here was limited, the results gave insight into the feasibility to adopt small coupons for the estimation of the mechanical properties of bamboo culms as a more practical and affordable alternative to those of full-culm tests.

- A discretised database was created for structural modelling and also for different aspects along the design process for the geometric, physical and mechanical properties.

These methods constitutes the first stage of the design framework to obtain the non-uniform properties of bamboo culms. Whilst some of the methods require further development or validation, these provide the grounds to a future framework that can be directly implemented in the bamboo industry.

### 10.1.2 Incorporation of the SBD into the design process

The second part of the design framework deals with the methods to incorporate the non-uniform properties of bamboo culms into the design process. These properties open a wide range of possibilities for the overall design process with bamboo, including a) an accurate representation of geometric properties of bamboo for structural modelling and analysis; b) the design and fabrication of connections with the specific geometry from each culm; c) the systematic selection of bamboo culms and their precise position for each of the elements in a structure (digitally and physically); and, d) the marking of culms to use as guidelines for assembly. In this thesis, the integration of the SBD into the design process was achieved by computational routines and are described below.

- A formulation for the generation of the geometry of reciprocal systems that take into consideration the non-uniform properties of bamboo culms was presented. This method is capable of modifying the position of the elements so that the eccentricities in each connecting point are according to the variable diameters of bamboo culms.
- Using the SBD, a method for the automatic selection and position of bamboo culms is presented. This allows to distribute the bamboo culms in a structure in such a way that it complies with some predefined constraints to maximise the position of the nodes with respect the position of the connections, and to minimise the overall bending stiffness of the structural system. This and the previous method for the generation of the geometry are run iteratively together within the design process.
- A method for linking the digital and physical models was developed to assist the assembly process and validate the physical geometry with the digital design.

These methods allows a new design approach with bamboo culms. Usually, the non-uniform properties are seen as a drawback for bamboo construction, but in this framework these properties are exploited so that they are used as design drivers in the proposed digital workflow. More generally, these methods allows to exploit the discretised properties from the SBD to minimise the uncertainties associated when assuming that bamboo culms are uniform elements. The series of methods described above can be further extended or customised for the type of project and structural system used.

### 10.1.3 Bamboo reciprocal structures

This thesis has shown the viability of using the design framework in bamboo reciprocal structures. It demonstrated the potential and advantages of introducing the non-uniform properties of bamboo culms into the design process for the more accurate estimation of the physical geometry of bamboo structures and structural analysis. Furthermore, two connection systems for bamboo culms were explored. The main findings and contributions are outlined below.

- Two connection systems were proposed and tested. While both require further development for its appropriate and safe use in bamboo structures, the results from the experimental tests from timber connection are promising. These connections showed the potential not only to transfer the forces and moments between elements, but also to take full advantage of the capacity of bamboo culms, which is very difficult to achieve in bamboo connections.
- The structural behaviour of bamboo reciprocal structures was investigated with a case study of a structure that can be used as a roof or envelope. It was found that modelling bamboo culms as uniform elements in general can overestimate the forces and moments, but the maximum forces and moments are not identified. Furthermore, using the mechanical properties of bamboo culms as constraints in the selection process of bamboo culms can significantly decrease the overall deflections of the system.

The insight gained from the implementation of the design framework for bamboo culms using reciprocal structures demonstrated the significance of using SBD in the bamboo industry. Although, the results presented here are limited to the structural system, connection systems, case studies, and type of methods devised, a more generalised approach can be further developed to be widely employed to different scenarios. The design framework opens new possibilities for the design and construction using bamboo culms as structural elements to contribute to sustainable construction.

## 10.2 Future work

The design framework must be further developed before the eventual transfer of these methods to the bamboo industry. It can be gradually implemented and validated as a project based first, before starting the eventual transfer of the methodology for the structural bamboo database (SBD) to plantations, so that customers can acquire the material together with the digital data of their properties. Project based means that the SBD is to be determined for the culms to be used in a project.

The validation of this framework must be done on a full structure, by performing loading tests as well as comparison of final geometry in the physical structure and digital geometry. If one of the designs of connection systems presented in this thesis are used,

then these must be further developed following the recommendations below, as these were developed only at conceptual design stage. Test methods to determine the strength and stiffness of each of the connections, are crucial for the full development of appropriate bamboo connections. During construction, the stability of the three-element modules should be monitored to gain insight into the appropriate assembly sequence and methods.

The methodology for the SBD must be validated using a larger number of bamboo culms, in both full culm and small coupons testing. In addition, the incorporation of other species common in construction, including Moso (*Phyllostachys pubescens*) and Tre Gai (*Bambusa stenostachya Hackel*) among others (refer to Subsection 2.1.1), is desirable. Furthermore, methods for the recording of the collected data as well as future modifications are recommended. These will be useful for example when a series of culms are cut and thus the inventory can reflect an update of available culms. Relationships between the dimensions of the culms and the changes caused by environmental factors are also desirable. This will allow a better monitoring of the culms before and after construction.

The methodology for the mechanical properties validates the bending equivalent modulus with a small number of guadua and oldhamii culms. This is crucial for the linear elastic analysis of bamboo reciprocal systems as the stiffness of bamboo is relatively low and bending is the main governing mechanism of reciprocal systems. However, the results suggests that the bimodulus behaviour is more relevant for the failure of bamboo than for the elastic properties. The bimodulus model presented here is linear elastic, but it can be modified to take into consideration the distribution of forces in the cross-section once the longitudinal compressive strength is exceeded in order to investigate further the failure mechanism.

The methods for incorporation of bamboo culms can be improved and extended in many ways. Optimisation methods within Rhinoceros and Grasshopper are desirable to prevent the need to transfer data between softwares. In addition, a direct link and update between CAD (Rhinoceros and Grasshopper) and structural analysis software will allow to update the results at each iteration during optimisation. The method of selection of the culms can be extended to minimise the amount of material waste, and to find the optimal culm for a single element for cases in which replacement of individual culms is required. In addition, the generalisation of the methods to incorporate these properties to any type of structural system is advisable.

Parametric analysis of the influence of all the geometric parameters of reciprocal systems on the structural behaviour could allow the development of guidelines that can be used at early design stages. Also, any type of tessellation and surfaces with different curvature will provide insight into the influence of the geometry on the structural behaviour.

Several technical issues were identified intrinsic of the methods being developed. Nevertheless, the focus was not so much on developing fully validated methods, but to gather enough data to use in the overall design framework and assess its feasibility as a suitable approach. Below, recommendations for further improvements to the methods presented

in this thesis are provided.

### 10.2.1 Structural bamboo database (SBD)

#### 10.2.1.1 Geometric properties

- The method for scanning bamboo culms should be further improved to prevent the need to use two users to scan bamboo culms, and therefore provide a more automated system that can be more efficient.
- New technologies, potentially low-cost in comparison with the Artec spider 3D scanner, can be explored to provide methods more accessible to the bamboo industry.
- A method to manually measure the out-of-straightness of bamboo in order to compare directly the results obtained using the 3D scanning is recommended to develop a fully validated method.
- Further methods for the automatic elimination of features such as branches are required to eliminate manual steps.
- Alternative and more accurate methods to measure the thickness of the bamboo culms at the ends are required, as the current method does not guarantee full contact between the inner part of the internode and the paper and thus can lead to overestimation of the thickness.
- The culm ends for the SBD should be cut at the middle of an internode to prevent the measuring of thickness very close to the nodes which can be influenced by the abrupt change of thickness around the intranode.
- During validation, it is important to collect the end samples before testing of full culm to prevent any possible damage to the end samples.

#### 10.2.1.2 Physical properties

- The moisture meter should be calibrated to account for other bamboo species common in the construction industry.
- Further validation for the proposed derivation to estimate the dry-density using results from the oven-dry method are required.
- The impact of the inner and outer layers of the culm wall thickness, observed for instance in the guadua species, is to be evaluated to define whether the areas corresponding to these layers can be ignored or not in the process for evaluating the volume fraction of bamboo.
- The method to analyse the volume fraction of fibres and not the volume fraction of vascular bundles assumes that there is a constant 8% of conducting tissue in all

the species. However, a validation of this assumption by comparing the results of this proposed method by measuring the volume fraction using higher magnification would be very valuable.

- The method for the quantification of volume fraction and its fibre distribution can be fully automated by segmenting the area of interest based on the background of the image.

#### 10.2.1.3 Mechanical properties

- The methodology for determining the mechanical properties was proposed and fully tested for the first time using guadua and oldhamii species. It is highly recommended that the experimental programmes (including both, full culm and small coupons) are carried out together, so that the full culm bending tests behaviour (stress-strain) and results (equivalent elastic modulus) can be used for developing an understanding of the relationship between the compressive and bending elastic modulus.

- In addition, it is recommended that tensile tests are added to the methodology with the aim of identifying the failure mechanism.

- Test methods on small coupons should be evaluated to prevent the presence of bending moments caused by the radial gradient. Additional instruments to locate the sample in the centre and prevent misalignments are recommended.

- Fabrication methods for small coupons are a significant part of the methodology that need to be taken into account. Validated automated methods for the fabrication of these samples are crucial for the implementation of this methodology in the bamboo industry.

- Sanding of the samples for mechanical testing is not recommended in any case, as the samples are prone to have an uneven surface that might influence the results. An additional sample for volume fraction analysis is recommended to avoid sanding the samples during preparation for image analysis.

- A robust method to estimate the angle of the tilted plane in the shear sample is required.

- A testing programme using thick and thin bamboo culms under bending loads would be very valuable for the identification of possible distinct failure mechanisms.

### 10.2.2 Incorporation of the SBD into the design process

#### 10.2.2.1 Structural modelling and analysis

- The influence of the ovalisation of the cross-section was found to be significant. Further detailing of the structural model of bamboo elements is required to evaluate

the effect of the shape of the cross-section on structural performance. However, it is important to take into consideration many aspects such as the direction of the loads in the structure, as in reciprocal systems these are oriented at different angles.

- Structural analysis considering horizontal load cases would give insight into the behaviour of bamboo reciprocal systems and the forces and moments developed in the connectors.

#### 10.2.2.2 SBD in structural morphology

- The method for the selection and position of bamboo culms in each of the elements in the structure can be optimised for time and efficiency and inside the Rhinoceros and Grasshopper environment.
- A simple method for the selection of the culms that minimises the deflections of the overall system was proposed. Since the results using this method were promising (decrease of 33% of displacements), further methods that can iteratively evaluate the deflections in the structure are recommended.
- A parametric analysis to investigate the behaviour of bamboo reciprocal systems considering other type of combinations other than those described in Table 9.2 are recommended to gain insight into the influence of the different parameters in the structural behaviour.
- Also, a dynamic database, an inventory where the culms can be updated as they are used so that the culms can be used twice in a structure if required (e.g. make two elements from one culm), thus maximising the usage of the culms, is desirable.

#### 10.2.2.3 Connection systems

- Further tests to investigate the rotational stiffness of the connections in the transverse direction (i.e. perpendicular to the connector) are required, as it was noted that the moments and shear forces generated were significant.
- For the timber connection, further tests to assess the transverse capacity of the bamboo culms are required. The fabrication methods of the timber connection and the direction of the fibre are important to prevent splitting of the timber blocks.
- Further investigations of the relationship between the geometric parameters of the timber connection and the rotational stiffness are required.
- The aluminium connection should be further developed by incorporating four vertical components instead of two in order to increase the rigidity of the connection.

#### 10.2.2.4 Construction

- Methods to asses the conditions of the bamboo culms just after delivery are required, to automate selection of culms in good condition, and assess if the presence of possible mould or bugs is not detrimental.
- A more robust method for marking the bamboo culms is required. Automated methods including robots can be useful for the identification of these marks in the culms, as the processes tested were time-consuming.

## 10.3 Summary

The proposed design framework does not intend to be a final output, but instead a starting point for the development of bamboo technology. The use of digital technologies to improve the construction industry as well the digital processes related to the design of building structures have started to be a common research topic especially in developed countries such as Germany, Switzerland, United States of America and England. As designers, architects, engineers or professionals in the construction industry we have the responsibility to transfer these technologies from research to practice, and to advocate for the implementation of new policies that enable the transferring of these to the developing and least developed countries to help addressing the inevitable urbanisation with sustainable, safe and resilient buildings.

This methodology is the first attempt to systematically capture the non-uniform properties of bamboo culms for its use in construction. It is expected to contribute to the development of a robust methodology and its transfer to the bamboo industry.

# Bibliography


Amada, S., Ichikawa, Y., Munekata, T., Nagase, Y., and Shimizu, H. (1997). Fiber texture and mechanical graded structure of bamboo. *Composites Part B: Engineering*, 28:13–20.

Amada, S., Munekata, T., Nagase, Y., Ichikawa, Y., Kirigai, A., and Zhifei, Y. (1996). The mechanical structures of bamboos in viewpoint of functionally gradient and composite materials. *Journal of Composite Materials*, 30:800–819.

Anastas, Y., Rhode-Barbarigos, L., and Addriaenssens, S. (2016). Design-to-construction workflow for cell-based pattern reciprocal free-form structures. *Journal of the International Association for Shell and Spatial Structures*, 57(2):159–176.

Arce-Villalobos, O. A. (1993). *Fundamentals of the Design of Bamboo Structures*. PhD thesis, Eindhoven University of Technology.

Artec-3D (2015). User guide - artect studio 10.

Artec-3D (2017). Max error/quality value in the artec studio workspace. `https://www.artec3d.com/portable-3d-scanners/artec-spider/`.

Ashby, M. (2011). *Materials selection in mechanical design*. Butterworth-Heinemann, Burlington, MA, 4th ed. edition.

ASTM-D4444-13 (2013). *Standard Test Method for Laboratory Standardization and Calibration of Hand-Held Moisture Meters*. West Conshohocken, PA, United States.

Atrops, J. (1969). Elastizität und festigkeit von bambusrohren. *Der Bauingenieur.*, 44:220–225. Quoted in Janseen (1981), and Arce (1993).

Bahtiar, E. T., Nugroho, N., Surjokusumo, S., and Karlinasari, L. (2013). Eccentricity effect on bamboo's flexural properties. *Journal of Biological Sciences*, 13(2):82–87.

Ballast, D. K. (2007). *Handbook of construction tolerances*. John Wiley.

Bambuver (2016). Bambuver.

BAND-IT (2015). Band-it - the ultimate band fastening system. `https://www.band-it-idex.com/`. [Online; accessed April, 2015].

Banik, R. L. (2015). *Bamboo silviculture, in Bamboo - The Plant and its Uses, Walter Liese and Michael Köhl (Eds.).* Springer International Publishing, 1 edition.

Baverel, O., H.Nooshin, and Kuroiwa, Y. (2004). Configuration processing of nexorades using genetic algorithms. *Journal of the International Association for Shell and Spatial Structures*, 45(145):99–108.

Baverel, O. and Pugnale, A. (2014). Reciprocal systems based on planar elements: morphology and design explorations. *Nexus Network Journal*, 16(1):179–189.

Baverel, O. L. (2000). *Nexorades: A family of interwoven space structures.* PhD thesis, University of Surrey.

Bechtel, S. and Norris, C. B. (1959). Strength of wood beams of rectangular cross section as affected by span-depth ratio. *Forest Products Laboratory - United States Department of Agriculture - Forest Service.*

BIS-IS-6874 (1973). *Method Of Tests For Round Bamboos.* India.

Bodig, J. and Jayne, B. A. (1982). *Mechanics of wood and wood composites.* Van Nostrand Reinhold Company.

Borg, S. F. (1962). *Fundamentals of engineering elasticity.* Van Nostrand.

Breuckmann, B. (2014). 25 years of high definition 3d scanning: History, state of the art, outlook. *Proceedings of the EVA London 2014 on Electronic Visualisation and the Arts*, pages 262–266.

Chilton, J. and Choo, B. (1992). Reciprocal frame long span structures. *In Proceedings of the International Association for Shell and Spatial Structures*, 2:100–109. Quoted in Larsen, 2008.

Chuma, S., Hirohashi, M., Ohgama, T., and Kasahara, Y. (1990). Composite structure and tensile properties of mousou bamboo. *Journal of the Society of Materials Science Japan*, (39):847–851.

Chung, K. and Chan, S. (2002). *INBAR Technical Report 23: Design of Bamboo Scaffolds.* International Network for Bamboo and Rattan - The Hong Kong Polytechnic University.

Chung, K. and Yu, W. (2002). Mechanical properties of structural bamboo for bamboo scaffoldings. *Engineering Structures*, 24(4):429–442.

ControlsGroup (2012). Controls - advantest 9 - instruction manual.

Correal, J. F. and Arbeláez, J. (2010). Influence of age and height position on colombian guadua angustifolia bamboo mechanical properties. *Maderas. Ciencia y Tecnología*, 12:105–113.

Daniel, I. M. and Ishai, O. (2006). *Engineering Mechanics of Composite Materials*. New York; Oxford: Oxford University Press, 2 edition.

Delmhorst (2011). Bd-2100 owner's manual - delmhorst - instrument co.

Dinwoodie, J. (2000). *Timber: its nature and behaviour*. London: E. & F. N. Spon.

Dixon, P. G. and Gibson, L. J. (2014). The structure and mechanics of moso bamboo material. *Journal of The Royal Society Interface*, 11(99).

Douthe, C. and Baverel, O. (2013). Morphological and mechanical investigation of double layer reciprocal structures. *Proceedings of the International Association for Shell and Spatial Structures (IASS) Symposium 2013, Poland*.

Douthe, C. and O.Baverel (2009). Design of nexorades of reciprocal frame systems with the dynamic relaxation method. *Computers and Structures*, 87(21-22):1296–1307.

Dremel (2012). Dremel - operating/safety instructions. `https://www.dremel.com/en/products/-/show-product/tools/4200-high-performance-rotary-tool`. [Online; accessed May, 2016].

Dunkelberg, K. (1985). *IL 31 Bambus-Bamboo*. Institute for Lightweight Structures.

Empson, C. (1836). Colombia: a cottage built of bamboo. coloured etching. Wellcome Library, London. [Online; accessed November 16, 2017].

Follet, P. R. and Jayanetti, D. L. (2008). *Bamboo in construction. In Shyam K. Paudel and Yan Xiao and Masafumi Inoue (Eds.) Modern Bamboo Structures*. Taylor (&) Francis.

Frey, P. (2011). Construire en bambou. simón vélez architects. *L'Architecture d'Aujourd'hui*, 387:78–85.

García, J. J., Rangel, C., and Ghavami, K. (2012). Experiments with rings to determine the anisotropic elastic constants of bamboo. *Construction and building materials*, 31:52–57.

Gatóo, A., Sharma, B., Bock, M., Mulligan, H., and Ramage, M. H. (2014). Sustainable structures: bamboo standards and building codes. *Proceedings of the Institution of Civil Engineers*, 167(ES5):189–196.

Gibson, L. J. (2005). Biomechanics of cellular solids. *Journal of biomechanics*, 38(3):377–399.

Gibson, L. J. (2012). The hierarchical structure and mechanics of plant materials. *Journal of the Royal Society Interface*, 9:2749–2766.

Gibson, L. J., Ashby, M. F., and Harley, B. A. (2010). *Cellular Materials in Nature and Medicine*. Cambridge: Cambridge University Press.

Glass, S. V. and Zelinka, S. L. (2010). *Wood Handbook - Wood as an Engineering Material. Chapter 04: Moisture Relations and Physical Properties of Wood.* Forest Products Laboratory.

Gnanaharan, R., Janssen, J. J., and Arce, O. (1994). Bending strength of guadua bamboo - comparison of different testing procedures. *INBAR Working Paper No.3, Kerala Forest Research Institute, India. International Network for Bamboo and Rattan. International Development Research Centre, Canada.*

Godina, M. and Lorenzo, R. (2015). Calibrating a composite material model for analysis and design of bamboo structures. *Proceedings: 10th World Bamboo Congress Korea.*

Gonzalez, R. C. and Woods, R. E. (2008). *Digital Image Processing.* Upper Saddle River, N.J. : Pearson Prentice Hall, 3rd ed. edition.

Goto, K., Kidokoro, R., and Matsuo, T. (2011). Rokkko mountain observatory. *The Arup Journal*, 2:20–26.

Grosser, D. and Liese, W. (1971). On the anatomy of asian bamboos, with special reference to their vascular bundles. *Wood Science and Technology*, 5(4):290–312.

Grosser, V. D. and Liese, W. (1974). Verteilung der leitbundel und zellarten in sprobachsen verschiedener bambusarten. *Holz als Roh-und Werkstoff/European Journal of Wood and Wood Products*, 32(12):473–482.

Hamdan, H., Hill, C., Zaidon, A., Anwar, U., and Latif, A. (2007). Equilibrium moisture content and volumetric changes of gigantochloa scortechinii. *Journal of Tropical Forest Science*, 19(1):18–24.

Harries, K. and Sharma, B. (2016). *Nonconventional and Vernacular Construction Materials.* Woodhead Publishing.

Harries, K. A., Bumstead, J., Richard, M., and Trujillo, D. (2017). Geometric and material effects on bamboo buckling behaviour. *Proceedings of the Institution of Civil Engineers - Structures and Buildings*, 170(4):236–249.

Harries, K. A. and Glucksman, R. (2016a). Part i: Technical report - bamboo test-kit-in-a-back pack. *International Network for Bamboo and Rattan - INBAR Technical Report No. 36.*

Harries, K. A. and Glucksman, R. (2016b). Part ii: User's manual - bamboo test-kit-in-a-back pack. *International Network for Bamboo and Rattan - INBAR Technical Report No. 36.*

Harries, K. A., Sharma, B., and Richard, M. (2012). Structural use of full culm bamboo: The path to standardization. *International Journal of Architecture, Engineering and Construction*, 1(2):66–75.

Harris, R., Haskins, S., and Roynon, J. (2008). The savill garden gridshell: design and construction. *The Structural Engineer*, 86(17):27–34.

Heinsdorff, M. (2013). *Bamboo Architecture - Design With Nature.* Design Media Publishing Limited.

Herakovich, C. T. (1998). *Mechanics of Fibrous Composites.* New York: John Wiley & Sons, Inc.

Heymann, G. (2015). The effect of bedding errors on the acccuracy of plate load tests: technical paper. *Journal of the South African Institution of Civil Engineering*, 57(1):67–76.

Hibbeler, R. C. (2011). *Mechanics of materials.* Pearson Education South Asia PTE LTD, Singapore ; London : Prentice Hall.

Hidalgo, O. (1978). *Nuevas técnicas de construcción con bambú.* Universidad Nacional de Colombia.

ICG (2012). *Norma Técnica Bambú - E.100 - III.2 Estructuras del RNE.* Perú.

Instron (2002). Instron series ix software - reference manual - software.

Instron (2004). Instron series 3300 load frames including series 3340, 3360, 3380.

IS-6874 (2008a). *Method of Tests for Bamboo.* India.

IS-6874 (2008b). *National Building Code of India (NBC), Part 6 Structural Design - Section 3 Timber and Bamboo: 3B Bamboo.* India.

IS-8242 (1976). *Method Of Tests For Split Bamboos.* India.

ISO (2004a). *ISO 22156 Bamboo - Structural Design.* Geneva, Switzerland, 1 edition.

ISO (2004b). *ISO 22157 Bamboo - Determination of physical and mechanical properties - part 1: requirements.* Geneva, Switzerland, 1 edition.

ISO (2004c). *ISO TR22157-2 Bamboo - Determination of physical and mechanical properties - part 2: Laboratory manual.* Geneva, Switzerland, 1 edition.

ISO (2019). *ISO 22157:2019 Bamboo structures - Determination of physical and mechanical properties of bamboo culms - Test methods.* Geneva, Switzerland, 1 edition.

Janssen, J. J. (2005). International standards for bamboo as a structural material. *Structural Engineering International*, 15(1):48–49.

Janssen, J. J. A. (1981). *Bamboo in building structures.* PhD thesis, Eindhoven University of Technology.

Janssen, J. J. A. (1995). *Building with Bamboo: A handbook*. Intermediate Technology Publications.

JG/T-199 (2007). *Testing Methods for Physical and Mechanical Properties of Bamboo Materials used in Construction Industry*. China.

Jiang, Z., Wang, H., Tian, G., Liu, X., and Yu, Y. (2012). Sensitivity of several selected mechanical properties of moso bamboo to moisture content change under the fibre saturation point. *BioResources*, 7(4):5048–5058.

Jubilee (2016). Jubilee clips. `https://www.jubileeclips.co.uk/`. [Online; accessed December, 2016].

Kaminski, S., Lawrence, A., Trujillo, D., Feltham, I., and López, L. F. (2016). Structural use of bamboo - part 3: Design values. *The Structural Engineer*, 94(12):42–45.

Kaminski, S., Lawrence, A., Trujillo, D., Feltham, I., and López, L. F. (2017). Structural use of bamboo - part 4: Element design equations. *The Structural Engineer*, 95(3):24–27.

Kollar, L. P. and Springer, G. S. (2003). *Mechanics of composite structures*. Cambridge University Press.

Kuka (2015). Kuka - kr 10 r1100 sixx.

Leica-Geosystems (2015). Leica disto s910 - the original laser distance meter. `https://lasers.leica-geosystems.com/uk/disto-3d-disto-pro-packs/disto-s910-pro-pack`. [Online; accessed December ,2016].

Lessard, G. and Chouinard, A. (1980). *Bamboo research in Asia - Proceedings of a workshop held in Singapore*. International Development Research Centre, 60 Queen Street, Ottawa.

Liese, W. (1987). Research on bamboo. *Wood Science and Technology*, 21(3):189–209.

Liese, W. (1998). *The Anatomy of Bamboo Culms*. International Network for Bamboo and Rattan, Beijing, China.

Liese, W. and Köhl, M. (2015). *Bamboo - The Plant and its Uses*. Springer International Publishing, 1 edition.

Liese, W. and Tang, T. (2015). *Properties of the Bamboo Culm, in Bamboo - The Plant and its Uses, Walter Liese and Michael Köhl (Eds.)*. Springer International Publishing, 1 edition.

Liese, W. and Weiner, G. (1996). Ageing of bamboo culms. a review. *Wood Science and Technology*, 30(2):77–89.

Limaye, V. D. (1952). Stregnth of bamboo ( *Dendrocalamus strictus*). *Indian Forester*, pages 558–575.

Lo, T. Y., Cui, H., Tang, P., and Leung, H. (2008). Strength analysis of bamboo by microscopic investigation of bamboo fibre. *Construction and Building Materials*, 7(22):1532–1535.

Lobovikov, M., Paudel, S., Piazza, M., Ren, H., and Wu, J. (2007). World bamboo resources - a thematic study prepared in the framework of the global forest resources assessment 2005. *Food and Agriculture Organization - FAO ; Non-wood forest products 18 edition*.

López, O. H. (1981). *Manual de construcción con bambu*. Estudios Técnicos Colombianos, Bogotá, Colombia.

Lorenzo, R., Lee, C., Oliva-Salinas, J. G., and Ontiveros-Hernandez, M. J. (2017). Bim bamboo: a digital design framework for bamboo culms. *Proceedings of the Institution of Civil Engineers*, pages 295–302.

MacLeod, I. A. (2005). *Modern Structural Analysis*. Thomas Telford.

Mahamood, R. M. and Akinlabi, E. T. (2017). *Functionally Graded Materials*. Springer.

MathWorks (2014). Graphics - matlab.

MathWorks (2016). Curve fitting toolbox - user's guide matlab.

McMullin, P. W. and Price, J. S. (2017). *Timber design*. Routledge - Taylor and Francis Group, New York.

McNeel, R. (2017). *Rhinoceros 3D*. Robert McNeel and Associates.

Menges, A., Schwinn, T., and Krieg, O. D. (2017). *Advancing wood architecture, - A computational approach*. Routledge - Taylor and Francis Group.

Meyer, H. and Ekelund, B. (1922). Tests on the mechanical properties of bamboo. *Proceeding Engineering Society China*, 22(7):141–169. Quoted in Janseen (1981), and Arce (1993).

Minke, G. (2012). *Building with Bamboo; Design and Technology of a Sustainable Architecture*. Birkhäuser Basel.

Mitch, D., Harries, K. A., and Sharma, B. (2010). Characterization of splitting behaviour of bamboo culms. *Journal of Materials in Civil Engineering*, 22(11):1195–1199.

Nogata, F. and Takahashi, H. (1995). Intelligent functionally graded material: Bamboo. *Composites Engineering*, 5(7):743–751.

NTC-5407 (2006). *Structural unions with Guadua Angustifolia Kunth*. Colombia.

Nugroho, N. and Bahtiar, E. T. (2012). Bamboo taper effect on center point bending test. *Journal of Physical Science and Application*, 2(9):386–391.

Nugroho, N. and Bahtiar, E. T. (2013). Bamboo taper effect on third point loading bending test. *International Journal of Engineering and Technology (IJET)*, 5(3):2379–2384.

Oasys-GSA (2017a). Oasys gsa. help guide. `https://www.oasys-software.com/wp-content/uploads/2017/12/gsa8.7_manual.pdf/`. [Online; accessed June 14, 2018].

Oasys-GSA (2017b). Oasys gsa. help guide. `https://www.oasys-software.com/wp-content/uploads/2018/04/gsa9.0_manual.pdf`. [Online; accessed November 11, 2018].

Obataya, E., Kitin, P., and Yamauchi, H. (2007). Bending characteristics of bamboo (phyllostachys pubescens) with respect to its fiber–foam composite structure. *Wood Science and Technology*, 41(5):385–400.

Ordóñez Candelaria, V. R. and Salomón Quintana, I. (2009). Consideraciones geométricas en la determinación de las propiedades en flexión estática de bambú. *Madera y Bosques*, 15(1):91–100.

Ota, M. (1950). Studies on the properties of bamboo stem. *Bulletin of the Kyushu University Forestry.*, 19(7):25–47. cited in Janseen (1991).

Otsu, N. (1979). A threshold selection method from gray-level histograms. *IEEE Transactions on Systems, Man, and Cybernetics*, pages 62–66.

Paletti-Profilsysteme (2012). Paletti. `http://www.paletti.de`. [Online; accessed July, 2016].

Parigi, D. and Kirkegaard, P. H. (2014). Design and fabrication of free-form reciprocal structures. *Nexus Network Journal*, 16(1):69–87.

P.G.Dixon, Ahvenainen, P., Aijazi, A., Chen, S., Lin, S., Augusciak, P. K., Borrega, M., Svedström, K., and Gibson, L. (2015). Comparison of the structure and flexural properties of moso, guadua and tre gai bamboo. *Construction and Building Materials*, 90:11–17.

Popovic, O. (1996). *Reciprocal frame structures*. PhD thesis, University of Nottingham.

Popovic, O. (2008). *Reciprocal Frame Architecture*. Amsterdam; London: Architectural Press.

Pugnale, A. and Sassone, M. (2014). Structural reciprocity critical overview and promising research design issues. *Nexus Network Journal*, 16(1):9–35.

Rao, A., Rao, V. R., and Williams, J. (1998). *Priory species of bamboo and rattan.* The International Plant Genetic Resources Institute and International Network for Bamboo and Rattan, Serdang, Malaysia, 1 edition.

Richard, M. J. (2013). *Assessing the Performance of Bamboo Structural Components.* PhD thesis, University of Pittsburgh.

Richard, M. J. and Harries, K. A. (2015). On inherent bending in tension tests of bamboo. *Wood Science and Technology.*

Rizzuto, J. and Larsen, O. P. (2010). Connection systems in reciprocal frames and mutually supported elements space structure networks. *International Journal of Space Structures*, 25(4):243–256.

Rizzuto, J. P. (2008). Dodecahedric mutually supported element space structure: Numerical modelling. *Journal of the International Association for Shell and Spatial Structures*, 49(1):3–18.

Rizzuto, J. P. and Hulse, R. (2007). Dodecahedric mutually supported element space structure: Experimental investigation. *International Journal of Space Structures*, 22(2):107–121.

Sénéchal, B., Douthe, C., and Baverel, O. (2011). Analytical investigations on elementary nexorades. *International Journal of Space Structures*, 26(4):313–320.

Shao, Z.-P., Fang, C.-H., Huang, S.-X., and Tian, G.-L. (2010). Tensile properties of moso bamboo (phyllostachys pubescens) and its components with respect to its fiber-reinforced composite structure. *Wood Science and Technology*, 44(4):655–666.

Sharma, B., Gatoo, A., Bock, M., and Ramage, M. (2015). Engineered bamboo for structural applications. *Construction and Building Materials*, 81:66–73.

Sharma, B., Harries, K. A., and Ghavami, K. (2013). Methods of determining transverse mechanical properties of full-culm bamboo. *Construction and Building Materials*, 38:627–637.

Song, P., Fu, C.-W., Goswami, P., Zheng, J., Mitra, N. J., and Cohen-Or, D. (2013). Reciprocal frame structures made easy. *ACM Transactions on Graphics*, 32(4):1–13.

Szabadszállási, T., Gáspár, Z., and Hegedüs, I. (2004). Central symmetric reciprocal frame structures in plane. *Proceedings of the International Association for Shell and Spatial Structures (IASS) Symposium 2004, Montpellier.*

Tam, C. P. T. (2004). Structural behaviour of the guadua angustifolia. connections in guadua. *Revista Ingeniería e Investigación*, (55):3–7.

Taylor, C. (2008). *Tolerances*, pages 917–947. Blackwell Science Ltd.

Thönnissen, U. (2014). A form-finding instrument for reciprocal structures. *Nexus Network Journal*, 16(1):89–107.

Thönnissen, U. (2015). *Reciprocal Frameworks Tradition and Innovation.* gta Verlag.

TRADA (2016). Wis 4-14 moisture in timber. *TRADA Technology Ltd*, pages 1–9.

Trujillo, D. (2007). Bamboo structures in colombia. *The Structural Engineer*, 85:6.

Trujillo, D. and Jangra, S. (2016). Grading of bamboo. *International Network for Bamboo and Rattan - INBAR Working Paper 79.*

Trujillo, D., Jangra, S., and Gibson, J. M. (2017). Flexural properties as a basis for bamboo strength grading - structures and buildings. *Proceedings of the Institution of Civil Engineers*, 170(4):284–294.

Ubidia, J. M. (2015). *Construir con bambú (Cana de Guayaquil). Manual de construcción.* Lima, Perú, 3 edition.

UK-Bamboo (2014). Uk bamboo supplies limited.

UN (2018a). Sustainable development - goals. `https://www.un.org/sustainabledevelopment/cities/`. [Online; accessed August, 2018].

UN (2018b). *World Economic Situation and Prospects 2018.* United Nations.

UN-Habitat (2016). 11 - sustainable cities and communities. sdg goal 11 monitoring framework.

Vaessen, M. J. and Janssen, J. J. (1997). Analysis of the critical length of culms of bamboo in four-point bending tests. *Heron*, 42(2):113–124.

Vahanvati, M. and Vahanvati, M. (2018). Giant grass - bamboo loveshack. Giant Grass.

Vélez, S. (2015). Simón vélez architects.

VISHAY (2017). Micro-measurements.

Vorontsova, M. S., Clark, L. G., Dransfield, J., Govaerts, R., and Baker, W. J. (2016a). *INBAR Technical Report No. 37 - World Checklist of Bamboos and Rattans.* INBAR - International Network for Bamboo and Rattan, ICBR - International Centre for Bamboo and Rattan, KEW Royal Botanic Gardens.

Vorontsova, M. S., Clark, L. G., Dransfield, J., Govaerts, R., Wilkinson, T., and Baker, W. J. (2016b). *World Atlas of Bamboos and Rattans.* INBAR - International Network for Bamboo and Rattan, ICBR - International Centre for Bamboo and Rattan, KEW Royal Botanic Gardens.

Wang, W. (2011). *Reverse engineering : technology of reinvention.* Boca Raton, FL : CRC Press.

Wegst, U. and Ashby, M. F. (2004). The mechanical efficiency of natural materials. *Philosophical Magazine*, 84(21):2167–2181.

Wegst, U. G. (2011). Bending efficiency through property gradients in bambooo, palm and wood-based composites. *Journal of Mechanical Behaviour of Biomedical Materials*, 4(5):744–755.

Wegst, U. G. and Ashby, M. F. (2007). The structural efficiency of orthotropic stalks, stems and tubes. *Journal of Materials Science*, 42(21):9005–9014.

Wu, K.-T. (1992). The effect of high-temperature drying on the antisplitting properties of makino bamboo culm *Phyllostachys makinoi* hay. *Wood Science and Technology*, 26(4):271–277.

Young, W. C., Budynas, R. G., Sadegh, A. M., and Roark, R. J. (2012). *Roark's formulas for stress and strain.* New York : McGraw-Hill Professional.

Yu, H., Jiang, Z., Hse, C., and Shupe, T. (2008). Selected physical and mechanical properties of moso bamboo (phyllostachys pubescens). *Journal of Tropical Forest Science*, (4):258–263.

Yu, Y., Fei, B., Zhang, B., and Yu, X. (2007). Cell-wall mechanical properties of bamboo investigated by in-situ imaging nanoindentation. *Wood and fiber science*, 39(4):527–535.

Zhou, A., Huang, D., Li, H., and Su, Y. (2012). Hybrid approach to determine the mechanical parameters of fibers and matrixes of bamboo. *Construction and Building Materials.*, 35:191–196.

# Appendices

# A Preparation of the culms prior to SBD

From Chapter 3 we have that the methodology to determine the SBD starts with the preparation of the bamboo culms for construction and material properties determination. The preparation consists of providing a clean surface to the culms, cutting the ends for fabrication of small coupons, identifying each individual culm with a label and creating a mark so that there is a reference between digital and physical culms.

The observations discussed below correspond to the first batch of bamboo culms of the oldhamii species that were used to determine all the properties of the SBD (refer to Chapters 4 to 6). These were delivered to the Structures Laboratory at UNAM University in Mexico City, where the author spent two research stays (of 6 and 3 weeks respectively) together with colleagues from the bamboo research group at UCL. This was the first time that all the processes were recorded from one batch of bamboo culms.

### Delivering and cleaning of bamboo culms

The bamboo culms were transported from the plantation Bambuver in Veracruz to UNAM. The culms arrived on a pick-up truck to UNAM (see Figure 1). These were unloaded from the truck and placed in a stacked position resting against each other on the top of wood pallets outside the Structures Laboratory at UNAM.

Some culms have knots at the nodes due to the emerging of branches. Small holes, possible produced by the presence of bugs, also affected some culms, and some culm ends presented mould and cracks (see Figure 2).

The outer surface of the culm was cleaned with a cloth to get rid of dust or particles that may interfere with the scanning process, and to have a clean surface to stick the labelling of the culm. This work was very manual and labour intensive. While handling the culms, it was very noticeable that some culms were much more green (e.g. higher moisture content or density) than others, as some were significantly heavier. No moisture content was recorded at this point, only for mechanical testing purposes.

After the whole preparation of the culms, these were stored inside the Structures

**Figure 1:** Delivering and unload of oldhamii bamboo culms.

**Figure 2:** Bamboo outer surface of oldhamii culms with marks just after arrival. Hole in the outer surface of the culm, and culm ends with mould.

Laboratory at UNAM for approximately six months prior to their use for construction.

### Labelling, reference point and cut of end sections

Figure 3 shows an schematic view of the culm in the longitudinal direction showing the positions where the labels (barcode tape), reference point and cuts shall be made in each bamboo. The labelling and reference point system was proposed by members of the bamboo research group at UCL.

After cleaning, the culms were labelled at each end by sticking a transparent barcode tape label. Four barcode tape were attached per culm, one at each end section and another one at 500 mm from the end of the culm after the end sections were cut (see Figure 3). The barcode was of the type code 128 and was generated with an Epson barcode creator,

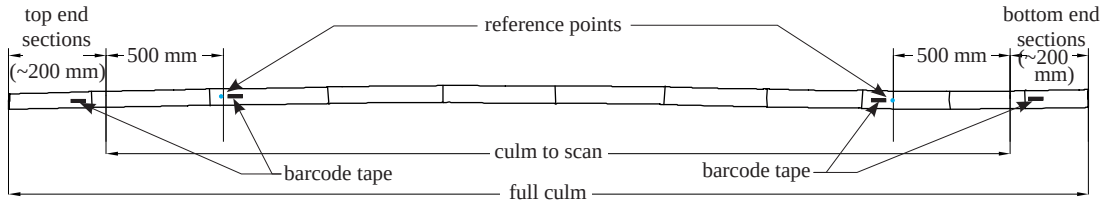


**Figure 3:** Longitudinal position of labelling of the culm, reference point and cut of end sections for fabrication of samples.

which can generate a barcode for an alphanumeric string (see Figure 4a). A disadvantage was that some stickers were peeling off when the culms were dragged in the floor or due to the friction while stacked against each other. In these cases, a new mark was made using a permanent marker. However, a more robust system for identification of the culms is required.

The reference mark was made as a small indentation with a Dremel 4200 speed rotatory tool (Dremel, 2012) using a bit with diameter of 2.4 mm high speed cutter no.190, which can be used in curved surfaces and in materials such as wood. The indentation was manually done near the barcode tape, 500 mm from the ends (see Figure 3). The bit was inserted as straight as possible into the outer surface of the culm as shown in Figure 4b. Only the head of the bit was inserted, so as to minimise the material removed.

The end sections were cut from the culm with a minimum length of 200 mm and preferably having a node. The cuts were made manually with a reciprocating saw Bosch (see Figure 5). If the end section has mould in the central cavity as shown in Figure 6a, the sections were discarded, and an another end section was cut from the same culm but from the next internode. As the end sections are to be used for mechanical properties, it was decided to avoid an extra parameter that can influence the results.

The end sections for all culms are shown in Figure 6b. During cutting, some of the culms presents splitting in the outer surface. The cuts were done as careful as possible to minimise the area of the splitting to prevent having samples affected by the removal

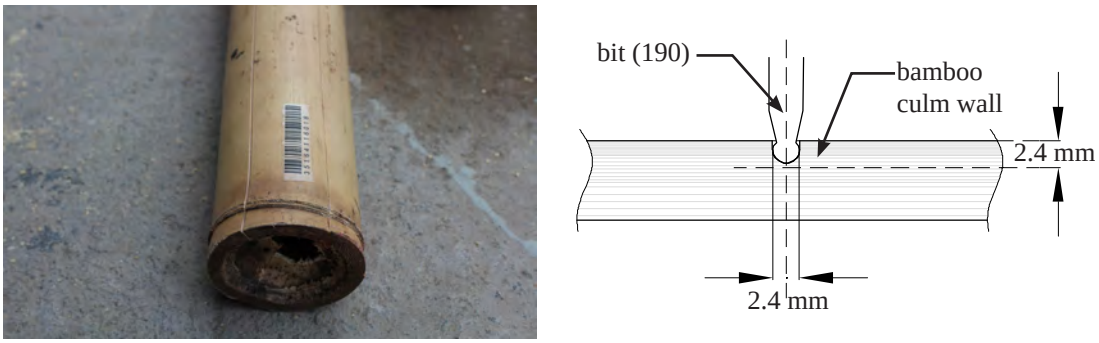


**Figure 4:** (a) Barcode tape on culm. (b) Indentation of bamboo outer surface for reference point.

**Figure 5:** Cutting of culm ends.

**Figure 6:** (a) Discarded end sections. (b) End sections ready for fabrication of samples.

of fibres. Using the japanese saw (refer to Appendix D) reduced the splitting considerably. However, this method is very time-consuming in comparison with the use of the reciprocating saw.

# B Stress-strain curves for full culm and small coupons

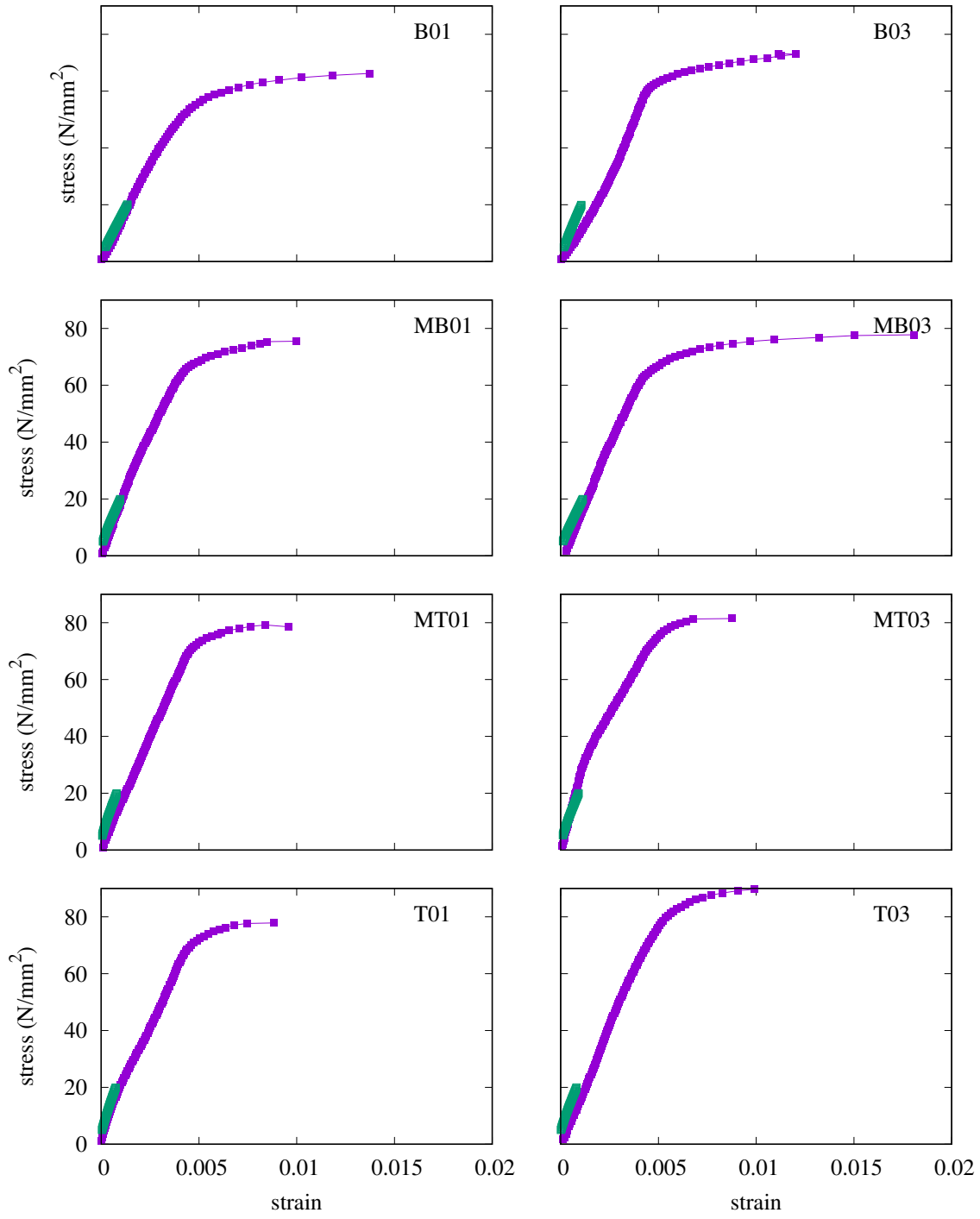


**Figure 7:** Stress-strain curve of all full culm and small coupon specimens for comparison.

# C Bimodulus material model for bamboo - full derivation

This appendix presents the full derivation of the bimodulus material model for a hollow circular section. The equations presented in colour red correspond to those introduced within the text in Subsection 6.2.2 and are numbered accordingly.

### Compatibility of deformations

According to the compatibility of deformations, the internal strains vary linearly through the cross-section. Assuming that the beam cross-section is sagging, the strains above the neutral axis are compressive strains and below the neutral axis are tensile strains. The maximum compressive and tensile strains at the top and bottom edge of the cross-section are proportional to the distance from the neutral axis

$$\frac{\epsilon_t}{x} = \frac{\epsilon_c}{2\hat{R} - x} \tag{6.72}$$

where $\epsilon_t$ and $\epsilon_c$ denote the tensile and compressive strains respectively, $x$ represents the distance from the neutral plane to the bottom edge of the beam cross-section, and $\hat{R}$ refers to the radius at the midplane of the cross-section thickness $t$, refer to Figure 6.29 and Table 6.8.

Consider two small elements of the cross-section in the radial direction located at opposite sides as shown in Figure 6.29. The tensile strains for a portion $d_\alpha$ located at $\alpha$ from the vertical axis is

$$\frac{\epsilon_t}{x} = \frac{\epsilon_\alpha}{y_\alpha - (\hat{R} - x)} \tag{B.1}$$

now substituting $y_\alpha$ from Table 6.8 and rearranging

$$\frac{\epsilon_t}{x} = \frac{\epsilon_\alpha}{\hat{R}(\cos\alpha - 1) + x} \tag{B.2}$$

then the tensile strain $\epsilon_\alpha$ for the element located at $\alpha$ is

$$\epsilon_\alpha = \frac{\epsilon_t\left[\hat{R}(\cos\alpha - 1) + x\right]}{x} \tag{6.73}$$

The compressive strains for a portion $d_\beta$ located at $\beta$ or $\pi - \alpha$ from the vertical axis as shown in Figure 6.29 is

$$\frac{\epsilon_c}{2\hat{R} - x} = \frac{\epsilon_\beta}{y_\beta + (\hat{R} - x)} \tag{B.3}$$

substituting $y_\beta$ from Table 6.8 and rearranging

$$\frac{\epsilon_c}{2\hat{R} - x} = \frac{\epsilon_\beta}{\hat{R}(\cos\beta + 1) - x} \tag{B.4}$$

to obtain the compressive strains $\epsilon_c$ as a function of the tensile strains $\epsilon_t$, the left hand side of the equation is substituted by the left hand side of Equation (6.72), and solving for $\epsilon_\beta$ we have

$$\epsilon_\beta = \frac{\epsilon_t \left[\hat{R}(\cos\beta + 1) - x\right]}{x} \tag{6.74}$$

**Equilibrium conditions**

To satisfy the equilibrium conditions, the tensile and compressive forces acting in the cross-section are equated

$$F_t = F_c \tag{6.75}$$

and according to Hooke's law for a linear elastic material, the forces in the element located at the tensile zone are obtained as

$$dF_t = 2E_t\epsilon_\alpha \, dA_t \tag{B.5}$$

and substituting $\epsilon_\alpha$ from Equation (6.73) and $dA_t$ from Table 6.8 into the equation we have

$$dF_t = \frac{2E_t\epsilon_t}{x}[\hat{R}(\cos\alpha - 1) + x](t\hat{R}\, d\alpha) \tag{B.6}$$

and rearranging

$$dF_t = \frac{2E_t\epsilon_t}{x} tR[(x - \hat{R}) + \hat{R}\cos\alpha]\, d\alpha \tag{B.7}$$

To obtain the tensile forces acting in the cross-section area located below the neutral axis, we integrate from 0 to $\theta$ the last term of the equation corresponding to the vertical distances from the neutral axis as

$$F_t = \frac{2E_t\epsilon_t}{x} t\hat{R} \int_0^\theta [(x - \hat{R}) + \hat{R}\cos\alpha]\, d\alpha \tag{B.8}$$

and solving

$$F_t = \frac{2E_t\epsilon_t}{x} t\hat{R}[(x - \hat{R})\theta + \hat{R}\sin\theta] \tag{6.76}$$

Similarly, the forces in the element located in the compressive zone are obtained as

$$dF_c = 2E_c\epsilon_\beta dA_c \tag{B.9}$$

However, in order to obtain the compressive forces as a function of the tensile elastic modulus $E_t$ and tensile strain $\epsilon_t$, the ratio of compressive elastic modulus $E_c$ to tensile elastic modulus $E_t$ is introduced as

$$n = \frac{E_c}{E_t} \tag{6.77}$$

therefore, substituting $E_c$, $\epsilon_\beta$ and $dA_c$ of Equation (B.9) for $E_t$ and $\epsilon_t$ from Equations

(6.77) and (6.73), and $dA_t$ from Table 6.8, we have

$$dF_c = \frac{2nE_t\epsilon_t}{x}[\hat{R}(\cos\beta + 1) - x](t\hat{R}\,d\beta) \tag{B.10}$$

and rearranging

$$dF_c = \frac{2nE_t\epsilon_t}{x}t\hat{R}[(\hat{R} - x) + \hat{R}\cos\beta]\,d\beta \tag{B.11}$$

To obtain the compressive forces acting in the cross-section area located above the neutral axis, we integrate from 0 to $\theta$ the last term of the equation corresponding to the vertical distances from the neutral axis as

$$F_c = \frac{2nE_t\epsilon_t}{x}t\hat{R}\int_0^{\pi-\theta}[(\hat{R} - x) + \hat{R}\cos\beta]\,d\beta \tag{B.12}$$

and solving

$$F_c = \frac{2nE_t\epsilon_t}{x}t\hat{R}[(\hat{R} - x)(\pi - \theta) + \hat{R}\sin\theta] \tag{6.78}$$

Now substituting Equations (6.76) and (6.78) into Equation (6.75) we have

$$\frac{2E_t\epsilon_t}{x}t\hat{R}[(x - \hat{R})\theta + \hat{R}\sin\theta] \quad = \quad \frac{2nE_t\epsilon_t}{x}t\hat{R}[(\hat{R} - x)(\pi - \theta) + \hat{R}\sin\theta] \tag{B.13}$$

and simplifying by cancelling out equal terms at both sides of the equation, we have

$$x\theta - \hat{R}\theta + \hat{R}\sin\theta = n[\hat{R}\pi - \hat{R}\theta - x\pi + x\theta + \hat{R}\sin\theta] \tag{B.14}$$

Finally, setting Equation (B.14) to zero and simplifying

$$(x - \hat{R} + n\hat{R} - nx)\theta + (\hat{R} - n\hat{R})\sin\theta - n\hat{R}\pi + nx\pi = 0 \tag{B.15}$$

After further simplifications

$$(1 - n)(x - \hat{R})\theta + (1 - n)\hat{R}\sin\theta + n\pi(x - \hat{R}) = 0 \tag{B.16}$$

or

$$(1 - n)[(x - \hat{R})\theta + \hat{R}\sin\theta] + n\pi(x - \hat{R}) = 0 \tag{6.79}$$

Solving Equation (6.79) gives the vertical position $x$, and the angle $\theta$ that defines the neutral axis in the cross-section.

### Bending moments

The internal moments acting in the cross-section correspond to the sum of the moments on the tensile and compressive zones as

$$M = M_\alpha + M_\beta \tag{6.80}$$

The moment in an element at the tensile zone is given by

$$dM\alpha = y_\alpha \, dF_t \tag{B.17}$$

and substituting $y_\alpha$ from Table 6.8 and Equation (B.7) into Equation (B.17), we have

$$dM\alpha = \frac{2E_t\epsilon_t}{x} t\hat{R}^2 \Big[(x - \hat{R})\cos\alpha + \hat{R}\cos^2\alpha\Big] d_\alpha \tag{B.18}$$

To obtain the moments acting in the cross-section area located below the neutral axis, we integrate the third term from 0 to $\theta$ as

$$M\alpha = \frac{2E_t\epsilon_t}{x} t\hat{R}^2 \int_0^\theta \Big[(x - \hat{R})\cos\alpha + \hat{R}\cos^2\alpha\Big] d_\alpha \tag{B.19}$$

and solving

$$M\alpha = \frac{2E_t\epsilon_t}{x} t\hat{R}^2 \left[(x - \hat{R})\sin\theta + \frac{\hat{R}}{2}\left(\theta + \frac{\sin 2\theta}{2}\right)\right] \tag{6.81}$$

Similarly, the moments for an element at the compressive zone are given by

$$dM_\beta = y_\beta dF_c \tag{B.20}$$

and substituting $y_\beta$ from Table 6.8 and Equation (B.11) into Equation (B.20) it gives

$$dM\beta = \frac{2nE_t\epsilon_t}{x} t\hat{R}^2 [(\hat{R} - x)\cos\beta + \hat{R}\cos^2\beta] \, d\beta$$

To obtain the moments acting in the cross-section area located above the neutral axis, we integrate the third term from 0 to $\pi - \theta$

$$M\beta = \frac{2nE_t\epsilon_t}{x} t\hat{R}^2 \int_0^{\pi-\theta} \Big[(\hat{R} - x)\cos\beta + \hat{R}\cos^2\beta\Big] \, d\beta \tag{B.21}$$

or

$$M\beta = \frac{2nE_t\epsilon_t}{x} t\hat{R}^2 \left[(\hat{R} - x)\sin\theta + \frac{\hat{R}}{2}\left[(\pi - \theta) + \frac{\sin 2\theta}{2}\right]\right] \tag{6.82}$$

Now, substituting Equations (6.81) and (6.82) into Equation (6.80) and simplifying and cancelling out equal terms at both sides of the equation, we have

$$M = \frac{E_t\epsilon_t t\hat{R}^2}{x}\left[(1-n)\hat{R}\theta + 2(1-n)(x - \hat{R})\sin\theta + \frac{1}{2}(1-n)\hat{R}\sin 2\theta + n\pi\hat{R}\right] \tag{6.83}$$

**Equivalent bending stiffness of the bimodulus model**

The flexural stiffness is estimated from the moment curvature relationship of the general bending theory. The governing equation is

$$M = EI\frac{d^2w}{dx^2} \tag{B.22}$$

where, $E$ is the elastic modulus, $I$ is the second moment of area, and $w$ is the deformation in the vertical direction. The strain of the beam cross-section at the distance $x$ from the neutral axis is

$$\epsilon_t = x\frac{d^2w}{dx^2} \tag{B.23}$$

therefore

$$\frac{M}{EI} = \frac{\epsilon_t}{x} \tag{B.24}$$

and solving for $EI$ it becomes

$$EI = \frac{M}{\epsilon_t/x} \tag{6.84}$$

Substituting Equations (6.83), (6.73) and $x$ from Table 6.8 into Equation (6.84), we have

$$EI = E_t t\hat{R}^2\Big[(1-n)\hat{R}\theta + 2(1-n)(x-\hat{R})\sin\theta + \frac{1}{2}(1-n)\hat{R}\sin 2\theta + n\pi\hat{R}\Big] \tag{6.85}$$

To estimate the equivalent bending elastic modulus $E_{eq,b}$, Equation (6.68) is substituted into Equation (6.85), and after rearranging we can obtain the expression of the ratio $E_{eq,b}$ to $E_t$ as

$$\frac{E_{eq,b}}{E_t} = \frac{1}{\pi\hat{R}}\Big[(1-n)\hat{R}\theta + 2(1-n)(x-\hat{R})\sin\theta + \frac{1}{2}(1-n)\hat{R}\sin 2\theta + n\pi\hat{R}\Big] \tag{B.25}$$

or, after simplification

$$\frac{E_{eq,b}}{E_t} = \frac{1}{\pi\hat{R}}\Big[(1-n)[\hat{R}\theta + 2(x-\hat{R})\sin\theta + \frac{1}{2}\hat{R}\sin 2\theta] + n\pi\hat{R}\Big] \tag{B.26}$$

To obtain $E_{eq,b}$ as a ratio of $E_c$, we multiply the right hand side of the equation by the inverse of the ratio $E_c$ to $E_t$ as in Equation (6.77) to get

$$\frac{E_{eq,b}}{E_c} = \frac{1}{\pi n\hat{R}}\Big[(1-n)[\hat{R}\theta + 2(x-\hat{R})\sin\theta + 1/2\hat{R}\sin 2\theta]\Big] + 1 \tag{6.86}$$

From assumption **b.3**, we have that the tensile forces are acting only in the area corresponding to the $\mathrm{v}_f$ of the cross-section calculated from Section 5.3 as in Equation (5.25). Then, the area for an element in the tensile zone is multiplied by the $\mathrm{v}_f$ as

$$dA_t = \mathrm{v}_f t\hat{R}d_\alpha \tag{6.87}$$

Therefore, the term $(1-n)$ is replaced by $(\mathrm{v}_f - n)$ in all the equations.

Finally, $E_{eq,b}$ is obtained by multiplying Equation (6.86) by the compressive elastic modulus as

$$E_{eq,b} = \frac{E_{eq,b}}{E_c} E_c \tag{6.88}$$

**Bending stresses**

Next, the maximum normal stresses at the top and bottom edge of the beam cross-section are calculated. According to Hooke's law

$$\sigma_t = E_t \epsilon_t \tag{6.89}$$

In order to substitute $E_t$ and $\epsilon_t$ into Equation (6.89), we rearrange Equation (6.83) to solve for $E_t$, and Equation (6.73) to solve for $\epsilon_t$, and obtain

$$E_t \epsilon_t = \frac{xM}{t\hat{R}^2\Big[(\mathrm{v}_f - n)[\hat{R}\theta + 2(x - \hat{R})\sin\theta + \frac{1}{2}\hat{R}\sin 2\theta] + n\pi\hat{R}\Big]} \tag{B.27}$$

by simplifying and multiplying both sides of the equation by $t$ and dividing both sides of the equation by $M$ we have

$$\frac{t\sigma_t}{M} = \frac{tE_t\epsilon_t}{M} = \frac{x}{\hat{R}}\left[\frac{1}{\hat{R}\Big[(\mathrm{v}_f - n)[\hat{R}\theta + 2(x - \hat{R})\sin\theta + \frac{1}{2}\hat{R}\sin 2\theta] + n\pi\hat{R}\Big]}\right] \tag{B.28}$$

and taking the right hand side of Equation (B.28) as the variable $K$ we have

$$\frac{t\sigma_t}{M} = \frac{tE_t\epsilon_t}{M} = \frac{x}{\hat{R}}K \tag{6.90}$$

where

$$K = \left[\frac{1}{\hat{R}\Big[(\mathrm{v}_f - n)[\hat{R}\theta + 2(x - \hat{R})\sin\theta + \frac{1}{2}\hat{R}\sin 2\theta] + n\pi\hat{R}\Big]}\right] \tag{6.91}$$

The maximum tensile and compressive stresses are located at $\gamma$=0 and $\gamma$=180° respectively (see Figure 6.30). Considering the bending stresses in tension for $\gamma \leq \theta$, we have

$$\sigma_\alpha = E_t\epsilon_\alpha = \frac{E_t\epsilon_t}{x}[\hat{R}(\cos\alpha - 1) + x] \tag{B.29}$$

similarly by multiplying both sides of the equation by $t$ and dividing both sides of the equation by $M$ we have

$$\frac{t\sigma_\alpha}{M} = \frac{t\sigma_t}{M}\left(\frac{1}{x}\right)[\hat{R}(\cos\gamma - 1) + x] \tag{B.30}$$

note that the first term of the right hand side of this equation is equal to Equation (6.90),

therefore by substituting Equation (6.90) we have

$$\frac{t\sigma_\alpha}{M} = \frac{\hat{R}(\cos\gamma - 1) + x}{\hat{R}} K \tag{6.92}$$

Similarly, the compressive bending stresses, for $\gamma > \theta$, we have

$$\sigma_\beta = E_c\epsilon_c = \frac{nE_t\epsilon_t}{x}[\hat{R}(\cos\beta + 1) - x] \tag{B.31}$$

and multiplying both sides of the equation by $t$ and dividing both sides of the equation by $M$ we have

$$\frac{t\sigma_\beta}{M} = \frac{nt\sigma_t}{M}\left(\frac{1}{x}\right)\Big[\hat{R}[\cos(\pi - \gamma) + 1] - x\Big] \tag{B.32}$$

now, substituting Equation (6.90) we have

$$\frac{t\sigma_\beta}{M} = \frac{n\Big[\hat{R}[\cos(\pi - \gamma) + 1] - x\Big]}{\hat{R}} K \tag{6.93}$$

Using Equations (6.92) and (6.93) and solving for the maximum tensile and compressive stresses in the beam cross-section respectively, we have

$$\sigma_\alpha = \frac{t\sigma_\alpha}{M}\frac{M}{t} \tag{6.94}$$

$$\sigma_\beta = \frac{t\sigma_\beta}{M}\frac{M}{t} \tag{6.95}$$

**Horizontal force equilibrium**

Assume a small element of length $\Delta z$ subjected to a force $\Delta F_t$ as shown in Figure 6.31. As the element is in equilibrium the forces satisfy

$$\Delta F_t = F_{tB} - F_{tA} \tag{6.96}$$

From Equation (6.76) we can calculate the tensile forces (for $\gamma \leq \theta$ ), and dividing both sides of the Equation (6.76) by the moment from Equation (6.83) we have

$$\frac{F_t}{M} = \frac{\frac{2E_t\epsilon_t t\hat{R}}{x}}{\frac{E_t\epsilon_t t\hat{R}^2}{x}} \frac{\mathrm{v}_f[(x - \hat{R})\gamma + \hat{R}\sin\gamma]}{\Big[(1-n)[\hat{R}\theta + 2(x - \hat{R})\sin\theta + \frac{1}{2}\hat{R}\sin 2\theta] + \pi n\hat{R}\Big]} \tag{B.33}$$

Simplifying,

$$\frac{F_t}{M} = \frac{2\mathrm{v}_f[(x - \hat{R})\gamma + \hat{R}\sin\gamma]}{\hat{R}\Big[(1-n)[\hat{R}\theta + 2(x - \hat{R})\sin\theta + \frac{1}{2}\hat{R}\sin 2\theta] + \pi n\hat{R}\Big]} \tag{B.34}$$

and introducing the constant $K$ from Equation 6.91 we have

$$\frac{F_t}{M} = \Big[2\mathrm{v}_f[(x-\hat{R})\gamma + \hat{R}\sin\gamma]\Big]K \tag{6.97}$$

Similarly, dividing each of the terms of the right hand side of Equation (6.96) by the moment and solving for each, we have

$$F_{tB} = \frac{F_{tB}}{M_B}M_B \tag{B.35}$$

$$F_{tA} = \frac{F_{tA}}{M_A}M_A \tag{B.36}$$

and substituting into Equation (6.96) we have

$$\Delta F_t = \frac{F_{tB}}{M_B}M_B - \frac{F_{tA}}{M_A}M_A = \frac{F_t}{M}(M_B - M_A) \tag{6.98}$$

where

$$M_B - M_A = \frac{dM}{dz}\Delta z \tag{6.99}$$

Note that the right hand side of the equation is the internal (vertical) shear force $V$, and $dz$ is the length of the infinitesimal element represented in Figure 6.31, thus

$$V = \frac{dM}{dz} \tag{6.100}$$

Now substituting Equation 6.100 into Equation (6.98) we have

$$\Delta F_t = \frac{F_t}{M}V\Delta z \tag{6.101}$$

By definition, the shear flow is the force per unit length in the longitudinal direction of the beam, therefore

$$q = \frac{\Delta F_t}{\Delta z} \tag{6.102}$$

Now, by substituting Equation (6.101) into Equation (6.102) we have

$$q = \frac{F_t}{M}V \tag{6.103}$$

Next, considering the transverse shear $\tau$ from a linear elastic material and the shear flow $q$, we have that

$$\tau = \frac{VQ}{It} \tag{B.37}$$

$$q = \frac{VQ}{I} \tag{B.38}$$

where $Q$ is the moment of the segment area about the neutral axis of the whole section,

the shear stresses can be calculated as a function of the shear flow as

$$\tau = \frac{q}{t} \tag{6.104}$$

The maximum shear stresses at the neutral plane are calculated by substituting Equation (6.103) into Equation (6.104) as

$$\tau = \frac{F_t}{M}\frac{V}{t} \tag{6.105}$$

Similarly, this can be calculated using the ratio compressive force $F_c$ to moment $M$ (for $\gamma > \theta$), by dividing Equation (6.78) by Equation (6.83) as

$$\frac{F_c}{M} = \frac{2n[(\hat{R}-x)(\pi-\gamma)+\hat{R}\sin\gamma]}{\hat{R}\Big[(1-n)[\hat{R}\theta+2(x-\hat{R})\sin\theta+\frac{1}{2}\hat{R}\sin 2\theta]+\pi n\hat{R}\Big]} \tag{B.39}$$

After simplification

$$\frac{F_c}{M} = \Big[2n[(\hat{R}-x)(\pi-\gamma)+\hat{R}\sin\gamma]\Big]K \tag{B.40}$$

# D Fabrication methods for small coupons

### Manual fabrication of the small coupons

The fabrication of the samples was initially done manually in order to gain understanding on the workability of bamboo to longitudinal and transverse cuts. Figure 8 shows the tools and the sequence of steps defined for the manual fabrication. The method is described by the following steps:

- *Marking for initial cut:* the internode section is marked with a mechanical pencil using a releasable cable tie of about 10 mm width to allow for self-adjustment to the culm surface. Cable ties with smaller width are not easily installed perpendicular to the circumference.
- *First cut:* the bamboo section is clamped in a vice by using the node section, and the first cut is done with a japanese saw using a long blade of 250 mm long and 0.5 mm thick with crosscut saw tooth form (see Figure 8 *g*).
- *Marking of coupons:* after the first cut is done, the end cross-sections are perpendicular to the internode, and it is proceed to mark all the coupons in the outer surface as well as the cross-section. The marks are done with a steel square as a guide.
- *Cut of coupons:* the bamboo section is clamped in a vice and all the sections are cut using the japanese saw. The section is rotated continuously in order to cut all the samples around the circumference. Figure 8 *f* shows the sequence of cutting patterns. First the longitudinal cuts are made followed by the transverse cuts.
- *Notch in shear specimen:* the curved rectangular prism for the shear specimen is then marked for the notch with 106.7 degrees opening using a flexible aliminium guide, and the piece is cut off as shown in Figure 8 *j*.

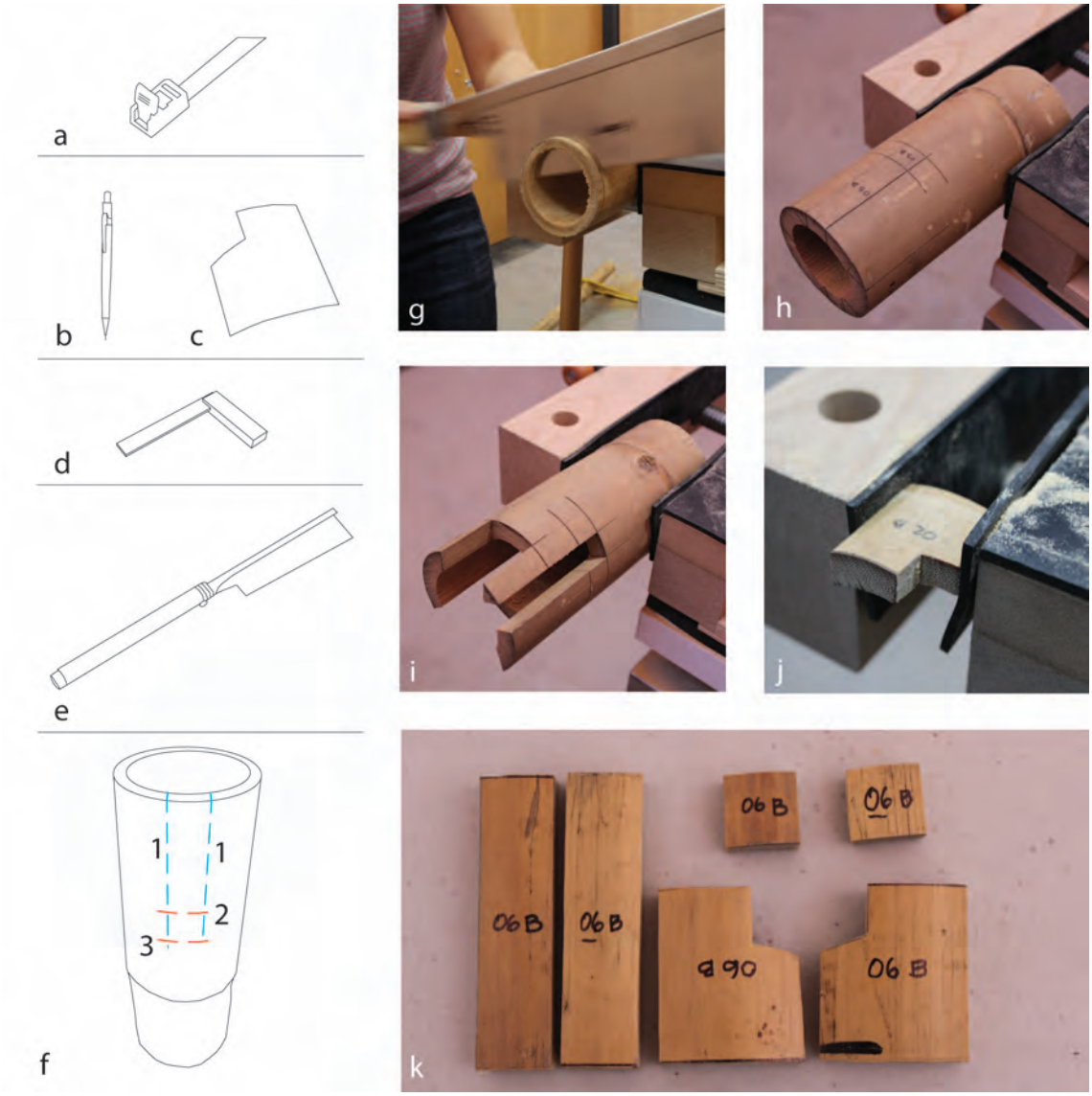


**Figure 8:** Tools and sequence of steps for manual fabrication of samples. The only tools required for manual fabrication are, releasable cable ties (a), mechanical pencil (b), flexible aluminium guide (c), metallic square (d), and japanese saw with crosscut saw and rip saw (e). (f) The sequence of longitudinal and transverse cuttings. The sequence of steps for fabrication are: first end cut (g), marking of the samples in the outer surface (h), clamping and cutting of the samples (i), marking and cutting of the shear sample (j), final cut samples (k).

### Automated fabrication of the small coupons

The automated fabriscation was developed and implemented by members of the bamboo research group at UCL. The author contribution to this was at the initial stages of the fabrication in the definition of the tool paths, in particular for the shear strength sample. The fabrication of the samples was done with a kuka robot arm together with a kress 1050 FME-P. Figure 9 shows the set up for the fabrication process.

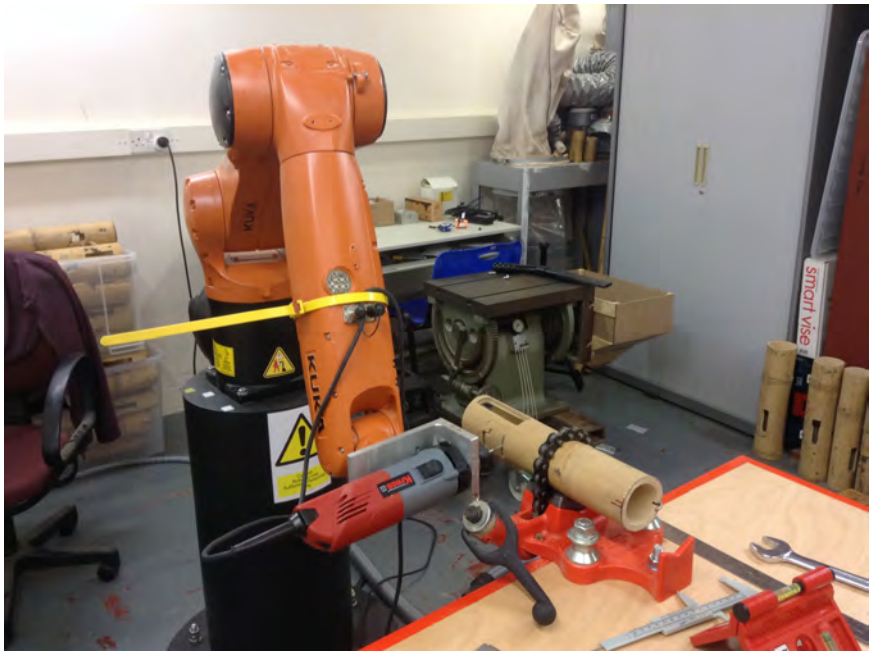


**Figure 9:** Digital fabrication of small coupons on a guadua section.

# E Geometric properties of full culms subjected to bending

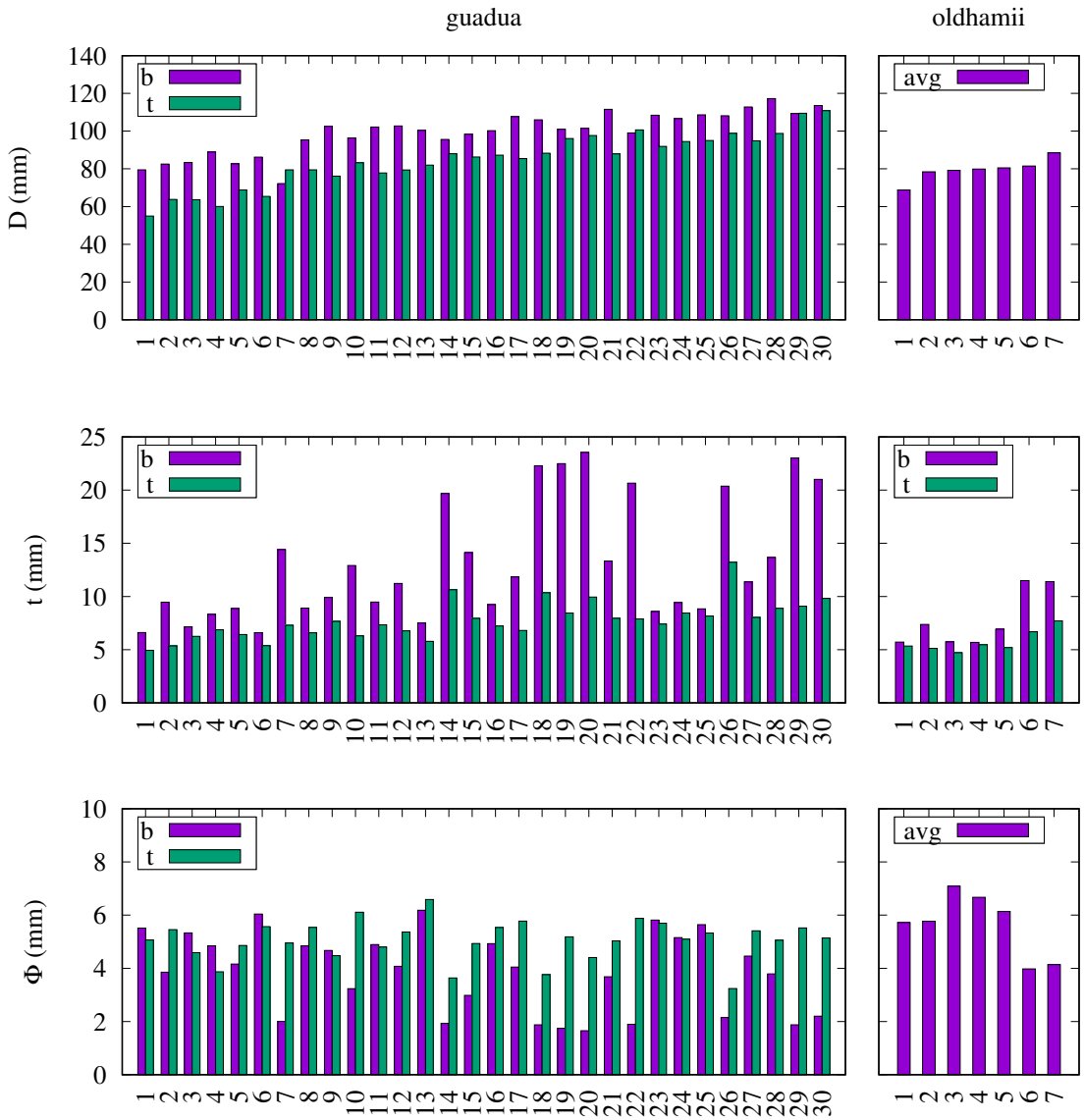


**Figure 10:** Geometrical properties of full culm subjected to bending tests.

# F Results of mechanical testing on small coupons

The average physical and mechanical properties for guadua and oldhamii species are provided in Table 1, and the relationships between mechanical properties and physical and geometric properties in Figures 11 and 12.

**Table 1:** Physical and mechanical properties obtained from small coupons.

| | | Guadua species | | | | |
|---|---|---|---|---|---|---|
| | | $E_c$ (N/mm$^2$) | $f_c$ (N/mm$^2$) | $f_v$ (N/mm$^2$) | $v_b$ | $\rho$ (kg/m$^3$) |
| bottom | mean | 18079 | 59.50 | 11.46 | 0.43 | 726.16 |
| | $SD$ | 3980 | 13.8 | 1.71 | 0.04 | 49.8 |
| | $CV$(%) | 22.0 | 23.1 | 14.9 | 9.3 | 6.9 |
| top | mean | 19234 | 57.54 | 11.97 | 0.42 | 722.5 |
| | $SD$ | 4438 | 11.2 | 2.25 | 0.03 | 85.4 |
| | $CV$(%) | 23.1 | 19.4 | 18.8 | 7.1 | 11.8 |
| culm | mean | 18741 | 58.3 | 11.76 | 0.42 | 724.0 |
| | $SD$ | 4262 | 12.3 | 2.1 | 0.04 | 72.4 |
| | $CV$(%) | 22.7 | 21.0 | 17.4 | 8.8 | 10.0 |
| | | Oldhamii species | | | | |
| | | $E_c$ (N/mm$^2$) | $f_c$ (N/mm$^2$) | $f_v$ (N/mm$^2$) | $v_b$ | $\rho$ (kg/m$^3$) |
| bottom | mean | 20217 | 67.15 | 12.50 | 0.44 | 705.80 |
| | $SD$ | 7085 | 8.54 | 2.86 | 0.06 | 76.61 |
| | $CV$(%) | 35.0 | 12.7 | 22.9 | 13.6 | 10.9 |
| top | mean | 20297 | 68.61 | 13.07 | 0.49 | 762.45 |
| | $SD$ | 7558 | 12.62 | 2.84 | 0.05 | 80.50 |
| | $CV$(%) | 37.2 | 18.4 | 21.7 | 10.2 | 10.6 |
| culm | mean | 20255 | 67.85 | 12.77 | 0.46 | 732.9 |
| | $SD$ | 7287 | 10.68 | 2.86 | 0.06 | 83.2 |
| | $CV$(%) | 36.0 | 15.7 | 22.4 | 13.0 | 11.4 |

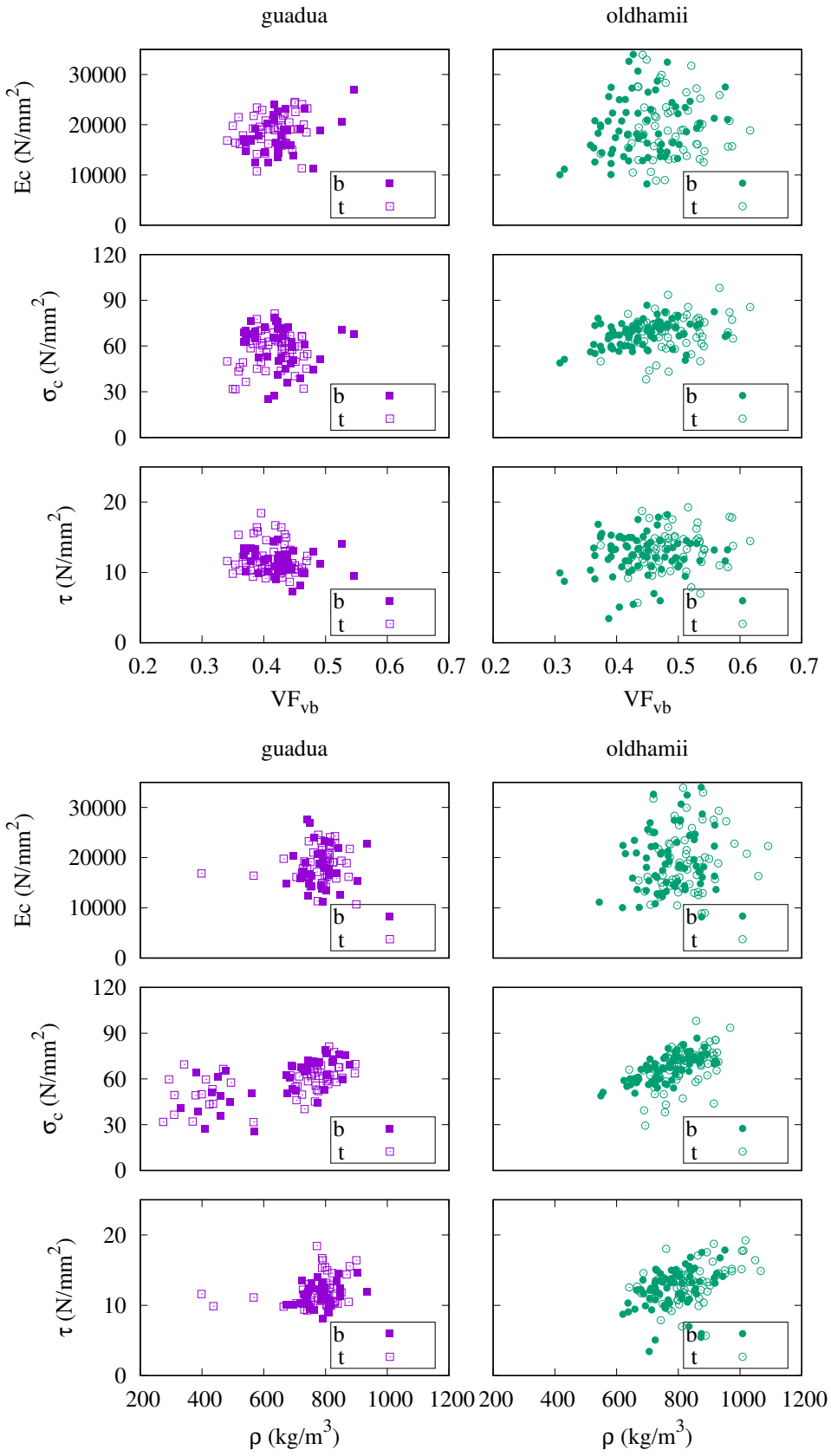


**Figure 11:** Relationships among $E_c$, $\sigma_c$ and $\tau_c$ against physical properties.

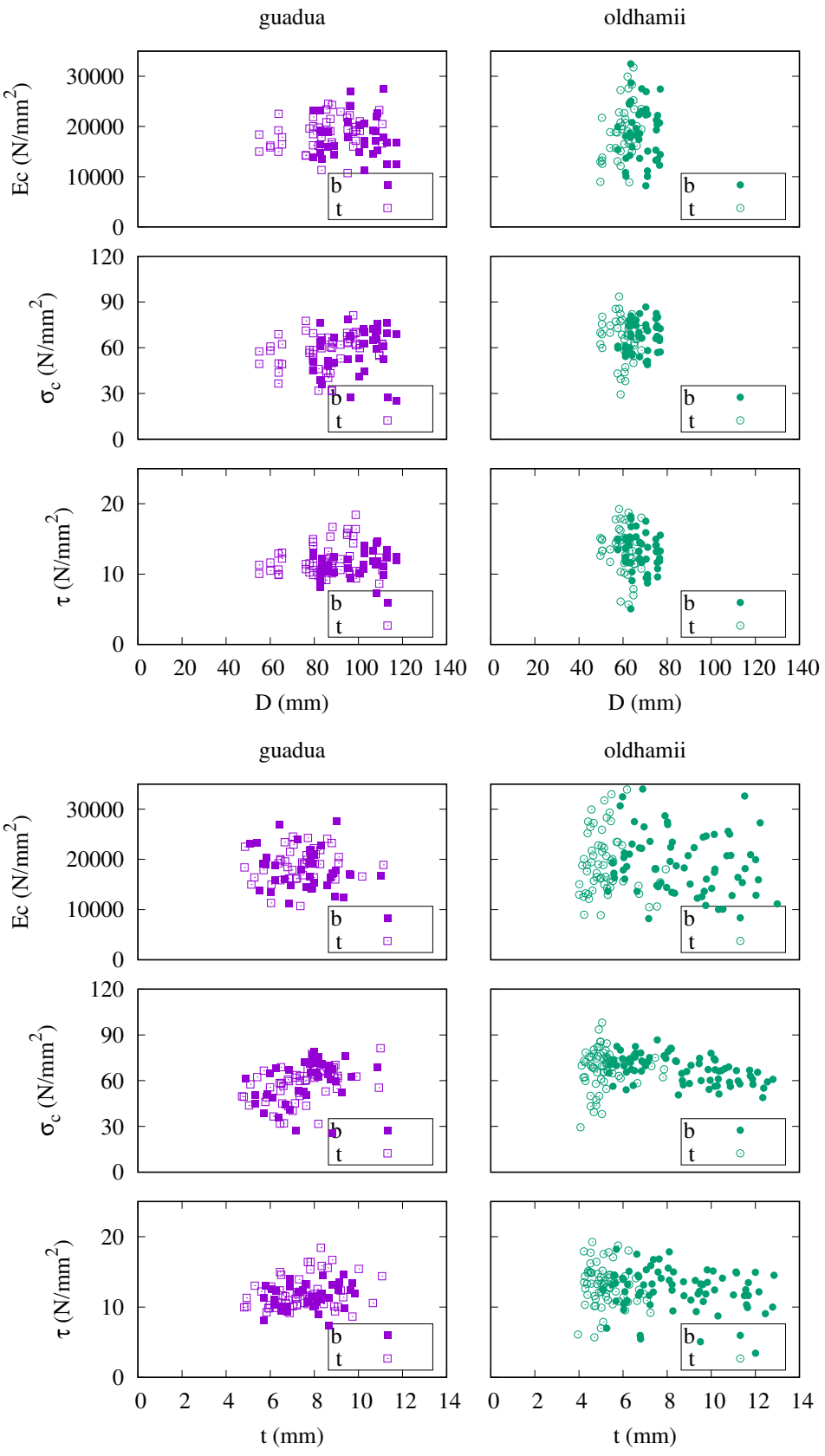


**Figure 12:** Relationships among $E_c$, $\sigma_c$ and $\tau_c$ against geometrical properties.

# G Fabrication methods for timber connections

This appendix reports on the fabrication of timber blocks for the connection systems. Four different methods to machine the groove in a timber block were explored with the aim of assessing the practicality of the fabrication of the timber connection system for bamboo culms.

Figures 13a and 13b shows a timber block fabricated with a manual milling machine using a four flute drilling bit straight of 8 mm. The curved finished was accomplished by sanding the surface with a oscillating spindle sander (see Figure 13c). Computer numerical control (CNC) was also explored as an automated method with a Roland Modela Pro II miller/router machine, using a drilling bit of four flute of 6 mm (see Figures 13e and 13f). Similar to the previous method, the groove surface was also sanded. Another method explored was machining the groove using a holesaw. However, the length of the drill bit was a limitation, as these holesaws are usually not long, and thus requiring to rotate the timber block 180° to cut the groove from both sides. Furthermore, only one timber block at a time can be machined. The last method uses the circular saw to create the grooves in the timber blocks as shown in Figure 14. Contrary to the previous methods, in this method the sharp stepped surface was used as final finishing. The circular saw was 254 mm in diameter and 1.75 mm in thickness. The thin thickness of the blade allowed for a smoother surface in comparison with the previous methods. The steps to fabricate the timber blocks using the circular saw are provided below:

- Create the longitudinal groove in the timber plank on one side
- Create the groove in the transverse direction of the timber plank on the other side (only for middle timber blocks)
- Cut each individual timber block at roughly 60° using a circular saw
- Sand the stepped surface of the groove to provide a smooth finish, if required, with a oscillating spindle sander
- Drill the four holes for the steel threaded rods in each of the timber blocks (1 mm clearance allowance in diameter)

The fabrication of the groove with all the methods tested was done cutting linearly in the longitudinal direction of the timber plank (i.e. the longitudinal direction of the fibre). This allowed simple set ups, that facilitates the fabrication. For example, the end mills for the CNC machine are always in the direction normal to the surface of the timber plank. However, during several built prototypes it was observed that having the groove in the longitudinal direction could induce splitting of the timber when the forces are applied through the steel threaded rods. To overcome this, a thin steel plate was used on the top of the timber blocks in order to provide a more evenly distribution of forces to the timber block through the steel plate and thus minimising the moments generated


**Figure 13:** Fabrication methods for the timber connection. (a) Rough milled surface. (b) Milled edge. (c) Sanding of the groove to provide smooth surface. (d) Fabrication of the groove with a holesaw. CNC milling of the groove in the longitudinal (e) and transverse (f) directions. Finished groove in the longitudinal (g) and transverse (h) directions. (i) Transverse cut of the with a circular saw.

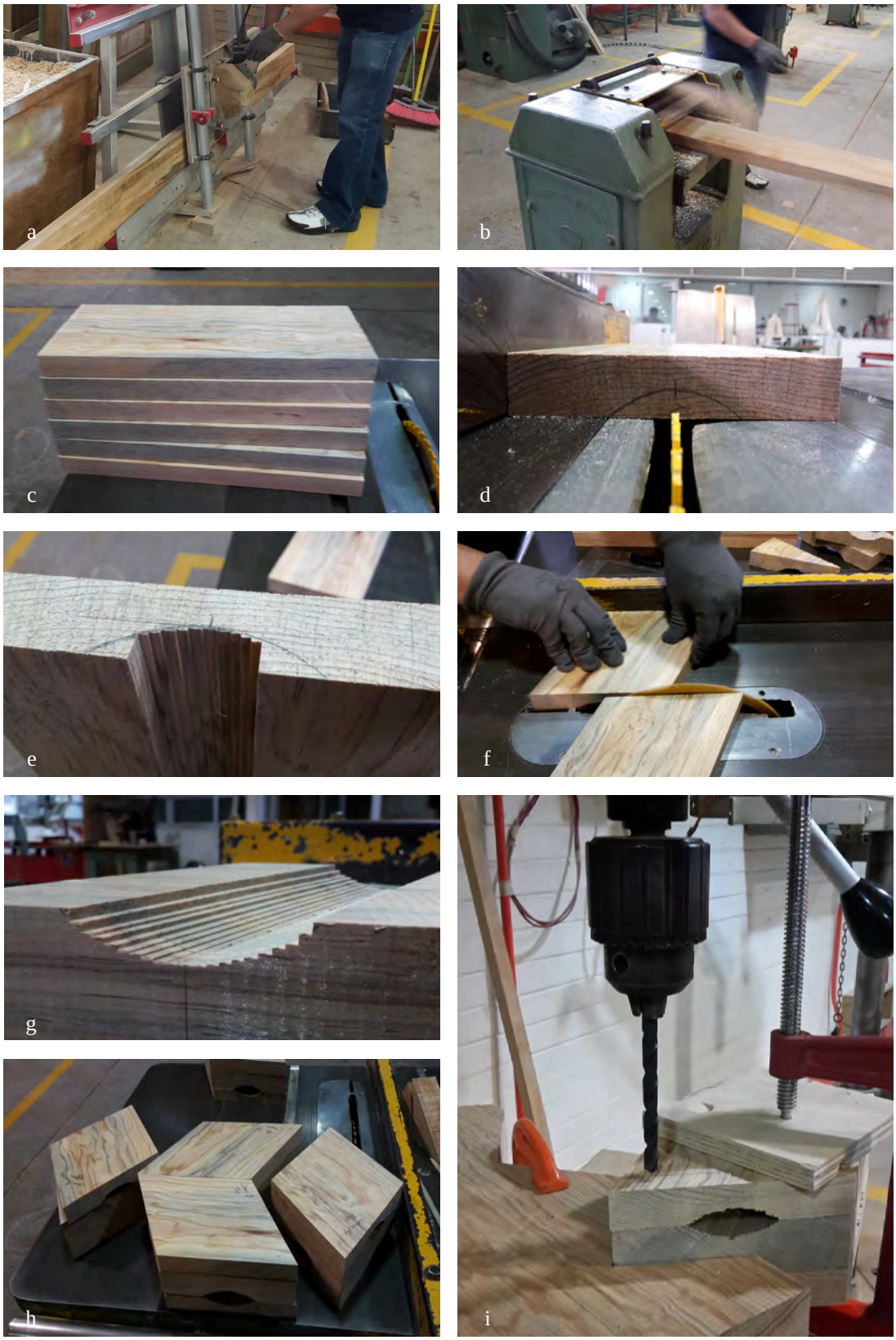


**Figure 14:** Fabrication method for the timber connection. (a) Longitudinal cut of timber planks. (b) Sander planner machine to create a flat surface. (c) Timber plank sections to use for each connection. (d) Cutting of the groove. (e) Groove cuts. (f) Transverse cutting. (g) Groove finishing. (h) Timber blocks. (g) Drilling of the holes.

at the midspan of the block, and therefore, minimising the deflections which might cause splitting of the timber blocks. Further design iterations considering the direction of the grooves, the timber material and the fabrication methods are required.

One of the drawbacks of using a CNC milling machine is the reach of the spindle. The size of the CNC used in this study is 500 × 400 × 125 mm, therefore a maximum of three timber blocks can be machined in one go. A set of three timber connections were fabricated using this method to assemble a three-element reciprocal module. However, for an entire structure this process might not be suitable as it will take a considerable amount of time. New robotic fabrication for timber (Menges et al., 2017), might be a suitable technology to overcome this issue, and adapt settings where multiple connections can be machined at the same time.

Additionally, the effect of the stepped surface of the groove, shall be investigated against the smooth surface achieved by sanding the groove, as this will reduce the fabrication time. Nevertheless, if the groove surface is not to be machined, care must be taken in the milling methods to provide a better quality finish without indentations or chips attached to the milling surface.

Overall, milling the groove using automated systems such as CNC was found to be very efficient, reducing human labour time and having the advantage to parametrically defined cutting pattern for each groove. Nevertheless, as the groove is not an intricate geometry, it can effectively be machined using alternative methods when automated systems (CNC or robotic machining) are not available. Further automated methods such as robotic fabrication tools, might allow for a more efficient process by increasing the area which can be programmed to be milled at the same time.

# H Marking of bamboo culms for assembly

This appendix presents two different methods developed for the location and marking of the position of the connections in the outer surface of bamboo culms. The marking jig method is proposed by the author and the marking block method is proposed by Dr. Rodolfo Lorenzo. The aim is to use a marking system as a guide for linking the position of bamboo culms in the digital and the physical models.

## Marks for different connection systems

The position and number of marks on bamboo culms for assembly depends on the type of connection system. Figures 15 and 16 shows the marking points and lines in the bamboo culms as well as the marking guides in the components for the two connection systems presented in Chapter 8.

The marking system consists of three steps. The first is to find the points from which the lines are to be marked and used as guidelines for the installation of the components of the connections. One single point per culm is required for the timber connection and two points per culm for the aluminium connection. The points in the culms for the timber connection corresponds to the intersection between the axis of the eccentricity and

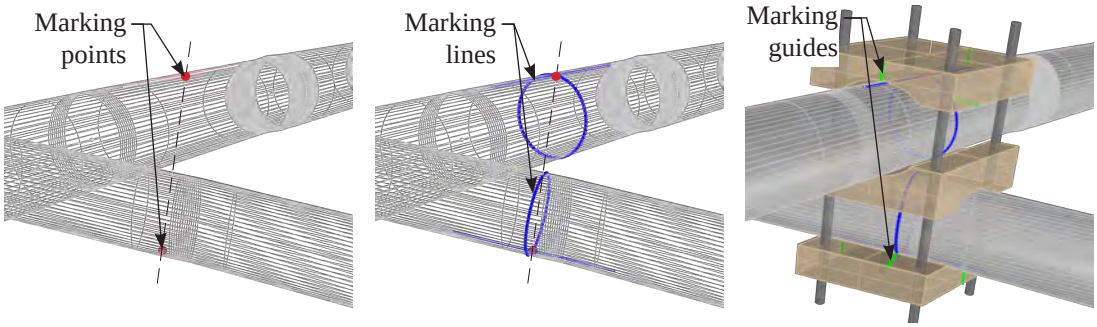


**Figure 15:** Marking points and lines in bamboo culms and marking guides in timber blocks.

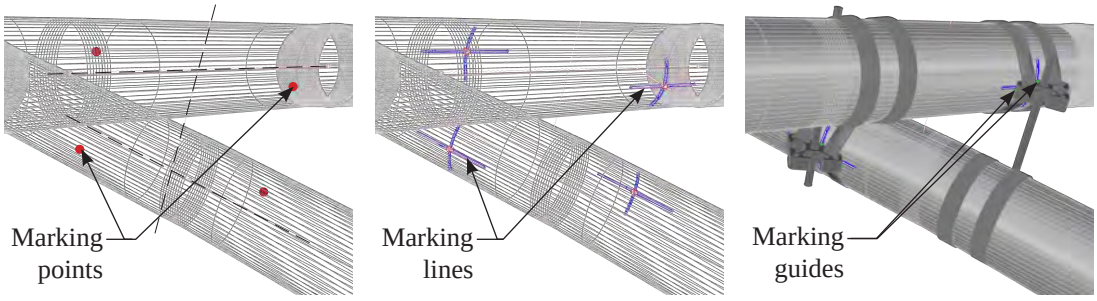


**Figure 16:** Marking points and lines in bamboo culms and marking guides in aluminium components.

the brep representing the culm. For the aluminium connection, the points in the culms represent the position of each aluminium component. The identification of these points in the bamboo culm is crucial, and this is done using one of the methods described below. After these points are located and marked, the second step is to create the marking lines in the longitudinal and around the circumference direction. Finally, the last step is to create the marks in the connection components (timber and aluminium) to match up the marking lines in the bamboo culms.

### Marking jig method

The marking system consists of a longitudinal jig equipped with a measuring tape, a right angle ruler and a rope to use as guide. Figure 17 shows an schematic figure of the jig. The bamboo culm rest upon two aluminium v-blocks, located just below the rope. This simple method is designed so it can be installed in any workshop bench.

The procedure to identify the position of the marks is two step. The first step is to place the culm in the v-blocks with the reference point in the vertical direction (i.e. pointing upwards). Then, the longitudinal distance between the reference mark and the connection is taken using the longitudinal measuring tape and the right angle ruler. The mark is created in the culm at the intersection between the ruler and the rope (see Figure 18). The second step is to find the actual marking point in the culm around the circumference. Using a flexible measuring tape, the length in the circumference is taken in the clockwise or anticlockwise direction to locate the position of the connection around the cross-section, where the marking point is created.

The longitudinal and circumferential distances are obtained directly from Rhinoceros (McNeel, 2017) using the data derived in Chapter 4. In general, this method is relatively simple to carry out. However, it does not consider the errors that can arise with very irregular culms, because the longitudinal directions in the jig are taken considering a straight line as a guideline.

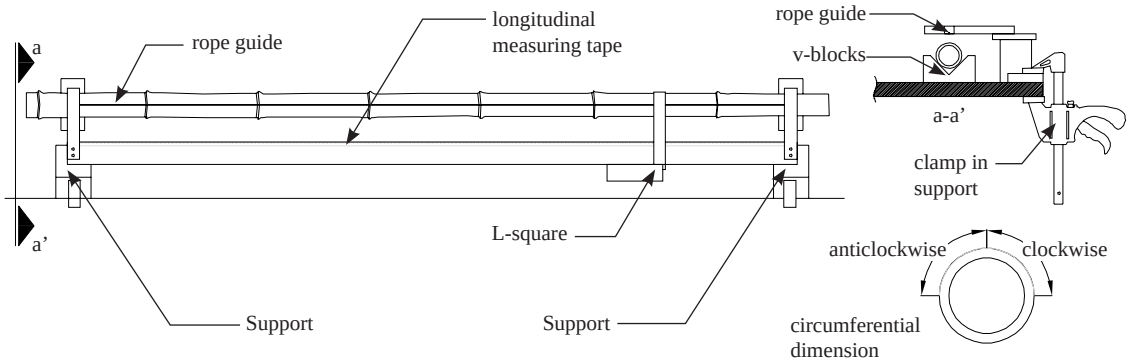


**Figure 17:** Set-up of marking jig.

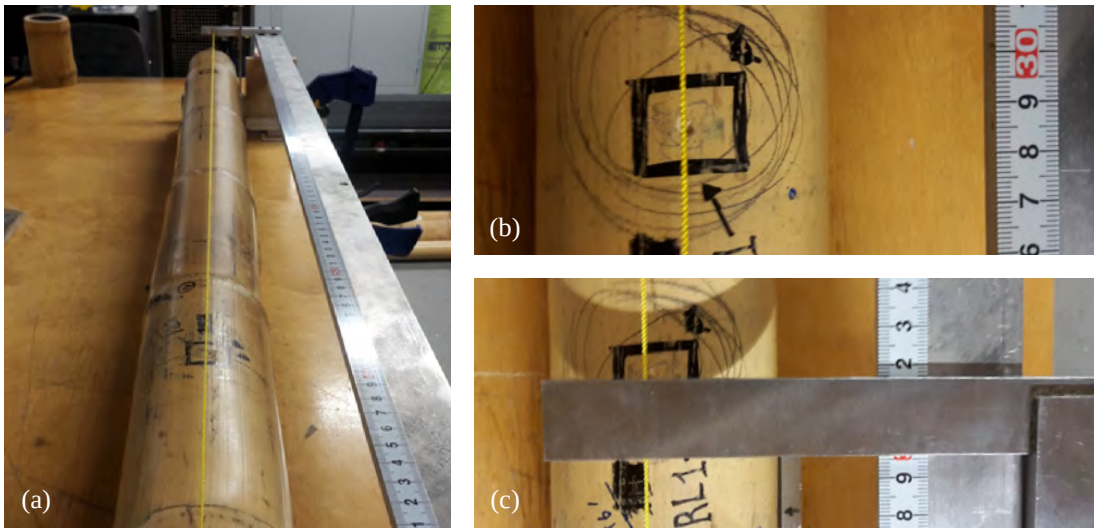


**Figure 18:** Marking jig for identification of position of connections.

## Marking blocks method

This method creates a three-dimensional triangulation between the reference point and two points at both sides of the marking point to identify the position of the connections. The method consists of two blocks, one for the reference point and another for the marking point used as guidelines (see Figure 19). The idea is to install one block in the reference point and then find the marking point by moving the other block around the surface of bamboo, until the lengths $b$ and $c$ are reached (see Figure 19a).

The geometry of the triangle (i.e. length of the sides, angles) and position are defined using the brep geometry created in Chapter 4 and the dimensions of the marking blocks. The position of point $A$ is known by the reference point, the position of points $B$ and $C$ are defined by the lengths $b$ and $c$, and the length $a$ is fixed. The reference and marking points are defined as shown in Figure 19b. The reference block is located using a small shaft that sits on the indentation made as reference point. For the marking block, the contact

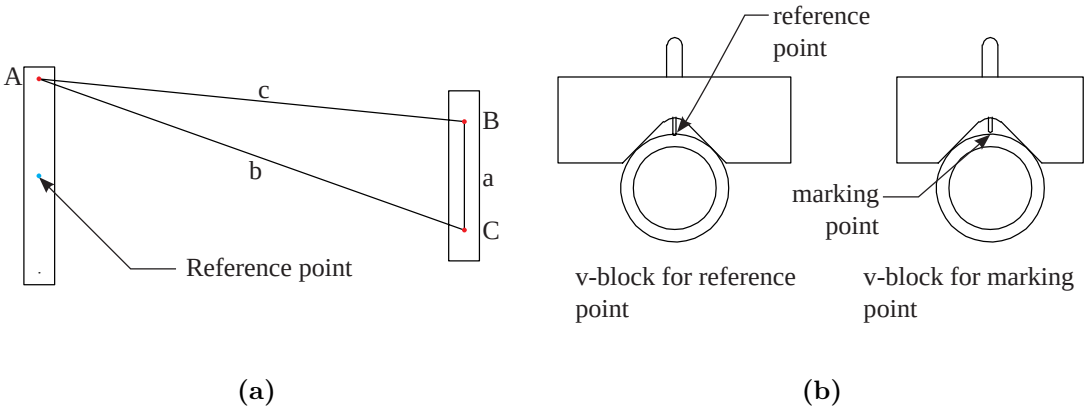


**Figure 19:** (a) Triangulation from reference point to marking point. (b) Marking blocks.

between the small shaft and the bamboo culm indicates the position of the marking point.

The first step is to clamp the bamboo culm to a workshop bench. Once the culm is clamped, the v-block for the reference point is installed as shown in Figure 20a. To find the position of the marking block, the v-block for marking point is installed loosely in the bamboo culm to allow for movement, and the distances $b$ and $c$ are taken with a measuring tape until these coincide with the distances in the model (see Figure 19b). Afterwards, the v-block is tighten and the mark is made using the small shaft as guide.

There are four points from which the triangulation can be taken from the v-block at the reference point (see Figure 21). The four corners of the v-block installed at the reference block can be used as guidelines. This allows for identification of marking points around all the circumference.

Similar to the previous method, the culm can be clamped in any workshop table to facilitate the installation. One advantage of this method is that it takes into account the out-of-straightness of the bamboo culm. However, the main drawback is the procedure, as it requires extra steps to clamp the culm, to install the v-block for the reference point

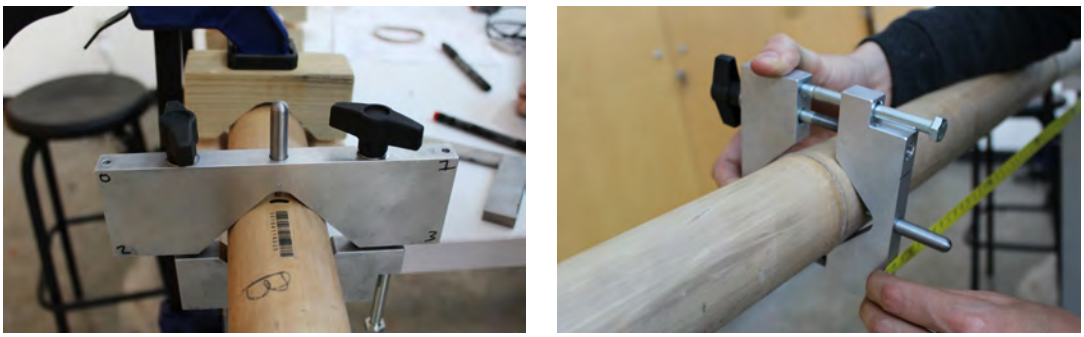

**(a)** **(b)**

**Figure 20:** (a) V-block for reference point. (b) V-block for marking point.

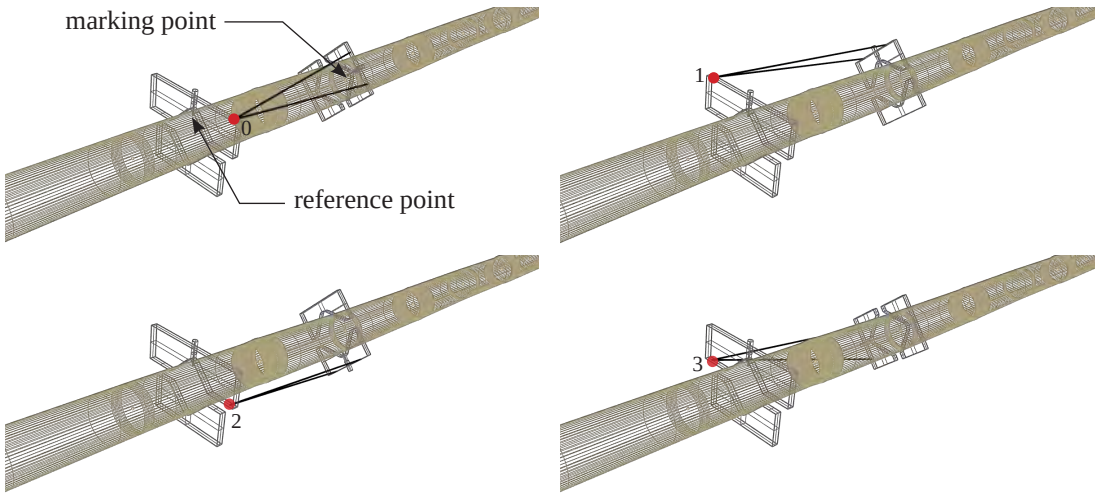


**Figure 21:** Marking blocks measuring positions.

and to find the position of the v-block for the marking point. In addition, for those points located at the surface of the bamboo facing downwards with respect the clamped position, the marking is non-trivial.

# I Assembly methods

This appendix presents the assembly methods for the two potential connection systems introduced in Chapter 8 and a proposal for the assembly method for reciprocal structures based on pre-assembled modules to facilitate the on-site construction process.

The majority of the research of reciprocal structures is focused on the geometrical aspects and the connection systems. There is very little information regarding the construction sequence. However, it is a non-trivial process, as these systems acquire stability gradually during the erection process, and it can temporarily lead to instabilities while some of the elements of individual modules are still not connected (Thönnissen, 2014). Emphasis is placed not only on the construction method but also on the guides and references used for assembling the elements at the correct position, including marking of the exact positions where the culms are to be connected to the components of the connection systems.

## Assembly of timber connection

The assembly process of a three-element module was done in sequence using the marking lines as guides (see Figure 22). For the first step, the components of one of the connections are installed with the nuts placed at both extremes of the steel threaded rod to provide enough clearance. The two bamboo culms corresponding to this connection are slide through the timber blocks, and when the marks of the bamboo coincide with those of the timber blocks, the neoprene sheets are installed and then the nuts are fixed.

The installation of a single timber connection provides enough rigidity between both

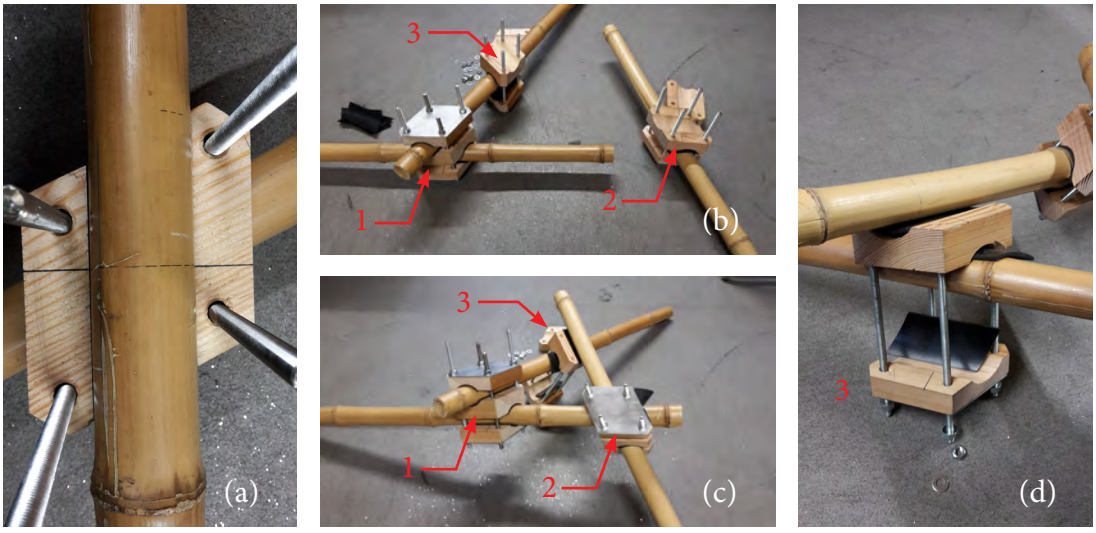


**Figure 22:** Assembly of the timber connections. (a) Marking of the timber blocks and bamboo culms. (b) Assembly of connection 1 and installation of bottom part of connections 2 and 3. (c) Connection 2 is loosely fixed. (d) Top timber block of connection 3 is installed, and connection 2 and 3 are fixed together.

culms. Then, once the first connection is installed, the position and direction of the two culms jointed is defined. The next step consists of installing the bottom part of the other two timber connections in their respective culms. After that, the two culms corresponding to the top part of those timber connections are placed in position. Then both connections are completely installed but loosely tighten, so that in the end both are fixed at the same time to prevent ended up with a crooked shape.

One of the issues during the assembly of these connections were the neoprene sheets. These were not attached to the timber blocks by any means and they were placed in position only by bearing pressure. Thus, especially for the last two connections it was difficult to keep them in place. In addition, the tolerances for the holes in the timber and steel plates is crucial. The connections shown in Figure 22 were easily assembled without any issue while sliding all the components through the steel threaded rods. The tolerance of the drilled holes was 1 mm in diameter. Nevertheless, for the connection shown in Figure 23, although the timber blocks were fabricated within tolerances, the drill holes in the steel sills were off from its centre by a maximum of 6 mm. This hindered the installation of the connection components, since these were not easily sliding through the steel threaded rods. Due to the lack of time it was not possible to fabricate again the steel sills.


**Figure 23:** Assembly of timber connection with a metal sill on top of timber blocks, and crack on timber block.

Furthermore, cracking of the timber blocks prior to installation was observed (see Figure 23). This was associated with the fabrication procedure. Since the grooves were machined in the longitudinal direction of the fibre to ease the process the bending forces applied to the timber block during assembly split easily the timber block. Although, the steel plates helped to keep the timber blocks in position, the direction of the groove for the top and bottom block shall be considered for future connections.

### Assembly of aluminium connection

The assembly sequence of a three-element module for aluminium connections is similar to that of the timber connections. First, one of the connections is fixed, and then the other

two are loosely installed in position to finally fixed them together by tightening the hose clips. In order to facilitate the assembly process, the vertical (i.e. steel threaded rods and packing) and the aluminium components were pre-assembled (two per connection). For each vertical component, one of the aluminium components was fixed, and the other was free to rotate so that the angle between both aluminium components can be adjusted during assembly (see Figure 24a). Note that this angle corresponds to the angle between both culms. This rotation was achieved by adding a double nut to the aluminium component for allowing rotations as shown in Figure 24b. By doing this, the length of the connection (i.e. the eccentricity) is fixed and only the angle between aluminium components (i.e. the angle between culms) was adapted during the assembly.

One of the major challenges was to have both vertical components parallel to each other. The modules were assembled on the floor, and although both vertical components were tightened together to prevent ended up with skew connections, the lack of rigidity of this system (prior to the full assembly of a three-element module only) hindered the installation of individual pre-fabricated components (i.e. vertical and aluminium components together) in the right direction. Furthermore, marking lines in the specific location of the aluminium components was crucial. Preliminary modules were assembled by marking only the position of the connection in the longitudinal direction, but it was very difficult to find the direction parallel to the eccentricity without reference to the position around the circumference of the culm.

Several clamping systems were tested including steel bands (BAND-IT, 2015) assembled with clips or buckles (see Figure 25) and metal hose clips (Jubilee, 2016). All the band-its tested allowed rotation of the bamboo culm in the longitudinal axis. Therefore, it was not possible to fix the aluminium component in position using these band systems. On the other hand, the worm drive steel hose clips (Jubilee, 2016) provided a clamping force enough to fixed the aluminium component into position. The torque applied to the clip was not measured. However, these were tighten until the screw fitted into the last possible tooth of the strap. If greater torque was applied to the screw, the screw did not

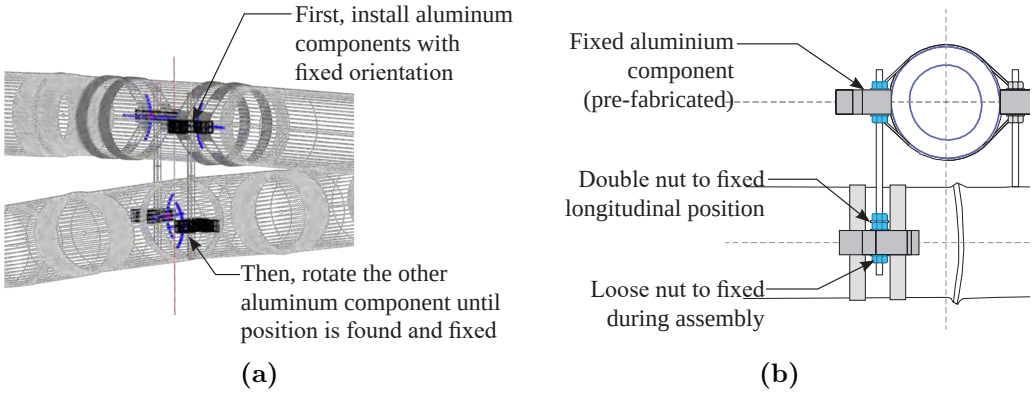


**Figure 24:** (a) Steps to assemble aluminium connection. (b) Double nut to allow rotations or aluminium component.

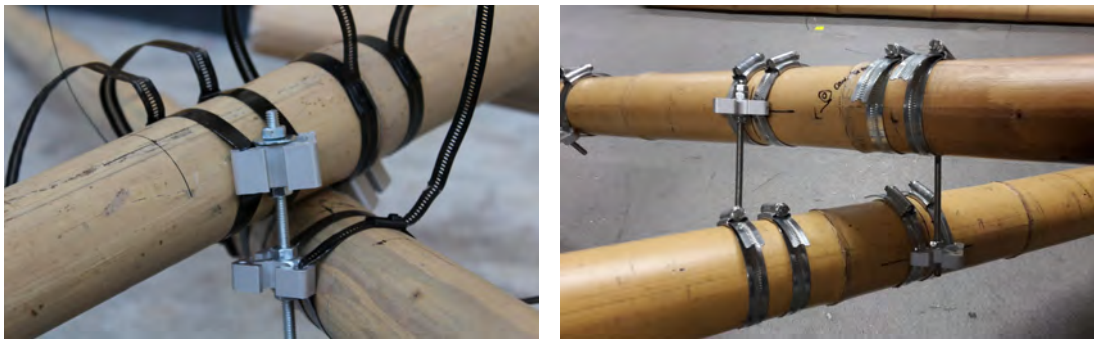

**Figure 25:** Assembly of aluminium connection with banding system and worm drive steel hose clips.

reach the next tooth of the strap. The hose clamps were fixed with a cordless screwdriver to facilitate and speed up the assembly process. No cracks on the culms were observed using this method.

### Assembly sequence of bamboo reciprocal structures

The assembly sequence proposed here was designed in view of preventing instabilities while assembling reciprocal structures. It consists of pre-assembling the majority of the elements as three-element modules in a controlled environment.

These pre-fabricated modules can be lifted with the help of adjustable props and jointed to adjacent modules minimising the amount of assembly that needs to be done on-site. See for example the sequence of elements presented in Figure 26, the modules corresponding to the elements in the faces (i.e. faces of the underlying mesh) labelled as 0 are to be assembled individually as a three-element module. A total of 17 steps are required to built the whole structure using this modular method, including the individual culms around the boundary. Figure 27 illustrates some of the steps of the sequence of

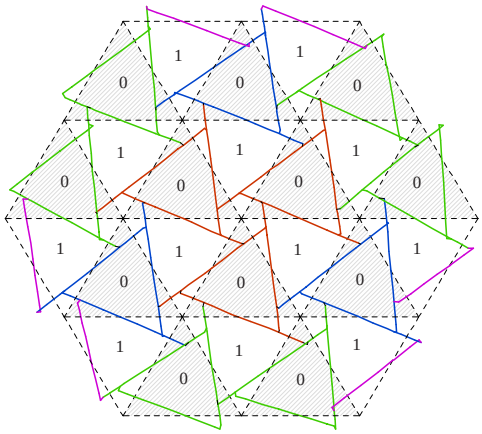

**Figure 26:** Assembly sequence for reciprocal structure with triangular tessellation of degree 6.

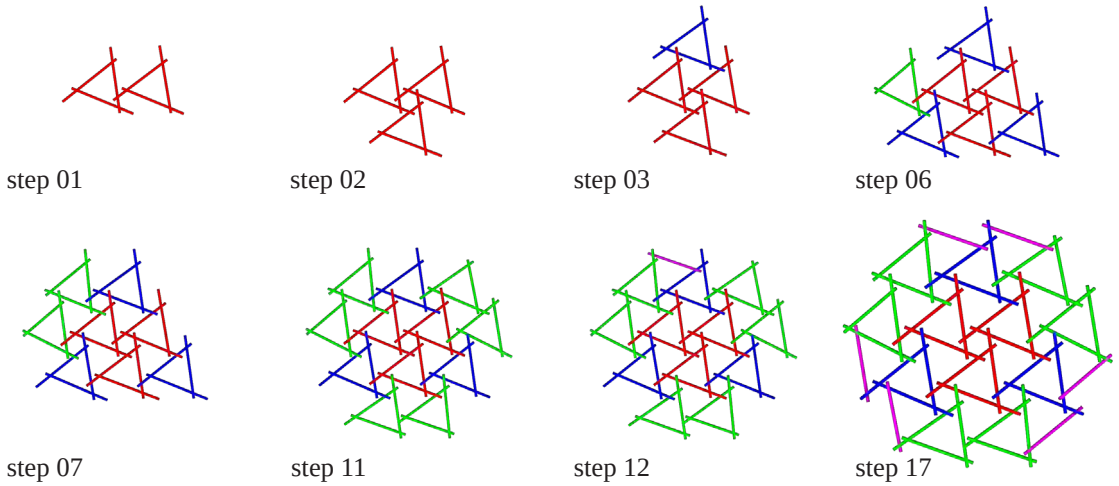


**Figure 27:** Construction sequence.

modules jointed together.

The structure shown in Figure 28 was assembled using this method. The shape of the structure was designed by Dr. Rodolfo Lorenzo. It was assembled with the oldhamii bamboo culms used for the determination of the SBD properties presented from Chapters 4 to 6. The bamboo culms were marked, prepared and assembled together with members of the bamboo research group of UCL at UNAM university during two research stays.

The geometry of the structure was measured using the six culms in the middle forming the hexagonal shape, the geometric error between the digital and physical model measured using a laser point is 12.8 mm, equivalent to 1% error. During the assembly the modules were lift and several temporary props were used. As the structure was built with the aim of assessing the assembly method and measuring the geometry, rather than evaluate its structural performance, the aluminium connections were not provided with packing in the vertical components. Therefore, the geometry was easily disturbed when the structure was moved or lifted. Further tests to evaluate the stability of the system using this method are required.

**Figure 28:** Reciprocal structure assembled using modular sequence.

# J Forces and moments in elements of bamboo reciprocal structure

The plots below show the comparison in magnitude of the forces and moments for the models 2, 3, 4 and 5. In order to compare the forces and moments among the different models, the horizontal axis was normalised to the quantity of elements in the structure. For example, in Figure 31b for the bending moments in the $z$ direction, there are 790 elements for the discretised and 204 for the equivalent model.

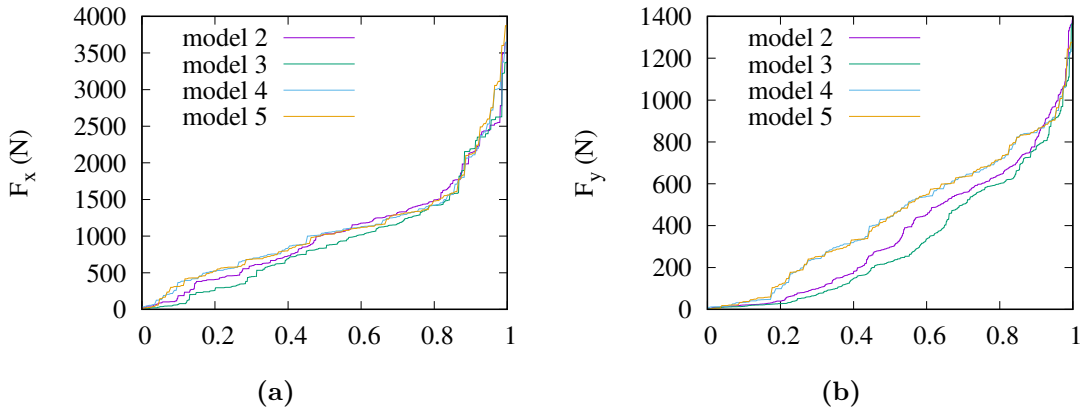


**Figure 29:** (a) Axial forces, $F_x$. (b) Shear forces, $F_y$.

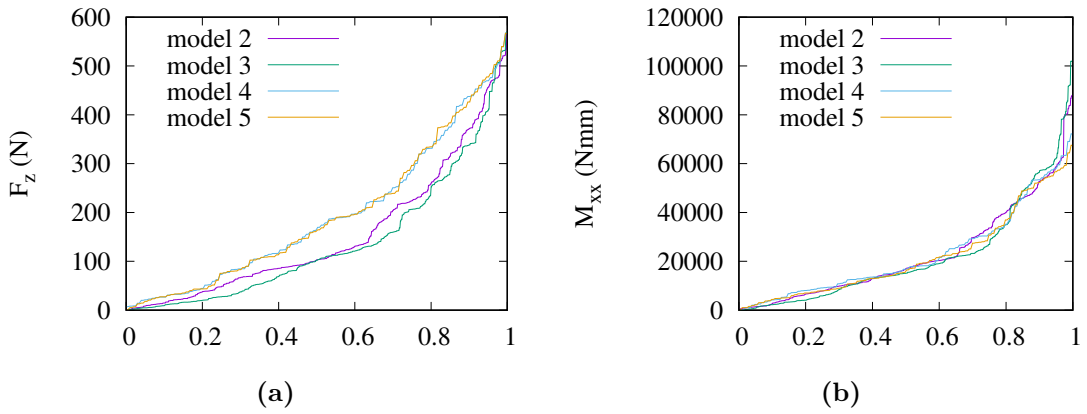


**Figure 30:** (a) Axial forces, $F_z$. (b) Torsion moments, $M_x x$.

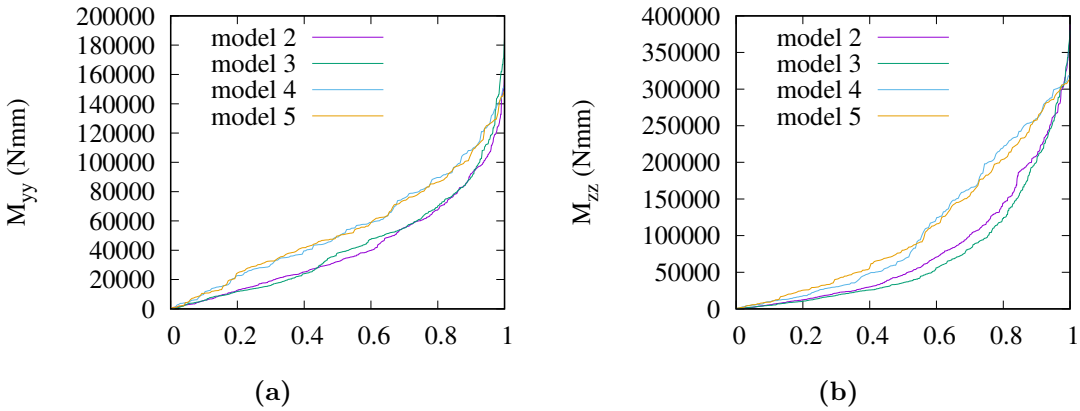


**Figure 31:** (a) Bending moments, $M_{yy}$. (b) Bending moments, $M_{zz}$.

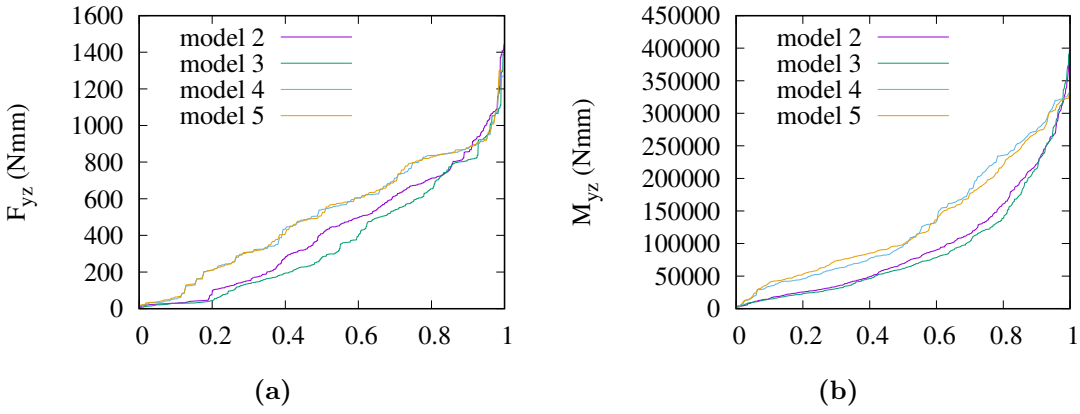


**Figure 32:** (a) Resultant of shear forces, $F_{yz}$. (b) Resultant of bending moments, $M_{yz}$.